

# **AN INVESTIGATION OF DIAMOND THIN FILM DEPOSITION ON STEEL SUBSTRATES**

**VOJTĚCH KUNDRÁT**

Doctor of Philosophy

**ASTON UNIVERSITY**

October 2015

©Vojtěch Kundrát, 2015

This copy of thesis has been supplied on condition that anyone who consults it is understood to recognise that its copyright rests with its author and that no quotation from the thesis and no information derived from it may be published without appropriate permission or acknowledgement.

# Summary

The motivation behind this work was the exploration of the possibility of diamond deposition on steel substrates for low friction and low wear applications. Materials such as tungsten carbide are commercially available as diamond coated tools, where the diamond coating greatly extends the tool lifetime and performance. The diamond deposition on steel differs in terms of limitations to the diamond deposition on tungsten carbide. The main limitations of steel are its sensitivity to elevated temperatures which are commonly used for diamond deposition and a large difference in the thermal expansion coefficients of steel and diamond. Overcoming those challenging limitations would result in an introduction of competitive products for many applications. This project was a pioneering work in diamond deposition on steel substrates at Aston University in co-operation with Teer Coatings Ltd (Miba group).

The main focus was on the use of an interlayer as a facilitator of enhanced diamond growth and its adhesion towards the steel substrate. Particular attention was given to amorphous carbon coating being a buffer layer for subsequent diamond growth, followed by the investigation of diamond film growth on tungsten coated steel substrates. Interlayers were deposited using the magnetron sputtering technique at Teer Coatings. Diamond thin films were deposited at Aston University using microwave plasma chemical vapour deposition (CVD) with methane and hydrogen as a deposition gas mixture. Investigation of diamond growth from amorphous carbon films coated on steel substrates was found despite the initial promising results to provide low diamond nucleation coverage resulting samples with a sparse population of diamond crystals. The focus of the study changed into an investigation of diamond growth on steel substrates coated with metallic interlayers. As an enhancement for diamond nucleation a pre-treatment of seeding the substrates with nanocrystalline diamond particles, transferred onto the substrates by immersion into a diamond suspension, was developed and used further in this work.

Tungsten coating was chosen as the main interlayer material for its diffusion barrier properties, carbide formation, specific thermal expansion coefficient and no inclination to hydrogen embrittlement. The direct tungsten deposition onto a substrate was found problematic and was initially solved by the development of a structured CrW interlayer (1  $\mu\text{m}$  thick) on which an optimization of diamond CVD deposition conditions was performed. The need for a reliable temperature measurement resulted in creation of a setup with thermocouple mounted at the bottom of a substrate holder and a suitable calibration of the setup to be able to calculate the temperature of the substrate surface.

CrW was found to have poor adhesion properties and a new MoW interlayer (1  $\mu\text{m}$  thick) possessing excellent adhesion characteristics was developed. The diamond films deposited using previously optimised diamond deposition conditions was found to be at 785 °C. The  $\approx 250$  nm thick diamond films showed a good adhesion strength while the MoW interlayer was proved to be an effective diffusion barrier. The previously optimised diamond deposition conditions were found to deteriorate the steel substrate's properties and further low temperature diamond deposition conditions were optimised for diamond growth at 650 °C. The resulting  $\approx 250$  nm thick films showed poor diamond adhesion characteristics due to weaker bonding between diamond and the substrate. The steel substrate did not undergo any softening during the diamond deposition. The effect of different diamond deposition temperatures, as well as the different thickness of the MoW interlayer on stress within diamond film, was studied. Lowest amount of compressive stress of 1.6 GPa was found for a sample coated with the thickest MoW (8.3  $\mu\text{m}$ ) and diamond deposition conditions at 650 °C. The sample showed superior adhesion upon Rockwell C indentation, while poor adhesion was observed by means of scratch testing using WC ball as an indenter.

Keywords: Adhesion; Microwave plasma CVD; Nanocrystalline; Sputtering; Stress

# Acknowledgements

I would like to give my thanks for the opportunity to work on this project which was supported by EPSRC Nanotechnology KTN Case Studentship.

Many thanks go to my supervisors, colleagues and people at Teer Coatings and Aston University. The support of my friends, girlfriend, parents and the rest of my family was also crucial. Thank you all for your help, encouragement and motivation during the course of my studies.

## List of Publications

1. V. Kunderát, X. Zhang, K. Cooke, H. Sun, J. Sullivan, and H. Ye, "A novel Mo-W interlayer approach for CVD diamond deposition on steel," *AIP Adv.*, vol. 5, no. 4, 2015.
2. T. Allsop, R. Arif, R. Neal, K. Kalli, V. Kunderát, A. Rozhin, P. Culverhouse, and D. Webb, "Photonic gas sensors exploiting directly the optical properties of hybrid carbon nanotube localized surface plasmon structures," *Light: Science & Applications*, vol. X, no. X, XXXX, accepted for publication
3. J. Li, S. Su, L. Zhou, V. Kunderát, A. M. Abbot, F. Mushtaq, D. Ouyang, D. James, D. Roberts, and H. Ye, "Carbon nanowalls grown by microwave plasma enhanced chemical vapor deposition during the carbonization of polyacrylonitrile fibers," *J. Appl. Phys.*, vol. 113, no. 2, p. -, 2013.
4. S. Su, J. Li, V. Kunderát, A. M. Abbot, and H. Ye, "Hydrogen-terminated detonation nanodiamond: Impedance spectroscopy and thermal stability studies," *J. Appl. Phys.*, vol. 113, no. 2, p. -, 2013.
5. S. Su, J. Li, V. Kunderát, A. M. Abbot, and H. Ye, "Hydrogen-passivated detonation nanodiamond: An impedance spectroscopy study," *Diam. Relat. Mater.*, vol. 24, pp. 49–53, Apr. 2012.

# List of Contents

List of Abbreviations .....	9
1 Introduction .....	17
1.1 Diamond and its properties .....	17
1.2 Nucleation and growth of thin films.....	19
1.2.1 Nucleation .....	20
1.2.2 Coalescence and coarsening of grains.....	20
1.2.3 Growth of coalescent film .....	21
1.3 Diamond film deposition .....	25
1.3.1 Composition of substrate materials .....	25
1.3.2 Pre-treatments .....	26
1.3.2.1 Scratching and ultrasonic agitation .....	27
1.3.2.2 Substrate biasing.....	28
1.3.2.3 Interlayer .....	28
1.3.3 Nucleation and growth of diamond film.....	29
1.3.3.1 Diamond nucleation.....	29
1.3.3.2 Diamond growth .....	32
1.4 Thin film deposition techniques .....	37
1.4.1 Magnetron sputtering .....	38
1.4.2 Chemical Vapour deposition .....	41
1.4.2.1 Hot Filament Chemical Vapour Deposition .....	42
1.4.2.2 Microwave plasma chemical vapour deposition .....	43
1.5 Stress development during the film deposition .....	46
1.5.1 Epitaxial stress.....	46
1.5.2 Intrinsic stress .....	47
1.5.2.1 Pre-coalescence stage .....	47
1.5.2.2 Coalescing stage.....	47
1.5.2.3 Film thickening stage.....	48
1.5.3 Thermal stress .....	50

1.6	Stress measurements .....	51
1.7	Thin film adhesion testing.....	54
1.7.1	Indentation .....	55
1.7.2	Scratch.....	58
1.8	Research summary, aims and objectives .....	61
2	Experimental .....	62
2.1	Characterization techniques.....	62
2.1.1	Microscopy.....	62
2.1.1.1	Optical microscopy .....	62
2.1.1.2	Scanning Electron Microscopy.....	63
2.1.1.3	Atomic Force Microscopy (AFM).....	65
2.1.2	Chemical and structural characterization.....	66
2.1.2.1	Raman spectroscopy.....	66
2.1.2.2	X-ray diffraction (XRD).....	68
2.1.2.3	X-ray photoelectron spectroscopy (XPS) .....	69
2.1.2.4	Ball crater .....	70
2.1.2.5	Indentation and scratch testing .....	70
2.2	Base material identification .....	71
2.2.1	Steel substrate .....	71
2.2.2	Silicon wafer.....	72
2.2.3	Nanocrystalline diamond powder .....	72
2.3	Coating deposition procedures.....	74
2.3.1	Magnetron sputtering of interlayers .....	74
2.3.1.1	Pre-coating procedures .....	74
2.3.1.2	Sputtering of amorphous carbon films .....	74
2.3.1.3	Sputtering of metallic films.....	74
2.3.2	Diamond film growth .....	75
2.3.2.1	Equipment .....	75
2.3.2.2	Nucleation enhancement.....	75
2.3.2.3	Diamond deposition procedure .....	76

2.4	Experimental design.....	77
2.4.1	Diamond deposition using DLC buffer layer .....	77
2.4.1.1	Initial experiments for diamond growth estimation .....	77
2.4.1.2	Experiments of diamond deposition repeatability .....	78
2.4.1.3	Diamond deposition on different DLC films .....	79
2.4.2	Diamond deposition on CrW interlayer .....	80
2.4.3	Diamond CVD deposition temperature calibration .....	81
2.4.4	Diamond Deposition on MoW interlayers .....	83
2.4.4.1	Magnetron sputtering of MoW interlayers .....	83
2.4.4.2	Diamond deposition on MoW-2 interlayer .....	84
2.4.4.3	Investigation of low temperature diamond CVD deposition .....	85
2.4.4.4	Diamond deposition on MoW-2,3,4 interlayers .....	86
3	Results .....	87
3.1	Diamond deposition using DLC buffer layer .....	87
3.1.1	Initial experiments for diamond growth estimation .....	87
3.1.2	Experiments of diamond deposition repeatability .....	90
3.1.3	Diamond deposition on different DLC films .....	93
3.2	Diamond deposition on CrW interlayer .....	99
3.2.1	Magnetron sputtering of CrW interlayer .....	99
3.2.2	Nanocrystalline diamond seeding experiment .....	101
3.2.3	Diamond deposition on CrW interlayer .....	104
3.2.4	Further optimization of diamond CVD deposition .....	109
3.2.5	Problematics of diamond deposition on CrW interlayer .....	112
3.3	Diamond CVD deposition temperature calibration .....	115
3.4	Diamond Deposition on MoW interlayers.....	118
3.4.1	Magnetron sputtering of MoW interlayers.....	118
3.4.2	Diamond deposition on MoW-2 interlayer.....	122
3.4.3	Investigation of low temperature diamond CVD deposition.....	125
3.4.4	Diamond deposition on MoW-2,3,4 interlayers .....	132

4	Discussion.....	143
4.1	Diamond deposition using DLC buffer layer .....	143
4.2	Diamond deposition of CrW interlayer .....	145
4.2.1	Magnetron sputtering of CrW interlayer .....	145
4.2.2	Nanocrystalline diamond seeding experiment .....	146
4.2.3	Diamond deposition on CrW interlayer .....	146
4.3	Diamond CVD deposition temperature calibration .....	148
4.4	Diamond Deposition on MoW interlayer .....	149
4.4.1	Magnetron sputtering of MoW interlayers .....	149
4.4.2	Diamond deposition on MoW-2 interlayer .....	150
4.4.3	Investigation of low temperature diamond CVD deposition.....	152
4.4.4	Diamond deposition on MoW-2,3,4 interlayers .....	154
5	Conclusions .....	158
6	Future work .....	161
7	List of References .....	162
8	Appendix .....	176

# List of Abbreviations

AFM	Atomic Force Microscopy
CTE	Thermal Expansion Coefficient
CVD	Chemical Vapour Deposition
DLC	Diamond-like carbon
EDS	Energy-Dispersive Spectroscopy
HFCVD	Hot Filament Chemical Vapour Deposition
LAMPCVD	Linear Antennae Microwave Plasma Chemical Vapour Deposition
ML	Monolayer
MPCVD	Microwave Plasma Chemical Vapour Deposition
NNP	Novel Nucleation Process
OM	Optical Microscopy
PVD	Physical Vapour Deposition
SEM	Scanning Electron Microscopy
TPA	Transpolyacetylene
WDS	Wavelength-Dispersive Spectroscopy
XPS	X-Ray Photoelectron Spectroscopy
XRD	X-Ray Diffraction

# List of Figures

Figure 1.1	Ternary diagram of carbon allotropes; taken from [1].	17
Figure 1.2	Face-centred structure of diamond; taken from [6].	18
Figure 1.3	Schematic models of the three crystal growth modes: (a) Frank-van der Merwe (layer by layer growth); (b) Stranski-Krastanov (layer plus island growth); (c) Volmer-Weber (island growth); $\theta$ states the amount of monolayers (ML) [24].	22
Figure 1.4	Two types of epitaxial crystal growth of polycrystalline film with: a) immobile grain boundaries; b) mobile grain boundaries.	23
Figure 1.5	Zone diagram example as devised by Movchan and Demchishin; $T_H$ represents homologous temperature; image taken and modified from [21].	24
Figure 1.6	Diamond nucleation from layer of amorphous carbon; taken from [75].	31
Figure 1.7	Schematic illustration of diamond CVD growth process; reactants undergo activation process and are then transported to the vicinity of the substrate; taken from [8].	33
Figure 1.8	Schematics of sputtering process; target atoms are being ejected through bombardment of argon kations, which are created in plasma due to collisions of argon atoms with electrons.	38
Figure 1.9	Comparisons of plasma reach in different magnetron setups; taken from [102].	39
Figure 1.10	Possible magnetron configurations; taken from [102].	41
Figure 1.11	Schematic of the HFCVD apparatus.	42
Figure 1.12	Examples of the two common setups of MPCVD; a) NIRIM-type reactor; b) ASTEX-type reactor; taken and modified from [5].	44
Figure 1.13	Schematic of tapered shields for increased surface-wave plasma uniformity [110].	45
Figure 1.14	Arrangement of microwave antennae [90].	45
Figure 1.15	Grains of polycrystalline film before (solid lines) and after (dashed lines) coalescence.	48
Figure 1.16	Simple model of polycrystalline film growth under low and high adatom nobilities after the initial coalescence stage, taken from [118].	49
Figure 1.17	Representative Raman spectrum of polycrystalline diamond film deposited on Ti-6Al-4V where the shift and splitting of the 1332 $\text{cm}^{-1}$ diamond peak is observable; other presented peaks are broad peaks of disordered (D) and graphitic (G) carbon and of transpolyacetylene (TPA); taken and modified from [135].	53
Figure 1.18	Schematics of surface and interface energies of a particle on substrate; $\gamma_f$ , $\gamma_s$ and $\gamma_{fs}$ are the film, substrate and interface energies, respectively; $\theta$ is the wetting angle; taken from [139].	54
Figure 1.19	Dependence of interfacial fracture toughness ( $\Gamma_{IC}$ ) on the stress direction; $\Gamma_{IC}$ rises exponentially between normal stress ( $\psi = 0^\circ$ ) and shear stress ( $\psi = 90^\circ$ ); taken and modified from [139].	55

Figure 1.20	Schematics of indentation process using conical indenter; force ( $P$ ) is exerted onto material and upon indenting the indenter reaches a certain maximal depth ( $h$ ), in case that the material deforms partially elastically, then after the load has been removed, then the resulting depth ( $h_r$ ) will be smaller than $h$ ; taken and modified from [143].	56
Figure 1.21	Film's adhesion quality according to HF system; images of indents similar to HF 1-4 can be considered as a pass, while HF 5 and 6 are a definite failure; taken and modified from [146].	58
Figure 1.22	Schematic of adhesion failure during a scratch test for hard coating on ductile substrate; taken from [148].	59
Figure 1.23	Examples of cracking and interfacial failure modes during scratch test; taken and modified from [149].	60
Figure 2.1	Schematics of SEM components; taken from [154].	63
Figure 2.2	Regions from which secondary electrons, backscattered electrons and X-rays can originate; taken from [154].	64
Figure 2.3	Schematics of AFM working principle with focus on how the recorded surface features are interpreted using the photodetector; taken from [157].	65
Figure 2.4	Schematic diagram of Raman spectroscopy equipment; CCD – charged coupled device, FL – focus lens, NF notch filter; taken from [160].	67
Figure 2.5	Schematics of ball crater method for determination of coatings thickness; taken from [173].	70
Figure 2.6	SEM image of EDS multiple point analysis on M42 steel.	72
Figure 2.7	(A) Raman spectra with subtracted PL background of nanocrystalline diamond powder used for diamond nucleation enhancement; diamond peak is identified at $1323\text{ cm}^{-1}$ ; broad $sp^2$ D and G peaks are also shown; (B) SEM image of loose nanocrystalline diamond powder.	73
Figure 2.8	Photo and a schematic drawing of half of the experimental setup for temperature diffusion investigation.	82
Figure 2.9	True values of linear thermal expansion coefficients of diamond, W, Mo, M42 steel; data taken from [182,183].	84
Figure 3.1	Optical microscopy images of diamond coated steel substrates with various Dymon-iC buffer layers; darker spots in the images represent clusters of diamond, with exception of images A3, B4 and C1, where the diamond coverage is large and only the white spaces in image A3 and B4 represent surface without diamond coverage.	88
Figure 3.2	SEM image of top surface of diamond coated sample with run number 67391; yellow circles in the left image are highlighting examples of the diamond's preferred growth in (111) direction.	89
Figure 3.3	SEM image of top surface of diamond coated sample with run number 67382, where ball-like shaped diamond dominates both of the images.	89
Figure 3.4	Macroscopic images of diamond coated samples 65733 and 67391.	89
Figure 3.5	Comparison of three different attempts to obtain the full diamond coverage as in case of diamond coated 67391 sample.	91
Figure 3.6	SEM image of diamond coated sample from 69063 run with identified points where EDS spectra was taken from.	92

Figure 3.7	Comparison of logged data of bias current and chamber pressure for 67391, 69063 and 68971 deposition runs; the unstable deposition conditions of 67391 run are clearly seen from the evolution of chamber pressure and bias current. ....	93
Figure 3.8	Overview of low magnification SEM images of diamond coated samples after CVD deposition conditions no. 1; samples were deposited with different DLC buffer layer thickness as well as with and without CrC interlayer, as is indicated in along the axis. ....	94
Figure 3.9	Overview of higher magnification SEM images of diamond coated samples after CVD deposition conditions no. 1; samples were deposited with different DLC buffer layer thickness as well as with and without CrC interlayer, as is indicated in along the axis. ....	95
Figure 3.10	SEM comparison of the difference in prolonged diamond nucleation stage from 1 hour (left side) to 3 hours (right side) with diamond growth conditions kept identical. ....	96
Figure 3.11	SEM comparison of the difference in the amount of methane gas used during the diamond growth stage; 1 vol. % CH <sub>4</sub> – left side; 2 vol. % CH <sub>4</sub> – right side. ....	97
Figure 3.12	SEM image overview of diamond coverage when different microwave power has been used during the diamond growth stage; 900 Watts – left side; 1000 Watts – right side. ....	97
Figure 3.13	SEM comparison of the difference between two stage diamond CVD deposition (left side) and one stage, growth only, diamond deposition (right side); overall duration of the CVD deposition was identical. ....	98
Figure 3.14.	Rockwell indents on (A) W coated M42 substrate and (B) CrW coated M42 substrate. ....	99
Figure 3.15	(A) SEM images of pure W deposited on M42 steel substrate; (B) CrW interlayer deposited on M42 steel substrate. ....	101
Figure 3.16	Drying maps on silicon substrates formed after the agitation process; all three samples were subject to 30 min ultrasonication in 0.2 wt. % nanodiamond suspension in water, images were taken after diamond CVD deposition. ....	103
Figure 3.17	Raman spectra of diamond films after agitation (left image) and dip-in method (right image) with various nanodiamond concentrations in the suspension (shown in the legend); diamond peak is clearly distinguishable in each of the spectra, also present are broad sp <sup>2</sup> bonded D and G peaks. ....	104
Figure 3.18	SEM dataset for the factorial design with respective deposition parameters shown along the axis. ....	106
Figure 3.19	Raman spectra for all the samples from the factorial design experiment; A – spectra with pronounced diamond peak; B – spectra without pronounced diamond peak; all the presented spectra show peaks of diamond, D and G sp <sup>2</sup> bonded peaks and two peaks belonging to transpolyacetylene (TPA). ....	107
Figure 3.20	Schematic cubes showing investigated responses from the factorial design with coloured experimental points based on the obtained results for each response; P stands for pressure and P <sub>M</sub> for microwave power. ....	109
Figure 3.21	Schematic factorial cube highlighting the results of the investigation from factorial design; each point of the cube represents one experiment; P stands for pressure and P <sub>M</sub> stands for microwave power; the red dots symbolise future experimental conditions identified for further investigation. ....	110

Figure 3.22	SEM results of diamond growth from the post-factorial experimental investigation.....	111
Figure 3.23	Adhesion failure of part of the CrW coated steel samples after sputtering deposition; coating's buckling and delamination can be seen in both of the images.....	112
Figure 3.24	Examples of delamination and cracking of CrW interlayer on M42 steel resulting from diamond CVD deposition.....	113
Figure 3.25	Examples of cracking and delamination of diamond films on CrW coated M42 steel.....	114
Figure 3.26	Temperature diffusion difference between samples surface and measured value depending on different pressure and gas as calculated from experimental data for the shallow holder.....	116
Figure 3.27	Temperature diffusion difference between samples surface and measured value depending on different pressure and gas as calculated from experimental data for the deep holder.....	117
Figure 3.28	Linear regression functions fitter for temperature diffusion data for hydrogen gas using the shallow holder.....	117
Figure 3.29	OM images of Rockwell C indents (left column) and general view of the surface (right column) for MoW-2,3,4 coated M42 steel discs.....	119
Figure 3.30	Topography SEM overview of MoW-2, MoW-3, MoW-4 coated M42 steel samples with a cross-sectional view of MoW-4 sample, where columnar growth of the MoW interlayer is visible.....	120
Figure 3.31	Comparison of X-ray diffractograms of MoW-2,3,4 with no scan offset (top left); stacked diffractograms of individual MoW coated samples using setup's offset from -10° to +10°.....	121
Figure 3.32.	SEM topography image (A) and deconvoluted Raman spectrum (B) of deposited diamond film of MoW-2 coated M42 steel; diamond, D and G sp <sup>2</sup> peaks and transpolyacetylene (TPA) peaks were identified; taken and modified from [188]......	122
Figure 3.33	SEM image of the start of delamination of diamond film within the scratch track using back scattered electrons imaging mode; the white arrow shows the direction of sliding of WC ball; taken from [188]......	123
Figure 3.34	SEM image of part of the scratch track; left – delaminated area; right – adherent area; rectangles A and B mark the areas of EDS scan; the white arrow indicates the direction of sliding of WC ball; taken from [188]......	124
Figure 3.35	EDS analysis of Diamond/MoW-2/M42 sample cross-section.....	125
Figure 3.36	CVD deposition parameters evolution depending on the amount of methane in hydrogen rich atmosphere with deposition temperature set at 650 °C... ..	126
Figure 3.37	Macroscopic images of various diamond deposition runs on M42 steel with MoW-2 interlayer at 650 °C; samples are 25 mm in diameter.....	127
Figure 3.38	SEM images of surface features of various diamond deposition runs on M42 steel with MoW-2 interlayer at 650 °C.....	128
Figure 3.39	SEM images of diamond surface of samples deposited at 15 Torr with 3 vol. % of methane (A) and 5 vol. % of methane (B). .....	129
Figure 3.40	Raman spectra of diamond films deposited at 15 Torr with 3 vol. % of methane (A) and 5 vol. % of methane (B); identified peaks in the spectra belong to diamond, D and G sp <sup>2</sup> peaks and two transpolyacetylene (TPA) peaks.....	130

Figure 3.41	5-30 N scratch tracks of diamond film on MoW-2 coated M42 steel. ....	131
Figure 3.42	1-15 N scratch tracks of diamond film on MoW-2 coated M42 steel. ....	131
Figure 3.43	SEM comparison of diamond films deposited under low and moderate CVD deposition conditions on MoW-2,3,4 coated steel substrates. ....	133
Figure 3.44	SEM images of 10-200 N indentation test with Rockwell type indenter; diamond films were deposited under low and moderate CVD deposition conditions on MoW-2,3,4 coated steel substrates. ....	135
Figure 3.45	SEM images of 10-200 N indentation test with WC ball 1/16" ( $\approx 1.6$ mm); diamond films were deposited under low and moderate CVD deposition conditions on MoW-2,3,4 coated steel substrates. ....	136
Figure 3.46	Raman spectra of adherent and delaminated diamond films deposited under low and moderate diamond CVD deposition conditions on MoW-2,3,4 coated steel substrates; identified peaks in are highlighted in the image of Raman spectrum for diamond film deposited on MoW-4 at low temperature (bottom left image), where the Raman peaks which are present in every image are identified as diamond, D and G $sp^2$ carbon and tow transpolyacetylene (TPA) peaks. ....	138
Figure 3.47	Comparison of Rockwell C indents on samples after low and moderate temperature diamond CVD deposition on MoW-2,3,4 coated steel substrates. ....	140
Figure 3.48	SEM images of Rockwell C indent of low temperature CVD deposited diamond film on MoW-4 coated steel substrate. ....	141
Figure 3.49	SEM images of 5-30 N scratch test on low temperature CVD deposited diamond film on MoW-4 coated steel substrate; image on the right hand side is a magnified part of the scratch track. ....	141
Figure 3.50	SEM image of 5-30 N scratch on low temperature CVD deposited diamond film on MoW-4 coated steel substrate with identified points where EDS spectra was taken from. ....	142
Figure 8.1	Copy of drawing of shallow sample holder. ....	176
Figure 8.2	Copy of drawing of deep sample holder. ....	177

## List of Tables

Table 2.1	Observable peaks in Raman spectra of diamond and amorphous carbon films as assigned by [125].	67
Table 2.2	Quantification of obtained EDS spectra of M42 in comparison with ASTM Standard specification for high speed tool steels (impurity limits are not included).	72
Table 2.3	Selected deposition conditions for diamond growth on DLC coated samples; deposition chamber had hydrogen-rich atmosphere.	78
Table 2.4	Difference in coatings in respect to the 67391 coating run.	79
Table 2.5	Deposited variations of Dymon-iC coating with respect to the thicknesses for present layers.	79
Table 2.6	Diamond CVD deposition conditions applied on varied Dymon-iC deposited films on steel substrates.	80
Table 2.7	CVD diamond deposition conditions used in this study.	86
Table 3.1	EDS analysis results of sample from 69063 run after diamond deposition.	92
Table 3.2	Coating procedure for 1.1 $\mu\text{m}$ thick CrW film; magnetrons 1 and 3 are without targets, magnetron 2 has Cr target and magnetron 4 has W target.	100
Table 3.3.	List of XPS detected elements in the region of delamination for CrW coated steel.	101
Table 3.4	Nanodiamond seeding investigation of concentration of nanodiamond powder and the duration of ultrasonic agitation.	102
Table 3.5	Deposition conditions investigation according to the factorial design.	104
Table 3.6	Diamond and G peak positions from Raman spectra of samples from factorial design.	107
Table 3.7	Overview responses obtained after the competition of factorial design; the examined effects are shaded for each sample according to how well the particular criteria has been fulfilled (white – best, dark – worst).	108
Table 3.8	Deposition conditions of further diamond growth investigation based on the results of the factorial design; the last two italicised experimental runs were for verification of reproducibility.	110
Table 3.9	Overview of the quality of obtained diamond films from the post-factorial experimental investigation, as determined from SEM images.	111
Table 3.10	List of XPS detected elements in the region of delamination of deposited diamond film.	114
Table 3.11	Fitting functions for Ar, H <sub>2</sub> and CH <sub>4</sub> gases for temperature diffusion measurement together with their respective coefficients of determination (R <sup>2</sup> ); x represents a pressure value and y represents a temperature on the back of substrate holder at given temperature of substrate surface and gas mixture.	115
Table 3.12	Values of coefficient of determination for linear regression functions fitted for each gas at given pressures for the relationship between temperature at the sample's surface and the temperature at the back of the substrate holder.	118

Table 3.13.	Time comparison of deposition steps used for MoW-2,3,4 coatings with their respective thicknesses.....	118
Table 3.14	Surface characterization of MoW-2,3,4.....	120
Table 3.15	List of peak positions of W(110) and the size of crystallites of MoW-2,3,4 coated steel samples. ....	122
Table 3.16	EDS spectra of delaminated and adherent regions of diamond film within the scratch region together with an unscratched region of diamond film. ....	124
Table 3.17	Experimental design of diamond deposition at 650 °C on MoW-2 coated M42 steel with pre-set pressures and methane concentrations in hydrogen-rich atmosphere.....	126
Table 3.18	Brief summary of structure and properties of diamond films grown at 650 °C on MoW-2 coated M42 steel substrates. ....	128
Table 3.19	Summary of averages of Rockwell C hardness of samples after the investigated low temperature CVD deposition conditions.....	129
Table 3.20	Comparison of surface thickness, surface roughness and Rockwell C hardness of diamond deposited at low and moderate temperatures on MoW-2,3,4 coated steel substrates. ....	133
Table 3.21	Summary of diamond peak positions derived from Raman spectra of diamond films deposited under low and moderate CVD deposition conditions on MoW-2,3,4 coated steel substrates. ....	139
Table 3.22	EDS analysis results of 5-30 N scratch on low temperature CVD deposited diamond film on MoW-4 coated steel substrate; points 1 and 2 are on adherent diamond film; points 3 and 4 are on delaminated part of the diamond coating.....	142

# 1 Introduction

## 1.1 Diamond and its properties

The family of carbon materials has grown substantially since the middle of the last century. Carbon's known possible  $sp^1$ ,  $sp^2$  and  $sp^3$  hybridizations of its valence configuration provide a large area of possible carbon forms. The most widely accepted classification of carbon structures these days is their division by the hybridization originating from the work of Heimann et al [1]. They were first to form a ternary diagram of carbon allotropes, as shown in Figure 1.1. The main three points of the diagram are defined by the pure hybridization states, while the rest of the diagram is composed from the materials possessing a mixture of the respective hybridizations. The aforementioned classification uses  $sp^n$  groups for allotropes possessing mixtures of hybridizations. Such groups possess  $n$  hybridization which is defined as being  $(1 < n < 3; n \neq 2)$ . The number of different carbon allotropes known up to now is large, with well-known materials as diamond, graphite, graphene, carbon nanotubes, fullerenes, amorphous carbon films and many others. For detailed descriptions of different carbon forms and different systems of their classifications the author recommends reading of [1–4]. In this work we will limit our description to diamond and its properties.



**Figure 1.1 Ternary diagram of carbon allotropes; taken from [1].**

Diamond is widely known in jewellery, but its applications in industry are also very well known. It is a metastable form of carbon, which is not formed under normal conditions at the surface of the Earth. The exploitation of man-made diamond happened in the late half of the 20<sup>th</sup> century and, ever since then, tooling industry among others has shown great interest in the use of diamond. Graphite is the thermodynamically stable allotrope of carbon at normal temperatures and pressures as opposed to diamond. Their standard enthalpies differ by just 2.9 kJ/mol, but a larger activation barrier separates the two phases from spontaneous conversion [5]. Therefore diamond is a metastable form of carbon, meaning that it is kinetically stable but not thermodynamically. Carbon atoms in diamond are bonded by covalent bond in sp<sup>3</sup> hybridization, forming the tetrahedral shape which has a face-centred cubic lattice crystallographic structure (Figure 1.22).



**Figure 1.2 Face-centred structure of diamond; taken from [6].**

Carbon atoms forming diamond are relatively light, small and have a very strong covalent bonds between each other. The strength of the bonding is 347 kJ/mol and so substantial amount of energy has to be enforced to remove a carbon atom which is bonded in diamond lattice. This makes diamond very hard and abrasion resistive material, but relatively brittle [7]. Short and strong bonds within diamond also gave rise to its ability to conduct heat at fast rates through high possible frequencies of atomic vibrations within the diamond crystal. With diamond's tightly packed rigid structure goes as well its lowest compressibility due to its large Young's modulus (1220 GPa), highest thermal conductivity at room temperature ( $2 \times 10^3 \text{ W m}^{-1} \text{ K}^{-1}$ ), high resistivity ( $10^{16} \text{ } \Omega \text{ cm}$  at 20 °C), wide bandgap (5.37 eV), good chemical inertness, broad optical transparency (ultraviolet to infrared region) and thermal oxidation resistance, just to highlight the main properties for which diamond is being exploited [5,8].

All those properties could be only partially exploited using bulk diamond, which can be found in the nature or synthesized at high temperatures and pressures. The development of chemical vapour deposition (CVD) processes enabled deposition of diamond thin films which raised great potential for further usage of diamond in a form of coatings. Examples of existing and possible mechanical applications of microcrystalline and nanocrystalline CVD made diamond thin-films are: diamond coated machining tools (drill bits, dies, grinding and cutting tools) for soft metals and wood [9,10], low wear parts (cog wheels, bearings) [11,12] and biomedical applications (knee and hip joints) [13–15].

An important question concerning diamond properties is if the size of diamond grains in the coatings has an effect of mechanical properties. The answer is mainly in the surface to volume ratio. Diamond crystals of a size smaller than 20 nm have most of their atoms on the surface of the crystals, which are bonded to various other elements. Consequently there are not many carbon-to-carbon  $sp^3$  bonds which would provide the diamond structure and its properties. Hence the diamond properties are highly dependent on the size of the crystals, and 20 nm size is thought to be the smallest size for diamond grains to still have the same properties like a bulk diamond [16].

The size and constitution of diamond films divide those coatings into two groups: microcrystalline and nanocrystalline diamond films. There are two types of diamond growth – with and without re-nucleation. Microcrystalline and nanocrystalline diamond coatings can be both grown without re-nucleation. When the diamond's nucleus is created, it grows larger in size and, depending on the duration of the growth time, it will stay nanocrystalline or it will become a microcrystalline diamond. Therefore, the thicker the coating becomes, the higher the roughness of the coating and the larger the respective crystals forming the coating will be. The second type of diamond growth is growth with re-nucleation, where surface roughness is independent of film thickness. Diamond grains grow and re-nucleate on themselves. This way, nanocrystalline coatings of various thicknesses can be produced. Diamond thin-films differ significantly depending on deposition parameters, substrate, pre-treatment and gas species in the chamber. All those variables influence crystal orientation, purity, grain size, defect density, which it then projected onto coating mechanical properties.

## **1.2 Nucleation and growth of thin films**

The regime of film growth determines the structure of the resulting film. Film's structure dictates its properties, which can differ dramatically as for example between diamond and amorphous carbon. Microstructural characteristic of polycrystalline films, such as grain size and orientation, controls the films performance and reliability in great variety of applications

ranging from electronic and photonic to mechanical. The specific microstructure of those films must be therefore reproducible to high degree and the deposition process has to be controlled from the step one. The deposition of the film can be divided into three consecutive steps of: nucleation, coalescence and growth. This section of the literature review will briefly demonstrate the principles behind those three steps.

### **1.2.1 Nucleation**

At the start of film deposition, atoms (or molecules) condense on the substrate surface and can undergo several processes such as re-evaporation, nucleation of cluster, being captured by existing cluster, diffusion into the substrate and being captured at possible existing defects. In case of ideally flat substrate the last two processes will not happen, but in reality they often do. Upon condensing the atoms form chemical bonds with surface atoms. Surface mobility of the atoms depends on the strength of the bonds between them, e.g. metallic, ion, van der Waals. Strongly bonded condensed adatoms (an adsorbed atoms) with substrate will have low surface mobility and can serve as nucleation sites. Weakly bonded adatoms will have high surface mobility and will diffuse to preferential nucleation sites where stronger bonding is possible. Those sites can be an already created nucleation sites or defects present at the substrate surface (e.g. point defects, grain boundaries, steps) with higher coordination number (number of neighbouring atoms). The difference in the binding strength depends on the nature of the substrate and the condensing species, as well as on the deposition process conditions, which can provide the condensing adatoms with additional energy and to be able to increase its surface mobility. Typical values for stronger bonding such as metallic, ionic and covalent in the 1-10 eV range, while weak bonding, such as van der Waals and hydrogen bonding are in the meV and several hundred meV range, respectively [17]. Mobile surface atoms can also form nucleation sites through collision with other mobile surface atoms, which is why the rate of nucleation depends on the deposition flux [18].

### **1.2.2 Coalescence and coarsening of grains**

Further growth of nuclei is facilitated either by direct impinging of condensing atoms, or through their migration over the surface to the already formed nuclei. The islands of new deposited material can grow, in principle, even when the deposition is interrupted despite the desire of achieving the lowest possible thermodynamic state. Islands of deposited material will be of different size and possibly orientation, which will affect their surface and interface energies. Atoms in smaller deposited islands will migrate through diffusion into the

larger islands in order to minimize the interfacial free energy of the system. This process is known under the name of coarsening, or Ostwald ripening [19].

Growing grains of material will eventually make a contact with other growing islands. At the critical distance from each other the grains form a grain boundary through certain amount of elastic straining. Grain boundary formation is energetically more favourable state in comparison to the free surface energies of two isolated grains. If the grains in contact cannot establish fixed volume equilibriums, the energy difference between the two grains will cause atomic diffusion flux to the more energetically stable grain, which will then grow further in size, while the small neighbouring grains will get smaller and can eventually disappear [20]. The rate of coarsening process depends on the grain and surface diffusivity of the material and the initial grain distribution over the substrate's surface. To what degree coarsening process influences the structure of freshly coalescent film is a function of deposition rate - high deposition rate will suppress the coarsening [21]. Kinetic models of nucleation, coarsening and crystal growth have been studied and are available in [22,23].

### **1.2.3 Growth of coalescent film**

The three possible recognised growth modes [24] are illustrated in Figure 1.3. Frank-van der Merwe (layer by layer growth) growth is characteristic for strong adhesive forces between the substrate and deposited atoms. After a monolayer of film is deposited on the substrate, it is followed by another monolayer which is somewhat more loosely bound to the first layer and so on (Figure 1.3a). Such type of growth can be seen in deposition of semiconductor on semiconductor. Volmer-Weber (island growth) growth is observed when deposited material bonds stronger to each other than it does to the substrate (Figure 1.3c). It's a typical type of growth of metals on insulators, or graphite, for example. Stranski-Krastanov (layer plus island growth) is a cross between the two previously described methods, where after the first few monolayers of newly deposited material abandons this type of growth as being no longer energetically favourable and island growth occurs (Figure 1.3b). The possible causes for the change from layer growth to island one are numerous - strain accumulation, molecular orientation, etc. Stranski-Krastanov growth is observed for example during deposition of silver on tungsten, molybdenum and silicon.

From thermodynamic point of view [25] the difference between layer by layer and island growth is in the sum of the substrate ( $\gamma_s$ ), interface ( $\gamma_i$ ) and film ( $\gamma_f$ ) free energies. When  $\gamma_s + \gamma_i > \gamma_f$ , the deposited film will spread over the whole substrate surface area in order to maintain the minimum energy following layer by layer growth. Similarly when  $\gamma_f + \gamma_i > \gamma_s$  the system will try to minimize the sum of free energies through growth of islands. Stranski-

Krastanov type of deposition cannot be generalised through simple equation due to the effects leading to the significant changes within its growth mode.



**Figure 1.3 Schematic models of the three crystal growth modes: (a) Frank-van der Merwe (layer by layer growth); (b) Stranski-Krastanov (layer plus island growth); (c) Volmer-Weber (island growth);  $\theta$  states the amount of monolayers (ML) [24].**

Once the deposited films have been formed, their thickening is expected to happen through epitaxial growth of existing grains even at relatively low deposition temperatures. Exception to this expectation is renucleation process when surface composition of as grown grains would be changing during the deposition. Such instability in the deposition is possible to happen even for films of relatively high purity. Impurities can still be absorbed at the surface of growth crystals which won't be compatible with grown structure and, therefore, will be rejected. Such impurity can act as a nucleation centre, to be accommodated as a defect within the grown crystal, or to cause twinning of growing crystal. Considering clean and appropriately controlled growth conditions, the coalescent new film can thicken in two possible ways depending on if its grain boundaries are mobile or not (Figure 1.4). Materials with mobile grain boundaries (e.g. Al, Ag, Au) can unify the orientation of the film grains through recrystallization process even at low deposition temperatures. Newly nucleated grains will grow at the expense of already existing grains. As seen in Figure 1.4b), the grains will enlarge with thickening of the growing film. Materials with immobile grain boundaries (e.g. W, Fe, Si) proceed their growth of columnar structure depending on the initial orientation of the nucleated grains. The grain growth is restricted to only the top surface of the grains where differently oriented grains compete with their growth speeds, as can be seen in Figure 1.4a). Specifically oriented grains with preferable fast growing planes will

eventually outgrow the rest and will dominate the surface, this phenomenon was first described and investigated by van der Drift [26].

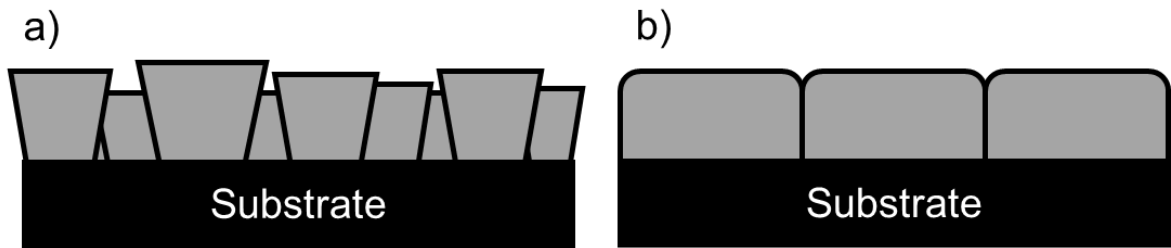


**Figure 1.4 Two types of epitaxial crystal growth of polycrystalline film with: a) immobile grain boundaries; b) mobile grain boundaries.**

Deposition temperature has a critical effect on the grown films through conversion of heat into kinetic energy of atoms influencing greatly the diffusion, which is a temperature dependant process. Similar film structures are observed for different materials when they are deposited at matching temperatures proportional to their melting temperatures, at so called homologous temperature -  $T_H$ . Homologous temperature is a function of  $T/T_M$ , where  $T$  is substrate's temperature and  $T_M$  is material's melting point (both in degrees Kelvin) [27]. Movchan and Demchishin [28] were the first to develop the so called zone diagrams where, depending on the value of  $T_H$ , one is able to determine what structure the resulting film will possess. Their work was limited on evaporated films where temperature was the main influencing mechanism. They devised three zones identifying the structure of deposited films (Figure 1.5). Zone 1 ( $T_H < 0.3$ ) was characteristic for low adatom mobility which led to continued grain growth of fibrous growth, fine grains or even amorphous structure with growth direction towards the flux of arriving adatoms. Zone 2 ( $0.3 < T_H < 0.5$ ) was characteristic for faceted growth of grains throughout the film's thickening due to the system having enough energy for surface diffusion processes. Zone 3 ( $T_H > 0.5$ ) was characteristic for recrystallization processes resulting in large grain formation. Expansion on the work of Movchan and Demchishin resulted in addition of zone T as being a transition zone between zone 1 and 2. There, the surface diffusion processes are possible, but grain boundary diffusion is severely limited, which leads to competitive crystal growth and to inhomogeneous grain size distribution throughout the film thickness (much like the example in Figure 1.4a). Further progress in deposition techniques through sputtering deposition processes changed the view on the zone modes significantly. The energy of arriving adatoms onto the substrate determines the adatoms mobility. The sputtering deposition is a process happening in gas environment and, therefore, energy of arriving adatoms is expected to change depending on the amount of collisions it encountered during its travel onto the substrate. Thorton [29] then expanded onto the zone diagrams by adding an axis

tracking the deposition pressure. Ion bombardment has also its role and influences the resulting structure of deposited films. Its benefits are seen especially for deposition of materials at zone 1, where the films suffer from low densities. Ion bombardment can increase atom mobility and nucleation rates, densify the coating and lower the roughness of obtained films [30].



**Figure 1.5 Zone diagram example as devised by Movchan and Demchishin;  $T_H$  represents homologous temperature; image taken and modified from [21].**

It is important to be aware of the usability of the particular zone models. The majority of the zone diagrams are developed for a precise group of similar materials, which are mostly refractory bcc metals (e.g. Cr, W, Mo). Materials from different groups have their diffusion characteristics bound to a different amounts of  $T_H$ . For example, a diamond cubic structure (e.g. diamond, Si) has one of the lowest diffusion characteristics and its grain boundary mobility is extremely low. Also the constructed zone diagrams does not usually incorporate influencing parameters such as the amount of impurities, alloying elements and deposition rates, so one has to be careful and consider their suitability for a particular deposition technique and the class of used materials. The thin film growth and different zone approaches are extensively reviewed in [20,21,30,31].

Deposition of amorphous coatings is specific due to the requirements of the deposition process. Amorphous films exhibit narrow range ordered structure with no ordering at large distances. In order to achieve such type of ordering, one can already deduce from the text above, that high deposition rates and low temperatures will be the two key parameters. Low temperature deposition will inhibit the adatoms diffusivity within the film effectively impinging them in the spot where they landed not allowing any further diffusion movements [25].

## 1.3 Diamond film deposition

Man-made diamond formation is divided into groups of diamonds grown under high-pressure high-temperature conditions and of diamonds grown under metastable diamond growth conditions. Condition for high-pressure high-temperature diamond synthesis are close to the natural diamond formation where diamond formation is thermodynamically favoured over the graphite formation. Broad range of free standing diamond particles from nanocrystalline to bulk diamonds are synthesised using this approach [32]. Deposition of diamond films using metastable diamond growth is the latter discovered technique, which developed due to the discovery of the relatively wide region where metastable diamond growth is possible [33]. Conditions suitable for metastable diamond film deposition and the deposition processes associated with diamond growth are reviewed in this chapter.

Metastable diamond growth is facilitated through deposition of carbon atoms from the gaseous phase under relatively low pressure in chemical vapour deposition systems. Deposition of diamond is unique in a sense that carbon can co-exist in three hybridised forms ( $sp^1$ ,  $sp^2$ ,  $sp^3$ ) which gives a great amount of range of existence for numerous carbon structures. Diamond CVD deposition conditions, where metastable growth of diamond is possible, are also a region where graphite formation is thermodynamically stable. Co-deposition of other various non-diamond carbon species (e.g. amorphous carbon, graphite) during the diamond film growth is, therefore, inevitable and for higher purity diamond films an etching medium has to be present during the deposition. In the case of CVD diamond growth it is typically atomic hydrogen, etching the other carbon species at higher rates than diamond, since diamond carbon bonds are stronger than carbon bonds of other carbon species. Also carbon has a higher affinity to form strong bonds and, therefore, the dissociation of carbon carrying gas is relatively energetically demanding [34].

### 1.3.1 Composition of substrate materials

Substrate materials, their chemical properties and the surface conditions are critical factors influencing early stages of diamond growth process. Growth of single crystalline diamond over large areas is limited to single crystal of diamond or iridium as substrates. Diamond grows best on diamond itself, since there are no problems with mismatch of lattice parameters, so the deposited carbon atoms can easily integrate themselves into the diamond lattice structure. Iridium is also capable of being a substrate for large area single crystalline diamond growth, due to its relatively small lattice mismatch compared to diamond and its affinity to carbon [35]. The diamond growth on the majority of foreign substrates is polycrystalline [16]. Depending on chosen substrate material, there is an incubation period before any diamond starts to form on the surface. Reasons for the existence of the

incubation period are the chemical interactions between substrate and plasma gases. Depending on the reactivity of the material surface there are three major groups of material with different carbon substrate interactions [36]:

- Little or no solubility of carbon: diamond, graphite, carbides, Cu, Ag, Au, etc.
- Carbon diffusion only: Pt, Pd, Rh, etc.
- Carbide forming: metallic – Ti, Zr, V, Ta, Cr, Mo, W, Fe, Co, etc.; covalent – B, Si, etc.; ionic – Al, Y, etc.

There are certain facts about the diamond nucleation on foreign substrates such as [36]: nucleation on cubic boron nitride occurs readily; nucleation on carbide forming substrates is few orders of magnitude higher than on non-carbide forming substrates; polycrystalline substrates have higher nucleation rates than single-crystalline substrates; diamond adheres better on carbide forming substrates than on non-carbide forming substrates. Diamond nucleation occurs readily on substrates forming amorphous diamond-like carbon (DLC) interlayer (e.g. Si, Mo).

The diffusion process in diamond CVD deposition plays an important role as well. Substrates with high carbon solubility (e.g. steel) cause a delay in the diamond growth process by supersaturating themselves with carbon at first, and only after reaching that point allowing the process of diamond nucleation to happen. Most of the CVD processes use elevated temperatures (> 700 °C) and these temperatures increase carbon diffusion into the substrate, which speeds up the diamond growth.

### **1.3.2 Pre-treatments**

Direct growth of polycrystalline diamond on foreign substrates follows Volmer-Weber growth mode, while epitaxially grown diamond follows either Frank-van der Merwem or Stranski-Krastanov growth modes [37]. Diamond has also relatively high surface energy and low sticking probability, which makes it not readily nucleating on polished surfaces [38]. Many pre-treatment methods were invented over the years to overcome the low sticking probability, to suppress diffusion of carbon atoms into the substrate material and to enhance the density of diamond nuclei created in the initial stages of growth. These methods include: scratching (using diamond or other abrasives), ultrasonic agitation (using diamond nanoparticles, diamond and other abrasives), surface biasing, chemical etching of substrate surfaces, deposition of interlayers (metal thin films, boron nitride, carbides and different carbon species) and many others [5,16].

### 1.3.2.1 Scratching and ultrasonic agitation

The most common pre-treatment for nucleation enhancement at the start of this millennium was scratching substrates with diamond paste [39] and, later, it was followed by ultrasonic agitation of substrates in nanodiamond suspension [40]. Both of these pre-treatments are successfully used to obtain high diamond nucleation densities and are also relatively easy to perform in laboratory conditions.

Scratching of substrate surface is usually performed with micron sized diamond powders, although reports showed that hard particles of different materials also enhance the diamond nucleation. The reasons of diamond nucleation enhancement behind this method are roughening the substrate, forming a large number of defects which will serve as a preferential nucleation sites for diamond, as well as embedding of diamond particles into the substrate's surface [41]. Unfortunately those processes do damage the substrate surface (especially when using micron meter size of diamond particles or more), can contaminate the material and are hard to apply to complex 3D shapes [36].

Ultrasonic agitation became the method of choice for most of the researches when nanocrystalline diamond powders made by detonation method [42] became available. Formation of nanodiamond colloid through ultrasonic agitation of diamond powder, followed by either ultrasonication or immersion of the sample into the colloid provides a great enhancements in subsequent diamond nucleation [40,43–45]. The common solutions for diamond dispersion are deionised water [43,44,46,47], isopropanol [48–50], methanol [45,51], ethanol [40,46] and acetone [52]. It is believed that the nanodiamond particles adhere to the substrate's surface by van der Waals forces, even if the nanodiamond particles are aggregated [53]. Detonated diamond powder is the most common seeding material, although good results were reported of seeding the substrates with adamantane [54] as well as mixtures of detonated diamond powder with metallic particles [44] with various enhancements to the seeding's quality. An interesting approach to obtain very high nucleation densities was named NNP (novel nucleation process) established by Rotter et al [55] which inserts one more step into the diamond growth process and that is a subsection of the substrates to a diamond CVD deposition for a brief period of time before seeding the substrates with nanodiamond particles, followed by diamond CVD growth. The process provides good stable results, but its problem lies precisely in the plasma exposure step before the nanodiamond seeding, which makes it rather complicated for possible industrial application.

### 1.3.2.2 Substrate biasing

Application of negative bias to the substrate during the initial stages of diamond deposition provides nucleation enhancement without damaging the existing surface profile as well as it helps to remove native oxides as in case of silicon wafers and increases the flux and mobility of adatoms [37]. Substrate biasing accelerates plasma ion species towards substrate's surface and promotes carbon diffusion into the substrate, leading to quicker carbon super-saturation of the substrate surface, which then speeds up the diamond nucleation process [56]. If the biasing is used for the whole deposition process, the resulting diamond coating is of nanocrystalline nature throughout its thickness [57]. Limitations of this technique are due to its applicability to only conductive and semi-conductive materials and more importantly, the problems with reproducibility of results [58,59].

### 1.3.2.3 Interlayer

Nucleation enhancement is achievable also through covering the substrate with thin films of metals [36] (Fe, Cu, Ti, Ni, Mo, W), boron nitride and carbon structures [60] (amorphous carbon, fullerenes, graphite), multi-interlayers [61] and others. Over-layers are changing the surface chemistry (sample surface energy, carbon saturation) and affects diffusion of plasma species into the bulk substrate. Efficiency of applied over-layers on nucleation enhancement differs greatly depending on the nature of substrate and selected interlayer system. Direct diamond film deposition onto steel substrates gives poor results in terms of diamond film growth, its adhesion to the steel surface as well as, due to the cross-diffusion of elements between steel substrate and as-grown diamond film [62,48]. Chemical elements, such as Fe and Co greatly affect diamond formation in terms of facilitating the formation of an amorphous carbon layer before any diamond growth is feasible, deteriorating adhesion between steel and diamond. At the same time diffusion of carbon into the steel causes carburization of steel substrate, which leads to a change in steel properties. In order to tackle the adhesion problem different types of interlayers have been used on ferrous substrates such as Cr, Ti, Mo, W, nitrides, carbides and multi-structured interlayers[62–64,51,65–69]. In respect to choosing a good interlayer, factors such as the material's carbide formation, diffusion barrier characteristics as well as thermal expansivity must be taken into account [65,66].

An interesting approach to interlayer deposition is deposition of non-diamond carbon coating which would provide a carbon buffer layer for diamond deposition and, in some cases (such as DLC coatings), even a significant proportion of already existing  $sp^3$  carbon bonded structures. Non-diamond carbon interlayers studied for diamond growth were: fullerenes [60] ( $C_{60}$ ,  $C_{70}$ ), graphite [36], carbides [37], amorphous carbon coatings

[60,61,70–74] and hydrocarbon oil [36]. It is thought that the diamond  $sp^3$  bonds present in the coating are able to withstand the plasma etching and to be used as potential diamond nuclei. Substrates displaying the highest diamond nucleation densities, as reported in the previously stated literature, were hard DLC coatings. Thickness of carbon interlayer can potentially have an important effect on the diamond deposition process, but this area has not been widely explored yet. Typically a thin amorphous carbon film of 50-100 nm was used for the subsequent diamond growth [70,71,73]. Thicker interlayers can supply the plasma with carbon species for longer times during the formation of diamond nuclei through constant hydrogen etching of weaker carbon  $sp^2$  bonds. Yang et al [61] used thicker DLC interlayer (0.4  $\mu\text{m}$ ) and the results of their work showed that, from DLC interlayers of higher thicknesses, one has to suppress the hydrogen etching efficiency in order to promote higher diamond nucleation densities. Variation of deposition conditions was demonstrated to change the quality of the diamond films and a two-step diamond growth was adopted for diamond deposition using carbon interlayer, which is covered in the following section. Another approach for enhancing the functionality of amorphous carbon films as an interlayer is further coating the interlayer with an overlay of thin metal, as demonstrated in [61].

### **1.3.3 Nucleation and growth of diamond film**

Diamond nucleation and growth are two different processes with the need of different process parameter settings. Research showed that changing the process parameters during diamond deposition from nucleation to growth stage significantly enhanced the coating quality [37,39,70,71,75]. Dividing diamond CVD process enable us to describe the preferred effects on deposition conditions in both processes [34]. Important factors needed to be taken into account in order to successfully deposit diamond films on foreign substrates are the state of the sample (surface roughness, cleaning process) and CVD deposition parameters (microwave power, chamber pressure, used gases, total gas flow and the position of the sample within the chamber).

#### **1.3.3.1 Diamond nucleation**

The process of diamond nucleation is not so far entirely understood and so far there is no widely accepted mechanism which would clearly explain this phenomenon [76]. Nevertheless, a substantial insight into the formation process has been gathered and is reviewed in this part of the chapter. High diamond nucleation rates are important in order to obtain good quality diamond films. The higher the concentration of diamond nuclei on the surface prior to the diamond growth, the denser and faster the diamond film will be formed

and grown, which provides the opportunity of deposition of films with better mechanical and optical properties, thinner coatings, less defects and more even surface.

Depending on the type of substrate (as reviewed previously) the nucleation stage will differ significantly from the diamond growth stage in terms of time and resulting coating. There is no need for the diamond nucleation stage on diamond substrate or substrate with good diamond seeding, which is why the diamond ultrasonic seeding process gathered wide popularity among the researchers. On any other substrate the diamond growth is usually non-epitaxial [36]. For the non-diamond seeded substrates the nucleation stage can be generally divided into several sub-stages as follows:

- a. Incubation period,
- b. 3D surface nucleation,
- c. Termination of nucleation and 3D growth of nuclei to grains,
- d. Faceting and coalescence of individual grains and formation of continuous film.

Nucleation can happen spontaneously even on non-diamond surface, but two conditions have to be fulfilled – the substrate surface has to be saturated with carbon and high energy sites have to be present (e.g. unsatisfied valences, active sites, dangling bonds). Diamond nucleation on non-diamond substrates mostly happens on intermediate layer of amorphous carbon, carbides or graphite. When those are not presented, they are formed during the incubation period on top of the foreign substrate's surface. The intermediate layer then provides potential places for diamond nucleation sites [37]. Singh [75] proposed diamond nucleation mechanism on a thin layer of amorphous carbon. He studied diamond nucleation on smooth copper mesh and used high resolution transmission microscopy to explore the diamond nucleation, which he then divided into seven consecutive steps (Figure 1.6):

#### Step I – Formation of carbon clusters

- Carbon clusters are formed on substrate surface due to the constant atomic hydrogen bombardment, causing change in local thermal conditions; there is a change in carbon structure from  $sp^1$  to  $sp^2$ .

#### Step II – Conversion of $sp^1$ to $sp^2$ and then to $sp^3$ bonding

- Molecular bombardment of activated hydrocarbon and atomic hydrogen gives substrate enough energy to transform  $sp^2$  bonded carbon into  $sp^3$  bonded. Atomic hydrogen promotes this reaction and stabilises the  $sp^3$  phase.
- Etching of all three carbon phases ( $sp^1$ ,  $sp^2$  and  $sp^3$ ) is taking place at the same time. The etching rate of unstable phase is ten times faster, then etching  $sp^3$  phase.

#### Step III – Crystallization of amorphous phase

- For crystallization to happen, the carbon bonding undergoes transition stage from  $sp^2$  bonded carbon, to disordered domain with  $sp^3$  bonded carbon and finally to  $sp^3$  bonded carbon.
- Carbon atoms have to rearrange themselves during recrystallization process to acquire minimum of surface energy. This rearrangement should favour (111) crystallographic orientation of plates based on the fact that (111) orientation has the lowest surface-free energy in the diamond crystal.
- The recrystallized region becomes a nucleus for subsequent diamond growth.

Step IV to VI – Growth of diamond crystal

- The disordered domain will always be a precursor for diamond growth during the whole process. Carbon atoms from this layer will diffuse inwards to the diamond nuclei.
- The initial shape of the formed diamond will be hemispherical and when the diamond reaches its critical size, it will acquire faceted crystallographic shape.

Step VII – Secondary growth of diamond

- Thickness of disordered domain on the diamond crystal is uneven and constantly changes (8- 14nm). This is due to the concentration fluctuations on the diamond surface.
- When the thickness of disordered domain exceeds the critical thickness (> 15 nm), it will enable recrystallization in that region which will lead to formation of new diamond nuclei.



**Figure 1.6 Diamond nucleation from layer of amorphous carbon; taken from [75].**

His theory complies with work of Feng et al [60,70–72] and Komvopoulos et al [73] who achieved higher diamond nucleation densities using substrates with already pre-deposited DLC interlayer.

The main outlook, or suggestions on how such nucleation enhancing deposition conditions for diamond CVD growth are stated here. Activity of atomic hydrogen during this process should be suppressed and more carbon species should be introduced to the process as well [77]. Plasma conditions should be less severe than for diamond growth, which means that there needs to be reductions in terms of temperature, chamber pressure and

microwave power [38]. This way there is a higher chance of the formation of diamond nuclei without it being etched away by atomic hydrogen before the nuclei can become stable. With higher chances of deposition of diamond nuclei, there are also higher chances in deposition of other non-diamond carbon species, such as: amorphous carbon, crystalline graphite, carbides. It is then very important to set the environment conditions in plasma at a level which will produce high density of diamond nuclei with tolerable amount of non-diamond carbon species together. Obtaining the highest possible nucleation densities goes against diamond quality [38]. While high methane concentration is used for the nucleation stage, the resulting diamond nuclei have a ball-like shape. No clear faceting is visible due to the fact that composition of those balls is a mixture of diamond, amorphous carbon and graphite [38,78].

### **1.3.3.2 Diamond growth**

Diamond quality and growth rates are very important aspects of diamond growth stage. Production of higher quality coating, which takes a shorter time to produce, is of great importance in terms of time and cost, which leads to better market competitiveness. Those two goals oppose each other in terms of process parameters. For high purity coatings the methane concentration is usually in the range of (0.5 – 1.5) vol. % level [78]. This low inlet of methane slows the diamond deposition process considerably because the effects of atomic hydrogen are more pronounced. Typical diamond CVD deposition conditions are a hydrogen-rich or argon-rich atmosphere with a low percentage of carbon carrying gas; most commonly methane, pressure in the region of 10-150 Torr, substrate temperatures of 700-1100 °C [76,79].

General scheme of diamond CVD proces [56] is shown in Figure 1.7 where hydrogen and methane enter high temperature and energy region and undergo an activation process leading to their dissociation. Activation starts a countless amount of reactions, where the gas species react with each other due to their high energy state of activation. As activated gas species are transported through diffusion, forced flow, and/or convection to the vicinity of substrate surface, where yet again a numerous reactions such as adsorption, desorption, diffusion and a range of chemical activations, will take place.



**Figure 1.7 Schematic illustration of diamond CVD growth process; reactants undergo activation process and are then transported to the vicinity of the substrate; taken from [8].**

Generic models [76] without the emphasis on stoichiometry describe the necessary process of diamond formation very well through a set of few equations:

- formation of free radical in plasma,



- Adsorption of hydrogen atom form diamond surface site ( $C_D$ ) - activation of the site,



- Addition of hydrogen to the diamond substrate,



- Addition of hydrocarbon radical to the diamond,



Initially the substrate's surface undergoes hydrogen termination, where majority of the surface active bonds are bonded with hydrogen. It is followed by hydrogen adsorption (2). Two reactions are then possible on such activated site of diamond surface: addition of another hydrogen (3) or addition of hydrocarbon radical (4). Due to the lower amount of hydrocarbon gases in the plasma in comparison with hydrogen, the replacement of hydrogen with hydrogen takes place many times more than the addition of hydrocarbon

radical on the activated diamond site. Creation of open sites on diamond surface is temperature dependant and the amount of open sites increases with the rise in temperature, therefore higher deposition temperatures leads to increase in diamond deposition rates. The set of reaction processes (2)-(4) led to a hydrocarbon radical addition to the surface [34].

The process of chemisorption of the newly added hydrocarbon specie to the adjacent hydrogen terminated diamond site ( $C_D H \dots \underline{CH}$ ) will happen through the processes of hydrogen abstraction and rearrangements of added hydrocarbon atoms [76]:

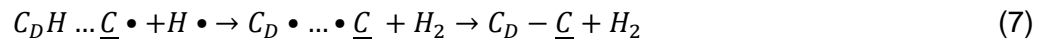
- Hydrogen adsorption from the adjacent diamond site,



- Hydrogen addition to the adjacent diamond site,



- Hydrogen adsorption from diamond site and formation of new carbon to carbon bond,



As one can see, the reaction (5) is very similar to (2) and reaction (6) is similar to (3). At this stage of chemisorption process, the speed depends on the amount of atomic hydrogen species only.

The most commonly used combination of chamber gases is combination of hydrogen/methane, argon/methane, or hydrogen/argon/methane. The less common gases to form the diamond CVD deposition atmosphere are other noble gases, hydrocarbon gases, halogens and addition of oxygen. Their respective specifics are described below.

Atomic hydrogen plays a crucial role thanks to its small size. Diamond has the highest bulk and surface densities of any known material [76] and, thus, most atomic and molecular species cannot terminate the bonds at the diamond substrate – they are simply too big. Atomic hydrogen is the regulating force for controlling the diamond quality. It etches away non-diamond carbon species more rapidly than diamond. Dissociation of atomic hydrogen is function of temperature. Increasing the temperature increases the dissociation rate [38]. Its role was already described in models of diamond growth in the previous section.

Hydrocarbon species supply the necessary carbon atoms for any diamond formation to happen during the diamond synthesis from gas phases. The discussion about which hydrocarbon gas is the most suitable for diamond CVD growth is still on-going [76], but the majority of researches use methane, as it is the basic hydrocarbon gas whose radicals are

the main supply of carbon atoms for diamond growth in CVD processes [34]. On the account of which hydrocarbon gas gives the most methyl radicals near the substrate during diamond growth in microwave plasma chemical vapour deposition – Leeds et al [80] did tests using methane, ethene and ethyne. They found out that, at high microwave powers ( $\geq 700$  W), the plasma composition becomes independent from the hydrocarbon precursor. At lower microwave powers it was methane which gave the highest amount methylene radicals in the plasma, followed by ethyne and the ethene yield lest of methane radicals.

Argon is used as a main part of the atmosphere with only hydrocarbon gas addition, or in combination with a small amount of hydrogen in most cases when argon is used [51,81–83]. Hydrogen was originally thought to be the essential part of diamond deposition in CVD systems, which was demonstrated as a wrong assumption by Gruen et al [84], who deposited nano and micro crystalline diamond film mixtures from argon and hydrogen-depleted fullerenes. The effects of argon-rich atmosphere are similar to the effects of increase of hydrocarbon gas within the system, or lowering of plasma density – they all lead to the lower size of diamond grains within the nanoscale region and larger proportion of non-diamond hydrocarbon species present within the diamond film [16]. The diamond growth mechanism is deemed to be in this case largely done through  $C_2$  dimers formed within the plasma at their adsorption onto the surface, but the exact mechanism is still unknown and disputed between the researches [85,86].

Oxygen addition in form of  $CO$ ,  $CO_2$ ,  $O_2$  or alcohol was recognised to have a beneficial effect on diamond growth rates and quality. Oxygen addition, even more importantly, enables lower diamond CVD deposition temperatures, than the most commonly used C-H only system. Addition of oxygen was found to have little effect on the amount of hydrogen and hydrocarbon radicals, for oxygen creates  $(OH)^\cdot$  radicals which have the same effect as hydrogen radicals in terms of etching non-diamond carbon species [6,8]. Care must be taken for too much oxygen present in the chamber can lead to oxygenation of the substrate surface and destruction of the diamond coating [6]. At low CVD deposition temperature the etching activity of atomic hydrogen is lowered and it is no longer able to etch effectively the non-diamond species on grown surface, but adding oxygen into the system facilitates the etching process [87]. Ternary phase diagram displaying diamond deposition regions within C-O-H gas mixtures have been made [88] and, with the progress in diamond deposition techniques, the ternary diagram has seen expansion of the area where diamond growth film is feasible [89]. C-O-H systems are nowadays commonly used for diamond CVD growth [90,46].

Halogen addition in form of halogenated precursor gases has a similar effect to the oxygen. It was found that their addition allows the use of lower CVD deposition temperatures

(250-750) °C [8]. The use of halogenated precursors was also reported [91] to increase diamond growth rate and its purity.

Nitrogen incorporation into the diamond lattice increases the intrinsic stress within diamond films through formation of vacancy defects through distortion of diamond lattice.[92] From tribology point of view the nitrogen addition is not desirable, while nitrogen vacancy centres have a potential in the field of sensing [93] and electronics [94]. It was found that nitrogen in form of N<sub>2</sub> gas is unreactive under typical diamond CVD deposition conditions, while addition of other nitrogen containing gases (NH<sub>3</sub>, NH<sub>2</sub> and HCN) has a profound effects on diamond growth [95,96]. The diamond growth rate is slower than in case of pure H<sub>2</sub> and CH<sub>4</sub> atmosphere, which is due to the formation of HCN from CH<sub>3</sub> radicals, which are more energetically preferable and, therefore, acting as a carbon sinks and slowing the diamond deposition rates.

Factors influencing the resulting structure of diamond growth are numerous. The main factors, which are commonly adjustable during the diamond deposition, are chamber pressure, microwave power, gas mixture composition and total gas flow. It was demonstrated [38,77,78] that gas flow variation has a minor influence on resulting diamond film, unless one selects an extreme deposition conditions. Since diamond deposition is temperature driven, the following observations are valid only for relatively narrow deposition condition process, due to the fact that they all are contributing to the resulting substrate temperature. Diamond morphology changes with increasing pressure: from ball-like shape diamond at low pressures into faceted diamond at high pressures. Higher amounts of pressure decrease the size of plasma ball, while at lower pressures with large size of formed plasma ball, more active species are delivered to the substrate's surface [38]. The effect of hydrogen etching is suppressed by the amount of carbon active species. Resulting coating consists of diamond nuclei and other carbon species at low pressures due to the inability of atomic hydrogen to rapidly etch the surface. Microwave power, or any other source of heat in case of other CVD deposition techniques, increases the area of activated gas. Leeds et al [80] observed higher diamond nucleation densities at lower microwave powers. At higher microwave powers the diamond nucleation density was lower, although the change of structure from ball-shaped diamond into faceted diamond was observed. Increasing the amount of hydrocarbon gas fed into the CVD chamber results in higher amount of carbon active species existing in the plasma [78]. The increase leads to higher deposition rates of carbon atoms on the substrate surface. When methane concentration is increased over a threshold value [36] (the value of the threshold depends on other process parameters) many different carbon species are co-deposited together with the diamond, therefore, if one aims for high purity diamond, the amounts of carbon carrying species will have to be kept at minimum [38].

## 1.4 Thin film deposition techniques

In this work two different deposition processes were being employed – magnetron sputtering and chemical vapour deposition. Both of the processes belong to the vapour deposition techniques for material deposition; typically in form of films, onto substrates. Magnetron sputtering technique is one of the physical vapour deposition techniques (PVD) where deposited materials are vaporized and transferred through vacuum or low pressure atmosphere onto substrates. Films can be deposited either in their pure form, or compounds can be formed by reactive deposition process involving co-deposition of different materials, or reaction with gaseous environment. Main PVD techniques are vacuum evaporation, sputter deposition and ion plating.

CVD techniques rely on decomposition of gases where the gaseous species are then deposited onto a substrate. Decomposition or dissociations processes are facilitated through thermal activation of gaseous species. Typically, the atmosphere for CVD processes involves gas containing the desired elements which are being deposited and a gas enhancing the dissociation processes (e.g. hydrogen). Since dissociation of the gases is a thermally induced process, it is possible to deposit coatings either by heating the substrate so that the dissociation process happens around the sample, or by using the plasma for the thermal activation process. The latter approach is common for deposition of majority of the films done by CVD, since the substrate does not need to be subjected to an overly high temperature.

Both PVD and CVD techniques have a wide range of possible applications and in some instances both of the techniques can be utilised to produce the same desired coatings (e.g. carbide and nitride coatings [97], amorphous carbon [98]). Besides, techniques combining the two deposition processes are being used in coating industry; an example can be Teer Coatings hybrid system [99]. The method of choice for films, which can be deposited by both of the techniques, depends on the coating's specific requirements. PVD deposition techniques are usually run at lower temperatures compared to CVD processes allowing therefore coating temperature sensitive substrates. Another benefit in favour of PVD techniques over CVD is the fact that, during CVD, a gaseous precursors and their by-products can often be toxic, flammable and/or explosive, so care must be taken with their handling and storage. CVD technique on the other hand, can uniformly coat more complicated surfaces than the PVD techniques [100]. Careful consideration, or suitability and cost are strongly advised when choosing between the two techniques.

The broad range of different PVD and CVD techniques is not the objective of this study and therefore, only the principles of the magnetron sputtering and plasma enhanced CVD

techniques will be described further. For more detailed and broader understanding of the topic the readers are referred to [18,101].

### 1.4.1 Magnetron sputtering

Magnetron sputtering technique developed from the basic sputtering technique, which uses a sputtering effect to transfer coating material onto a substrate from a target by ion bombardment. The target (block of material which is used for the material transfer onto the substrate) is bombarded by ionised plasma particles (most commonly argon gas) generated by glow discharge plasma. The bombarding ions transfer energy to the surface of the target which causes sputtering of atoms from the target surface. Sputtered atoms are then subsequently deposited onto the substrate, forming a coating layer. Ions in the plasma are generated by atomic collisions with the electrons leading to their ionisation and creation of additional electrons. Ionised atoms are then drawn to the target, which is connected to a negative voltage. Schematics of the whole process can be seen in Figure 1.8. However, this setup has its limitations in efficiency in terms of deposition rates and substrate temperatures [102]. The mean free path of electrons is relative long, meaning that the electrons are able to reach the anode (substrate) with high energy and overheat the substrate, but not producing the ions which are needed for the sputtering process. Furthermore, the electrons can be absorbed by the chamber walls which also contributes to the equipment's low efficiency [103].

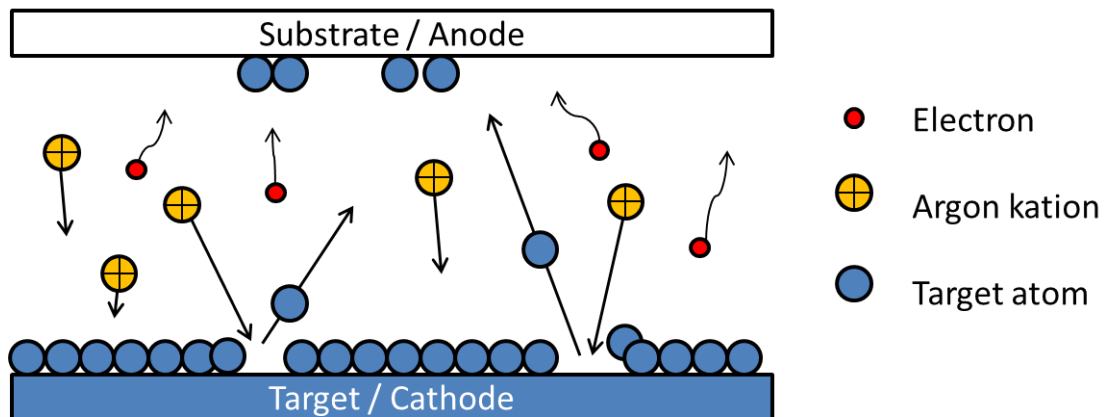


**Figure 1.8 Schematics of sputtering process; target atoms are being ejected through bombardment of argon kations, which are created in plasma due to collisions of argon atoms with electrons.**

In order to improve the sputtering technique efficiency the use of magnetic field has been considered in order to restrict the electrons movements to the vicinity of the sputtering targets. This approach yielded desired results and magnetron sputtering technique, where

sets of magnets are installed behind the targets, has been utilised. Positioning the magnets in a way that their magnetic lines are parallel to the target's surface leads to formation of an electron trap. The electrons are not able to escape from the magnetic field and provide higher plasma ionization close to the target, increasing the plasma efficiency. Sputtered atoms are not affected by the magnetic field present since they do not possess any charge. Increased plasma ionisation leads to an increase in sputtering rates. Furthermore, increased ionisation efficiency allows plasma to be maintained at lower pressures and lower operating voltages [102].

Figure 1.9 displays three different versions of possible magnetron setup. On the left there is a conventional magnetron setup, where one clearly sees the high plasma concentration in the vicinity of the target. In the event of placing the substrate within the region of high plasma concentration the substrate would be subjected to constant ion bombardment, which influences on the coating's properties. Temperature rise, increased stress within the film and a lower grain size, are just few examples of possible effects of excessive ion bombardment, which clearly identifies the need of control of ion bombardment, so it can be optimised and tailored for obtaining the beneficial effects of it while eliminating any undesired effects. In case positioning the substrate outside of the plasma region (as is schematically shown in the Figure 1.9 – left hand side), the substrate will be surrounded with low plasma density, which would lead to insufficient ion bombardment in order to influence on the film growth and properties [102,104].



**Figure 1.9 Comparisons of plasma reach in different magnetron setups; taken from [102].**

A better control of the plasma region and, consequently, of the coating quality, was enabled by the invention of unbalanced magnetron sputtering, which uses different strengths of the outer and inner magnets. In case of having a magnetron with weaker outer magnets (Figure

1.9 – called Type 1), the magnetic field line is directed partially to the chamber walls causing partial electron losses onto these walls, and insufficient plasma density near the target is a possible outcome. However, in case of a setup with weaker magnets in the centre of the magnetron (Figure 1.9 – called Type 2), plasma region spreads far more than with the conventional magnetron setup. This change in magnetic field allows some electrons to travel closer to the surface of the substrate and cause ion bombardment of the surface, which can be controlled, although electron losses on the reactor walls are also present in this case [102]. Ion bombardment has been found very helpful during the coating process when appropriately used, as well as it has an added benefit of being a very effective pre-cleaning process prior to the coating's deposition [102,104]. The amount of ion bombardment on the substrates surface can be adjusted by the target-to-substrate distance and varied by different type and amount of biasing of the substrate. Typically, during the cleaning process, more voltage is applied to the substrate than to the targets, causing an increase of plasma ionization near the substrate surface, hence causing an increase in the ion bombardment [104].

Magnetron sputtering technique is scalable in size of desired coating area, as well as to the sputtering rates, which can be varied simply by the use of multiple magnetrons. Figure 1.10 shows a possible arrangements of how opposing magnetrons can co-operate with each other in terms of formation of ionised plasma field. The vertically opposed magnetic polarities on magnetrons (close-field configuration) enhance not only sputtering rates, but also prevents electron losses on the chamber walls, giving higher plasma density. The second possible magnetron setup has identical magnetic polarities (mirrored configuration) which, as opposed to the close-field configuration, enable losses of electrons on the chamber walls. Mirrored configuration has its uses for specialized applications, but close-field arrangement is more preferred in industry [102,105].



**Figure 1.10 Possible magnetron configurations; taken from [102].**

Typical operating substrate temperatures for the close-field unbalanced magnetron sputtering technique are below 250°C during the whole sputtering process [99]. Additional lowering of the temperature can be at the expense of the deposition rates [102]. Although substrate temperatures are relatively low, the temperatures of magnetrons are high. More than 80% of the electric power supplied to the magnetrons is transformed into heat [106] forcing the active cooling of target and magnets being incorporated in the setup.

### **1.4.2 Chemical Vapour deposition**

Chemical vapour deposition technique is used for deposition of thin-film coatings onto various solid substrates. Great variety of materials, of which a selection can be found in [107], were deposited using this technique. The most simplified principle of CVD involves a chamber with heated substrate, and precursor gas. Chemical reactions will occur near the hot substrate which will result in thin-film formation on the substrate's surface. The process is accompanied with production of by-products that are extracted from the chamber along with the unreacted precursor gases. Due to the great variety of materials which can be deposited using CVD technique, there are many different types of CVD. Basic CVDs either

use hot-wall reactors or cold-wall reactors. The range of enhanced CVD deposition techniques is vast, ranging from hot filament, combustion, ion, plasma and others [108].

The diamond CVD growth principle is to create diamond crystals by dissociation of carbon-containing gas. Carbon atoms then react with the surface of the substrate and organise themselves into crystals [86]. Growing diamond films in simple thermal CVD process were too slow, therefore enhanced CVD techniques are being used almost exclusively: hot filament, direct current discharge, plasma jet, radio frequency plasma and microwave plasma. The mentioned techniques are very different to each other in the sense of growth rate, coated area, quality of the coatings, stability during the process and temperature of the substrate [8].

The most promising techniques for the large area and good quality diamond films are microwave plasma CVD (MPCVD) and hot filament CVD (HFCVD). In both cases the commonly used carbon carrying gas is methane, which is diluted in hydrogen. The two of those techniques will be described in the following sections.

#### 1.4.2.1 Hot Filament Chemical Vapour Deposition

The hot filament technique is, as its name suggests, a thermal enhanced CVD process. The setup needed for HFCVD (see Figure 1.11) is relatively simple, which caused its wide spread within the researchers.

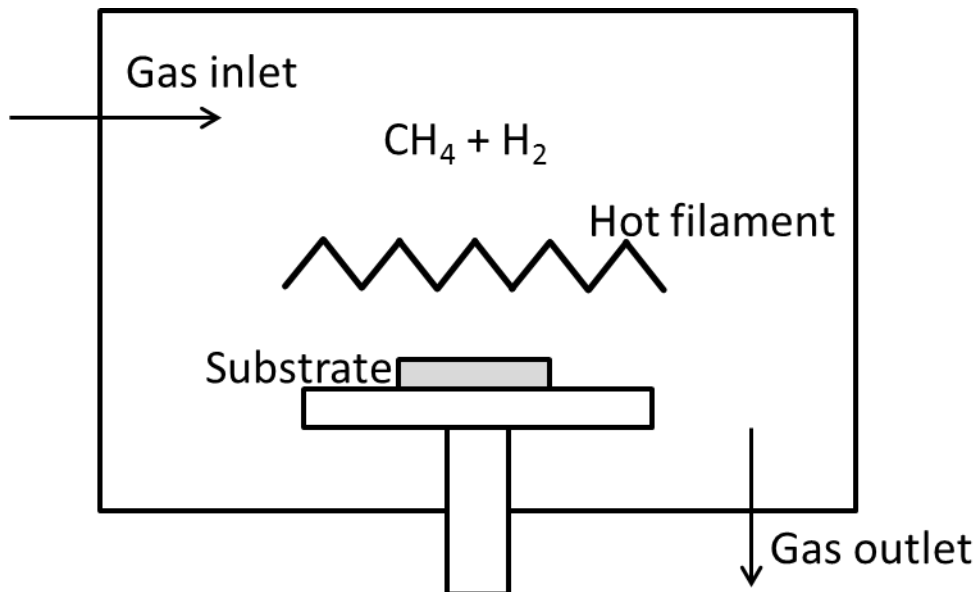


Figure 1.11 Schematic of the HFCVD apparatus.

For operation of HFCVD vacuum chamber, gas inlet and outlet with a rotary pump and filament are the only things which are needed. The filament requires to have a high melting point (such as tungsten) and is positioned close to the substrate. The filament's main role is to dissociate the gas species, but because of its proximity to the substrate and the temperature which it is operating at (2000–2300 °C), it inevitably heats the substrate as well [8]. Furthermore the filament also reacts with the carbon carrying gas and undergoes carburization of its surface. This carburization reaction delays the diamond growth in the initial stages due to the consumption of part of the carbon atoms [79].

Temperature upper limit for the filament material restricts the maximal gas temperature during deposition. The deposition rates for HFCVD are fast (up to several microns per hour) and the HFCVD are easily scalable and can deposit diamond over large areas [6]. HFCVD downfalls are mainly due to the presence of the filament close to the substrate material. Contamination of diamond film by the filament material is difficult to avoid, which is a problem for films deposited for electronic industry [5]. Also the degradation and bending of the filament and generation of carbon flakes during the deposition are some of the disadvantages of this technique [79].

#### **1.4.2.2 Microwave plasma chemical vapour deposition**

MPCVD is the most popular type of deposition where deposition of diamond thin films is utilised. Microwaves supplied to the reactor chamber make the molecules of gas to oscillate and collide with each other, which leads to the gas activation. Atomic hydrogen and other activated species within the chamber are produced by electron impact dissociation of molecular hydrogen and other molecules. MPCVD processes differ from other types of CVD in their ability to produce radicals with high kinetic energies. Taking hydrogen as an example, the process can be explained through its binding energy, which for hydrogen is 4.5 eV. Due to the mass difference of impaction electron and molecule of hydrogen, the impact energies have to be far higher than 4.5 eV to dissociate the molecule (more than 9.5 eV) [8]. The difference in energies needing for activation will then leave resulting plasma species with considerable amount of energy, making them capable of being more active at the substrate's surface [6].

Figure 1.12 shows schematics of the two most common MPCVD setups. Microwaves are generated in the magnetron (mostly they possess a frequency of 2.45 GHz due to the widespread of such setups lowering the manufacturing prize) and the wave guide then directs them to the deposition chamber. Tuners installed in the wave guide are used to minimize the number of reflected microwaves back towards the magnetron. Ionised gas

inside the chamber forms a plasma ball which can be contactless with surrounding walls and substrate [34].



**Figure 1.12 Examples of the two common setups of MPCVD; a) NIRIM-type reactor; b) ASTEX-type reactor; taken and modified from [5].**

The great advantage of MPCVD systems is that microwave deposition is an electrode-less process. Therefore, any contamination from electrode erosion is excluded. The limiting factor of MPCVD is its scalability. The classic MPCVD setups (Figure 1.12) offer only possibilities to coat parts of several inches in diameter [6,34]. The next limitation is the close presence of the plasma ball to the substrate surface. The processes inside the plasma ball generate a great amount of heat and the heat is then inevitably transferred into the substrate. In recent years however a novel CVD apparatus called Linear Antennae Microwave Plasma Chemical Vapour Deposition (LAMPCVD), which revolutionized the MPCVD process and brought greater potential to an industrial utilization of MPCVD coated diamond parts, was developed.

The use of linear antennae introduced a new setup which uses surface wave type of microwaves generated by linear slot antennae. The new key feature of LAMPCVD is in generating low-temperature large-area surface wave plasma. The pioneering work on nanocrystalline diamond grown in the LAMPCVD was done by Tsugawa et al [90]. They demonstrated the deposition of nanocrystalline diamond coatings on a substrate with temperature even less than 100 °C [87]. A second research group utilising LAMPCVD for diamond film deposition was the group of Fendrych et al [109]. LAMPCVD provides uniform, good quality nanocrystalline diamond coatings over large substrates.

The key difference in plasma generation in comparison to classic MPCVD setups is that microwaves generated from the antennae ionize only a thin layer of gas around the antennae (very much like hot filament setup). The antennae are placed in the quartz tubes where they are air-cooled on the inside. Taper-shaped outer shields are used to obtain uniform surface wave plasma by reflecting the microwaves to the substrate surface (Figure 1.13) [110].



**Figure 1.13 Schematic of tapered shields for increased surface-wave plasma uniformity [110].**

Generated plasma then diffuses downward to the substrate where diamond deposition takes place (Figure 1.14). Microwaves do not penetrate the bulk of the plasma. They do not reach the surface of the substrate either and, consequently, cannot heat it. Therefore, it is possible to deposit diamond even at temperatures below 100°C [46]. The great advantage of LAMPCVD is its ability to coat large areas. Other MPCVDs are not able to do so, due to the restrictions caused by the microwave wavelength – typical maximal coated area for them is (10-15) cm<sup>2</sup> [110].



**Figure 1.14 Arrangement of microwave antennae [90].**

Research groups that were using LAMPECVD are so far using methane in hydrogen-rich plasma with oxygen addition as a working environment and are able to produce

nanocrystalline diamond films with grain size in tens of nanometres [90,46,109]. The largest coated area with ND was done by Tsugawa et al [90] over the area of 30x30 cm<sup>2</sup>. The LAMPCVD setup caught up with HFCVD systems, in terms of the scalability of both of the systems, is only dependant on the investment into the equipment. Currently LAMPCVD systems are available to buy from Seki Diamond (sekiamond.com).

## 1.5 Stress development during the film deposition

Certain degree of stress is commonly found in all amorphous and polycrystalline and single crystalline films grown by one of many PVD techniques. The stress accumulated within a thin coating can reach levels where plastic deformation will occur spontaneously without any need of triggering mechanism (such as mechanical impact, bending force, etc.). The origin of stress within thin films can consist of epitaxial stress (lattice mismatch between substrate and film while grown epitaxially), intrinsic stress (stress developed during film's deposition or growth) and thermal stress (resulting from different thermal expansivities of substrate and film). The type of plastic deformation depends on the type of stress present in the film. Films under compression can relieve the stress through blister formation or delamination. Film under tension can relieve the stress through cracking or peeling. The unit of stress measurements is Pascal and its typical values ranging from minus several GPa (compressive stress) to plus several GPa (tensile stress). This section will be limited to thin film deposition, meaning that the thickness of substrate is substantially larger than the thickness of deposited film.

### 1.5.1 Epitaxial stress

Epitaxial stress exists between two single crystalline surfaces forcing the newly grown crystal to initially grow matching the lattice parameters of the substrate. In case of two materials of different lattice constants, it leads to development of stress at the interface of the two materials. Equation (8) describes this stress calculation, where  $E_{\text{film}}$  is film's Young's modulus,  $d_{0,\text{film}}$  and  $d_{0,\text{sub}}$  are strain-free lattice spacing of calculated materials.

$$\sigma = E_{\text{film}} \cdot \frac{d_{0,\text{sub}} - d_{0,\text{film}}}{d_{0,\text{film}}} \quad [\text{GPa}] \quad (8)$$

When lattice spacing of film is larger than the one of substrate, the resulting film stress will be compressive, which is denounced by minus sign by convention and vice versa [111]. This study reports on growth of polycrystalline diamond films and sputtered polycrystalline and amorphous coatings on steel substrates, where epitaxial growth of film on substrate is not expected [112].

## 1.5.2 Intrinsic stress

Certain amount of stress is commonly found in all amorphous, polycrystalline and single crystalline films grown by one of many PVD techniques. Generally films are being deposited under non-equilibrium conditions, which leads to number of possible defects being developed and co-formation of different structures. Stress evolution in polycrystalline films develops with dependence on the nature of the film, deposition conditions, rate of deposition and the level of contamination [113].

Stress development in thin films can be of different nature at different depths of the deposited film. It is possible to divide the stress development into two groups: stress before coalescent film is deposited and stress arising from the film growth.

### 1.5.2.1 Pre-coalescence stage

During the initial stage, the deposited material forms individual islands as separate nucleation events at energetically favourable places. It was understood that those clusters of deposited material are under compressive stress due to capillary forces being exerted on the isolated clusters [114]. The behaviour of deposited islands of solids is similar to the behaviour of liquids on solid surface and can be described by modified Laplace formula:

$$\Delta p = \frac{2f}{r} \quad [\text{GPa}] \quad (9)$$

Where  $\Delta p$  is Laplace surface pressure,  $f$  is surface stress and  $r$  is a radius of the sphere. Surface capillary forces are constraining the lattice structure and are the cause of the compressive stress. As can be seen from equation (9), with growing size of the island the force exerted onto the islands will decrease [115].

### 1.5.2.2 Coalescing stage

The island coalescence mechanism was first identified by Hofman et al [116,117]. They identified that two island surfaces growing at close proximity will spontaneously snap together to form a grain boundary as demonstrated in Figure 1.15. The joining process dictates their partial displacement due to the adhesion of the material to substrate which imposes elastic strain on the growing crystals. The idea behind the approach is that the net surface free energies for separate grains are greater than free energy system of joined grains, including a relatively low energy of grain boundaries.

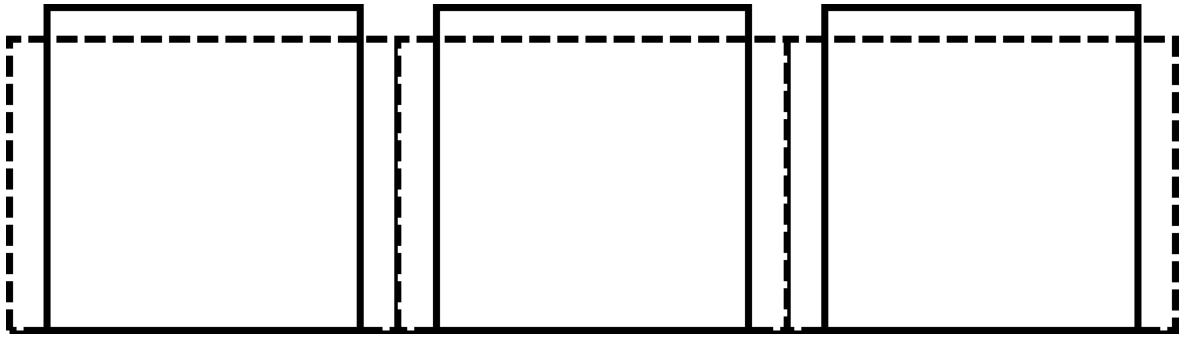


**Figure 1.15 Grains of polycrystalline film before (solid lines) and after (dashed lines) coalescence.**

The tensile stress of coalescing grains can be calculated using the size of gap ( $\Delta$ ) which separates them, as

$$\sigma = \frac{E_f}{1-\nu} \cdot \frac{\Delta}{L} \quad [\text{GPa}] \quad (10)$$

Where  $\sigma$  is stress,  $(E_f/1-\nu)$  is biaxial film modulus,  $E_f$  and  $\nu$  are Young's modulus and Poisson's ratio of the deposited material, respectively, and  $L$  is the diameter of the grain. Nix and Clemens [118] and later Freund and Chason [119] improved the model of coalescence of individual islands into a film further improving the calculation accuracy.

### 1.5.2.3 Film thickening stage

The further stress development within the newly coalescent film depends strongly on the atomic mobility of deposited material and the deposition condition. In case of further epitaxial film growth the tensile stress value from the process of coalescence will be 'copied' and uniformly strained films can be deposited. Such process is typical for materials with low adatom mobility. Materials of high adatom mobility, like FCC metals of relatively low melting points, tend not to sustain the tensile stresses imposed from coalescence stage, which leads to the coatings relaxation. The exact stress behaviour is governed by the deposition temperature. Thurner and Abernamm [120] demonstrated on chromium and iron that, in case of their deposition at room temperature, the stress within the film will stay in tensile mode. While if the deposition was carried out at increased temperatures, the adatom mobility increased, and the stress within grown film fell into slightly compressed state as the film thickness increased.

The differences for the low and high adatom mobility polycrystalline film growth are displayed in Figure 1.15. The  $z_0$  is the initial thickness of the coating when it's coalescent from individual islands and  $L$  is, as mentioned, the diameter of individual grains. In case of low adatom mobility materials the arriving atoms do not provide any relaxation to the film

which grows epitaxially further in the stresses state. High mobility adatoms, on the other hand can diffuse into the grain boundary area, which is energetically favourable. Atom insertion in the grain boundaries leads to the grain boundaries not being able to snap together, as in case of film coalescent mechanism, hereby providing relaxation of tensile stress [118].



**Figure 1.16 Simple model of polycrystalline film growth under low and high adatom mobilities after the initial coalescence stage, taken from [118].**

Grain boundaries within polycrystalline films have an important role of determination of resulting stress. Chason et al [114] developed a model explaining the preferential diffusion of adatoms into the grain boundaries and derived an equation for resulting total stress within the as-grown film. During the deposition, impinging atoms raise the chemical potential of individual crystals from its equilibrium, which leads to:

$$\sigma = \sigma_i - \sigma_c N_{gb} \left( \frac{a}{h} \right) \quad [\text{GPa}] \quad (11)$$

Where  $\sigma$  is the total stress,  $\sigma_i$  and  $\sigma_c$  are tensile and compressive stresses, respectively.  $N_{gb}$  is the number of added atoms to the grain boundary region,  $a$  is the nominal atomic size and  $h$  is the film's thickness. In this case the  $\sigma_c$  is expressed as  $\sigma_c = E\alpha a/L$ , where  $\alpha$  is a geometric shape factor. From equation (11) it is seen that in case of high mobility of adatoms, the grain boundary will get populated, and the  $N_{gb}$  will increase causing the compressive stress to dominate the film. Adatoms with low mobility will not have sufficient energy to diffuse into the grain boundary region and, therefore, the value of  $N_{gb}$  will equal to zero and the deposited film will stay under tensile stress.

Nevertheless, the resulting stress within the film is influenced greatly by many factors, some of which have not been mentioned, as for example co-formation of different materials, impurities incorporation and ion bombardment.

Ion bombardment occurs during various deposition processes – sputtering, chemical vapour deposition. Films produced under ion bombardment are often reported [121,122] to be under biaxial compressive stress through formation of lattice defects and densification of the film.

### 1.5.3 Thermal stress

Thermal stress is an extrinsic type of stress which develops after the coated substrate is brought to a different temperature than the deposition temperature. It arises from different thermal expansion properties of substrate and the deposited film. Thermally induced stresses can result in material's deformation and this property has been widely used by society through the use of bimetal plates. The bending of the bimetal plate depending on temperature change has been an indicator of appropriate temperature in ovens for decades. In case of deposition of thin films for their further mechanical application, the thermally induced stresses are not desirable. Thermal expansivity of material can be described by material's linear thermal expansion coefficient (CTE, or  $\alpha$ ). Thermal stress is regarded [123–126] to be the most significant cause of adhesion failures for materials with large differences between their CTEs. Prime example is deposition of diamond on steel, where their mismatch of CTEs in the region between 20-800°C are  $2.8 \times 10^{-1} \text{ K}^{-1}$  and  $12.5 \times 10^{-6} \text{ K}^{-1}$  for diamond and M42 steel, respectively. Thermal stress in thin films on thick substrate can be calculated as:

$$\sigma_{th} = \frac{E_D}{1-\nu} \int_{T_1}^{T_2} (\alpha(T)_D - \alpha(T)_S) dT \quad [\text{GPa}] \quad (12)$$

Where  $E_D$  and  $\nu$  are Young's modulus and Poisson's ratio of diamond,  $\alpha(T)_D$  and  $\alpha(T)_S$  are thermal expansion coefficients of diamond and substrate, and  $T_2$  and  $T_1$  at deposition and room temperatures, respectively.

## 1.6 Stress measurements

Stress within deposited films can be either measured in-situ, or more commonly, the residual stress is measured. In-situ measurement is possible on flexible substrates where the stress developed within the system can bend the tested sample. Measuring the curvature of the sample relates directly to the amount of stress within the system at the given time. Most commonly used material for substrate nowadays are silicon wafers which gave name to this type of measurements – wafer curvature measurements. The relationship between stress and bending of the substrate/film was first observed by Stoney, who also devise an equation which nowadays bears his name:

$$\sigma = \frac{1}{6} \left( \frac{E_S}{1-\nu_S} \right) \frac{t_S^2}{t_F} \frac{1}{R} \quad [\text{GPa}] \quad (13)$$

Where  $E_S/(1 - \nu_S)$  is biaxial modulus of substrate,  $t_S$  and  $t_F$  are substrate's and film's thicknesses, respectively.  $1/R$  is experimentally determined curvature of the substrate/film system. The equation for wafer bending progressed since its first appearance and elastic anisometry of used materials is being taken into consideration [127]. The most common approach to the actual measurements of the warpage is done through the use of single or multiple laser beams, measuring their deflection as the sample deforms.

Ex-situ measurements are measurements of residual stress which is sum of all possible stresses enforced upon the sample during and after the film's deposition. There is a great number of ways how to measure the residual stress, such as x-ray diffraction, neutron diffraction, nanoindentation, curvature measurements, etc. [128,129]. Here, the author will limit to briefly introducing methods of x-ray diffraction and Raman spectroscopy stress measurements.

X-ray diffraction is the concept of deriving the strain from the diffractograms in the shift of diffraction peak positions in comparison to the unstressed state of particular material and can be described as:

$$\sigma = \frac{E_F}{(1-\nu_F)} \frac{(d^{hkl} - d_0^{hkl})}{d_0^{hkl}} \quad [\text{GPa}] \quad (14)$$

Where  $E_F/(1 - \nu_F)$  is biaxial modulus of film,  $d^{hkl}$  and  $d_0^{hkl}$  are values of lattice spacing of {hkl} lattice planes for strained and strained-free film. For further information regarding x-ray diffraction stress analysis author advises a deep review of Welzel et al [130].

The use of Raman spectroscopy for stress measurements originates from work of Anastassakis [131] on residual stress observations in silicon. It was concluded that the strain within crystals affects the phonon frequencies which results in the shifting of the Raman peak position. Since then, the Raman spectroscopy became largely popular for investigation of stress related effects in microelectronics on materials such as Ge, GeAs, GaN, silicides which are commonly used materials in semiconductor industry [132]. Several groups were working on establishing models of using Raman spectroscopy data for stress measurements of diamond thin films from which the work of Ager and Drory [133] developed a model of common biaxial stress within diamond films with various crystallographic orientation, including polycrystalline diamond films. They observed diamond peak shift to a higher wavelengths and its splitting into two separate peaks in case of polycrystalline diamond under compressive stress. An example of such spectra can be seen in Figure 1.17. The shifting and the splitting of the diamond peak is observable due to the impact of the stress/strain onto the phonon frequencies. It is a well-documented phenomena which was observed with many materials, such as diamond, silicon and quartz [134]. Both the peak shifting and its splitting are related to the strains along the crystallographic axes of the diamond structure. They calculated equations of stress calculation within polycrystalline diamond films, which are:

$$\sigma = -1.08 (v_S - v_0) \quad [\text{GPa}/\text{cm}^{-1}] \quad (15)$$

$$\sigma = -0.384 (v_D - v_0) \quad [\text{GPa}/\text{cm}^{-1}] \quad (16)$$

Where  $v_S$  and  $v_D$  are the observed maxima of diamond peak intensities for singlet and doublet phonons, respectively. While  $v_0$  is unstressed position of diamond peak ( $\approx 1332 \text{ cm}^{-1}$ ). The singlet phonon peak refers to the diamond peak of lower wavenumber, which is made of gathered signal from parallel polarization. The doublet phonon peak lies at higher wavelengths and is due to the parallel polarization of backscattered signal from the investigated surface.



**Figure 1.17 Representative Raman spectrum of polycrystalline diamond film deposited on Ti-6Al-4V where the shift and splitting of the 1332 cm<sup>-1</sup> diamond peak is observable; other presented peaks are broad peaks of disordered (D) and graphitic (G) carbon and of transpolyacetylene (TPA); taken and modified from [135].**

Often, in case of nanocrystalline diamond films, it is not possible to distinguish between the singled and doublet peaks though the relatively large peak broadness and through diamond peak being only partially visible due to high intensity of the D peak of amorphous carbon [136,137]. In such case, a middle value centred between the two peaks has been considered and a new equation has been put forward by Ralchenko et al [7,123]:

$$\sigma = -0.567 (v_m - v_0) \quad [\text{GPa}/\text{cm}^{-1}] \quad (17)$$

Where  $v_m$  is the position of diamond peak identified in Raman spectrum where no splitting of the diamond peak has been observed, therefore:

$$v_m = \frac{1}{2} (v_S + v_D) \quad [\text{cm}^{-1}] \quad (18)$$

It is worth to mention that care must be taken when acquiring the Raman spectra in case of diamond films with respect not to be heating the film. It was shown [138] that diamond Raman peak can shift to lower wavelength with increase of temperature. High laser powers can therefore overheat the diamond film locally, which can affect the peak position, or even change the structure of diamond film.

## 1.7 Thin film adhesion testing

Coating's adhesion is one of its very important properties enabling coatings to perform their intended function. A brief description of principles of adhesion and how it can be assessed is deemed to be necessary to describe in order to highlight the problematics of thin films deposition.

Thermodynamically adhesion can be defined as a given amount of energy which is necessary to supply in order to de-bond two materials creating more of free surfaces. The work required can be described as:

$$W_A = \gamma_f + \gamma_s - \gamma_{fs} \quad [J] \quad (19)$$

Where  $W_A$  is the true work of adhesion,  $\gamma_f$  and  $\gamma_s$  are film and substrate surface energies and  $\gamma_{fs}$  is the interface energy. Figure 1.18 shows directions of the forces acting upon the surface and interface energies in case of a particle on substrate arrangement. The work of adhesion is a constant for given specific combination of film and substrate and depends on the type of bonding formed between the film and substrate, as well as on the level of substrate's surface contamination prior to the deposition of the film [139].



**Figure 1.18 Schematics of surface and interface energies of a particle on substrate;  $\gamma_f$ ,  $\gamma_s$  and  $\gamma_{fs}$  are the film, substrate and interface energies, respectively;  $\theta$  is the wetting angle; taken from [139].**

In practice adhesion is assessed through film delamination from the substrate. Plastic deformation of film and/or the substrate is usually involved in the de-bonding process and therefore the obtained values of adhesive work is not only the value of true adhesion energy, but rather a sum of the energies. The work excreted and measure has been termed a practical work of adhesion ( $W_{PA}$ ) which is described as:

$$W_{PA} = W_A + U_F + U_S + U_{Fric} \quad [J] \quad (20)$$

Where  $U_F$  are  $U_S$  are energies spent on plastic deformation on film and substrate and  $U_{Fric}$  is loss of energy through friction. It is important to note that the  $U_F$ ,  $U_S$  and sometimes  $U_{Fric}$  as well are functions of true work of adhesion. The amount of energy dissipation being spent on  $U_F$ ,  $U_S$  and  $U_{Fric}$  has a relation to the direction of the stress being applied to the coated

surface. Figure 1.19 shows the dependence of interfacial fracture toughness ( $\Gamma_{IC}$ ) of the angle of applied stress from pure normal stress ( $\psi = 0^\circ$ ) and pure shear stress ( $\psi = 90^\circ$ ). It is seen that the energy losses spent on  $U_F$ ,  $U_S$  and  $U_{Fric}$  is progressively increasing between the application of normal and shear stresses [140].



**Figure 1.19 Dependence of interfacial fracture toughness ( $\Gamma_{IC}$ ) on the stress direction;  $\Gamma_{IC}$  rises exponentially between normal stress ( $\psi = 0^\circ$ ) and shear stress ( $\psi = 90^\circ$ ); taken and modified from [139].**

The results of adhesion test of film/substrate system therefore depends strongly on the testing procedure as well as on the material characteristics of the bonded materials. Nevertheless, the interfacial toughness is of a crucial importance whichever type of testing is used. In the field of tribology there are hundreds of variations of different adhesion testing methods which are beyond the scope of this work and therefore the two techniques used in this study will be described – indentation and scratch tests. Other adhesion testing methods are for example bending, Scotch tape, impact, etc. and are reviewed in [141,142].

### **1.7.1 Indentation**

Indentation and nanoindentation tests are typically used to determine mechanical properties such as hardness and elastic modulus of bulk materials and thin films. Indenter is brought in contact with the substrate and force ( $P$ ) is applied onto the indenter. Substrate deforms under the load applied and that results in the indenter reaching a certain penetration depth ( $h$ ) depending on the materials and test conditions used as can be seen in Figure 1.20.



**Figure 1.20 Schematics of indentation process using conical indenter; force ( $P$ ) is exerted onto material and upon indenting the indenter reaches a certain maximal depth ( $h$ ), in case that the material deforms partially elastically, then after the load has been removed, then the resulting depth ( $h_f$ ) will be smaller than  $h$ ; taken and modified from [143].**

The process can be monitored and load/displacement curves are obtained that way. Maximum given force is applied to the indenter resulting in the maximum depth of penetration. If plastic deformation occurs within the substrate, then the final recording depth of penetration after indenter's unloading will reach a certain depth of  $h_f$ . Selection of various indenters have been established with conical, pyramidal and spherical shapes. Mostly used material for indenter manufacturing is diamond, followed by tungsten carbide indenters for spherical indentations. The stresses induced by the indenter depend on the indenter's geometry. Blunt penetrators (e.g. spherical shaped) result in compressive stress being enforced onto the substrate, while sharp indenter causes tensile and compressive stresses due to its geometry of the wedge-like shape [113]. The elastic modulus can be estimated from the unloading curve in load/displacement diagram, which is based on deduction that initial unloading has to be completely elastic and is reviewed in [144]. Values of hardness are obtained through indenting the substrates with predefined loads and examining the resulting imprint which is left after the indentation on the substrate's surface and as well are reviewed in [144].

Indentation of thin films has specific challenges due to the fact that the substrate is no longer a solid bulk material. In order to be able to derive the hardness and elastic modulus of the film only the penetration depth of the indenter; as a rule of thumb, must be below  $\leq 10\%$  of the thickness of the film, otherwise the interference of the substrate can become significant. Effects accompanying the indentation of films are the film's cracking and delamination as a means of response to the induced indentation stress. Those effects can influence on the

results of mechanical characteristics, but at the same time can be used for determination of fracture toughness of the interface and residual stresses in the coatings [143].

Thin films which are significantly thinner than the depth of indentation has very little effect on how the substrate will deform upon indentation. The indenter forces the substrate material to deform itself and the film if forced to displace accordingly to the substrate unless it releases the stress through disattachment from the substrate. Elastic energy of the film is the driving force of the interface delamination. It consists from residual stresses (such as stress from thermal expansion mismatch and stress originating from the type of growth of film) and the stress induced by the indenter onto the test piece. Adhering film is displaced radially within its plane under the force of the indenter which was identified as the main contribution of the total of elastic energy in the film during the indentation. Out of plane bending is also present due to the vertical displacement of the substrate where only a negligible amount of elastic energy can be stored [113].

During the indentation process the thin film first absorbs the applied stress through elastic deformation and after the stress overcomes the limit of possible elastic deformation the film starts to deform plastically, or fractures. Hard and brittle materials such as diamond film releases the accumulated stress through cracking, buckling, or spallation. Observed cracking around the indents is not a sign of adhesion failure in itself. Only film's delamination and/or buckling are indicators of interfacial adhesion failure [49]. Figure 1.21 shows standardised Rockwell C [145] indentation assessment. No signs of films delamination and buckling up to level HF 4 can be considered as a pass, while HF 5 and 6 are results of definite adhesion failure [146,147].



**Figure 1.21 Film's adhesion quality according to HF system; images of indents similar to HF 1-4 can be considered as a pass, while HF 5 and 6 are a definite failure; taken and modified from [146].**

### **1.7.2 Scratch**

Scratch testing can be thought of as an indentation test with added movement of the indenter along the surface of the sample. Principle of adhesion test through scratch method is in drawing an indenter across the coated surface with increasing normal loads being applied to the indenter. When adhesion failure occurs then the value of normal load upon the failure is taken as a measure of film/substrate adhesion. Compressive stress is induced into the material as the indenter progresses along the scratch track as is displayed in figure Figure 1.22. The film/substrate deforms elastically up to a point when the induced stresses are too high and the film and/or substrate are being plastically deformed. In case of hard and brittle films the excess of energy is released through film cracking and interfacial detachment can be observed. The tested samples are also a subject to tensile stresses which result from the passing indenter and can cause a cracking of the film after the load of indenter is released [148].



**Figure 1.22 Schematic of adhesion failure during a scratch test for hard coating on ductile substrate; taken from [148].**

The interpretation and usefulness of scratch testing depends strongly on the substrate and film material as well as on the geometry and testing conditions applied during the scratch test. For soft films on hard substrate the film will deform plastically and the values of critical load are then assigned to the value of normal load when the coating has been stripped off the substrate. Quantification and assessment on this type of scratch tests is difficult as well as for cases of hard substrate and hard film and soft film with soft substrate. The most practical use of scratch test is adhesion testing of hard films on softer substrates, where bucking, spallation and delamination resulting from interfacial adhesion failure occurs. Such deformation makes the quantification of the obtained results somewhat possible [149].

Three failure modes are recognised: film cracking, spallation and chipping. Examples of both cracking and spallation are displayed in Figure 1.23. Chipping tends to occur in thicker coatings and is similar to the lateral cracking regimes in bulk ceramics [149]. The type of the observed failure depends on intrinsic (loading rate, scratching speed, indenter dimensions and material, equipment design) and extrinsic (substrate and coating properties such as hardness, elastic modulus, residual stress, friction coefficient and surface

roughness) factors rendering the scratch testing results to be semi-quantitative due to the effect of all of the as mentioned factors [150].



**Figure 1.23 Examples of cracking and interfacial failure modes during scratch test; taken and modified from [149].**

The two mechanisms of adhesion failure during the scratch tests are buckling and spallation. Buckling is observed ahead of the moving indenter and is common for thin films which are able to bend elastically to the applied stress. Interfacial defects or not as strong interfacial bonding allows a crack to propagate along the interface. Once formed buckle will get in contact with approaching indenter and the film which can lead to a spallation, or the buckling effect can disappear under the compression force of indenter showing itself as a crack. Spallation can be divided into two: wedge and recovery spallation. Wedge spallation occurs for coatings which are thicker and therefore can't buckle to relieve the induced stresses. It comprises of sloping cracks being formed separating the film which are with approaching indenter wedged under the film in the direction of the scratch test, causing spallation. Recovery spallation occurs behind the passing indenter due to the system's elastic recovery after unloading. Substrate; which has been plastically deformed forming scratch track, doesn't allow complete elastic recovery of the system, which results in film's spallation on both sides of the scratch track [149].

## **1.8 Research summary, aims and objectives**

The research in the deposition of diamond films has been intensive over the past few decades and already substantial knowledge has been achieved. Direct examples of it are companies already offering a range of diamond coating systems (e.g. Carat Systems, Seki Diamond Systems and OptoSystems), and other companies already focusing on deposition of diamond films on tooling materials such as tungsten carbide (e.g. Diamond Tool Coating, Contour Technodiamant and Datron). However the applicability of diamond thin films on relatively cheap and affordable materials, such as steel, hasn't been yet perfected and so far no commercial application of diamond coated steel parts has been seen. The aim of this research was to explore the feasibility of deposition of well adherent diamond films on steel substrates for low wear applications.

Two main focus points have been explored during this work. Firstly, to assess the feasibility of using amorphous carbon films as a nucleation enhancing layer for subsequent diamond growth, which would eliminated the need of mechanically enhancement of diamond nucleation. It encompassed testing a selection of different amorphous carbon thin films deposited by magnetron sputtering influencing on their structure and thickness through the variation in deposition conditions. Diamond growth deposition conditions were also warried in order to optimise the diamond thin film deposition process.

The second aim was mainly focused on overcoming an important problem with CVD diamond film deposition on steel – the large difference in their thermal expansion coefficients. The chosen approach was through the use of different magnetron sputtered films, which were based on tungsten. The impacts of CVD deposition, interlayer thickness and composition on the stress levels in the diamond films and their adhesion to steel substrates were assessed directly by indentation and scratch tests and indirectly by Raman spectroscopy.

## 2 Experimental

### 2.1 Characterization techniques

Techniques which are able to identify the structure of diamond and amorphous carbon coatings are vital for researchers in order to know where their experimental work is heading to. There is a broad range of techniques available to identify atomic and molecule structures. However one must be very careful about their suitability and accuracy when assessing carbon species. Some techniques are also not suitable due to the demands for sample preparation. For example the use of transmission electron microscopy is complicated due to the need to use ultra-thin samples, or to use only the imprint of the sample's surface, otherwise the electron beam is not able to penetrate the sample and no data are collected. In this chapter, the most commonly used techniques will be briefly assessed – microscopy, Raman spectroscopy, X-ray diffraction and X-ray photoelectron spectroscopy, scratch and indentation testing.

#### 2.1.1 Microscopy

Microscopy techniques enable humans to further zoom into the objects to assess their structure and properties. The resolution capability of human eye to differentiate between two objects close to each other is in the region of 0.2-0.3 mm. Human eye limitations were overcome by microscopy techniques, starting with optical microscopy.

##### 2.1.1.1 Optical microscopy

Optical Microscopy (OM) is deemed to be standard equipment which is widely spread and used in many fields of science and industry when resolution in micron region is desirable. The technique uses sets of magnifying lenses to produce an enlarged image of the observed objects through a great variety of possible configurations which can be seen in [151]. Limitation of classic optical microscopes lies in light diffraction, which restricts the point to point resolution capability of optical microscopes to a distance of roughly half the wavelength of light used. It can be calculated using Ernst Abbe's formula created at the end of 19<sup>th</sup> century:

$$d_0 = \lambda/2(\eta \cdot \sin \theta) \quad [\text{nm}] \quad (21)$$

Where  $d_0$  is lateral resolution,  $\lambda$  is light wavelength and  $\eta \cdot \sin \alpha$  is known as numerical aperture of the objective, where  $\eta$  is refractive index of imaging medium and  $\theta$  is one half of the angle of objective's opening. The theoretical value of maximum resolution of optical microscopes using visible light is in the region of 0.2  $\mu\text{m}$  [152]. Recent advances in

overcoming the diffraction limits imposed on optical microscopy enhanced the lateral resolution down to the region of 50-100 nm though the use of newly developed lenses, laser beam illumination and oxide microspheres [153].

In the course of this work OM technique was used for the identification of possible microscopic flaws in deposited films as well as to analyse the results of tribological tests. The equipment used was Olympus BX41 microscope with long working distance objectives with a total magnification of 50x to 500x.

### **2.1.1.2 Scanning Electron Microscopy**

Scanning Electron Microscopy (SEM) is an essential equipment for the study of surface and near surface of thin films. Its working principle can be seen in Figure 2.1. The electron gun emits a beam of electrons which are accelerated by presence of an anode. Electron beam is then focused by a set of lenses which are essentially magnetic coils. The used acceleration energy of electron beam is typically in the region of 1 keV to 30 keV. Scan coils then divert the electron beam to form a scanning pattern on the surface, which can be later interpreted as an image on a computer screen. Electrons impacting the surface and near surface of the sample react with the atoms within the studied sample. A variety of interactions can be used as a signal providing information about the sample.



**Figure 2.1 Schematics of SEM components; taken from [154].**

The interaction of the electron beam with sample's atoms produces various secondary emissions such as Auger electrons, cathodoluminescence, secondary electrons, backscattered electrons and x-rays, as well as it produces heat (through absorption). Typically SEM is equipped for detection of secondary electrons, backscattered electrons and x-rays. It is worth to mention that incident electrons get scattered within the sample forming a pear shaped region of penetration. Figure 2.2 shows regions of possible origin of secondary electrons, backscattered electrons and X-rays. As it can be seen from the image, the depth where respective products of the incidents are generated differs significantly. Therefore, it is necessary to take into account that, for example, any chemical composition obtained from the X-ray analysis is not related to the sample's surface only, but to the near surface region as well. Two types of instruments are being used for detection of material's chemical composition using X-rays – energy-dispersive spectroscopy (EDS) and wavelength-dispersive spectroscopy (WDS). EDS measures all energies of arriving X-ray photons at the same time, while WDS measures counts of only arriving X-rays of specific wavelength at a given time. WDS technique is more accurate, although substantially more time consuming.



**Figure 2.2 Regions from which secondary electrons, backscattered electrons and X-rays can originated; taken from [154].**

The reported values and features which were able to be resolved by SEM techniques are in a nanometre region, depending on the SEM equipment and settings [155]. Depth of focus is also far superior to what optical microscopy can offer. High lateral and spatial resolution is achieved through the use of electrons which possess a very short wavelength, as for example 0.007 nm at electron acceleration voltage of 30 kV [154,155].

Two types of SEM were employed in the course of this study: a Cambridge Stereoscan 200 with an EDAX EDS system and Philips XL-30 FEG Environmental SEM with an Oxford Instruments INCA EDS system capable of imaging non-conductive samples without significant charging effects. Both SEMs were used for images of coatings' topography and for observation of tribological tests. Stereoscan's EDS was used for local composition identification, while EDS of Phillips SEM was used for creating a line scans of sample's cross-section. Origin software was used for data processing. Line scan data were smoothed by adjacent averaging method with 5 points per window for better clarity of presented data. No conduction enhancing layer was deposited onto the diamond coated samples.

### **2.1.1.3 Atomic Force Microscopy (AFM)**

AFM belongs to the group of scanning probe microscopy techniques. The resolution of AFMs can be down to Armstrong scale for high end equipment, careful sample preparation and measurement conditions, although typical spatial resolution of AFMs is in the region of 30 nm due to the convolution of the tip end, while lateral is much higher, at around 0.1 nm [156]. The principles of the technique are based on repulsive forces being formed between two objects which are brought close to each other. AFM uses scanning probes which consist of a cantilever with a sharp tip, typically made out of silicon. The tip is in continuous or intermittent contact with the sample during the scan depending on the choice of scanning mode. The schematics of AMF setup can be seen in Figure 2.3.



**Figure 2.3 Schematics of AFM working principle with focus on how the recorded surface features are interpreted using the photodetector; taken from [157].**

The laser beam is focused on the top of the cantilever and deflects from the cantilever's surface as the cantilever responds to the surface topography, which it copies under user defined force which is acting against the repulsive force. The laser deflection is monitored by a four-section photodetector which represents the sample's surface features. AFM Autoprobe M5 in contact mode was used in this work. Sample's topography, coating's thickness and RMS roughness was measured using this technique. Data processing was done using Gwyddion software.

## **2.1.2 Chemical and structural characterization**

### **2.1.2.1 Raman spectroscopy**

Raman spectroscopy is a relatively fast and powerful technique for determination of bonding states at samples surface and near-surface. No special sample preparation and ease of use made the Raman spectroscopy widespread. Lasers of single radiation frequency (selection of ultra-violet to infra-red lasers is available) are used to irradiate the sample, resulting in excitation of molecules to different vibration and/or excitation states. Raman scattering is a type of inelastic scattering where incident photons disturb the molecule's electron cloud, causing molecular motion and excitation into a virtual state. Most of such incidents do not involve almost any energy transfer between the phonon and the molecule during the scattering process, which is called Rayleigh scattering. In case that there is energy transfer between the phonon and the molecule during the scattering, such process is called Raman scattering. Raman spectroscopy therefore measures the energy difference between the energies of incident phonons and after they have been scattered. The schematic diagram of Raman spectroscopy instrument is shown in Figure 2.4. Light phonons generated by laser are directed onto the sample and scattered light is being detected. Before the scattered light reaches the spectrometer, it is focused and filtered using notch filter. Notch filter is the most common of the possible approaches of how to block Rayleigh scattering and from oversaturation the spectrometers detector in order to obtain relevant information about the sample. Spatial resolutions of Raman spectrometers using microscope as a part of the setup is in the single digit micron region [158,159].



**Figure 2.4 Schematic diagram of Raman spectroscopy equipment; CCD – charged coupled device, FL – focus lens, NF notch filter; taken from [160].**

Interestingly, pure metals do not exhibit any Raman scattering due to the presence of free electrons screening the possible interactions of phonons with nuclei [161]. Nevertheless, Raman spectroscopy is a very useful technique in the field of carbon materials [162–164]. The most dominant peaks in Raman spectra for diamond and amorphous carbon materials are shown in Table 2.1.

**Table 2.1 Observable peaks in Raman spectra of diamond and amorphous carbon films as assigned by [125].**

Peak position [cm <sup>-1</sup> ]	Typical FWHM [cm <sup>-1</sup> ]	Peak identification [-]
1000-1150	40-80	transpolyacetylene
1332	5-10	Diamond (sp <sup>3</sup> )
1345	250	D peak (sp <sup>2</sup> )
1430-1470	80	Transpolyacetylene
1520-1580	100	G peak (sp <sup>2</sup> )

G and D peaks are signals generated by sp<sup>2</sup> bonded carbon atoms and their respective abbreviations stand for graphitic (G) and disordered (D). G peak originates from stretching vibration of sp<sup>2</sup> sites which can be in form of aromatic rings, or C=C bonded. D peak originates from breathing mode of only of the sp<sup>2</sup> sites in form of rings [98]. The origin of the two peaks assigned in Table 2.1 to transpolyacetylene is still by some identified as a signal originating from existence of nanocrystalline diamond [136]. The peaks existence was shown to match the peaks of transpolyacetylene [137], which in the case of nanocrystalline

diamond, is formed at the grain boundaries of nanocrystalline diamond films grown in hydrogen-rich plasmas and it is now generally accepted [165]. An important fact about interpretation of Raman spectra, where diamond and  $sp^2$  carbon sites are present, is the intensity difference between the  $sp^2$  and diamond bonded carbon which depends on the laser wavelength. In case of visible and near-infrared light, the  $sp^2$  sites can easily dominate and even overshadow the diamond peak due to the higher polarizability of  $\pi$  states over the  $\sigma$  states, which results in  $sp^2$  sites having 50-250 times larger intensities than  $sp^3$  diamond sites [166]. On the other hand ultraviolet light source, the light's wavelengths is low enough to excite the  $\sigma$  states of both  $sp^2$  and  $sp^3$  sites, which gives a more informative view about the  $sp^3$  bonded carbon in the films [167]. Nevertheless, visible Raman spectroscopy is still the main type of Raman spectroscopy used for microcrystalline and nanocrystalline diamond film characterization due to the cost of the ultraviolet laser sources, which limits their availability to researchers [168,169].

Raman spectroscopy equipment used through this study was a Renishaw InVia Raman microscope equipped with solid state laser of 532 nm wavelength and maximum power output of 100 mW. Typical conditions for spectra acquisition were magnification 20x, 3 accumulations, laser power of 10 mW, exposure time of 10 seconds and automatic cosmic ray removal selected. Origin software was used for baseline correction to eliminate the fluorescence contribution and, where needed, the spectra were deconvoluted using Gaussian deconvolution. Raman spectroscopy was used as a tool to prove the existence of diamond within the deposited films and also for biaxial stress measurements which were derived from diamond peak positions according to equations (15-17), on page 52.

### 2.1.2.2 X-ray diffraction (XRD)

XRD technique is a tool for study of crystals and their structures. Circa 95% of solids possess crystalline structure, which makes XRD technique a very useful tool. The technique uses X-ray radiation directed onto a sample under specified angle. The X-ray beam interacts with a sample and, in case of suitable orientation of crystallographic planes within the sample, the X-rays are reflected constructively and are detected by the XRD equipment. The condition of constructively diffracting X-rays has to fulfil Bragg's Law:

$$2d_{hkl} \sin \theta = n\lambda \quad (22)$$

Where  $\lambda$  is the wavelength of incident X-rays,  $\theta$  is the angle of incident beam,  $d_{hkl}$  is the interplanar spacing between two adjacent crystallographic planes and  $n$  is the integer. The integer part has to be a whole number in order for the X-rays to be diffracted constructively [170].

In this work a Bruker D8 Advance XRD in Bragg-Brentano geometry was used. In Bragg-Brentano geometry the X-ray lamp has the same angle in respect with the surface of sample as the detector. XRD equipment was fitted with a LYNXEYE high speed strip detector and a copper anode ( $\lambda = 1.5406 \text{ \AA}$ ).  $K\beta$  radiation was removed using a Nickel filter and the diffraction patterns were corrected for  $K\alpha_2$  removal using Bruker EVA software version 4.0. Patterns were recorded using a coupled  $2\theta$  scan with a step size of  $0.02^\circ$  and a dwell time of 1 second per step. Diffractograms were obtained for magnetron sputtered interlayers for subsequent diamond growth in order to verify their purity and assess their respective structures. The size of crystallites was calculated using Scherrer equation:

$$D = K\lambda/L \cos \theta \quad [\text{nm}] \quad (23)$$

Where  $D$  is mean crystallite size,  $K$  is shape factor and  $L$  is instrumental broadening. The values for  $K$  and  $L$  used in this study were 1 and 0.05, respectively.

### 2.1.2.3 X-ray photoelectron spectroscopy (XPS)

X-ray photoelectron spectroscopy is based on photoelectric effect of investigated material emitting core electron after being irradiated by X-rays. The obtained spectrum from XPS measurement represents intensities of different binding energies. The calculation of specific binding energy ( $E_B$ ) is calculated using X-ray's photon energy ( $h\nu$ ), electron's kinetic energy ( $E_K$ ) and equipment's work function ( $W$ ) as seen in equation (23).

$$E_B = h\nu - E_K - W \quad [\text{eV}] \quad (24)$$

Core electron's specific energies depend on the type of the bonding they were part of and, therefore, both bonding states as well as element counts can be obtained from the spectra. XPS is a surface sensitive technique with penetration depth of up to only 10 nm making it a far superior technique for surface studies than, for example, Raman spectroscopy, EDS, or XRD [171]. XPS technique still gets attention in the field of identification of  $sp^3/sp^2$  ratio in amorphous carbon and diamond films. However it was proven that XPS technique to this date cannot determine accurately the  $sp^3/sp^2$  ratio by using either deconvolution of C 1s spectra [163,172] or by obtaining the value of D-parameter from C KLL spectra [172] for amorphous carbon films or diamond coatings. XPS technique was used in this study to identify the source of observed delamination within multi-layered coatings.

#### 2.1.2.4 Ball crater

Ball cratering is a very simple and low cost method originally used for the determination of thickness of thin films. Hard wearing ball of known dimensions is used to grind a small crater (Figure 2.5), reaching the coating's substrate, which provides a cross-sectional view of the coated film when viewed under optical microscope. Coating's thickness then can be calculated as follows:

$$d = \sqrt{R^2 - R_1^2} - \sqrt{R^2 - R_2^2} \quad [\text{nm}] \quad (25)$$

Where  $d$  is the film thickness,  $R$  is the radius of the used crating ball,  $R_1$  and  $R_2$  are the radii of the two formed circles at the top of the coating and at the interface (as seen in Figure 2.5). The ball crating technique can also give information about the coating's adhesion. The accuracy of ball crating technique is estimated to be in the region of  $\pm 0.1 \mu\text{m}$  [173]. During the course of this study the ball crating method was used to assess the thickness of magnetron sputtered coatings.



**Figure 2.5 Schematics of ball crater method for determination of coatings thickness; taken from [173].**

#### 2.1.2.5 Indentation and scratch testing

Hardness tester Wilson Rockwell B503-R was used for Rockwell C indents for adhesion assessment of magnetron sputtered films and tests were performed according to the ISO 6508 norm [145]. Intents were analysed under OM in order to assess the coating's adhesion.

Teer Coating's ST3001 Scratch Tester [174] was used for indentation and scratch testing of the diamond coated samples. The equipment consists of a motorised stage, a loading system and a data logging unit. Use of multi selection of different indenters is possible, together with various modes of operation. During a static indentation test, an applied load and acoustic emission are recorded in real time. Testing conditions such as loading and unloading rates, range of applied load, type of indenter and other can be fully adjusted by the operator. Similarly, scratch test can be operated in adjustable modes of continuous progressive or constant loads and repetitive scratching. Applied loads, caustic emission data and friction are possible to be recorded in real time during the scratch test. Broad variability of possible selection of indenters and adjustment of the individual testing conditions are the same as for the indentation mode. Diamond coated samples were tested using ST3001 in both indentation and scratch regimes. Afterwards the tested samples were examined under OM and SEM and correlated with the logged data from the testing process.

## **2.2 Base material identification**

### **2.2.1 Steel substrate**

Unless otherwise specified, steel discs of 25 mm diameter and thickness of 3 mm made of M42 high-speed steel (catalogue name given by American Iron and Steel Institute, European equivalent is EN 1.3247) were used. Steel discs were purchased from China from Hangzhou Dongxing Telecommunication Material Co., Ltd. M42 steel is a molybdenum high-speed tool steel which is primarily used for machining where hardness of tools very much determines their lifetime. Its relatively high content of cobalt provides the steel with a higher thermal stability of up to approximately 650 °C [175].

Steel substrates obtained from the manufacturer were tested for hardness and their EDS element spectra was acquired in order to verify the authenticity of the obtained substrate material before any further experimental work. Rockwell C intents were carried out on 10 randomly selected steel samples with three Rockwell C intents each. Resulting average hardness was 65 HRC with hardness values deviation from the average by  $\pm 1$ . Further verification by EDS is presented in Figure 2.6 displaying the SEM image of a line of EDS point whose average values are then compared in Table 2.2 with the allowed tolerance for each of specific elements by ASTM norm.

Average values of ten point EDS scan fit well within the specified element ranges of ASTM A600-92 norm with only the exception of molybdenum which is averaged 0.5 wt. % below the normal specified range. Given the limitations of ten point EDS scan in terms of sampling volume the experimental data present a very good match with the reference data.

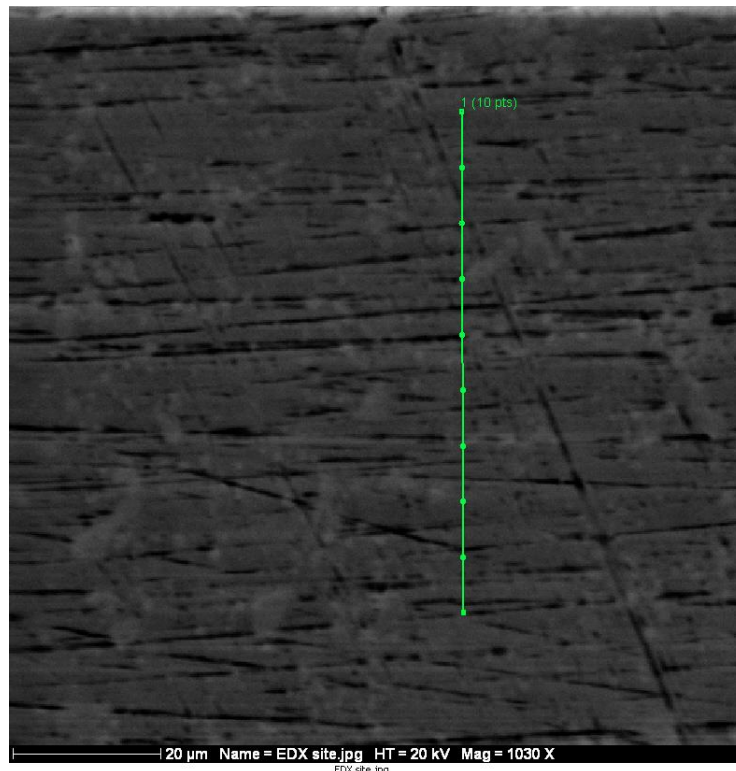


Figure 2.6 SEM image of EDS multiple point analysis on M42 steel.

Table 2.2 Quantification of obtained EDS spectra of M42 in comparison with ASTM Standard specification for high speed tool steels (impurity limits are not included).

Element	C	Si	V	Cr	Mn	Fe	Co	Mo	W
EDS Wt. %	1.1	0.3	1.1	3.8	0.3	74.9	8.5	8.5	1.5
ASTM standard wt. % range [176]	1.05 -	0.15 -	0.95 -	3.50 -	0.15 -	*	7.75 -	9.00 -	1.15 -
	1.15	0.65	1.35	4.25	0.40		8.75	10.00	1.85

### 2.2.2 Silicon wafer

Polished silicon wafers of (111) orientation, supplied by Cemat Silicon S.A., of  $\approx 0.5$  mm thickness were used as an alternative to steel substrates. The wafers were cleaved into squares of 15x15 mm.

### 2.2.3 Nanocrystalline diamond powder

The purity of nanocrystalline diamond powder was checked using Raman spectroscopy and its Raman spectra is presented in Figure 2.7(A). The parameters used to obtain the spectra were: 532 nm laser wavelength, 10 mW laser power, 3 accumulations, 20 times' objective and automatic cosmic rays removal. SEM image of loose nanocrystalline diamond powder

is in Figure 2.7(B). Even though the resolution is drastically low in order to be able to detect the size of diamond crystallites, the aggregated clouds are easily recognisable.

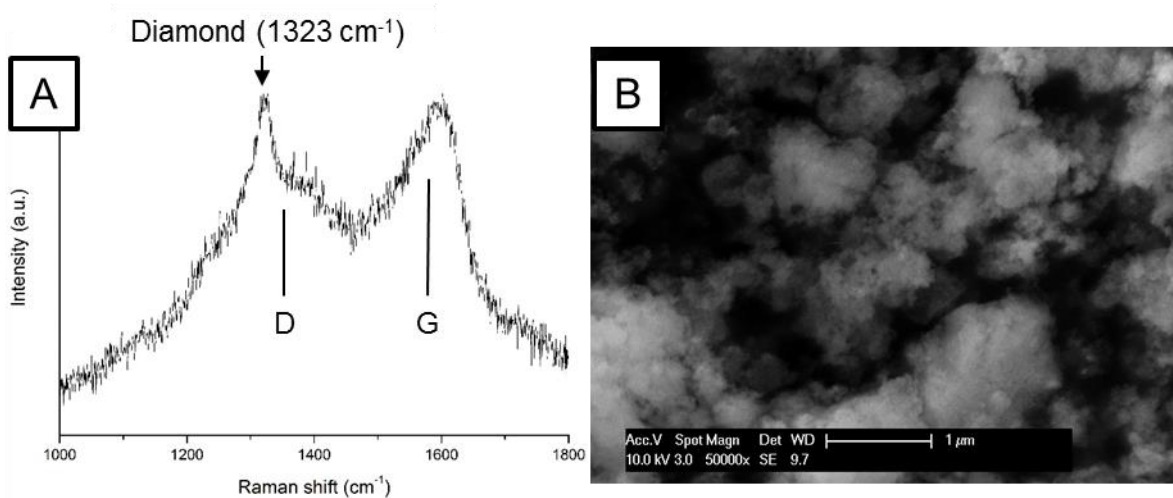


**Figure 2.7 (A) Raman spectra with subtracted PL background of nanocrystalline diamond powder used for diamond nucleation enhancement; diamond peak is identified at  $1323\text{ cm}^{-1}$ ; broad  $\text{sp}^2$  D and G peaks are also shown; (B) SEM image of loose nanocrystalline diamond powder.**

The quality of nanocrystalline diamond powder is of high importance in order to achieve a well seeded substrate for subsequent diamond film growth. The documentation provided with the powder used in this work stated the maximum size of diamond nanoparticles being  $<10\text{ nm}$  and the metal traces being  $\leq 3\%$ . Since there has not been any evaluation of how much carbon content of this powder is of  $\text{sp}^3$  and not  $\text{sp}^2$  nature, a Raman spectroscopy was employed to verify the powder's composition. The observed diamond peak was downshifted from the one of bulk diamond by  $9\text{ cm}^{-1}$  to  $1323\text{ cm}^{-1}$  and also had a relatively broad with  $\text{FWHM} \approx 30\text{ cm}^{-1}$ . Very similar results were reported by Preiffer et al [177] for nanocrystalline diamond powder with an average grain size of  $5\text{ nm}$ . The diamond peak in Raman spectrum was downshifted to  $1321\text{ cm}^{-1}$  with significant peak broadening of  $\text{FWHM} = 35\text{ cm}^{-1}$ . These observed changes are due to optical phonon confinement effects [178] which arise when the investigated material is of nanocrystalline nature and become more pronounced with decrease of the size of crystals [179]. Further observable peaks are related to the  $\text{sp}^2$  bonded carbon namely the G peak at  $1602\text{ cm}^{-1}$  with left shoulder and a broad D peak at around  $1350\text{ cm}^{-1}$ . The nanocrystalline diamond powder was used as obtained from the manufacturer with the stated purity of  $\geq 97\%$ . The individual diamond crystals within the powder are typically covered with a nanometre layer of  $\text{sp}^2$  bonded carbon. This is thought to be the reason of the presence of D and G peaks in the nanocrystalline diamond powder spectra. The Raman intensity of  $\text{sp}^2$  bonded carbon is 50-250 times higher [98] than the intensity of  $\text{sp}^3$  bonded carbon when visible light lasers are employed for excitation of Raman spectra.  $\text{Sp}^2$  sites have lower bandgap than  $\text{sp}^3$  sites and are therefore easier to

excite when visible light is used for Raman spectroscopy investigation. The higher the laser wavelength the higher intensity of  $sp^2$  over the  $sp^3$  sites will be visible in the spectra [166]. On those basis it is reasonable to assume that the composition of the diamond powder is mostly diamond and not  $sp^2$  bonded carbon.

## **2.3 Coating deposition procedures**

### **2.3.1 Magnetron sputtering of interlayers**

#### **2.3.1.1 Pre-coating procedures**

Steel samples were hand grinded on a rotary pre-grinder polishing device (Metaserv), using first sandpaper of 120 grit on the whole surface of the substrate to ensure a clean surface, free of corrosion and contaminations. One side of the substrate was then grinded using abrasive papers up to 1200 grit. The surface RMS (root mean squared) roughness was 27.7 nm on average, as measured by AFM scans over  $900 \mu m^2$  area. Both steel and silicon wafer samples were then acetone cleaned for 10-15 minutes in an ultrasonic bath (Decon F5 Major). Afterwards, they were acetone washed and dried either under hot air from a hairdryer or self-dried in the ambient atmosphere.

#### **2.3.1.2 Sputtering of amorphous carbon films**

Dymon-iC coatings were deposited using a Teer UDP 850 hybrid unbalanced magnetron sputter ion-plating plasma enhanced CVD deposition system[99]. Substrates were plasma-ion-cleaned prior to deposition. A chromium layer was first deposited by DC magnetron sputtering using argon as the working gas, followed by a chromium carbide layer by the addition of butane. Finally, a layer of hydrogenated amorphous carbon (diamond-like carbon, DLC) was deposited using a pulsed DC bias and a capacitive coupled electrode with a 13.56-MHz RF generator. The maximum substrate temperature was estimated to be below 250 °C. Positioning of the samples within the chamber varied and will be addressed later.

#### **2.3.1.3 Sputtering of metallic films**

Deposition of metallic interlayers was done by industrial close-field-magnetron-sputtering coating equipment (UDP 650) made by Teer Coatings Ltd. The UDP 650 is equipped with four magnetrons arranged at 90°. In case of sputtering deposition of metallic films in this study, only two opposing target were used. Samples were mounted onto disc plate supports which were attached to a central column in the coating chamber and were rotated under

constant speed of 4-5 rpm to ensure good uniformity of obtained coatings. The distance of the samples from the axis of rotation was always fixed on 13.5 cm. The maximum substrate temperature was estimated to be below 250 °C, as in the case of deposition of Dymon-iC coating.

## **2.3.2 Diamond film growth**

### **2.3.2.1 Equipment**

Seki ASTeX AX5010 microwave plasma CVD deposition system was used for diamond deposition throughout this work. The equipment has a glass bell-jar type of reactor chamber with molybdenum sample holder. The system's microwave power source is operating at a frequency of 2.45 GHz, with maximum output power of 1.5 kW and with three microwave tuners positioned along the waveguide, leading from the magnetron to the quartz bell-jar reactor. At present, it has methane as a carbon carrying gas with hydrogen and argon gases as the main atmosphere gases. The substrate holder has a 0.5 mm deep and 26 mm in diameter recess in the middle. The sample holder stage is without any means of substrate heating/cooling. More description and visualization can be found on the manufacturer's website ([sekidiamond.com](http://sekidiamond.com)).

Its initial setup with dual wavelength pyrometer (made by Williamson) provided unsatisfactory temperature values due to high deviation in measured data (in the range of hundreds of degrees Celsius). Reasons for such inaccuracy are in the MPCVD equipment design of very small see-through aperture and glass bell-jar see-through surface being easy to deposit carbon material on. The unstable temperature readings demanded for more accurate method of measuring of the temperature on the surface of the sample. The approach of using thermocouples was chosen as the most suitable with the current experimental setup and will be described in the experimental part of the thesis.

### **2.3.2.2 Nucleation enhancement**

Initially used, nucleation enhancement was done through the magnetron sputtering deposition of amorphous carbon layers which was described in previous section. An alternative approach of nanodiamond seeding was established during the course of this work.

Prior to diamond CVD deposition, all samples were cleaned at Aston University. The cleaning process consisted of: ultrasonication of samples in acetone (3 minutes), rinsing

the samples in acetone, ultrasonication in deionised water (3 minutes), rinsing the samples in deionised water and drying in flow of nitrogen gas.

In cases where diamond nucleation enhancement happened through diamond seeding, the following procedure was performed in between the cleaning step and the sample placement into the CVD reactor chamber. A suspension of nanocrystalline diamond powder in deionised water was prepared through ultrasonication lasting thirty minutes. Samples were then dipped into a prepared solution, typically for the duration of thirty seconds, and were afterwards rinsed with deionised water in order to remove the excess of diamond particles. As a last step the samples were dried in the flow of nitrogen gas. Nanocrystalline diamond powder used for the diamond seeding pre-treatment was purchased from Sigma-Aldrich. The powder was used as obtained, without any further purification or any other alteration. Particle size given by the manufacturer is  $< 10$  nm with  $\leq 3$  % of metal traces. Typically prepared nanodiamond solution contained 0.2 wt. % of nanodiamond particles, which were weighed using Sartorius BP211D microbalance.

### **2.3.2.3 Diamond deposition procedure**

ASTeX AX5010 CVD system uses a design when samples are loaded into the chamber from the bottom of the reactor chamber. The molybdenum substrate holder is supported on a steel tube and samples are elevated on this supporting stage into the glass bell-jar chamber. After a test piece has been loaded, the deposition procedure was carried out as follows:

- chamber evacuation into a region of  $10^{-3}$  Torr using a rotary pump,
- switching on the cooling mechanism (water chiller + two fans),
- enabling a dilution flow of nitrogen into the rotary pump,
- release of the intended gas mixture into the chamber,
- setting up a base pressure of 5-10 Torr,
- starting the microwave generator and striking the plasma,
- adjusting the pressure and microwave power to the intended values,
- elimination of reflected microwaves using the waveguide tuners when needed.

It was found and understood that the design of the ASTeX AX5010 chamber make striking plasma at pressures higher than 10 Torr relatively difficult, with plasma appearing only under the substrate holder without any migration into the intended region which is in the middle of the glass bell-jar. Using the lower pressure to strike the plasma provides, on the other hand, a stable formation of plasma ball in the centre of the chamber. The plasma ball is formed usually in between 450-500 Watts being introduced into the chamber depending on the exact value of the base pressure and the specific gas mixture. The procedure used to switch off the deposition system was as follows:

- microwave power cut-off,
- restriction of gas flowing into the reactor,
- releasing the chamber pressure,
- waiting for the samples to cool down through radiation cooling,
- nitrogen dilution gas cut-off,
- sealing the chamber,
- venting of the chamber using nitrogen gas.

The dilution of exhaust gas from the rotary pump by nitrogen has been adapted as a safety precaution in case of hydrogen or methane getting trapped within the pipe work before reaching the fume cupboard. The CVD system at Aston University has also a safety interlock for activation of microwave power. In order to be able to do so both cooling fans and water chiller have to be running. In between the experiments the equipment is left pumped down to the region of  $10^{-3}$  Torr with a hermetically closed chamber.

## **2.4 Experimental design**

### **2.4.1 Diamond deposition using DLC buffer layer**

#### **2.4.1.1 Initial experiments for diamond growth estimation**

Initial experiments were set to give an outlook on how the diamond grows on steel substrates with DLC coating as a buffer layer. Selected samples for the diamond CVD growth experiments were test pieces of M42 high-speed steel samples coated with commercially available Dymon-iC DLC coating (produced by Teer Coatings Ltd. Miba group) obtained during deposition of coatings for Teer Coating's customers. Samples were of disc shape with dimensions of 30 mm in diameter and 3 mm thickness. The Dymon-iC coatings are composed of Cr base layer followed by CrC transition layer, with DLC coating on top. Dymon-iC coating was applied from both sides and had an uncoated part where they were clamped to a stand during the magnetron sputtering deposition. Respective thicknesses of Cr+CrC and DLC layers were  $\approx 1.2 \mu\text{m}$  and  $(0.6 - 1.3) \mu\text{m}$  as measured using the ball crater method. The coating's structure was also varied through adjusting the magnetron sputtering deposition condition depending on the optimal deposition required for particular customer's needs. Since Dymon-iC is a commercial product, the exact recipes for sample depositions will not be revealed in this work. Such deviation in the thickness and structure of the DLC films was chosen in order to rapidly assess the suitability of different DLC substrates for diamond deposition. Further investigation of diamond CVD deposition using DLC buffer layer would be then based on the selected DLC recipe. Twelve samples were selected and used to the diamond deposition and were tagged according to their

magnetron sputtering run numbers used by Teer Coatings. All investigated samples were deposited using biaxial sample rotation.

Diamond CVD deposition conditions were selected as a combination of deposition conditions reported in literature [37,71,72] when diamond growth was performed on previously DLC coated substrates as well as the previously optimised deposition conditions which were in use at Aston University. Prior to the diamond deposition and sample cleaning, the part of the Dymon-iC coated samples which would be in direct contact with the substrate holder was removed using sandpaper. This operation was done due to the possible effects of the carbon film being released during the CVD deposition into the chamber's atmosphere making the results unrepeatable. The CVD deposition was divided into two stages – nucleation enhancing state and growth promoting stage. The exact parameters used during the CVD process are in Table 2.3. Temperature of the diamond CVD deposition process was monitored using dual wavelength thermocouple attached to the MPCVD equipment. After the diamond deposition the samples were left in the chamber to cool down in the flow of hydrogen for 30 minutes. SEM, optical microscopy and macro imaging were employed to assess the initial results of effectiveness of Dymon-iC coating as a buffer layer for deposition of diamond films.

**Table 2.3 Selected deposition conditions for diamond growth on DLC coated samples; deposition chamber had hydrogen-rich atmosphere.**

Deposition stages	Power	Pressure	CH <sub>4</sub> conc.	Gas flow	Duration
	[W]	[Torr]	[vol. %]	[sccm]	[min]
Nucleation	800	20	10	100	60
Growth	1000	40	2	100	240

#### **2.4.1.2 Experiments of diamond deposition repeatability**

Based on results from previous experimental work; when the Dymon-iC recipe providing full coalescent coverage of diamond film after MPCVD deposition was identified, the next efforts were in repeating the result and its further improvement. Three different diamond deposition runs were selected to try to reproduce the results, the respective coatings differences are summarised in Table 2.4. Coating 69063 had an identical coating recipe with the coating of run number 67391, only samples were clamped together in one clamp so that their back would not get coated, eliminating the need of sanding down the DLC coating from the sample's backside. Samples of coating 68971 were mounted on plates to protect their backsides and the deposition times for Dymon-iC coating were shortened in order to obtain the same thickness. Lastly the coating run numbered 68567 was used as a trial run of the new version of Dymon-iC coating with higher hardness than its predecessor.

**Table 2.4 Difference in coatings in respect to the 67391 coating run.**

Coating number	Rotation	Coating recipe adjustment
69063	Biaxial	Identical recipe
68971	Uniaxial	Adjusted deposition times due to uniaxial rotation
68567	Uniaxial	Newly developed recipe in Teer Coatings Ltd.

Diamond CVD deposition conditions were identical to those used for diamond growth for sample 67391 (Table 2.3). CVD deposition was carried at a minimum of two samples for each of the different DLC coated substrates.

### 2.4.1.3 Diamond deposition on different DLC films

This experimental work was performed on the basis of unsatisfactory results of repeatability of obtained full coalescent diamond film which had been attempted previously. This work is an expansion of the previously studied sample run of 68567.

Eight different coatings run were deposited in total for the investigation of the effects of variation of the interlayer system. Coatings were based on Dymon-iC coating with varied thickness of the DLC film as well as the thickness of the presence of CrC interlayer. Table 2.5 shows the run numbers with the thicknesses of Cr, CrC and DLC films. The thickness of deposited films was obtained from ball crater measurements as well as SEM cross-section scans applied in some cases. All the magnetron sputtered deposition runs were tested for the coatings adhesion and all passed the Rockwell C indentation test without any visible delamination or other coatings failure.

**Table 2.5 Deposited variations of Dymon-iC coating with respect to the thicknesses for present layers.**

Coating number	Cr	CrC	DLC
	[ $\mu\text{m}$ ]	[ $\mu\text{m}$ ]	[nm]
68567	400	800	1000
68535	400	800	500
69539	400	800	250
69552	400	800	125
69741	400	-	1000
69748	400	-	500
69759	400	-	250
69764	400	-	125

Samples were diamond coated using MPCVD equipment and then investigated for their diamond coverage and coalescence. Previously selected deposition conditions were applied to all the samples together with certain variations in the CVD deposition conditions, following the results of previous experiments. CVD deposition conditions which were applied are listed in Table 2.6. After the CVD diamond deposition, the samples were cooled down to room temperature in flow of nitrogen.

Optical microscopy, SEM and EDS techniques were employed in investigation of the efficiency of diamond coverage and coatings structure.

**Table 2.6 Diamond CVD deposition conditions applied on varied Dymon-iC deposited films on steel substrates.**

Growth condition	Stages	Microwave power	Pressure	CH <sub>4</sub> conc.	Total gas flow	Duration
		[W]	[Torr]	[vol. %]	[sccm]	[min]
1	Nucleation	800	20	10	100	60
	Growth	1000	50	2	100	240
2	Nucleation	800	20	10	100	180
	Growth	1000	50	2	100	240
3	Nucleation	800	20	10	100	60
	Growth	1000	50	1	100	240
4	Nucleation	800	20	10	100	60
	Growth	900	50	1	100	240
5	Growth only	900	50	1	100	300

#### **2.4.2 Diamond deposition on CrW interlayer**

Tungsten coating was chosen as an interlayer material for diamond deposition on steel substrates from a broad range of possible other more commonly used interlayers such as chromium, titanium, molybdenum, their carbides, nitrides and different multi-layered systems [62–64,51,65–69]. Tungsten have not been used extensively as an interlayer for diamond growth, although the reported results for diamond grown with tungsten interlayer were encouraging. Tungsten interlayer was mainly used on silicon substrates [82,83,180] and little on metallic substrates [123,181]. Several key properties make tungsten an exceptional interlayer: it is an excellent diffusion barrier against iron [66] and carbon [65], yet at the same time it is a strong carbide forming material [66] and its thermal expansion coefficient lays in between steel's and diamond's expansion coefficients for temperatures between ambient and typical diamond growth conditions [182,183]. Adhesion of sputtered

tungsten to the steel substrate is rather poor, as will be seen in the results of the experimental work. To overcome the difficulty, a multilayer system of CrW (steel/Cr/CrW/W) was adopted and will be described later.

The primary goal of this experimental work was to optimise the CVD diamond deposition conditions for the MPCVD setup available at Aston University. Factorial design [184] of three factors with two levels each was selected for determination of the most suitable CVD deposition conditions for diamond growth. Factors and their levels which were investigated were: microwave power (500-600 Watt); chamber pressure (20-30 Torr) and methane volume concentration (1-5 vol. %). The values of levels for selected factors were determined from observation of shape and position of the plasma ball in the chamber reactor, so that the plasma ball is stable and well centred for any of the level combination. Other deposition conditions such as total gas flow and cooling procedure were the same. The responses which were being investigated were coating's adhesion, coalescence, crystallinity and diamond quality.

The method of seeding the substrate with nanodiamond powder through its immersion in the nanocrystalline diamond suspension was selected due to the technique widespread, its relative simplicity and for the literature reports on high diamond nucleation densities [40,43–45,52]. Outsourced from literature, different nanodiamond seeding procedures were assessed on silicon wafer samples. The difference in agitation time and amount of nanodiamond powder were assessed.

The surface features of diamond coated samples were examined with optical and scanning electron microscopy. The quality of obtained diamond films was determined through Raman spectroscopy.

### **2.4.3 Diamond CVD deposition temperature calibration**

Real time temperature detection in the CVD deposition chamber is of high importance in order to be able to understand how the diamond film deposition influences on the substrate materials and even more importantly to be able to determine the difference between CVD diamond deposition conditions. The most informative temperature during the CVD deposition is the temperature at the top of the sample's surface, since it is where the diamond is being grown. Temperature detection by thermocouple was selected as the optimal option in the current MPCVD setup, with the thermocouple being mounted at the back of the substrate holder. In order to make this approach possible, new substrate holders had to be manufactured with means of securing a good and stable contact of the thermocouple with the surface of the substrate holder. Two new substrate holders were

manufactured from molybdenum – one with shallow recess (one inch diameter and 0.5 mm deep) and one with deep recess (one inch diameter and 3 mm deep). The thermocouple is possible to attach with a screw and a washer; tightening it between the washer and the substrate holder backside. The technical drawings created in order for the holders to be manufactured can be found in appendix (Figure 8.1 and Figure 8.2). Method of mounting thermocouples on the backside of the substrate holder was chosen in order to protect the thermocouples from the active plasma atmosphere. The thermocouples used were K-type thermocouples and the mounting screw with washer were from titanium.

For the investigation of the temperature difference between the sample substrate's temperature and the temperature reading obtained through the thermocouple at the back of a substrate holder, a series of experiments was devised. A HFCVD chamber with a pyrolytic sample stage heater was adjusted and used for the purpose. Figure 2.8 shows a photo and a schematic drawing of the experimental setup. The sample and the molybdenum sample holder were placed upside down on the quartz stage.

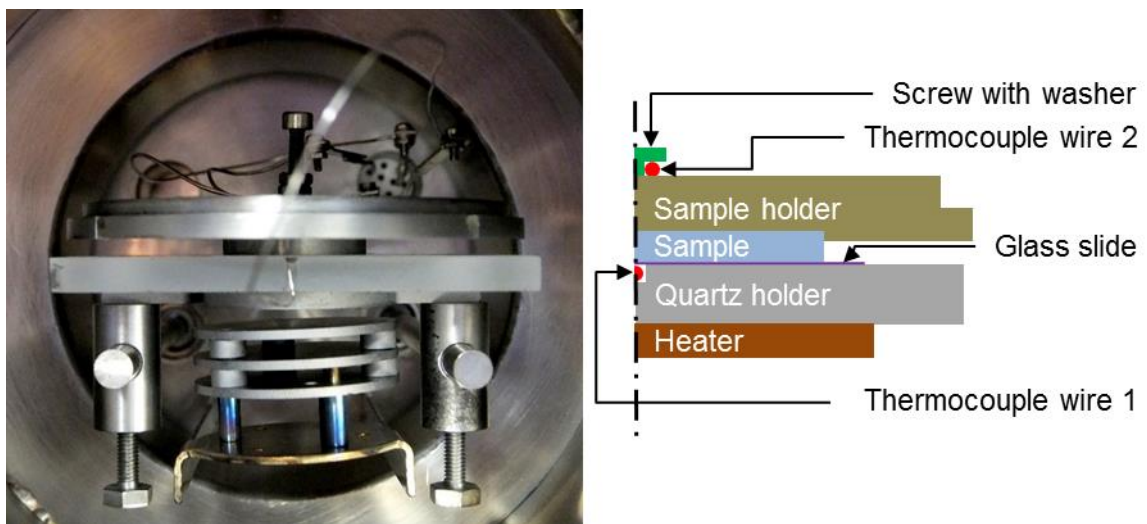


**Figure 2.8 Photo and a schematic drawing of half of the experimental setup for temperature diffusion investigation.**

The quartz stage had a 1 mm groove machined into its top surface and through this groove a K-type thermocouple ran, measuring the sample surface temperature. The temperature at the back of the substrate holder was measured as intended, using the thermocouple's trapped bead between the holder and the washer. In order to prevent an unwanted contact between the sample surface and thermocouple, a quartz glass slide of thickness of 0.1 mm was placed between the quartz holder and the sample.

This way, a series of experiments at measured surface temperature 600, 700 and 800 °C, was performed for pure CH<sub>4</sub>, H<sub>2</sub> and Ar gasses at pressure of 5, 10, 15, 25, 50, 75 and 100 Torr – repeating each parameter setting three times with waiting times of min of 45 min for

each reading to be stabilised before taking the reading. Gas flow rate was maintained either 10 or 50 sccm during the tests. Several temperature readings of gas mixtures have also been taken as well as gas flow rate was varied for several identical temperature diffusion reading to verify that the experimental setup will be accurately working under those conditions.

## **2.4.4 Diamond Deposition on MoW interlayers**

### **2.4.4.1 Magnetron sputtering of MoW interlayers**

Good adhesion to the steel substrate of the newly deposited MoW interlayer was paramount after the observed unsatisfactory results of the pure W and CrW magnetron sputtered coatings. Molybdenum was chosen as an adhesion promoting layer for two main reasons. Firstly, Mo is a well-known bonding layer between steel and other deposited coatings [185], and secondly, Mo and W have total miscibility as shown in their binary diagram [186]. Furthermore, the values of linear thermal expansion coefficient (CTE) of Mo lies in between CTE of M42 steel and W, as can be seen in Figure 2.9. The figure depicts the values of true linear thermal expansion coefficient for diamond, W, Mo and M42 steel. Based on the values of true CTEs it is seen that the selected design of M42/Mo/MoW/W/diamond layered system forms a gradient between the different values of true CTEs aiming on softening the impact of the thermal expansion coefficient mismatch induced stresses within the samples after the diamond CVD deposition.

The MoW coating was deposited using the same magnetron sputtering deposition procedure as was used in the case of CrW coating. The samples were first tested for their adhesion by indentation before any further tests were carried out. After successful results of the adhesion test, three different thicknesses of MoW film were deposited and used for further diamond growth. The MoW films were further characterised using OM, SEM, AFM, SEM, EDS and XRD techniques.



**Figure 2.9 True values of linear thermal expansion coefficients of diamond, W, Mo, M42 steel; data taken from [182,183].**

#### **2.4.4.2 Diamond deposition on MoW-2 interlayer**

The previously determined optimised diamond CVD deposition conditions were used for the deposition of diamond films on MoW-2 coated steel substrates. There were two main focuses for this work. The first focus of the work was on analysis of resulting diamond film, its structure, thickness and diamond growth rates and to assess its tribological properties through the use of scratch testing. The second was on the determination of the functionality of MoW-2 interlayer in terms of its intended diffusion barrier properties.

The diamond seeding process utilising the dip-in method was used during the sample preparation and the post-deposition cooling was kept the same as in the case of diamond deposition of CrW coated steel substrates. Substrate surface temperature, an important deposition parameter, was finally possible to measure.

The deposited diamond coatings were subject to SEM, Raman spectroscopy and EDS in order to investigate the composition of the sample. Scratch testing in continuous progressive load mode was used to study the diamond film adhesion. Rockwell C indents were performed to assess the overall sample hardness. The MoW-2 diffusion barrier properties were assessed using EDS line scan of a prepared cross-sectional view of the sample's structure after the diamond deposition.

### **2.4.4.3 Investigation of low temperature diamond CVD deposition**

The investigation of low temperature diamond CVD deposition conditions was based on the ability to determine the substrate surface temperature during the deposition process. Temperature threshold of 650 °C was selected for the investigation. The value was based on being lower than eutectoid temperature of steel, which is in the region of 720 °C. Since the theoretical thermometer inaccuracy of  $\pm 50$  °C the chosen CVD deposition temperature still accounts for the possible inaccuracy related errors.

Three main control parameters were set in order to be able to form an investigation matrix: substrate temperature, chamber pressure and methane concentration in hydrogen atmosphere. Total gas flow was kept constant for every deposition at a value of 200 sccm. Microwave power was used as the means of being able to control the substrate temperature with the other temperature influencing parameters fixed to a selected value. The set values of chamber pressure were based on observations of the CVD deposition stability while the substrate surface temperature was kept at 650 °C. At lower pressures the plasma ball shifts its position to the top of the bell jar chamber (away from the substrate) and that leads to high deposition of carbon species on the walls of the chamber. At too high pressures the microwave power has to be lowered (in order to maintain the temperature of 650 °C at the substrate's surface) and the plasma ball becomes too small and cannot sustain its existence leading to its spontaneous disappearance.

The temperature readings were taken after the temperature would stabilize itself. In practice that was after 1 hour from the time the CVD deposition started. Upon changing the deposition parameters the chosen delay time for establishing the substrate temperature was 30 minutes. Every selected temperature was checked for reproducibility. Since it is relatively hard to precisely adjust the substrate temperature down to one degree Celsius, the investigated deposition conditions were thought to be at 650 °C as long as the substrate temperature remained in the region of 640-650 °C.

After the matrix of nine diamond CVD deposition conditions was acquired, a CVD deposition using those identified diamond CVD conditions was carried out on MoW-2 coated steel substrates. The resulting set of diamond coated samples was analysed with Raman spectroscopy and SEM to identify the resulting diamond films deposited under the newly established CVD condition, which were then further analysed to understand the growth speeds and tested for their adhesion properties. All the samples were also tested for their overall Rockwell C hardness to establish the effect of the deposition conditions and the reliability of the thermocouple temperature measurements.

#### 2.4.4.4 Diamond deposition on MoW-2,3,4 interlayers

A set of experiments have been designed to investigate the effect of diamond CVD deposition temperature and the influence of interlayer thickness on the level of stress in diamond deposited films. Three different thicknesses of MoW interlayers, together with previously identified optimised diamond CVD deposition conditions at low and moderate temperatures, have been used in this investigation. The used MoW interlayers have been fully characterised in the earlier body of this work. The used diamond CVD deposition conditions were the previously identified and optimised conditions which can be seen in Table 2.7.

**Table 2.7 CVD diamond deposition conditions used in this study.**

Deposition	P <sub>M</sub>	P	CH <sub>4</sub> conc.	Gas flow	Duration	T
[-]	[Watt]	[Torr]	[vol. %]	[sccm]	[hours]	[°C]
Moderate T	550	25	3	200	2	785
Low T	440	15	3	200	4	650

The selected methods for stress assessment were indentation and calculation of stress from obtained Raman spectra of adherent diamond films. Rockwell C indentation (Wilson Rockwell Hardness Tester Series 500) and a scratch test device (Teer Coatings, ST-3001) were employed for the indentation tests. The ST-3001 was used in static indentation under continuous progressive load mode. Selected indenters were Rockwell diamond indenter and WC-Co ball of 1/16" inch in diameter ( $\approx 1.6$  mm). Initial load and final load were 10 N and 200 N, respectively. Loading and unloading rates were 50 N/min. The diamond film thickness, structure, sample hardness, surface roughness were also investigated.

## 3 Results

### 3.1 Diamond deposition using DLC buffer layer

#### 3.1.1 Initial experiments for diamond growth estimation

Optical microscopy images of the results of diamond deposition on steel substrates with Dymon-iC buffer layer are shown in Figure 3.1. Sample 67391 (image C1 in Figure 3.1) has a full coverage of diamond film, as was later confirmed by SEM images, which can be found in Figure 3.2. Other samples with good coverage, but not coalescent diamond films are 66083 (image A3 in Figure 3.1) and 67382 (image B4 in Figure 3.1). The rest of the samples display isolated diamond particles on their surface (shown under the optical microscope as a black dots).

Further investigation and verification that the obtained coating is a diamond film was carried out with SEM on two samples recognised by optical microscopy – sample 67391 (Figure 3.2) and sample 67382 (Figure 3.3). The SEM images of sample 67391 show a fully coalescent microcrystalline diamond film with dominant (111) crystal orientation, which is easily recognised by the pyramid-like shapes pointing perpendicularly to the surface. Yellow circles in the left image highlight few of the (111) oriented crystals for better clarity. Opposite to it, sample 67382 displays semi-crystalline ball shaped diamond with average size of the balls estimated to be 3.2  $\mu\text{m}$ .

Samples after diamond deposition were showing a characteristic carburised area, which was shielded by a clamp during the magnetron sputtering deposition as can be seen in Figure 3.4. Image of sample 65733 shows no visible uniform coverage on its surface, while sample 67391 shows the delamination of part of the diamond film which occurred after the diamond deposition process during the sample cooling. The thickness of the only coalescent diamond film obtained with a clear delamination interface was sample 67391. Profilometer measurement showed that obtained diamond film was 5.2  $\mu\text{m}$  thick. The diamond deposition results suggested that the structure and thickness of DLC buffer layer plays a crucial role for successful diamond coating being deposited in a relatively short time (5 hours). Based on the finding of OM and SEM methods, the recipe of Dymon-iC number 67391 was selected for further investigation.

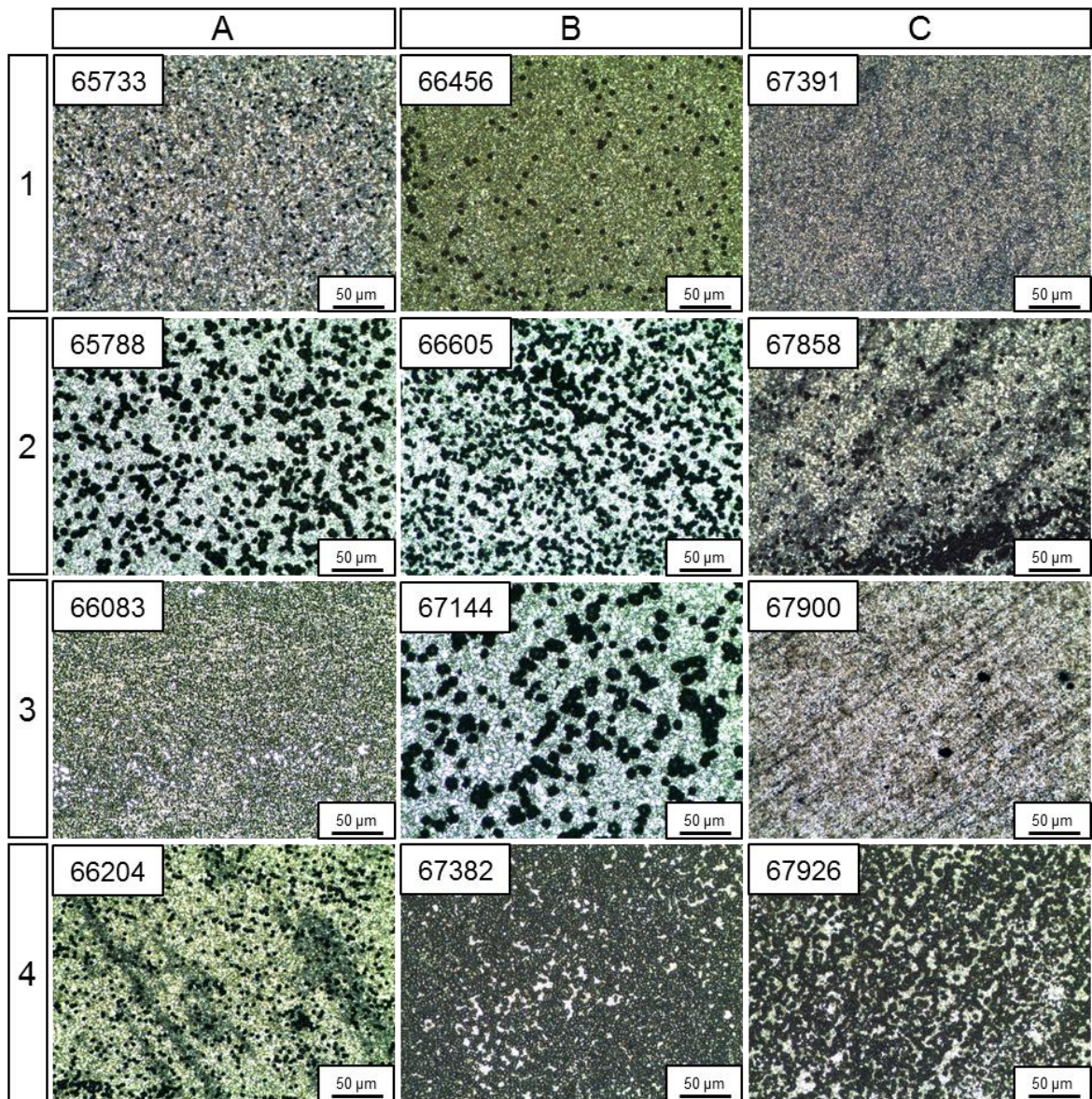


**Figure 3.1** Optical microscopy images of diamond coated steel substrates with various Dymon-iC buffer layers; darker spots in the images represent clusters of diamond, with exception of images A3, B4 and C1, where the diamond coverage is large and only the white spaces in image A3 and B4 represent surface without diamond coverage.

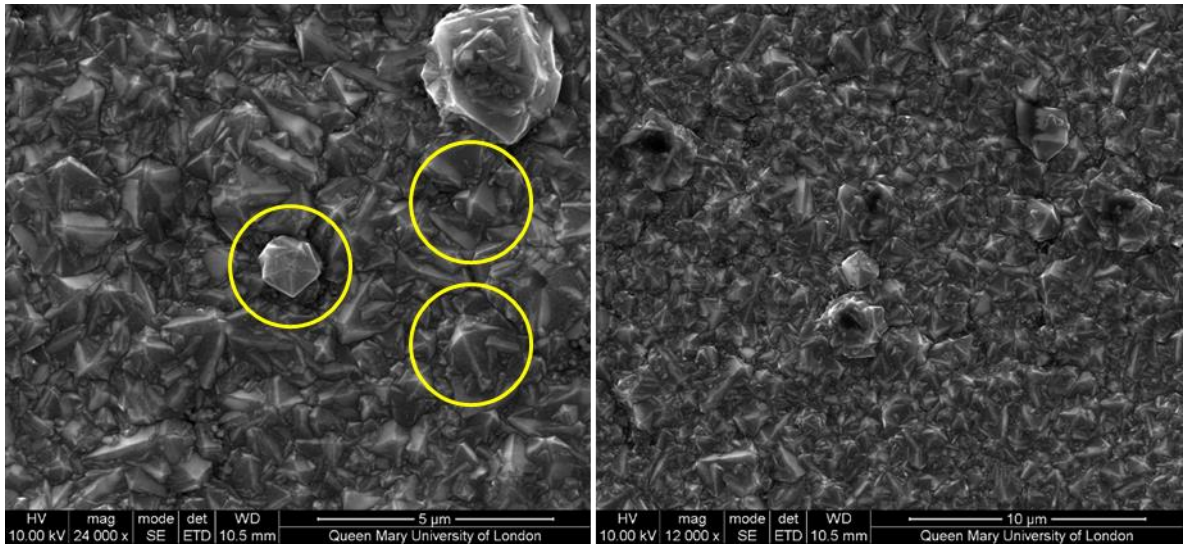


**Figure 3.2 SEM image of top surface of diamond coated sample with run number 67391; yellow circles in the left image are highlighting examples of the diamond's preferred growth in (111) direction.**

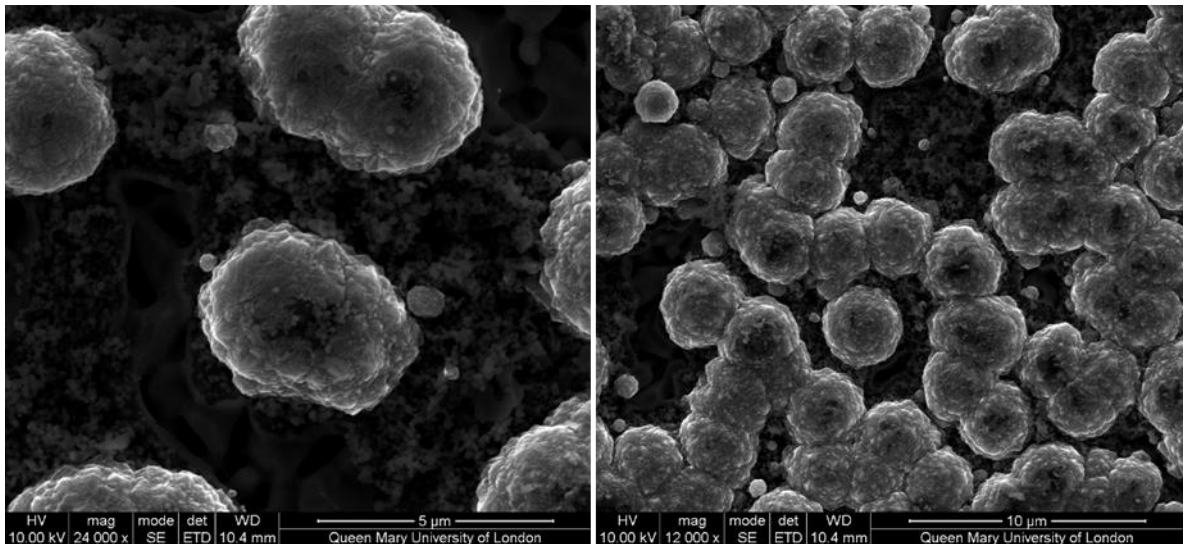


**Figure 3.3 SEM image of top surface of diamond coated sample with run number 67382, where ball-like shaped diamond dominates both of the images.**

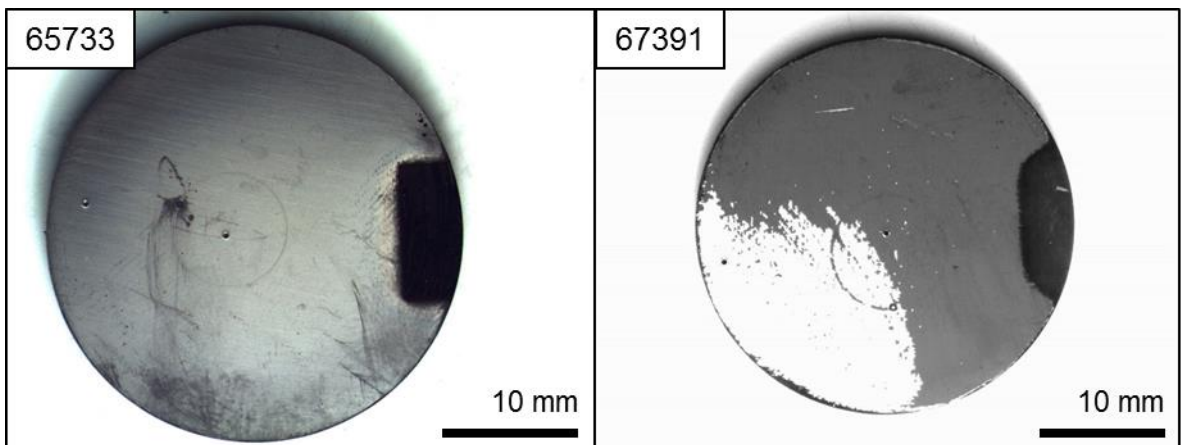


**Figure 3.4 Macroscopic images of diamond coated samples 65733 and 67391.**

It is worth mentioning that the temperature measurements of the CVD deposition process were not reliable at this point of the work. The readings, by using the dual wavelength pyrometer mounted at the top of the CVD deposition equipment, were unstable and differed greatly from one another, even during the same deposition conditions being applied for few hours when the temperature at the top of the substrate should be stabilised. A small see-through aperture and a relatively long distance between the pyrometer and the sample surface contributed to being unable to get stable temperature readings. Therefore, only minimal values of the actual deposition temperature were possible to obtain. Those were 750 °C for nucleation stage and 1000 °C for diamond growth stage. Such temperature measurements are not very useful and, therefore, the temperature readings using the pyrometer will not be mentioned further in this work. Nevertheless, the temperature measurements do not influence on the repeatability of the CVD deposition.

### **3.1.2 Experiments of diamond deposition repeatability**

SEM images in Figure 3.5 summarise the obtained results of diamond obtained from diamond coverage on the DLC coated substrates. As can be seen a ball-like shaped diamond is sparsely distributed on the sample surfaces. None of the diamond CVD processed samples bore any close resemblance to the diamond coated samples of 67391. The Dymon-iC coating 68567 shows the highest amount of diamond coverage, which is, nevertheless, still poor.

It has been observed that, after the diamond deposition, it was relatively easy to remove the species deposited on the substrate surfaces by hand, revealing silver coloured coating on the top of the sample. The adhesion of deposited species was very poor and the silver colour suggested that the diamond CVD growth process diminished DLC interlayer as well as the CrC interlayer through severe hydrogen etching process. Figure 3.6 shows SEM image of diamond CVD coated sample from 69063 run with areas selected for EDS point analysis, from which the results can be seen in Table 3.1. The EDS data were recorded under 10 keV imaging and were taken from three structurally different places on the sample. Based on the SEM image and the EDS weight % ratio of present C, Cr and Fe, the different areas represented by the the three numbered points were identified. Point 1 was identified as Cr coating, point 2 was identified as CrC and point 3 as carbon in a form of ball-like diamond (as seen in Figure 3.6). One can notice that a significant proportion of the detected elements is Fe, which is present in every point analysis, as well as that there is a substantial proportion of detected Cr in point 3, which has been assigned to diamond. The reason for observing those elements in the EDS analysis are due to the portion of sample from where the data are obtained. As was shown in Figure 2.2 on page 64, the X-rays

detected from the sample originate from regions below the actual sample's surface, where Fe is already present in the steel substrate and therefore was detected during the EDS analysis. The same reasoning applies to the Cr detected in point 3. It is also worth to mention that there are accuracy limitations in detection of light elements, such as C.

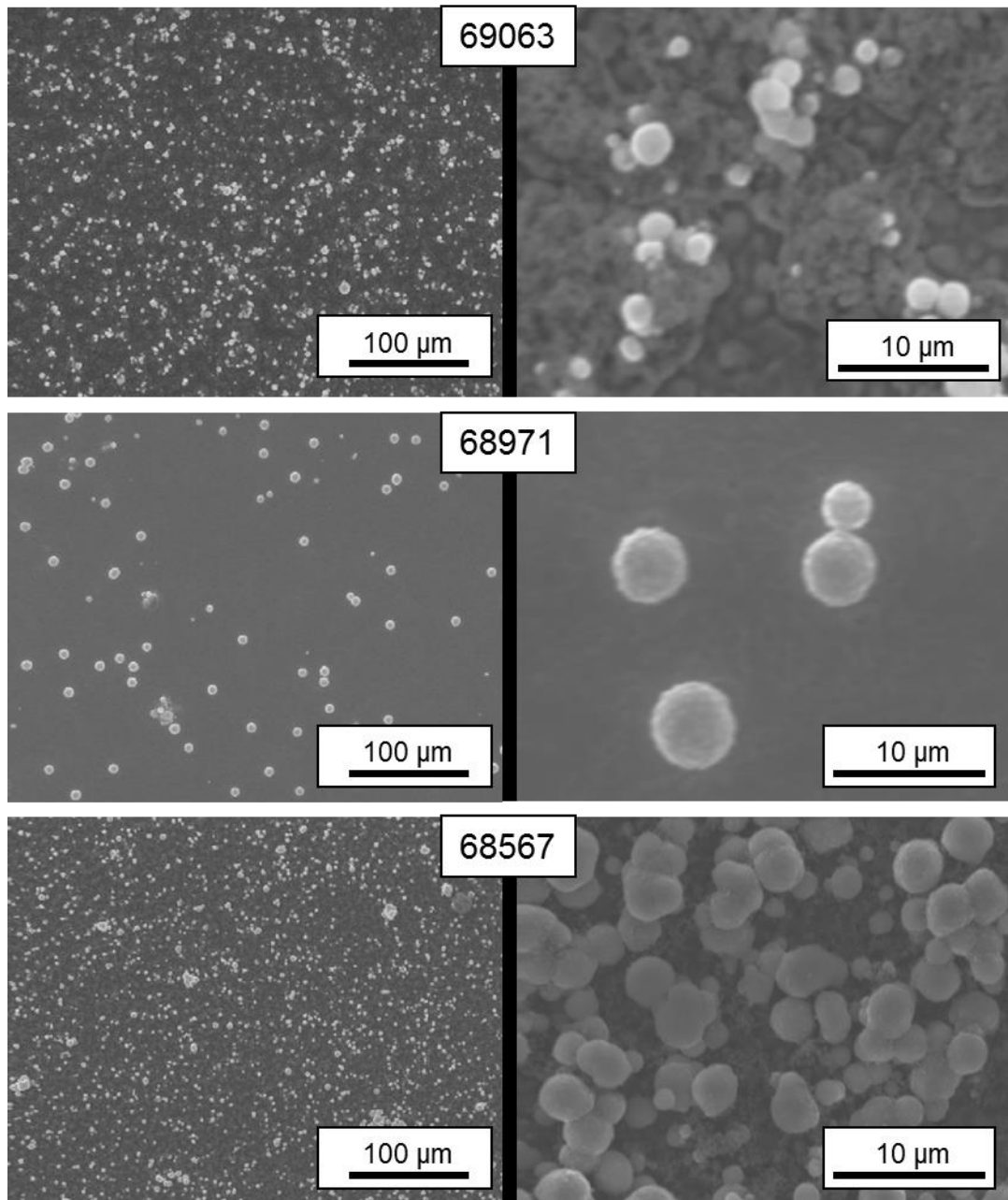


**Figure 3.5 Comparison of three different attempts to obtain the full diamond coverage as in case of diamond coated 67391 sample.**

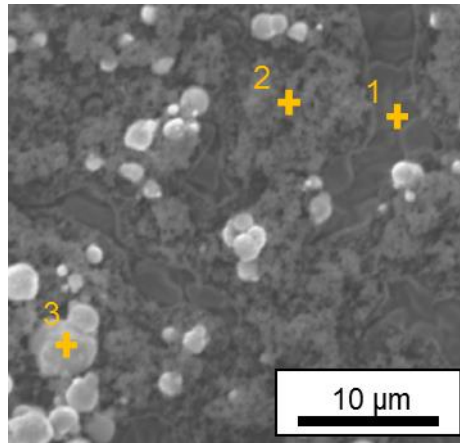


**Figure 3.6 SEM image of diamond coated sample from 69063 run with identified points where EDS spectra was taken from.**

**Table 3.1 EDS analysis results of sample from 69063 run after diamond deposition.**

EDS Points	Weight %		
	C	Cr	Fe
1	0.96	73.72	25.32
2	24.13	48.97	26.60
3	83.43	11.16	5.41

Close examination of the possible reasons for not being able to repeat the results of diamond growth of sample 67391 found that the process of DLC layer deposition was accompanied by several problems. The main possible reasons for the difference in obtained quality of the deposited diamond are unstable bias current and chamber pressure. The comparison of bias current and chamber pressure is documented in Figure 3.7 for the 67391, 68063 and 68871 coating runs. Unstable bias current is closely related to arcing problematics. The reasons of fluctuation in chamber pressure readings are, on the other hand, not clearly understood and were attributed to a deposition anomaly caused by temporary malfunction of the system responsible for pressure control.

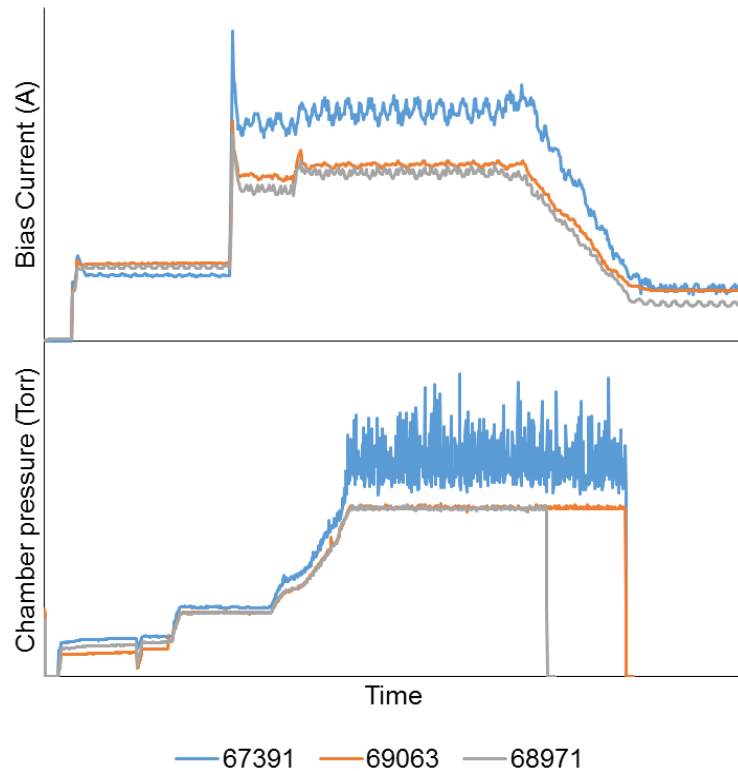
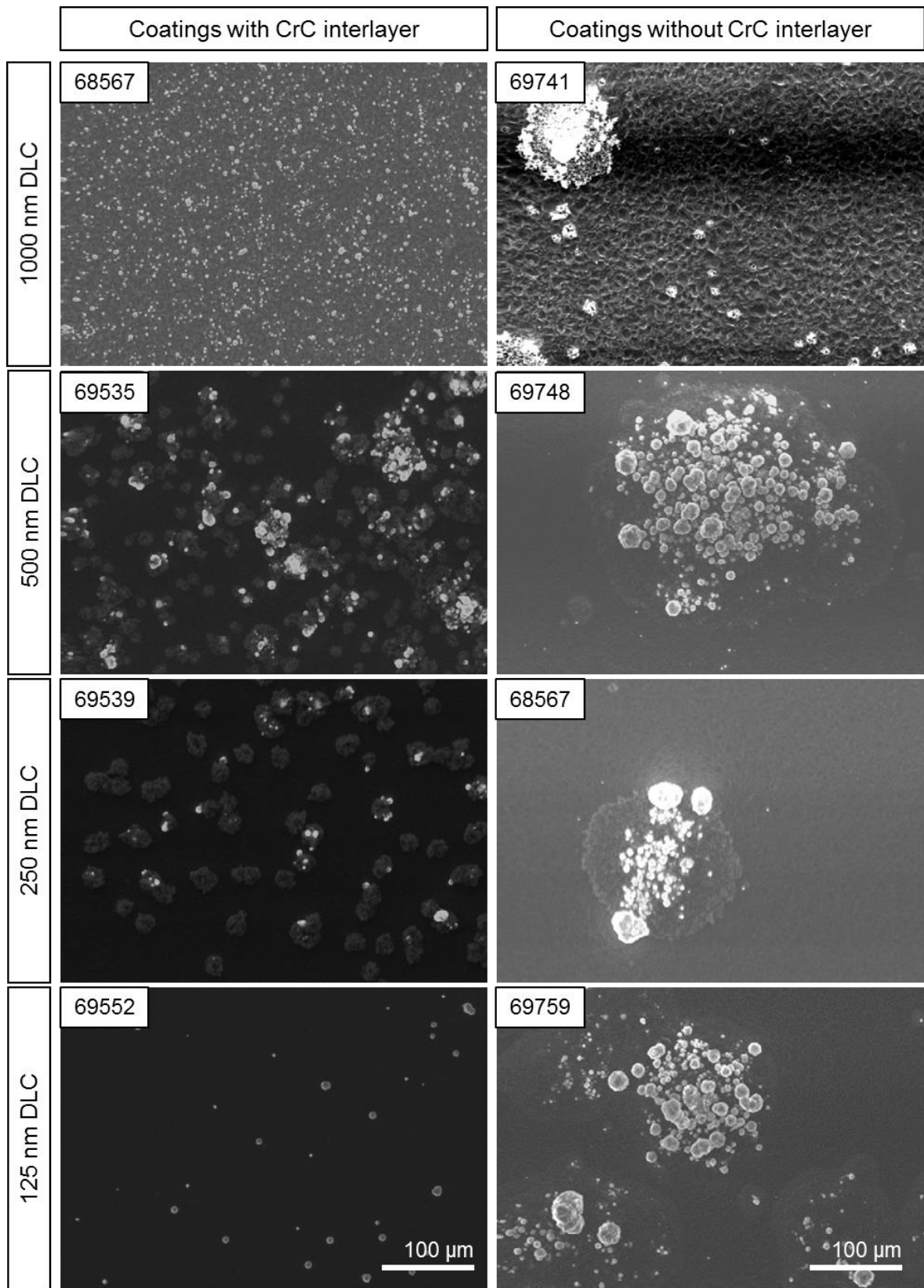


**Figure 3.7 Comparison of logged data of bias current and chamber pressure for 67391, 69063 and 68971 deposition runs; the unstable deposition conditions of 67391 run are clearly seen from the evolution of chamber pressure and bias current.**

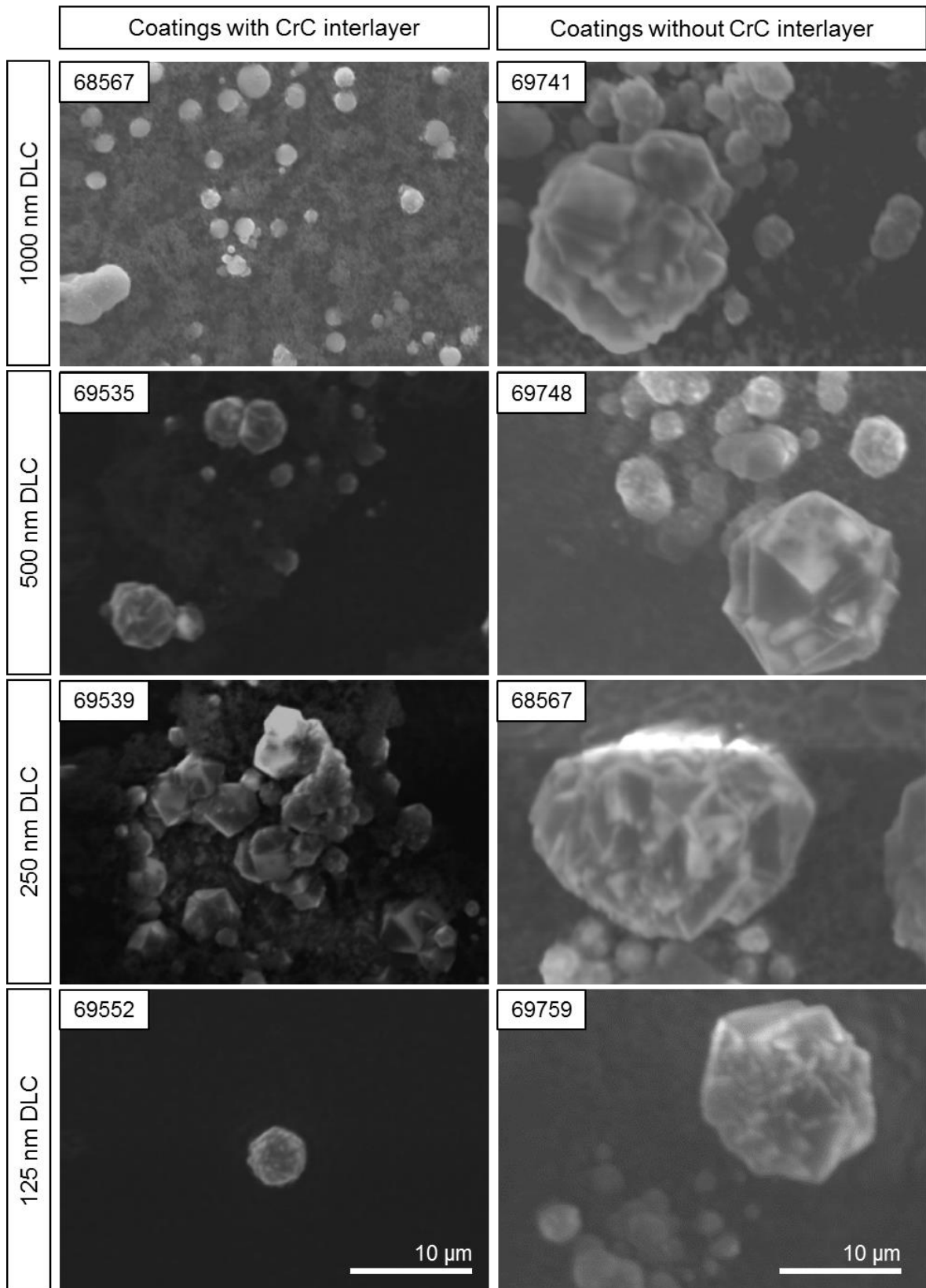
### 3.1.3 Diamond deposition on different DLC films

Figure 3.8 and Figure 3.9 show SEM images of the diamond coated samples with the coating conditions number 1 (Table 2.6, page 80) at lower and higher magnification, respectively. Several observations can be drawn from the obtained figures. Firstly, there was no clear effect of the thickness of DLC interlayer on the diamond coverage when substrate with the same structured coating (Cr only and Cr+CrC) underneath the DLC films is considered. There is a slight tendency of decrease of diamond coverage for samples with CrC interlayer (left column) as the DLC thickness decreases, but none for the samples without it (right column). Secondly, the diamond coverage for coatings with CrC interlayer tends to have more even coverage although it is still sparse. Thirdly, the process of diamond growth on DLC with or without interlayer seems to have identical progress. Initial nucleation centres are formed within the DLC coating, while other parts of the coating are being etched away at higher speeds. The diamond nuclei grow and form localised clusters of diamond. The surface, where no diamond nuclei had grown over the critical size to be able to withstand the hydrogen etching, is being etched away. In the case of poor nucleation densities, which has been documented in this experiment, all the amorphous carbon and carbide interlayer would be etched away while a certain number of diamond grains will grow.

Upon their coalescing to form a film the individual diamond crystals will be already sizeable and there will be no DLC or CrC layers present within the coating.



**Figure 3.8 Overview of low magnification SEM images of diamond coated samples after CVD deposition conditions no. 1; samples were deposited with different DLC buffer layer thickness as well as with and without CrC interlayer, as is indicated in along the axis.**



**Figure 3.9 Overview of higher magnification SEM images of diamond coated samples after CVD deposition conditions no. 1; samples were deposited with different DLC buffer layer thickness as well as with and without CrC interlayer, as is indicated in along the axis.**

Lastly, the size of diamond particles is noticeably bigger in case of samples without CrC interlayer than those grown on samples with sputtered CrC interlayer. Well faceted

diamond particles of  $\geq 10 \mu\text{m}$  are observable on all the samples without CrC interlayer, while the diamond particles on the samples with CrC sputtered interlayer have size of diamond particles of  $\leq 5 \mu\text{m}$ .

Variation of CVD deposition parameters has been employed on DLC coated samples in order to determine and verify the substrate's suitability and importance on diamond growth, together with identification of trends in diamond coverage dependence on the CVD deposition parameters. Prolonging the nucleation enhancing stage of diamond CVD deposition was found not to have any significant effect on diamond coverage as can be seen on two examples in Figure 3.10. Figure 3.11 shows an example of the difference in methane concentration during the diamond growth promoting stage. Higher diamond coverage was achieved this way while, ironically, the size of diamond particles decreased. Difference in microwave power, as it can be seen in Figure 3.12, also did not produce much difference. The structures formed on the sample surfaces are of similar look and coverage. Finally, a test of difference in case two stage diamond deposition and one stage diamond deposition are used can be seen in Figure 3.13. It was found that in this case as well there was almost no difference in how the structures were deposited on the samples.

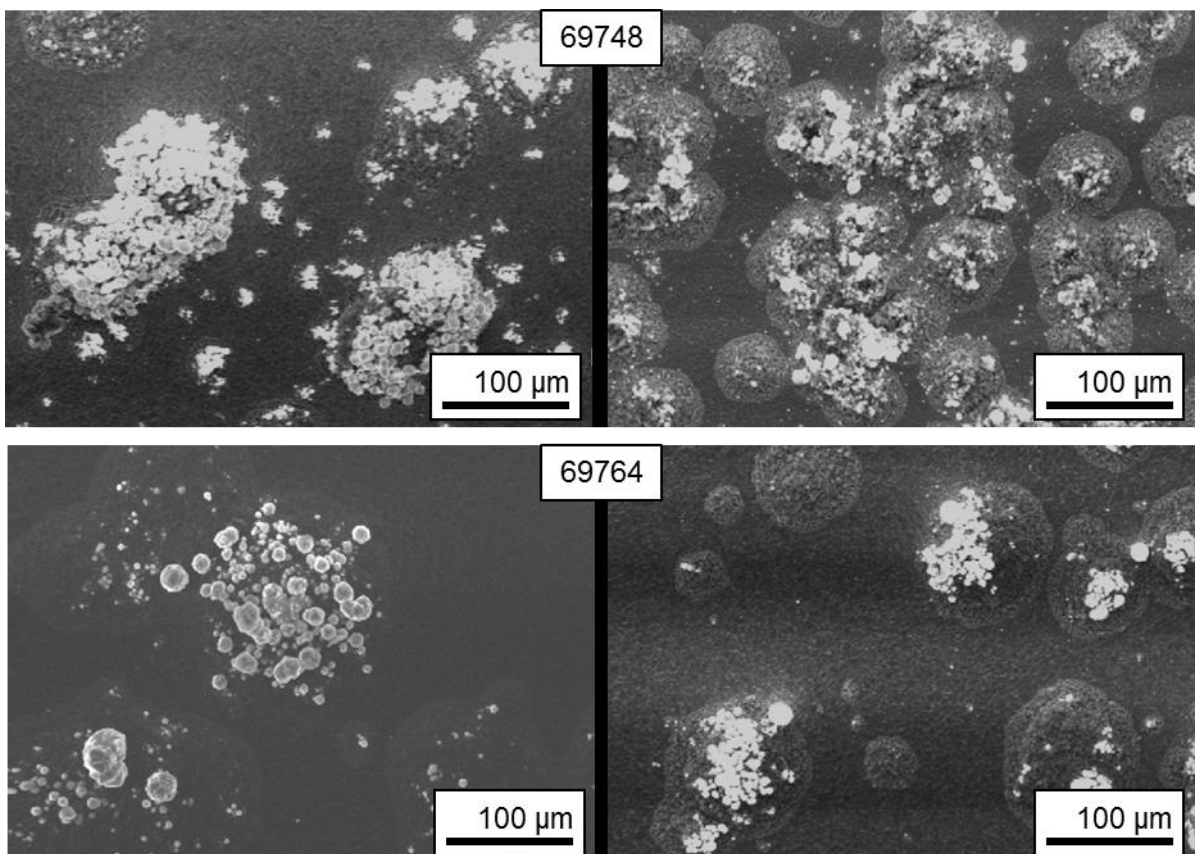


**Figure 3.10 SEM comparison of the difference in prolonged diamond nucleation stage from 1 hour (left side) to 3 hours (right side) with diamond growth conditions kept identical.**

It was concluded that a radical change in the approach to deposition of interlayers as well to diamond deposition is needed. The investigated regions and combination of interlayers and types of diamond growth did not provide a stable method of deposition of coalescent diamond films.

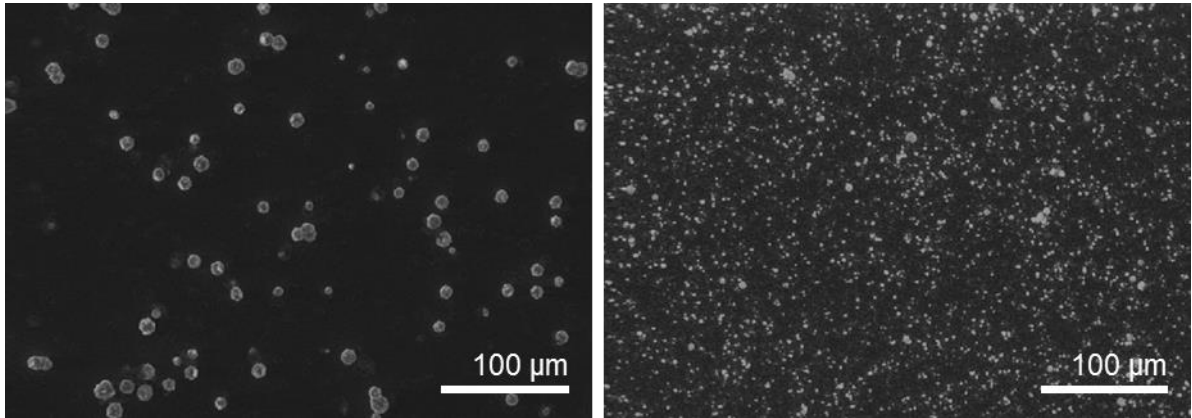


**Figure 3.11 SEM comparison of the difference in the amount of methane gas used during the diamond growth stage; 1 vol. % CH<sub>4</sub> – left side; 2 vol. % CH<sub>4</sub> – right side.**

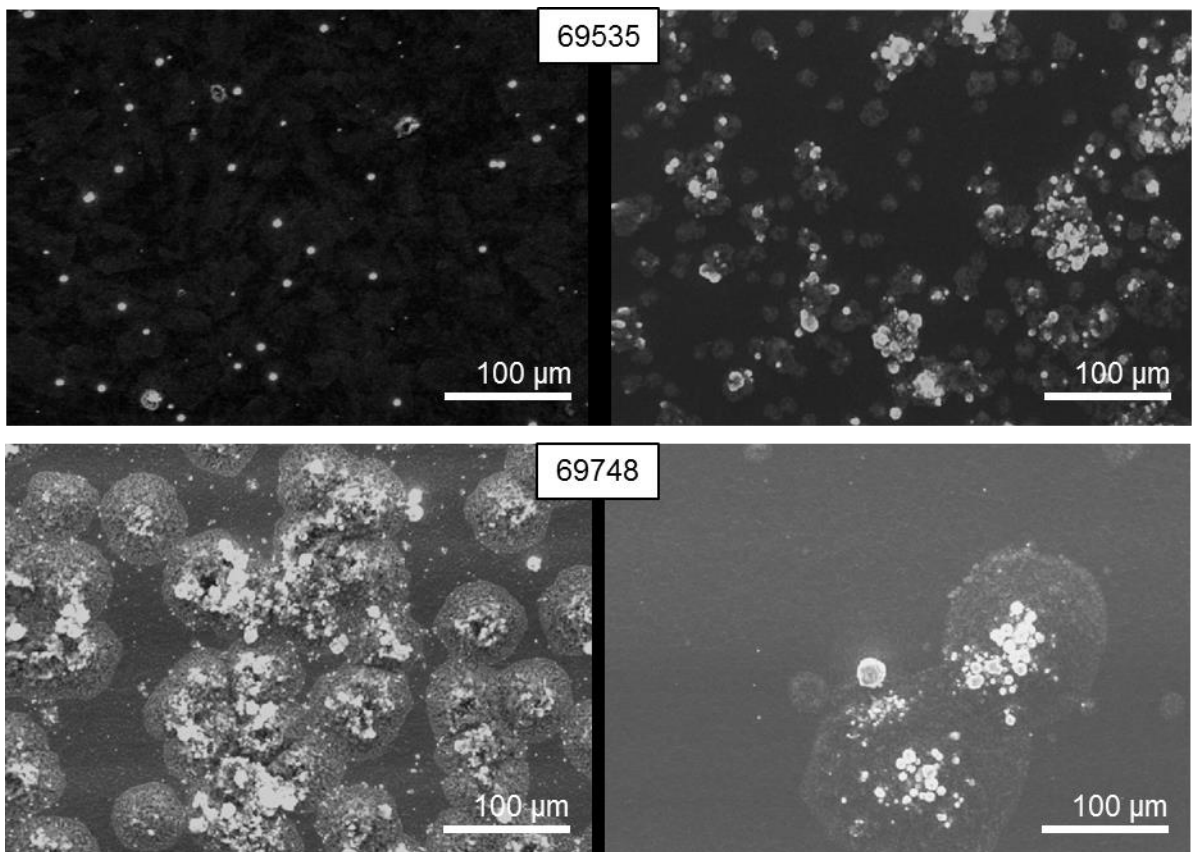


**Figure 3.12 SEM image overview of diamond coverage when different microwave power has been used during the diamond growth stage; 900 Watts – left side; 1000 Watts – right side.**

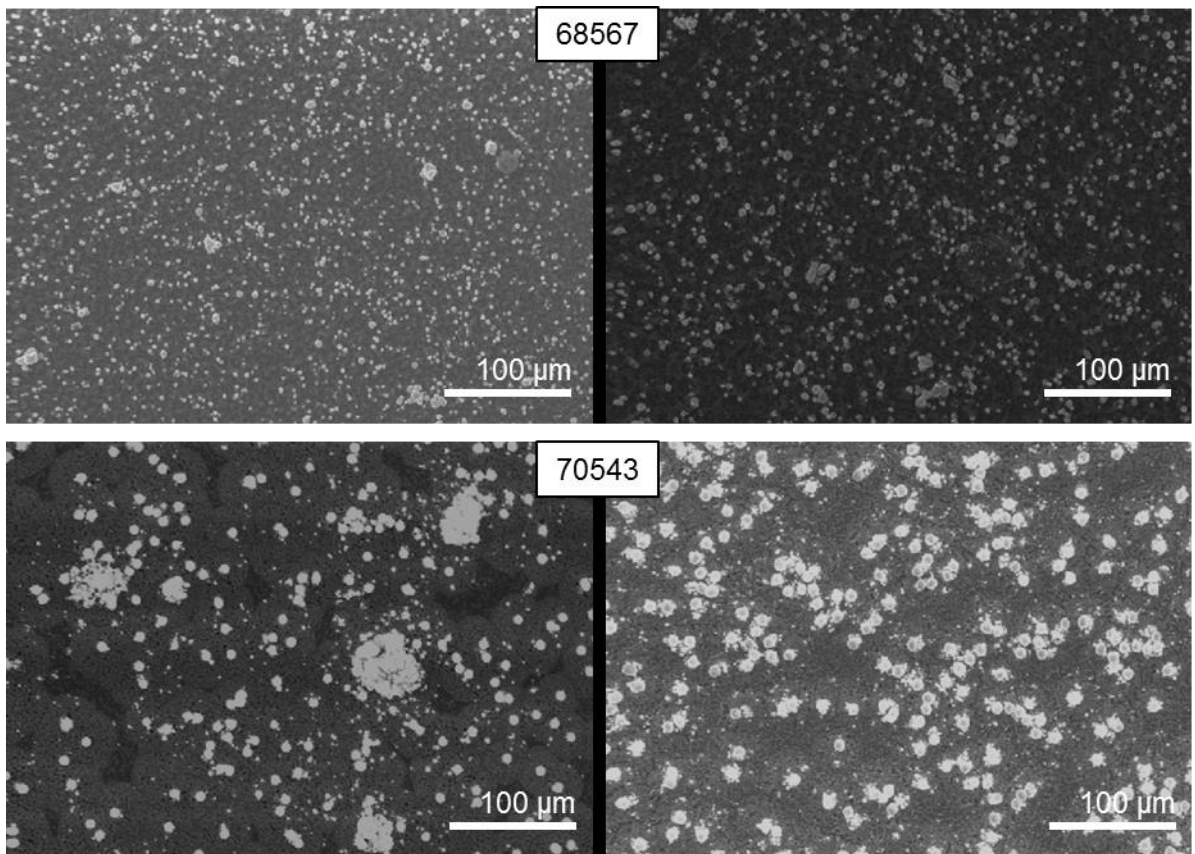


**Figure 3.13 SEM comparison of the difference between two stage diamond CVD deposition (left side) and one stage, growth only, diamond deposition (right side); overall duration of the CVD deposition was identical.**

## 3.2 Diamond deposition on CrW interlayer

### 3.2.1 Magnetron sputtering of CrW interlayer

Rockwell C indentation tests of initial deposition trials of pure W, followed by CrW interlayer are shown in Figure 3.14. The coating thicknesses were  $\approx 1 \mu\text{m}$  for tungsten-only (A) and  $\approx 1.1 \mu\text{m}$  for CrW coating (B). The thickness measurements were performed using the ball crater method. Coating's spallation around the Rockwell C indent is visible in both cases, although in case of CrW coating, the spallation is significantly less pronounced and the CrW coating was considered acceptable for the optimization of diamond CVD growth conditions.

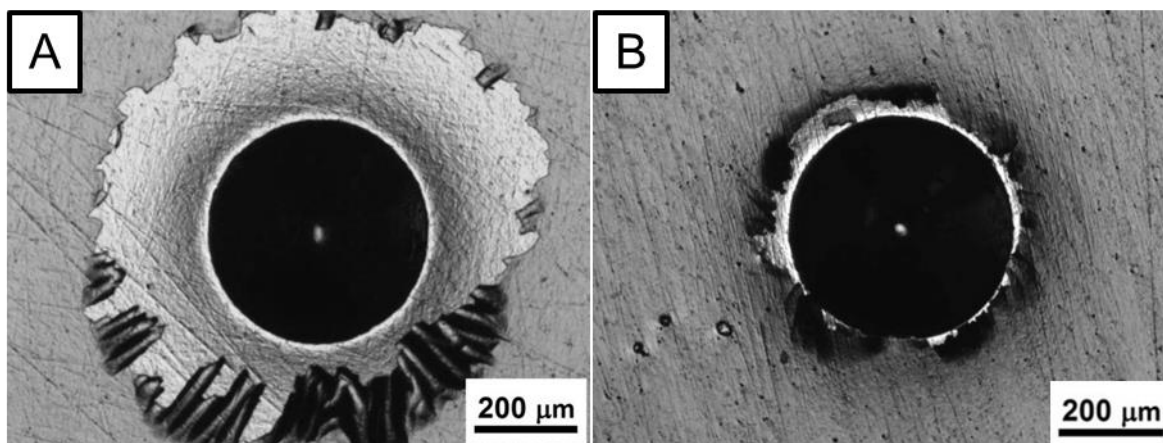


**Figure 3.14. Rockwell indents on (A) W coated M42 substrate and (B) CrW coated M42 substrate.**

The exact parameters used for magnetron sputtering of the CrW are displayed in Table 3.2. The coatings were performed in three steps: cleaning, coating 1 and coating 2. Only two targets were used for the CrW deposition – Cr target on magnetron 2 and W target on magnetron 4. The two remaining ones were covered with aluminium foil to prevent their contamination. During the cleaning step, argon cations are used to etch a few nanometres of substrate surface and to etch away any remaining contaminants which have not been removed during the ultrasonication cleaning step. This step enhances subsequent adhesion of the deposited films. Coating 1 step focuses on the deposition of a Cr-only layer (100 – 200 nm thick) with initial increase of chromium deposition over the first 60 seconds of the Cr deposition. The start of Coating 2 step, the first 300 seconds, is a changeover between depositions of 100% Cr to 100% W. The changeover period was done to further enhance the bonding between the two materials by interlocking their atoms, creating a gradient transition CrW layer (100-200 nm thickness). After the deposition run, the magnetron sputtering deposition chamber was evacuated and left to cool down to room temperature. The rest of the deposition time is devoted to the deposition of a W layer ( $\approx 800 \text{ nm}$  thickness). The exact thickness of Cr, CrW and W layers has not been measured and the

values of respective thicknesses are based on the sputtering process parameters, the sputtering rates of respective metals and the expertise of the operating personnel.

**Table 3.2 Coating procedure for 1.1  $\mu\text{m}$  thick CrW film; magnetrons 1 and 3 are without targets, magnetron 2 has Cr target and magnetron 4 has W target.**

Step number	1	2	3	Units
Step type	Cleaning	Coating 1	Coating 2	
Total step time	120	240	3300	[s]
Sample rotation	4	4	5	[rpm]
Set Ar flow	10	18	18	[sccm]
Bias mode	Pulsed	Pulsed	Pulsed	[-]
Bias frequency	250	250	250	[kHz]
Bias pulse width	500	500	500	[nsec]
Bias start set point	200	90	50	[V]
Bias ramp time	120	60	30	[s]
Bias end set point	450	50	45	[V]
Mag 1 start set point	0	0	0	[W]
Mag 1 ramp time	0	0	0	[s]
Mag 1 end set point	0	0	0	[W]
Mag 2 start set point	0.2	1	4	[W]
Mag 2 ramp time	120	60	300	[s]
Mag 2 end set point	0.2	4	0	[W]
Mag 3 start set point	0	0	0	[W]
Mag 3 ramp time	0	0	0	[s]
Mag 3 end set point	0	0	0	[W]
Mag 4 start set point	0.08	0.1	1	[W]
Mag 4 ramp time	0	60	300	[s]
Mag 4 end set point	0.08	0.1	6	[W]

A comparison of the surface morphology of the pure W and CrW layers is displayed in Figure 3.15, where W-only coating is on the left (A) and CrW coating is on the right (B). The structures of the surfaces are very similar, with the main difference being that the surface of CrW consists of slightly larger features than the one of pure W.

In order to verify where the observed delamination happened, an XPS investigation of delaminated region took place. The delaminated area, which still partially adheres to the surface, was taken off using tape, making it possible to study both sides of the delaminated region. Table shows the obtained XPS spectra. The spectrum acquired from the substrate's

surface as well as from the tape is dominated by carbon and oxygen species, which is of common occurrence due to the low penetration depth of XPS (<10 nm). Those are then effectively a components of bonded atoms and molecules at the sample's surface. Fe and W were both detected on the substrate's and tape's surface, while concentration of Fe was significantly higher on the substrate's side. Cr was only detected at the back of the delaminated coating (tape), while Mo was only detected at the substrate, which is one of the alloying elements from which M42 steel consists. Those results provide a direct evidence that the delamination happened at the interface between steel and the Cr base layer of the CrW coating, from which the presence of Fe on both, the substrate and the tape, is the key confirmation.

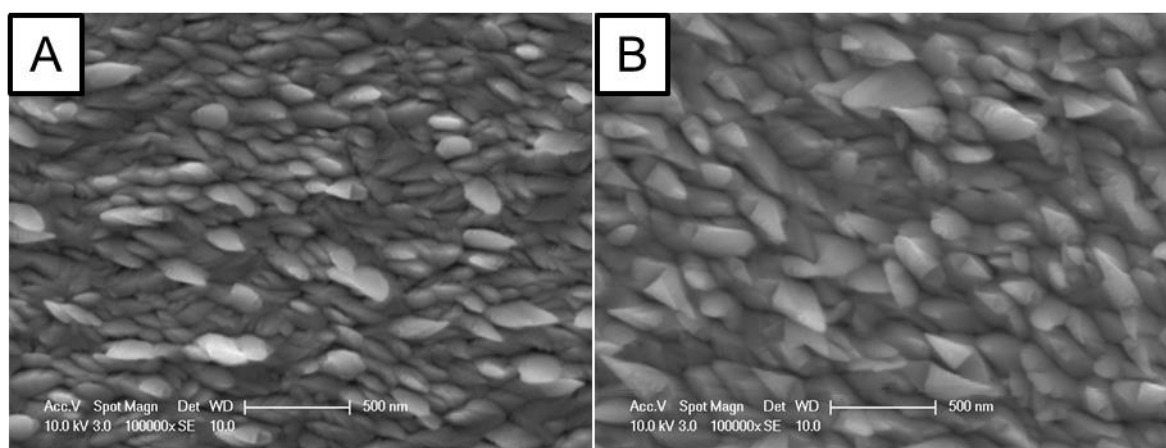


**Figure 3.15 (A) SEM images of pure W deposited on M42 steel substrate; (B) CrW interlayer deposited on M42 steel substrate.**

**Table 3.3. List of XPS detected elements in the region of delamination for CrW coated steel.**

Element	Substrate	Tape
	At. %	At. %
C	53.04	46.36
W	0.33	1.30
Fe	2.13	0.57
O	43.09	49.39
Mo	1.41	-
Cr	-	2.38

### 3.2.2 Nanocrystalline diamond seeding experiment

A new diamond nucleation promoting technique had to be applied in order to achieve rapid growth of diamond film. The chosen technique was seeding the substrate's surface with nanodiamond powder prior to the diamond CVD deposition. The technological steps for optimal seeding (high diamond coverage, while using a minimal resources) were the focus

point of this experiment. The Nanodiamond seeding procedure consisted of preparation of ultrasonically dispersed nanodiamond suspension in deionised water. Samples were suspended vertically in the suspension during the agitation process. After the ultrasonic treatment, the samples were flushed with deionised water to remove any excess of diamond powder from the surface and were dried in the flow of nitrogen gas. Table 3.4 shows the influence of agitation time and nanodiamond concentration on the resulting roughness of diamond film after the subsequent diamond growth. The diamond growth conditions were kept constant for all the deposited samples. The value of RMS (root mean squared) roughness were taken as a measure of the quality of the seeding pre-treatment. The RMS values shown in the table are averages of a minimum of three scans, each of an area of 30x30  $\mu\text{m}$ . Raman spectra were taken in order to verify the diamond quality.

**Table 3.4 Nanodiamond seeding investigation of concentration of nanodiamond powder and the duration of ultrasonic agitation.**

Sample	Agitation time	Nanodiamond concentration	RMS roughness
	[min]	[wt. %]	[nm]
Si027	0.5	0.2	25.1
Si034	15	0.2	14.5
Si036	30	0.2	17.0
Si033	60	0.2	15.0
Si031	30	0.1	20.5
Si036	30	0.2	17.0
Si030	30	0.5	13.6
Si028	30	0.8	31.3

The values of RMS roughness, as it can be seen in Table 3.4, are in the range of  $\approx 14$  to 31 nm. The lowest roughness values with different concentration of nanodiamond powder were for concentrations of 0.2 wt. % and 0.5 wt. %. Results of agitation time variation showed an improvement in surface smoothness from 0.5 minutes to 15 minutes; after that, the resulting surface roughness did not vary significantly. It was also observed that drying the samples after the agitation pre-treatment, results quite often in the formation of maps, where an excess of residual nanocrystalline powder was left due to the drying process. Using isopropanol or ethanol as a washing medium, heating up the samples, leaving the samples to dry naturally, flushing the excess of diamond for longer times and using post-ultrasonication in pure deionised water did not solve the problem and drying maps were still present on the sample. Some examples of such maps can be seen in Figure 3.16, where the middle image is considered to be acceptable.

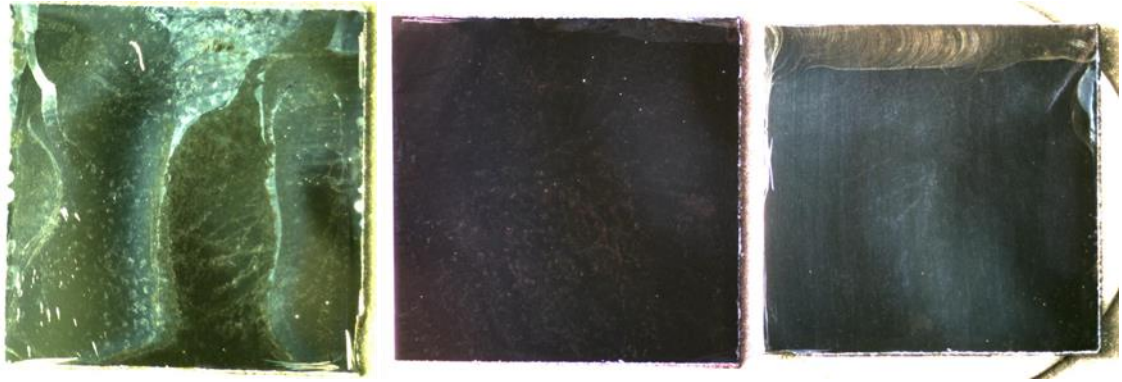


**Figure 3.16 Drying maps on silicon substrates formed after the agitation process; all three samples were subject to 30 min ultrasonication in 0.2 wt. % nanodiamond suspension in water, images were taken after diamond CVD deposition.**

The dip-in method was tried in order to overcome the map formation related problem. The method consists of forming the same nanodiamond suspension through agitation, which is then followed by immersion of the sample into the suspension for a brief time. The drying and cleaning process were the same as for agitation method. 0.2 wt. % of nanodiamond powder was dispersed in deionised water and the solution was agitated for thirty minutes. The results proved to be more repeatable without such significant marks after the cleaning process. Average RMS roughness for as pre-treated samples was 29.1 nm over the same AFM scanning area. This increase in roughness was accepted as tolerable in exchange for higher reproducibility.

Raman spectra were taken for agitation pre-treatment as well as for the modified dip-in version and can be seen in Figure 3.17. The spectra were taken after identical diamond CVD deposition and are very similar to each other. The diamond peak is clearly observable in the spectra for all the deposited samples. All the samples have also presented G and D peaks at relatively low intensities.

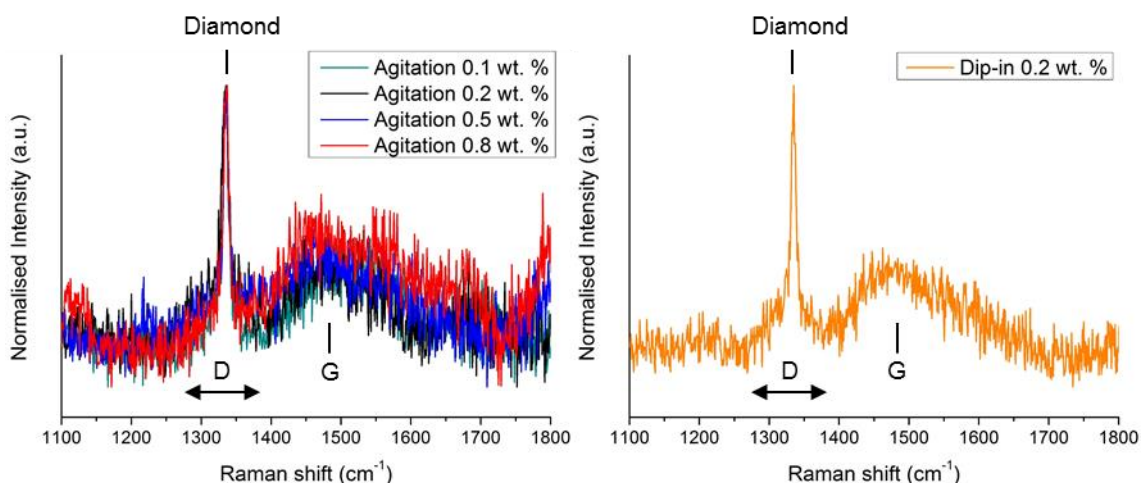


**Figure 3.17 Raman spectra of diamond films after agitation (left image) and dip-in method (right image) with various nanodiamond concentrations in the suspension (shown in the legend); diamond peak is clearly distinguishable in each of the spectra, also present are broad  $sp^2$  bonded D and G peaks.**

### 3.2.3 Diamond deposition on CrW interlayer

A factorial design of three factors with two levels each was selected for the diamond growth investigation. The chosen factors to investigate the optimization of the diamond growth stage were the chamber pressure, the microwave power and the methane concentration. The respective levels for each factors and their combination is summarised in Table 3.5. Other variables of the CVD deposition process, pre-treatment and cooling sample were kept the same for every investigated sample. The CVD deposition conditions which were constant were: time of deposition (2 hours) and total gas flow (200 sccm). Radiation cooling for 3 hours in an evacuated chamber was used to minimize any rapid temperature quench, which would impose sudden cooling related stresses onto the sample. Four randomly selected deposition conditions were selected to ensure reproducibility.

**Table 3.5 Deposition conditions investigation according to the factorial design.**

Sample	Pressure	Power	CH <sub>4</sub> conc. in H <sub>2</sub>
	[Torr]	[Watt]	[vol. %]
CrW11	20	500	1
CrW13	30	500	1
CrW10	20	600	1
CrW06	30	600	1
CrW12	20	500	5
CrW14	30	500	5
CrW09	20	600	5
CrW15	30	600	5

The investigated responses were the coating's adhesion, the coalescence, the crystallinity and the diamond quality. The film's coalescence and crystallinity were determined by SEM, adhesion was observed by OM and SEM and films quality was assessed through Raman spectroscopy. For clarity and ease of comparison, the SEM and Raman spectroscopy data will be presented first, closely followed by an overview table and a figure which summarise the findings.

The SEM images of the coatings surface are presented in Figure 3.18. Facetted diamond films as well as ball-like shaped diamond were formed in the selected CVD deposition region for the optimization of the diamond growth. Fully coalescent films as well as surfaces where diamond is sparsely distributed were also identified. Samples CrW06, CrW13 and CrW15 in particular, showed to be promising in terms of the crystallinity and the coalescence. Those three samples were also the ones where visible delamination had happened at least over part of the diamond surface. In case of CrW13, the delamination of the diamond film happened over the whole sample.

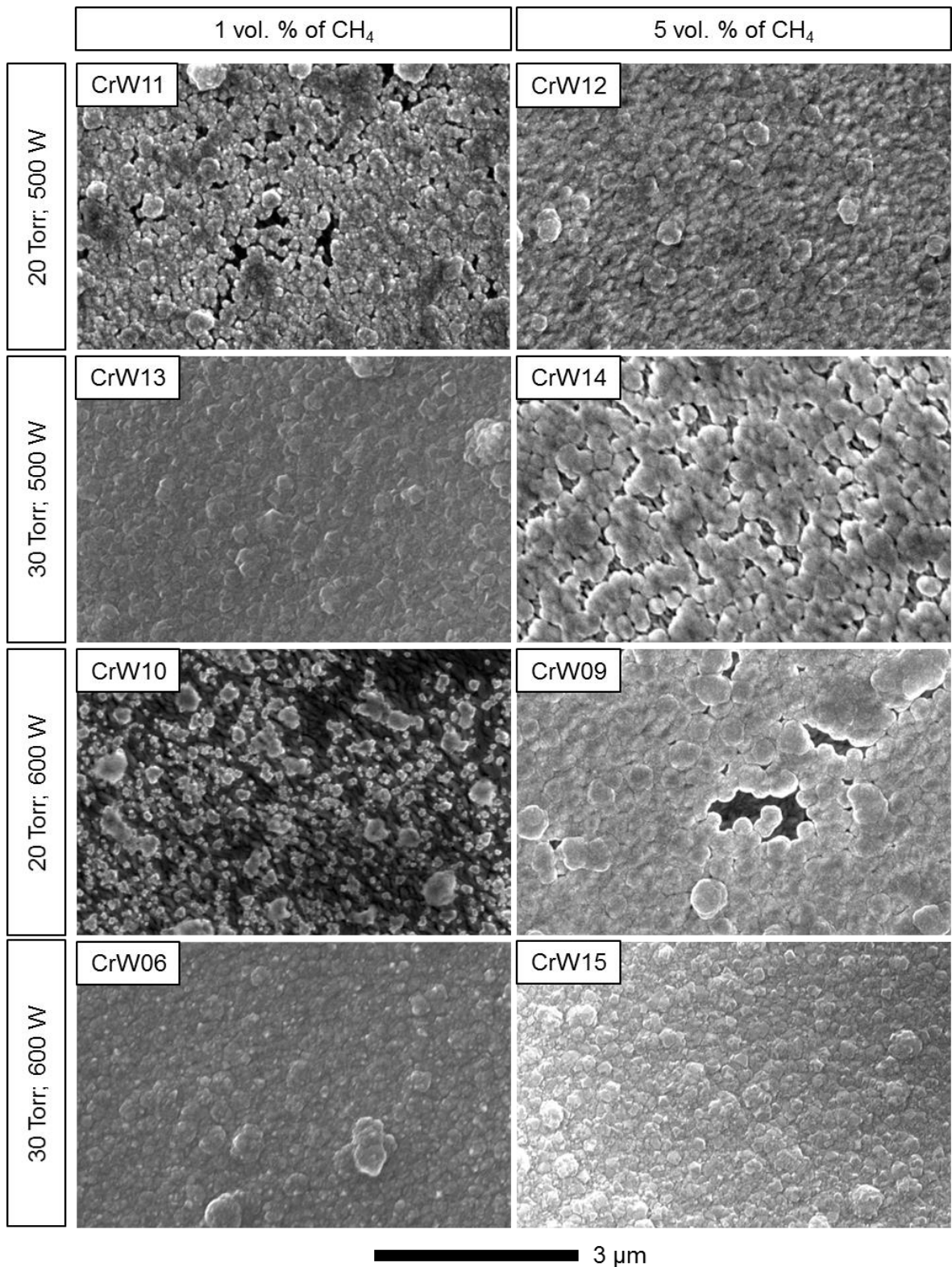


**Figure 3.18 SEM dataset for the factorial design with respective deposition parameters shown along the axis.**

The Raman spectra of deposited diamond films are displayed in Figure 3.19 and the identified diamond and G peak positions for each film are summarised in Table 3.6. The Raman spectra were divided into two groups – one group of spectra with a pronounced and easy to identify diamond peak (A) and another group where the diamond peak is not easily

seen (B). Only one sample, namely CrW13, showed a very pronounced diamond peak. The remaining two coatings from the (A) group have still a clearly detectable diamond peak, but in both cases the intensity of the  $sp^2$  D peak is almost comparable to the one of the diamond. Raman spectra from the (B) group look very much alike and the intensity of the D and the diamond peaks are making the spectra almost seen as only one peak being at around  $1340\text{ cm}^{-1}$ . A closer examination revealed that, except CrW11, the rest of the spectra possessed an identifiable diamond peak. In all the acquired spectra there are also other peaks present, along the aforementioned diamond, D and G peaks and transpolyacetylene peaks are present at  $1100\text{-}1200\text{ cm}^{-1}$  and  $1450\text{-}1550\text{ cm}^{-1}$ . Also with the exception of CrW13 sample, the positions of the diamond peaks are shifted towards higher wavenumbers which correspond to various degrees of stress present in films. The same observation applied to the position of G peaks which follow a similar trend.

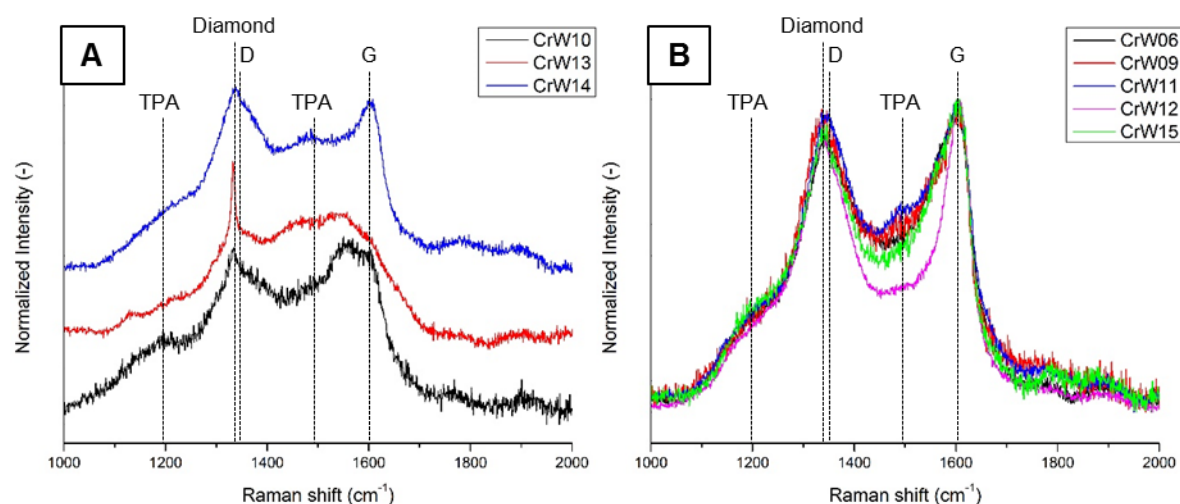


**Figure 3.19 Raman spectra for all the samples from the factorial design experiment; A – spectra with pronounced diamond peak; B – spectra without pronounced diamond peak; all the presented spectra show peaks of diamond, D and G  $sp^2$  bonded peaks and two peaks belonging to transpolyacetylene (TPA).**

**Table 3.6 Diamond and G peak positions from Raman spectra of samples from factorial design.**

Sample	Diamond peak	G peak
	$\text{cm}^{-1}$	$\text{cm}^{-1}$
CrW11	- *	1605.4
CrW13	1332.9	1599.1
CrW10	1333.4	1600.3
CrW06	1337.7	1603.3
CrW12	1338.2	1606.5
CrW14	1337.3	1604.0
CrW09	1334.1	1606.6
CrW15	1338.8	1606.1

\* CrW15 showed distinct peak at  $\approx 1343.8\text{ cm}^{-1}$  which was assigned to D peak.

As mentioned, Table 3.7 and Figure 3.20 display the summarised responses which were identified as important for the diamond growth. A distinct relationship of good crystallinity corresponding with a good coalescence was observed. A connection between the coating delamination and a good diamond crystallinity/coalescence was also obvious. The investigated responses showed that the factors under investigation are fully dependent on each other in the selected region of this investigation. Therefore, an adjustment of one of the parameters will not have the same effect on the resulting diamond film, if it will be used with different values of the rest of the parameters due to the complexity of the deposition system.

**Table 3.7 Overview responses obtained after the competition of factorial design; the examined effects are shaded for each sample according to how well the particular criteria has been fulfilled (white – best, dark – worst).**

Sample	Pressure [Torr]	Power [Watt]	CH <sub>4</sub> in H <sub>2</sub> [Vol. %]	Delamination	Crystallinity	Coalescence	Diamond peak in Raman spectrum
CrW11	20	500	1	None	Semi	Partial	Not visible
CrW13	30	500	1	Yes	Facetted	Yes	Pronounced
CrW10	20	600	1	None	Semi	No	Pronounced
CrW06	30	600	1	Yes	Facetted	Yes	Detected
CrW12	20	500	5	None	Semi	Yes	Detected
CrW14	30	500	5	None	Ball-like	Partial	Pronounced
CrW09	20	600	5	None	Semi	Partial	Detected
CrW15	30	600	5	Yes	Facetted	Yes	Detected

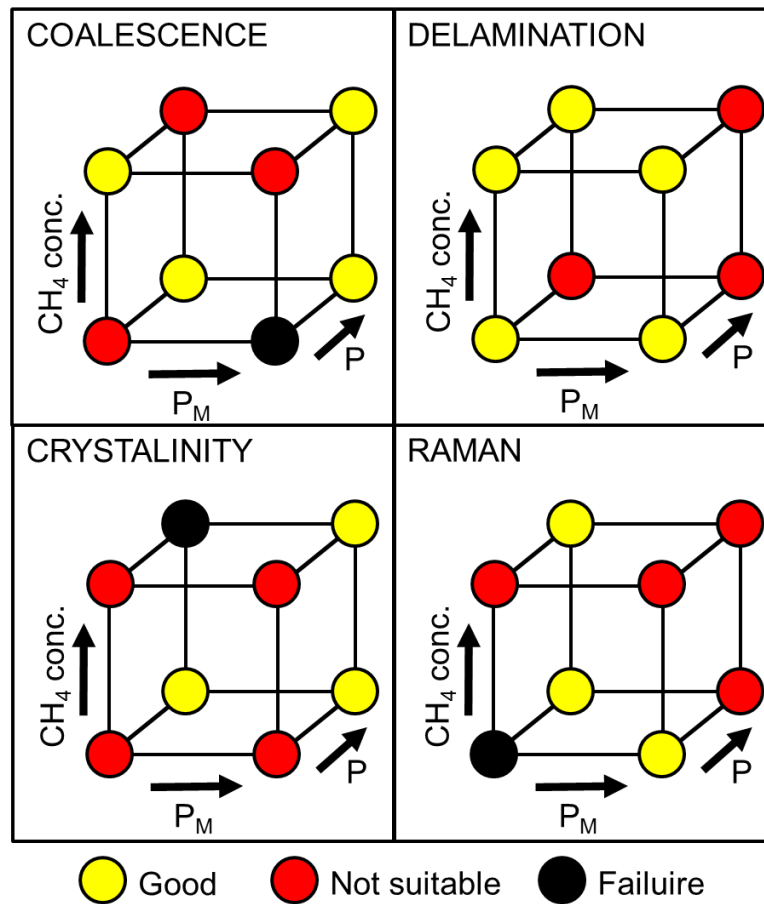


**Figure 3.20 Schematic cubes showing investigated responses from the factorial design with coloured experimental points based on the obtained results for each response; P stands for pressure and P<sub>M</sub> for microwave power.**

### 3.2.4 Further optimization of diamond CVD deposition

Factorial cube, a compact summary of the results of the factorial design is seen in Figure 3.21. The points at each corner of the cube were assigned to a specific feature of the resulting diamond film, which were: good adhesion, crystallinity and low coverage. Linking the best result of diamond crystallinity with results of adherent diamond film of good to acceptable coalescence highlighted four possible combinations of further improvement of the quality and properties of diamond CVD growth. Those points were highlighted in red and were subsequently investigated. The newly identified diamond CVD deposition conditions are displayed in Table 3.8.

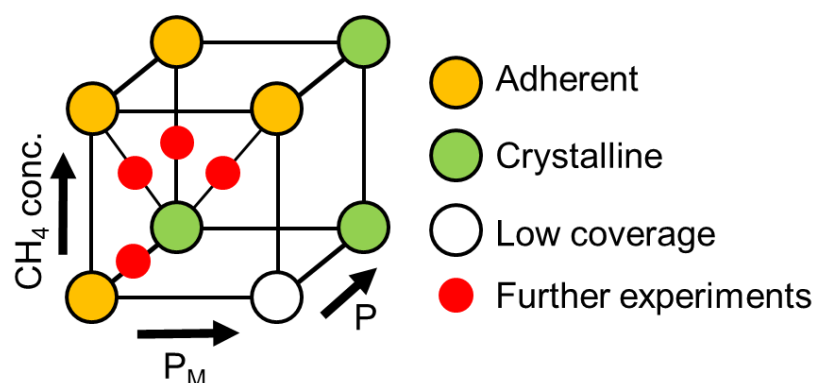


**Figure 3.21 Schematic factorial cube highlighting the results of the investigation from factorial design; each point of the cube represents one experiment; P stands for pressure and  $P_M$  stands for microwave power; the red dots symbolise future experimental conditions identified for further investigation.**

**Table 3.8 Deposition conditions of further diamond growth investigation based on the results of the factorial design; the last two italicised experimental runs were for verification of reproducibility.**

Sample	Pressure	Power	CH <sub>4</sub> conc. in H <sub>2</sub>	Total gas flow	Deposition time
	[Torr]	[Watt]	[vol. %]	[sccm]	[hours]
CrW20	25	500	1	200	2
CrW22	25	500	3	200	2
CrW23	25	550	3	200	2
CrW24	30	500	3	200	2
<i>CrW21</i>	<i>25</i>	<i>500</i>	<i>1</i>	<i>200</i>	<i>2</i>
<i>CrW25</i>	<i>25</i>	<i>550</i>	<i>3</i>	<i>200</i>	<i>2</i>

SEM images of the top surface of investigated samples can be seen in Figure 3.22. Samples CrW23 and CrW24 possessed good crystallinity, followed by CrW20, while the diamond CVD deposition conditions for sample CrW22 did not provide a fully coalescent diamond film. Delamination, crystallinity and coalescence comparison for the newly investigated samples is given in Table 3.9. The coating's quality has been assessed based on the SEM images from Figure 3.22. From the two most crystalline samples the diamond film on CrW24 showed large diamond delamination and CrW23 passed all three criteria. Repeating of the diamond deposition conditions as used in CrW23 gave the same positive results.

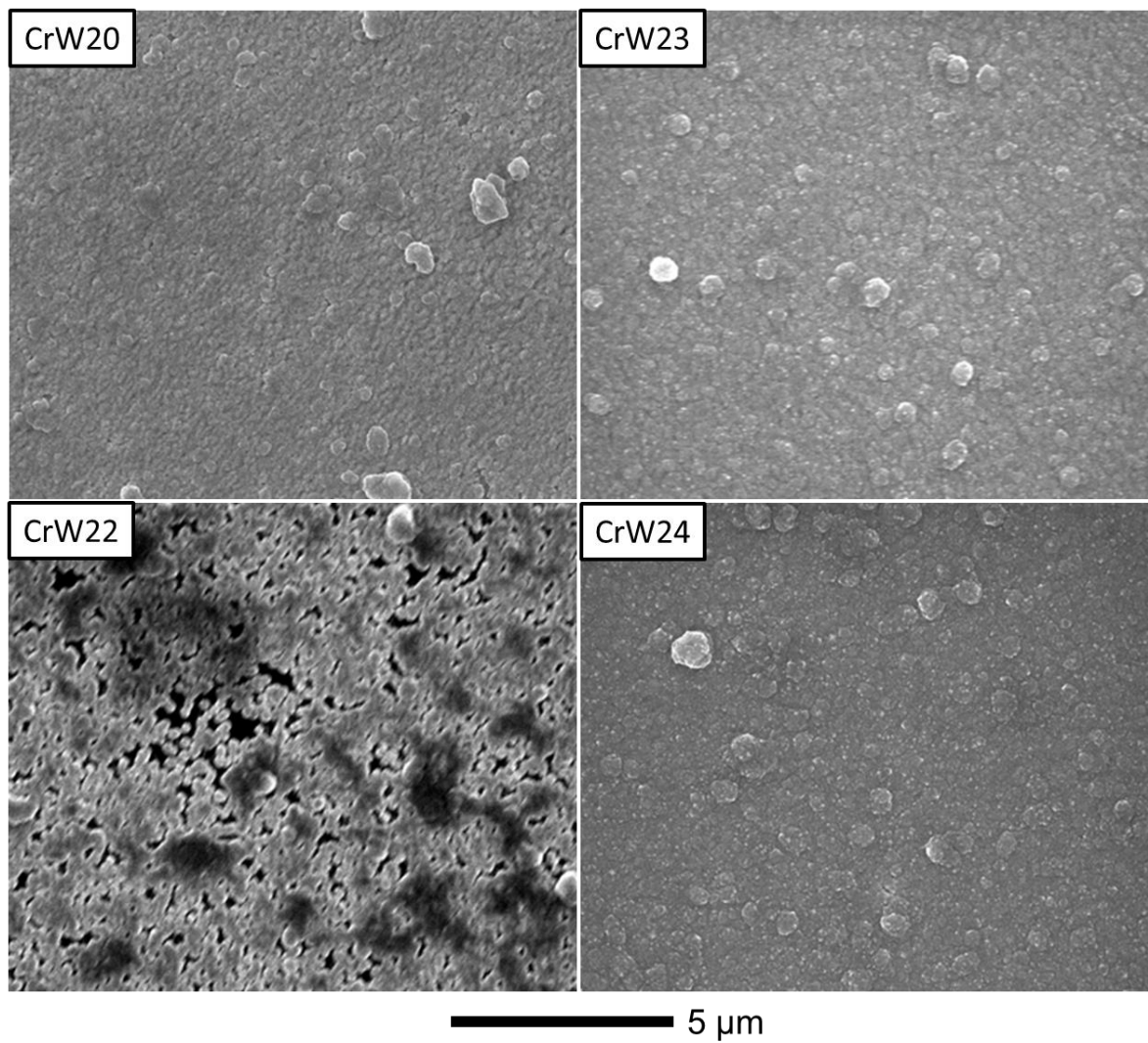


**Figure 3.22 SEM results of diamond growth from the post-factorial experimental investigation.**

**Table 3.9 Overview of the quality of obtained diamond films from the post-factorial experimental investigation, as determined from SEM images.**

Sample	Pressure	Power	CH <sub>4</sub> in H <sub>2</sub>	Delamination	Crystallinity	Coalescence
	[Torr]	[Watt]	[vol. %]			
CrW20	25	500	1	None	Semi	Partial
CrW22	25	500	3	None	Ball-like	No
CrW23	25	550	3	None	Facetted	Yes
CrW24	30	500	3	Yes	Facetted	Yes

### 3.2.5 Problematics of diamond deposition on CrW interlayer

Numerous problems were observed during the diamond CVD growth on the CrW coated steel substrates. First of all it was found that part of the newly deposited CrW coated samples experienced spontaneous adhesion failure of CrW coating as can be seen in Figure 3.23. There, two microscopy images show the delaminated area of the coating's edge, while a buckling adhesion failure dominates the surface with still semi-adherent film.

Secondly, it was observed that occasionally samples with adherent CrW film would experience CrW failure during and after the diamond deposition, as can be seen in figure Figure 3.24. The two top images are examples of interlayer delamination failure during the diamond CVD process which was observed through the wall of the glass bell-jar reactor. It can also be seen that the surface of tungsten is covered in what it presumed to be carbon species. The two lower images are examples of post deposition interlayer cracking which propagated into the diamond film resulting in diamond film cracking or delamination. In the images one can see that the top surface of CrW film, where the diamond film delaminated, looks identical to the SEM image of magnetron sputtered CrW (Figure 3.15, page 101).

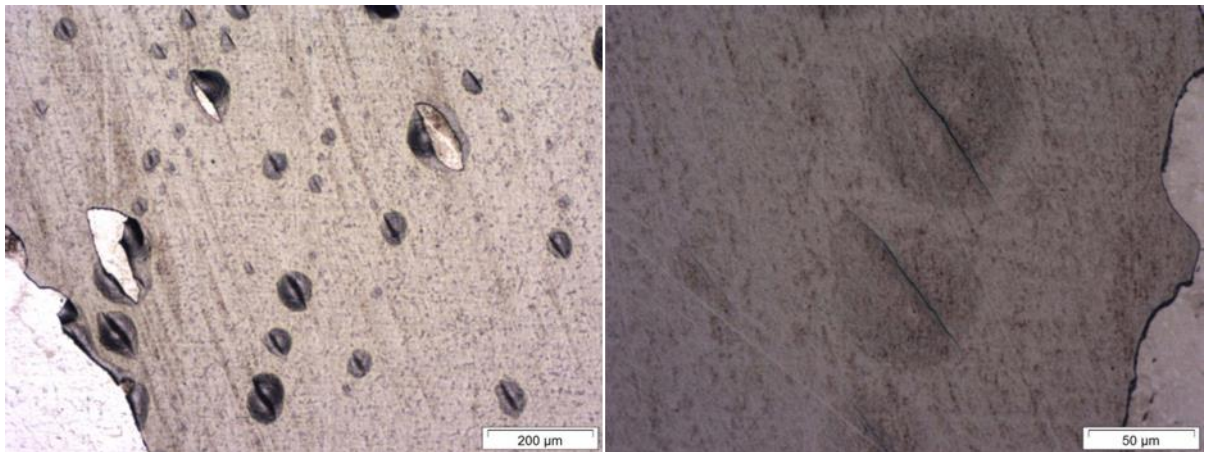


**Figure 3.23 Adhesion failure of part of the CrW coated steel samples after sputtering deposition; coating's buckling and delamination can be seen in both of the images.**

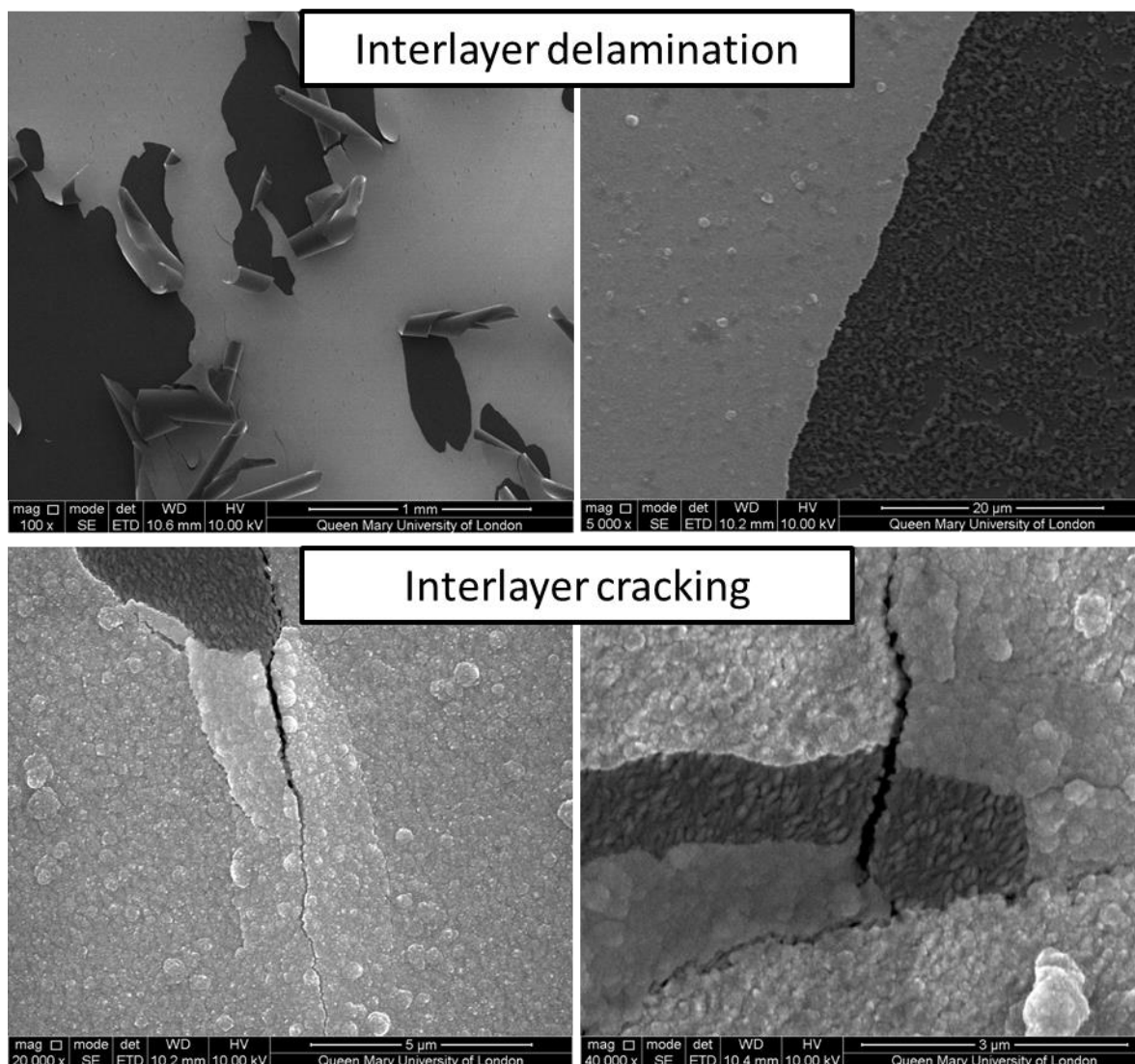


**Figure 3.24 Examples of delamination and cracking of CrW interlayer on M42 steel resulting from diamond CVD deposition.**

Finally, it is the previously highlighted diamond adhesion problem. Fully coalescent diamond films showed great tendencies for delamination during, or after the cooling stage of diamond CVD deposition process. Examples of such diamond delamination can be seen in Figure 3.25. Table 3.10 contains a list of elements detected by XPS on substrate as well as on the bottom surface of delaminated film collected by tape. There has been no evidence of steel elements, such as Fe and Mo, being present at either the substrate, or the tape side eliminating the possibility of the delamination happening at the steel/CrW interface. No Cr detection also eliminated the possibility of CrW interlayer cohesion failure. The strong presence of W at the substrate side and its minimal detected presence at the tape side showed that the delamination originated from the W/diamond interface. Elements such as Si and O and majority of C were detected partially due to the exposure of the investigated surface to the atmosphere and also due to the results being contaminated by the elements

of the used tape. Part of the C detected at the tape side most likely originates from the diamond structure and likely part of the C detected at both the substrate side and the tape side originates from the tungsten carbides, which formed at the W/diamond interface.

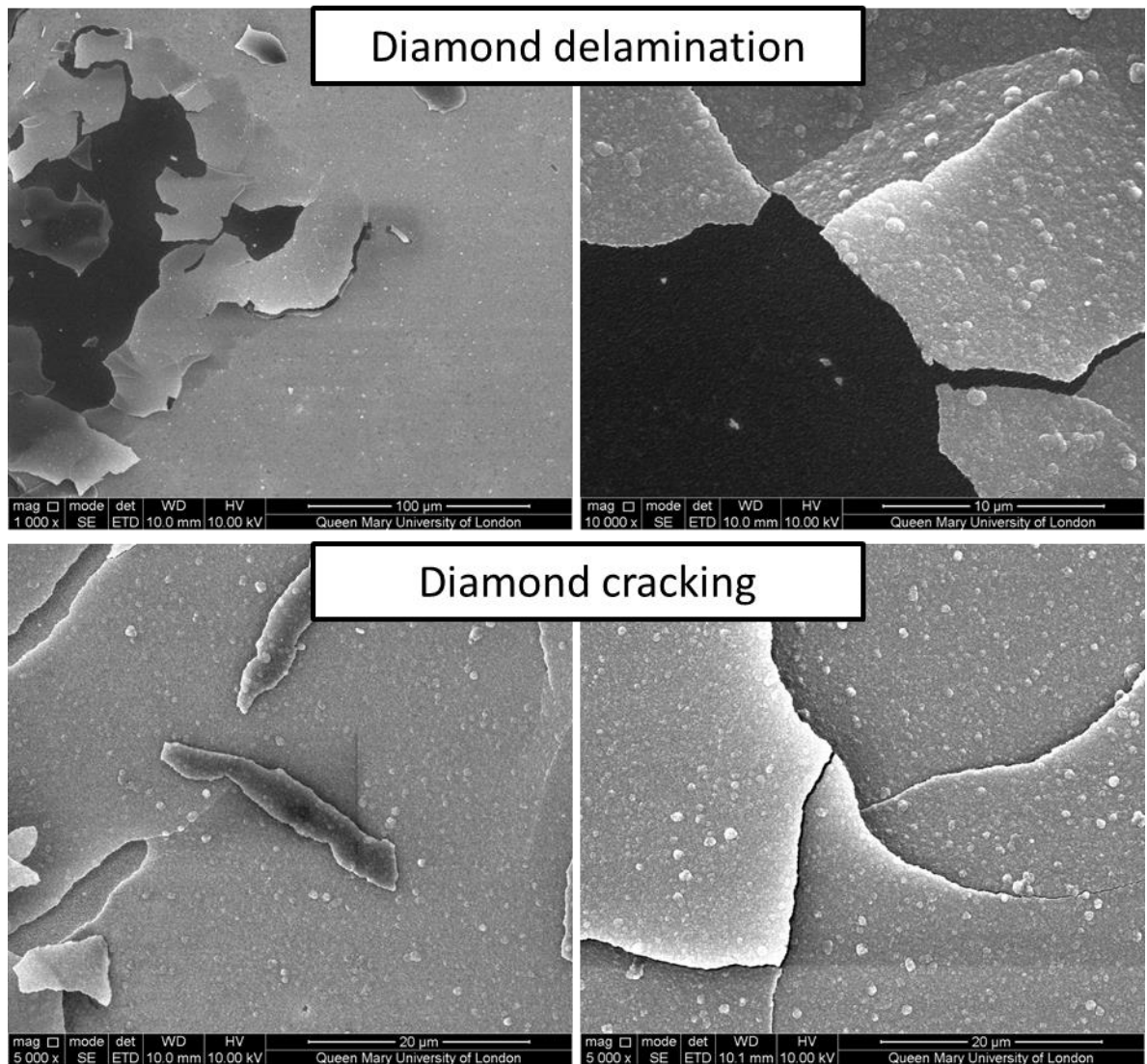


**Figure 3.25 Examples of cracking and delamination of diamond films on CrW coated M42 steel.**

**Table 3.10 List of XPS detected elements in the region of delamination of deposited diamond film.**

Elements	Substrate	Tape
	At. %	At. %
C	47.21	54.36
W	9.48	0.09
Fe	-	-
O	24.33	23.98
Mo	-	-
Cr	-	-
Si	18.98	21.57

### 3.3 Diamond CVD deposition temperature calibration

Process temperature is an important value, which strongly influences on the possibly materials which can be coated with particular film. The developed thermocouple temperature detection setup for the MPCVD equipment used at Aston University was described in section 2.4.3, together with the calibration procedure, through which it would be possible to calculate the temperature at the top of the samples, where diamond deposition takes place.

Single temperature readings for the various conditions of temperature diffusion experiment have been plotted for each of the gas and substrate holder and the most fitting functions have been assigned to every gas. Table 3.11 shows the selected fitting functions together with their respective coefficients of determination. Arithmetic average of coefficients of determination is in the range of  $\geq 0.985$  with an average of 0.992 for Shallow holder measurements and 0.993 for deep holder measurements.

**Table 3.11 Fitting functions for Ar, H<sub>2</sub> and CH<sub>4</sub> gases for temperature diffusion measurement together with their respective coefficients of determination (R<sup>2</sup>); x represents a pressure value and y represents a temperature on the back of substrate holder at given temperature of substrate surface and gas mixture.**

Gas and substrate temperature	Shallow holder		Deep holder	
	Fitting function	R <sup>2</sup>	Fitting function	R <sup>2</sup>
Ar 600 °C	$y = 17.489\ln(x) + 356.46$	0.9828	$y = 25.620\ln(x) + 355.37$	0.9936
Ar 700 °C	$y = 17.949\ln(x) + 412.36$	0.9938	$y = 30.855\ln(x) + 397.06$	0.9923
Ar 800 °C	$y = 24.390\ln(x) + 450.89$	0.9955	$y = 38.276\ln(x) + 442.45$	0.9954
H <sub>2</sub> 600 °C	$y = 38.433\ln(x) + 292.01$	0.9974	$y = 42.702\ln(x) + 294.19$	0.9980
H <sub>2</sub> 700 °C	$y = 42.619\ln(x) + 339.20$	0.9968	$y = 48.029\ln(x) + 338.36$	0.9962
H <sub>2</sub> 800 °C	$y = 44.803\ln(x) + 394.27$	0.9975	$y = 53.490\ln(x) + 382.46$	0.9909
CH <sub>4</sub> 600 °C	$y = 23.953\ln(x) + 360.13$	0.9850	$y = 26.469\ln(x) + 366.55$	0.9882
CH <sub>4</sub> 700 °C	$y = 27.597\ln(x) + 413.11$	0.9872	$y = 35.371\ln(x) + 401.07$	0.9958
CH <sub>4</sub> 800 °C	$y = 30.288\ln(x) + 467.00$	0.9880	$y = 34.244\ln(x) + 500.01$	0.9856

Using the fitted logarithmic functions from Table 3.11 figures of temperature diffusion behaviour were created for the shallow holder (Figure 3.26) and for the deep holder (Figure 3.27). On both of the graphs a similar behaviour is noticeable for every gas at the set sample surface temperature (written in the legend after the gas abbreviation). The measured temperature at the back of the substrate holder evolves very similarly over the investigated pressure range for every set substrate's surface temperature. A clearer visualisation of this

observation is given in Figure 3.28 which compares the temperature at the sample surface with the temperature at the back of the substrate holder at given pressures. A linear relationship between those two temperatures is observable. Fitted linear functions are completing the study together with values of coefficient of determination are displayed in Table 3.12.

Experiments of possible influence of different gas flow rates showed that there is no influence of gas flow rate on the obtained experimental data in the chosen range of 10 – 100 Torr. The difference in temperature readings reached a maximum of 2 °C which is within the equipment accuracy. Similarly the test of measuring gas mixtures showed that simple calculation of vol. % of different gases in the gas mixture does provide an accurate means of calculation of substrate surface temperature. Again, the predicted temperature at the back of the holder differed only by the maximum of 2 °C.

It is worth to mention that even though the deep substrate holder was manufactured and calibrated, it was not used throughout this study. All the deposited samples were deposited while being placed on the shallow substrate holder.

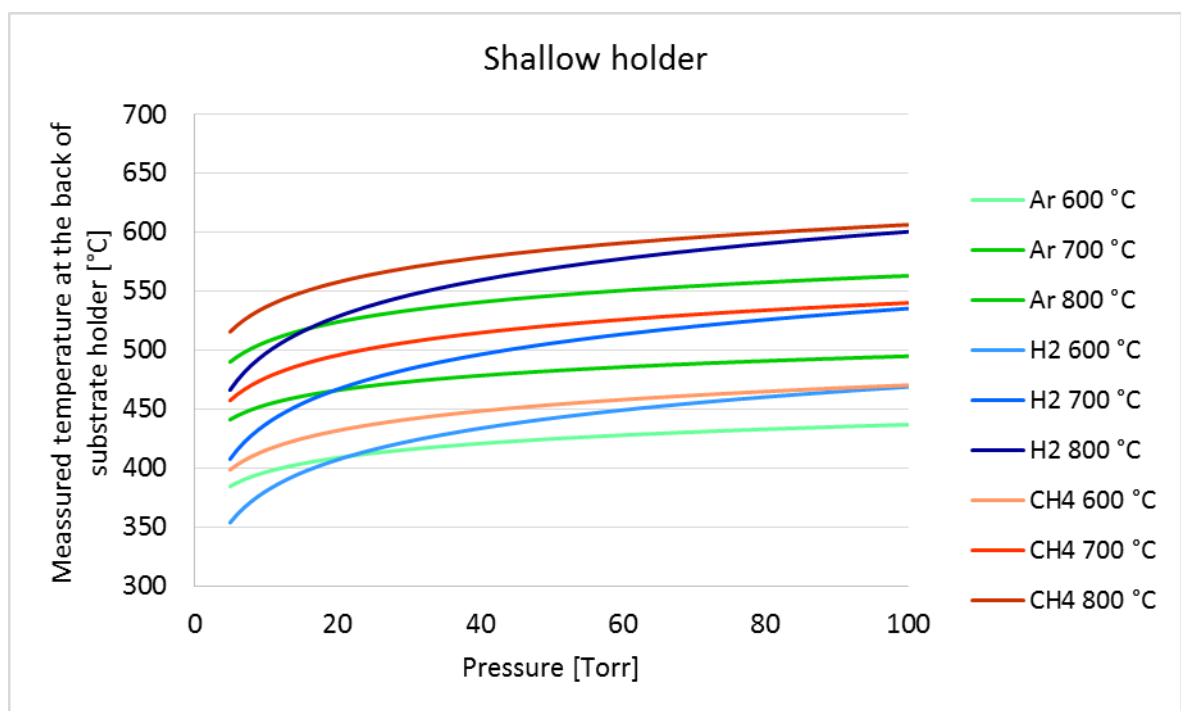


**Figure 3.26 Temperature diffusion difference between samples surface and measured value depending on different pressure and gas as calculated from experimental data for the shallow holder.**

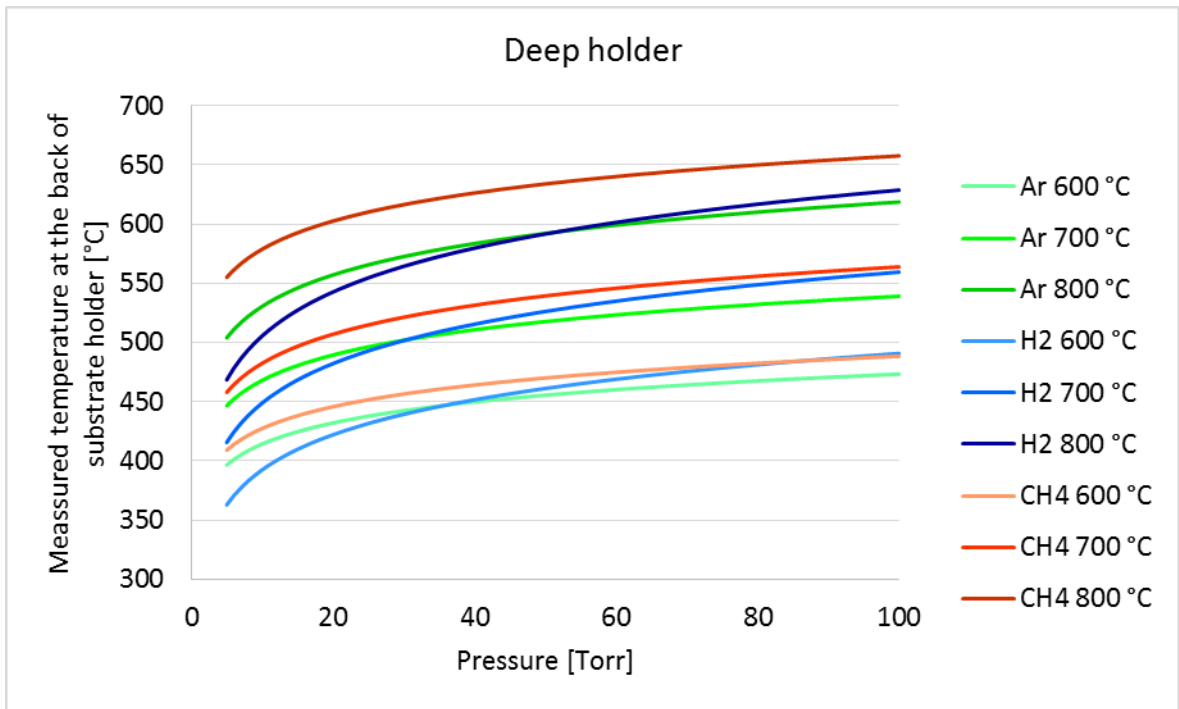


**Figure 3.27** Temperature diffusion difference between samples surface and measured value depending on different pressure and gas as calculated from experimental data for the deep holder.

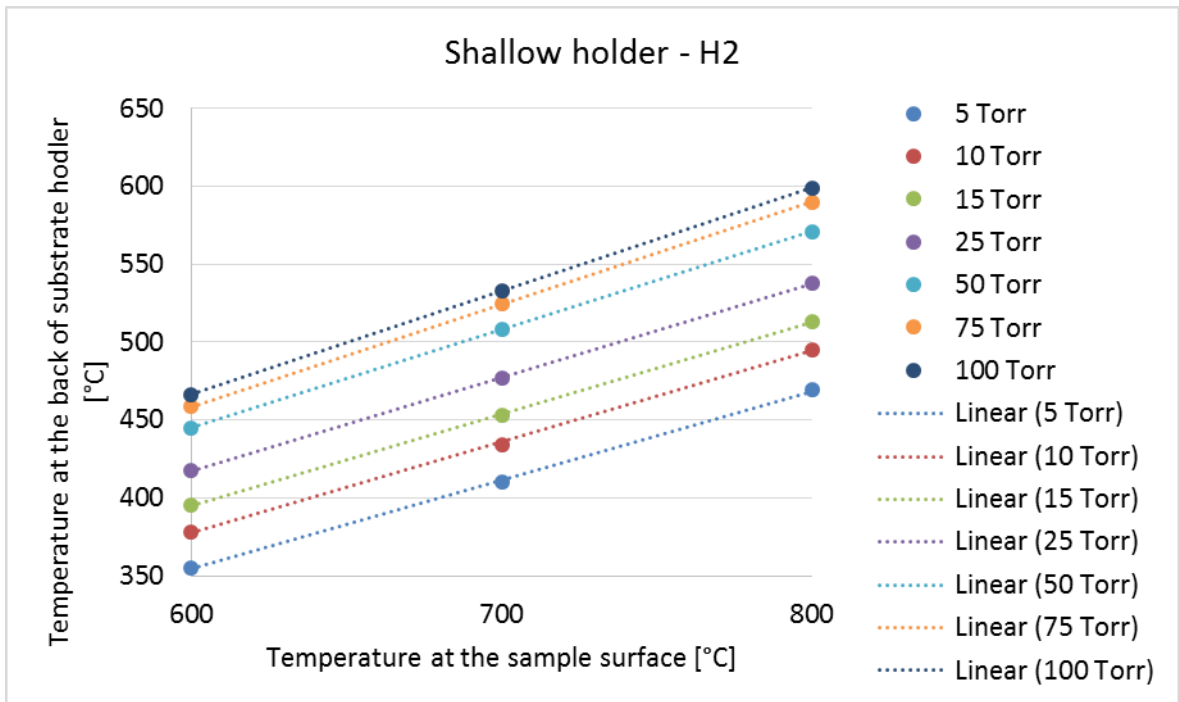


**Figure 3.28** Linear regression functions fitter for temperature diffusion data for hydrogen gas using the shallow holder.

**Table 3.12 Values of coefficient of determination for linear regression functions fitted for each gas at given pressures for the relationship between temperature at the sample's surface and the temperature at the back of the substrate holder.**

Pressure	Shallow holder			Deep holder		
	Ar	H <sub>2</sub>	CH <sub>4</sub>	Ar	H <sub>2</sub>	CH <sub>4</sub>
5 Torr	0.9992	0.9995	1.0000	0.9978	0.9992	0.9788
10 Torr	0.9994	0.9996	0.9999	0.9979	1.0000	0.9827
15 Torr	0.9997	0.9999	0.9999	0.9983	0.9996	0.9850
25 Torr	1.0000	0.9999	0.9997	0.9988	0.9998	0.9860
50 Torr	0.9989	1.0000	0.9997	0.9972	1.0000	0.9900
75 Torr	0.9977	1.0000	0.9999	0.9963	0.9998	0.9939

## 3.4 Diamond Deposition on MoW interlayers

### 3.4.1 Magnetron sputtering of MoW interlayers

Deposition of MoW films was carried out following the same deposition conditions for the sputtering process as was previously used for CrW. The deposition conditions are therefore exactly the same as the ones in Table 3.2 on page 100 with the only difference being that the Cr target has been replaced with Mo target and adjustment in deposition times of Step 3 of the magnetron sputtering process. The deposition time difference is summarised in Table 3.13 where data for each of the multi-layered coatings obtained using the ball crater method is also presented.

**Table 3.13. Time comparison of deposition steps used for MoW-2,3,4 coatings with their respective thicknesses.**

Coating	Step 1 - cleaning	Step 2 - deposition	Step 3 - deposition	Film thickness
MoW-2	1200 s	240 s	3300 s	
MoW-3	1200 s	240 s	15300 s	4.5 μm
MoW-4	1200 s	240 s	31600 s	8.3 μm

To avoid time consuming testing, the as-sputtered MoW films were first tested by Rockwell C indentation (Figure 3.29, left column) and examined by OM (Figure 3.29, right column), as a means of initial characterization of adhesion and topography. As seen from the Rockwell C indents, no coating delamination failure was found around the indents. It can also be seen from the OM images, that there was a distinct elimination of the observable grinding marks with the increase of MoW interlayer thickness.

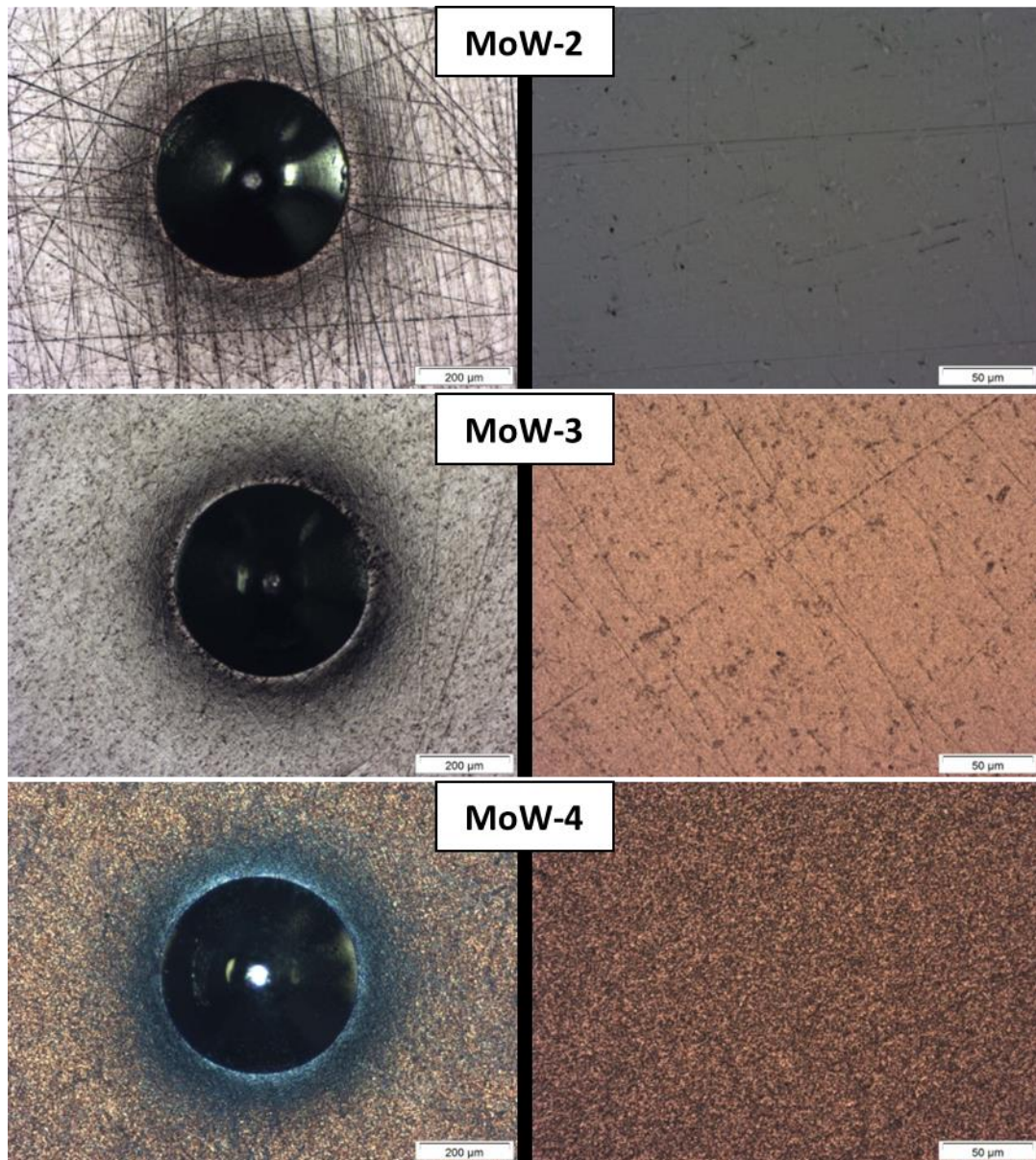


**Figure 3.29 OM images of Rockwell C indents (left column) and general view of the surface (right column) for MoW-2,3,4 coated M42 steel discs.**

The film thickness values, roughness data and hardness values for each of MoW-2,3,4 coated substrates as well as the RMS roughness values are summarised in Table 3.14, where it is seen that roughening of sample surface is linked with the increase of MoW interlayer thickness. Surface roughness data presented were averaged values of three scans over 30x30 μm area. The thickness of the MoW-2 layer is the same as for the previously deposited CrW coating. The measured hardness of the coated steel discs did not differ from the steel hardness which was measured before the deposition (if inaccuracy of  $\pm 1$  is taken into account). Therefore the hardness of the steel was not altered by being coated.

**Table 3.14 Surface characterization of MoW-2,3,4.**

Substrate	Thickness	RMS roughness	Hardness
[-]	[ $\mu\text{m}$ ]	[nm]	[HRC]
MoW-2	1.1	19.2	65
MoW-3	4.5	31.7	64
MoW-4	8.3	66.3	64

Further characterization of the surface features and the orientation of the top W layers was carried out using SEM imaging (Figure 3.30). The surface structure of deposited MoW films from SEM images showed gradual increase in size of the tungsten grains from  $\approx 100$  nm in case of MoW-2 to up to well defined micron size structures in the case of MoW-3 and MoW-4. Figure 3.30 also shows a cross-sectional view of MoW-4 identifying the growth system during the magnetron sputtering process as columnar.

EDS area scans with minimal scan sizes of  $100 \mu\text{m}^2$  were used for initial examination of any possible surface contamination. The obtained results were used with electron beam power of 10 keV and only 100% concentration of W was detected.

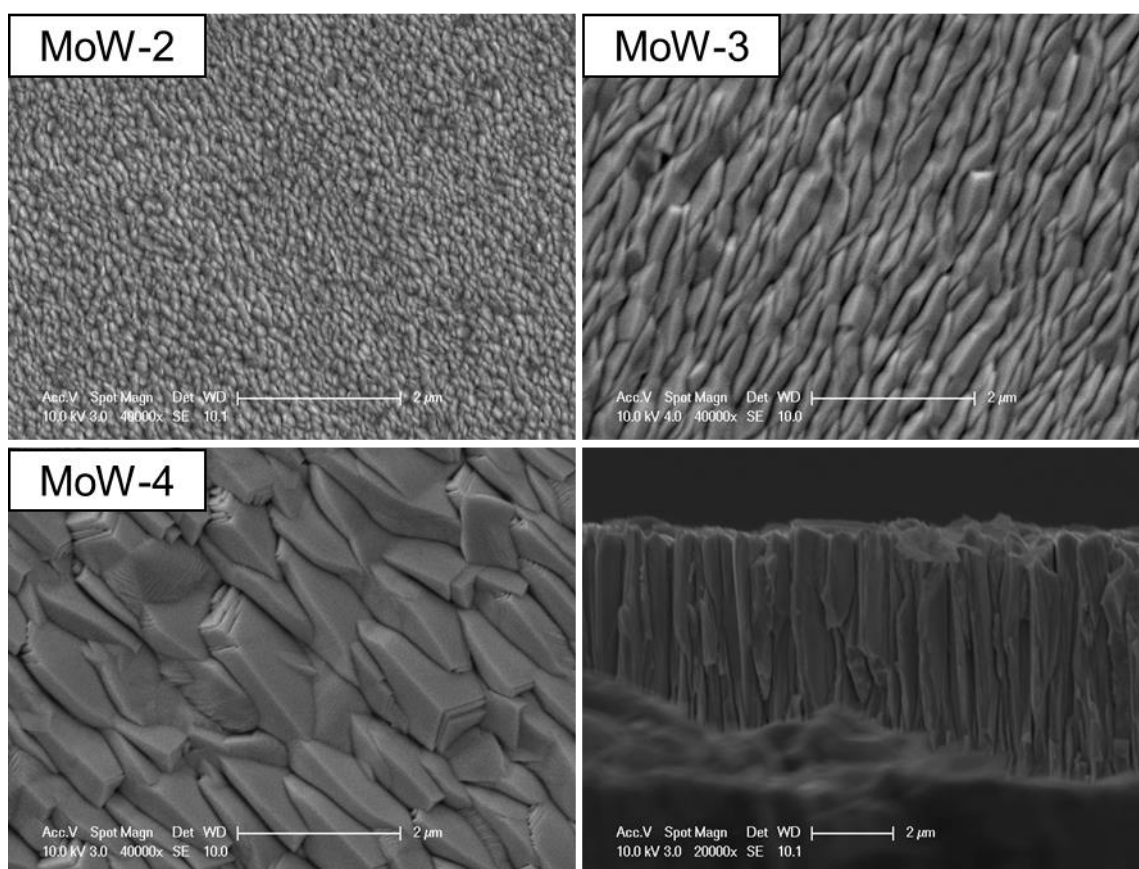


**Figure 3.30 Topography SEM overview of MoW-2, MoW-3, MoW-4 coated M42 steel samples with a cross-sectional view of MoW-4 sample, where columnar growth of the MoW interlayer is visible.**

Chemical and structural composition evaluation of the coating's top surfaces was further studied by XRD technique and Figure 3.31 displays the resulting diffractograms. From the comparison image of diffractograms taken for all three MoW-2,3,4 coatings (top left corner) it is seen that the chemical composition is pure tungsten in all cases. The two present tungsten peaks are W (110) at  $\approx 40.3^\circ$  and W (220) at  $\approx 87^\circ$  [187]. No cross-contamination of the pure W layer with Mo or any other element was detected. The diffractograms from which the comparison image is composed of, were taken without any instrumental offset. The inserted cut-out in the graph is an enlarged main W (110) peak which was used for calculation of the crystallite size. The precise peak positions were used for calculation of the size of crystallites for MoW films and are summarised in Table 3.15. The resulting graphs in Figure 3.31 display obtained diffractograms for each of the respective MoW coatings at different offsets were taken while the samples were rotating. The stacked diffractograms displayed are taken at  $1^\circ$  steps with offset from  $-10^\circ$  to  $+10^\circ$ . The acquired diffractograms enabled to further determine the crystal orientation and growth direction with respect to the substrate's surface, which was identified as  $\langle 110 \rangle$  for all three MoW coatings. A new peak at  $\approx 131.2^\circ$  belonging to W (321) was also detected with the tilting of the setup, which is particularly pronounced in the case of MoW-4.

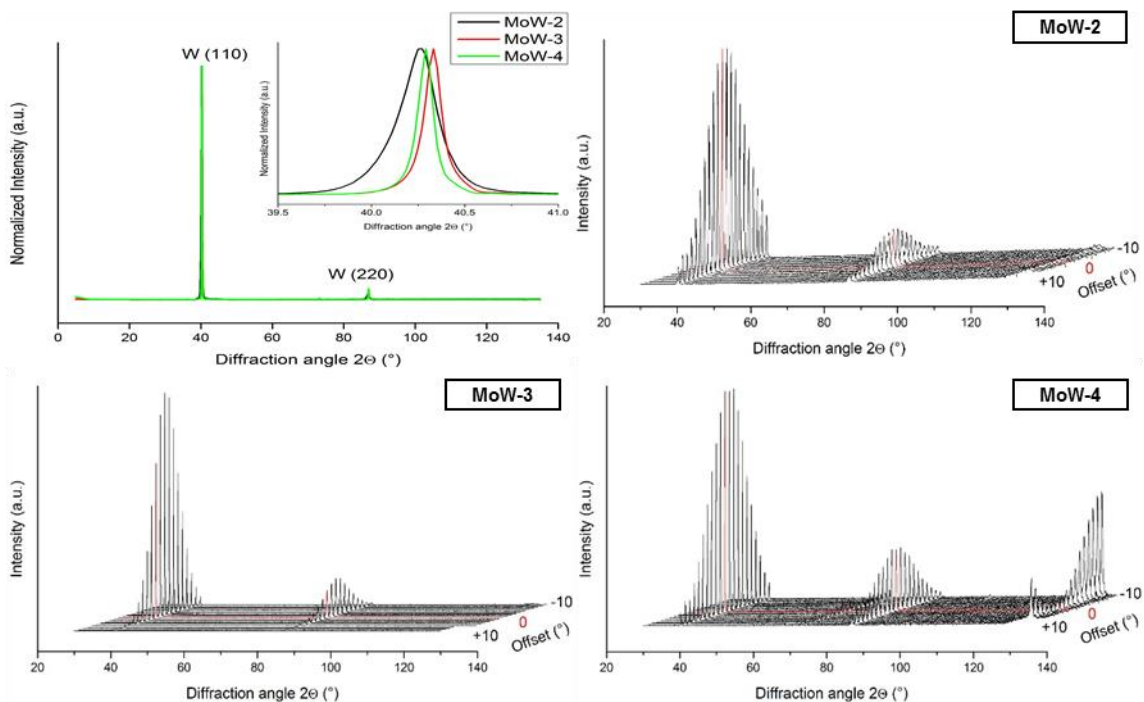


**Figure 3.31 Comparison of X-ray diffractograms of MoW-2,3,4 with no scan offset (top left); stacked diffractograms of individual MoW coated samples using setup's offset from  $-10^\circ$  to  $+10^\circ$ .**

**Table 3.15 List of peak positions of W(110) and the size of crystallites of MoW-2,3,4 coated steel samples.**

Sample	Crystallite size	Peak position
	(nm)	(°)
MoW-2	41.27	40.26
MoW-3	97.25	40.33
MoW-4	113.3	40.29

### 3.4.2 Diamond deposition on MoW-2 interlayer

The measured substrate surface temperature during the diamond CVD deposition was 785 °C, making the CVD deposition conditions of moderate temperature, which is commonly reported in literature. Figure 3.32(A) shows the topography image of deposited diamond film on a MoW-2 coated steel sample. The deposited diamond film looks identical to the diamond film coated CrW sample. The individual diamond grain size was estimated from SEM images to be 140 nm on average. Figure 3.32(B) shows the deconvoluted Raman spectrum of the deposited diamond film. Diamond peak was located at position of 1332 cm<sup>-1</sup>. Sp<sup>2</sup> hybridised D and G peaks (1345 cm<sup>-1</sup> and 1598 cm<sup>-1</sup>, respectively) were identified, together with two peaks associated with transpolyacetylene (1255 cm<sup>-1</sup> and 1490 cm<sup>-1</sup>).

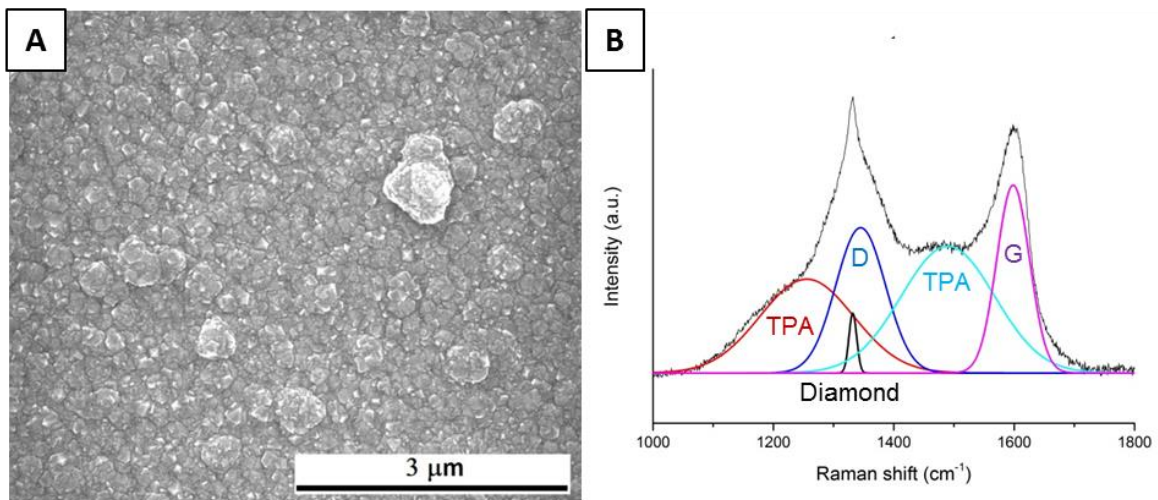


**Figure 3.32. SEM topography image (A) and deconvoluted Raman spectrum (B) of deposited diamond film of MoW-2 coated M42 steel; diamond, D and G sp<sup>2</sup> peaks and transpolyacetylene (TPA) peaks were identified; taken and modified from [188].**

The diamond CVD deposition conditions lead to overall sample softening as was observed on values of Rockwell C hardness. Initial hardness of MoW-2 coated steel was 64 HRC, while hardness of a diamond coated sample showed a decrease to an average value of 61 HRC. The average thickness for diamond films deposited was 245 nm with an accuracy of ± 20 nm and growth rate being ≈ 120 nm/h. The average RMS surface roughness was estimated to be 72 nm over 30x30 μm scanning areas.

Adhesion assessment was performed by a scratch test under continuous progressive load. WC ball (5 mm) was used as an indenter with applied force of 5-30 N, loading rate of 100 N/min and velocity of 10 mm/min. The critical load was derived from the distance to the first sign of diamond delamination from the racetrack. Ten scratches were performed on two diamond coated samples with arithmetic mean value of the first diamond delamination being 11.4 N. The minimal and maximal values of adhesion failure derived from the scratch test results were 8.5 N and 17.4 N. During the scratch tests a WC ball was smeared over the diamond surface adhering to the sample. Figure 3.33 shows the racetrack after performing the scratch test. The mode of diamond adhesion failure was identified as a buckling spallation. Notably, the adhesion failure occurred only within the scratch region.



**Figure 3.33 SEM image of the start of delamination of diamond film within the scratch track using back scattered electrons imaging mode; the white arrow shows the direction of sliding of WC ball; taken from [188].**

Samples were freed of diamond delaminated debris and an SEM examination was carried out to determine the delamination interface. Figure 3.34 shows such a region within the scratch racetrack. The white arrow indicates the direction of the scratch and the highlighted areas A and B correspond to the EDS spectra taken, with the results displayed in Table 3.16. On analysing both the SEM image and the EDS spectra it was confirmed that the right side of the image is still-adherent diamond film with a smooth overlay of part of WC ball which got smeared over the racetrack due to the presence of cobalt, which is used as a binder for sintering of WC materials. The left side of the image is the pure tungsten top layer of the MoW-2 coating, with carburised top surface. The EDS spectra also shows a chemical composition with an unscratched area of diamond coated MoW-2.

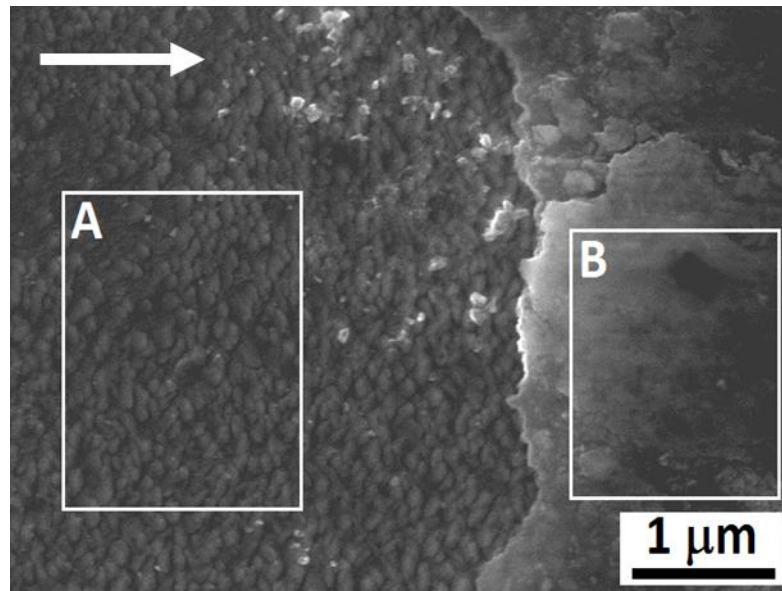


**Figure 3.34 SEM image of part of the scratch track; left – delaminated area; right – adherent area; rectangles A and B mark the areas of EDS scan; the white arrow indicates the direction of sliding of WC ball; taken from [188].**

**Table 3.16 EDS spectra of delaminated and adherent regions of diamond film within the scratch region together with an unscratched region of diamond film.**

Elements in wt. %	C	W	O	Co	Mo	Fe
A - delaminated	3.66	96.34	-	-	-	-
B - adherent	26.48	68.29	3.73	1.5	-	-
Unscratched region	45.79	54.21	-	-	-	-

The effectiveness of the MoW-2 interlayer was assessed from the EDS cross-section line scans over the diamond/MoW-2/steel and can be seen in Figure 3.35. Carbon intensity is naturally the highest in the region of diamond films and decreases rapidly upon encountering the W-rich side of the Mo-W interlayer. Very similar results can be seen with iron, where its intensity drops at the start of Mo/steel interface. Co is also present in M42 steel (typically around 8 wt. %) and its EDS profile follows the same trend as iron. For clarity of data presentation Co distribution was not added into Figure 3.35.

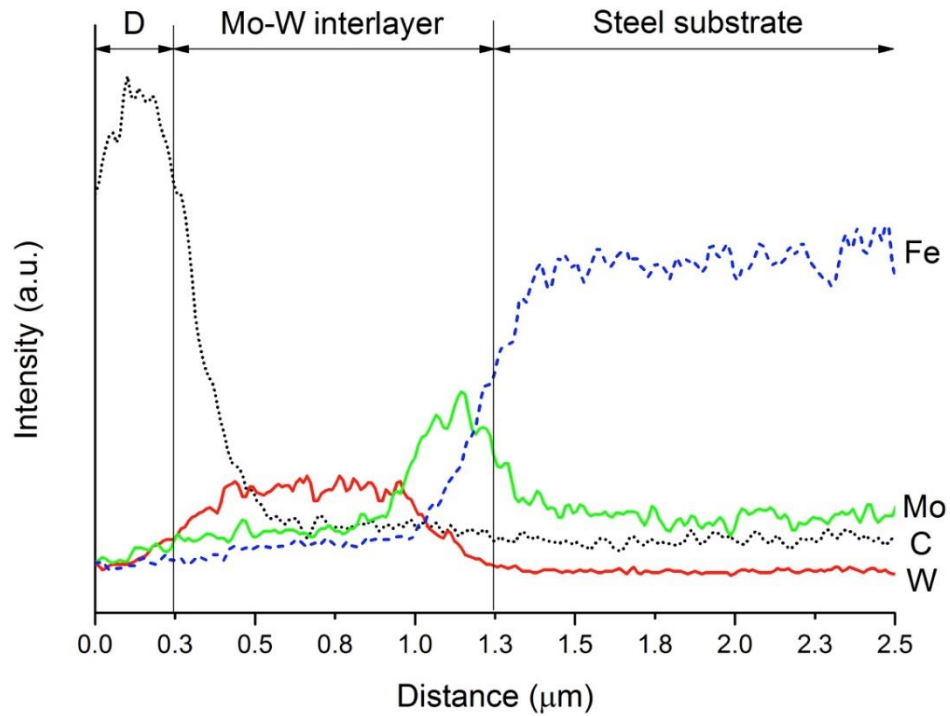


**Figure 3.35 EDS analysis of Diamond/MoW-2/M42 sample cross-section.**

### **3.4.3 Investigation of low temperature diamond CVD deposition**

Figure 3.36 shows identified diamond CVD deposition conditions for substrate surface kept at 650 °C. Decrease of methane concentration led to a need to increase microwave power in order to maintain identical substrate surface temperature. Also it was observed that microwave power is the major parameter in substrate surface temperature determination as the increase of pressure from 15 to 20 Torr forced only relatively small changes on microwave power in order to maintain the same substrate temperature. Nine deposition conditions were identified and are summarised in Table 3.17 together with the determined deposition temperatures.

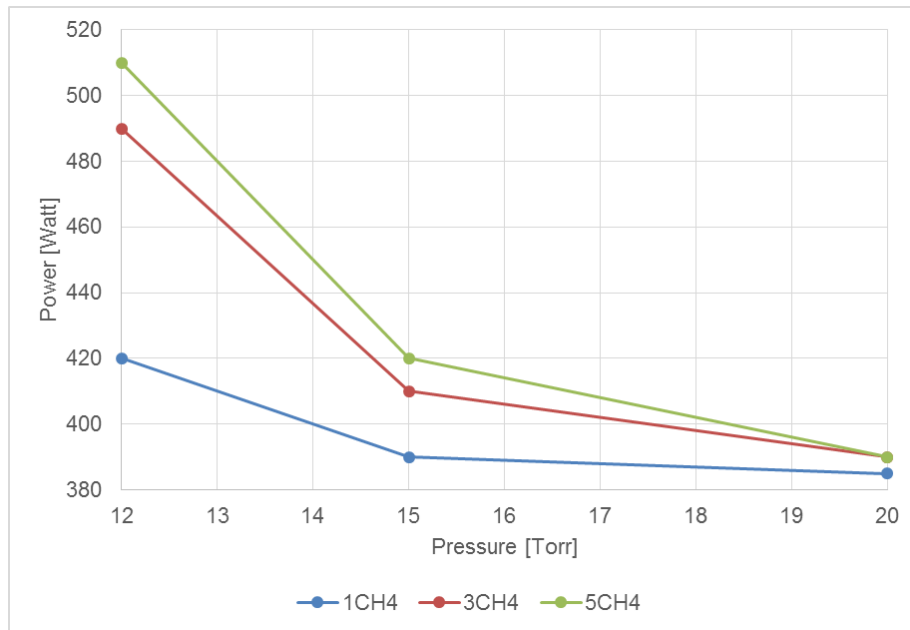


**Figure 3.36 CVD deposition parameters evolution depending on the amount of methane in hydrogen rich atmosphere with deposition temperature set at 650 °C.**

**Table 3.17 Experimental design of diamond deposition at 650 °C on MoW-2 coated M42 steel with pre-set pressures and methane concentrations in hydrogen-rich atmosphere.**

Sample	Power	Pressure	CH <sub>4</sub>	Time	Temperature
[-]	[Watt]	[Torr]	[vol. %]	[hours]	[°C]
MoW044	420	12	1	6	649
MoW040	390	15	1	6	644
MoW042	385	20	1	6	646
MoW028	550	12	3	4	649
MoW030	440	15	3	4	649
MoW031	430	20	3	4	648
MoW043	510	12	5	6	646
MoW039	420	15	5	6	645
MoW041	390	20	5	6	648

Macro images of the diamond samples after the diamond CVD deposition are displayed in Figure 3.37, followed by SEM images of the CVD deposited films which can be seen in Figure 3.38. As can be seen, the deposition time for samples deposited under 3 vol. % of methane differs from the other deposition times, which was caused by author's mistake and was taken account for interpretation of the data.

Samples deposited at 1 vol. % of methane showed a tendency to low adhesion of deposited diamond films. In the images of the three samples there are visible regions where it was possible to partially or totally take away the CVD deposited film (good example being the sample deposited at 1 vol. % of methane and 20 Torr in Figure 3.37). SEM images of those coatings revealed that the diamond deposition growth rates were too slow, resulting in non-coalescent films. Increase of methane vol. % increased the diamond deposition rates and

deposited films at 3 and 5 vol. % of methane were fully coalescent with only one exception. The exception was a sample deposited at 12 Torr and 3 vol. % of methane where the diamond growth speed was not able to form a coalescent diamond film during the given deposition time. Three samples showed signs of partial delamination of CVD deposited films with deposition parameters of 20 Torr + 3 vol. % CH<sub>4</sub>, 20 Torr + 5 vol. % CH<sub>4</sub> and 12 Torr + 5 vol. % CH<sub>4</sub>. The main observation on the structure and properties of the CVD deposited films are summarised in Table 3.18, where the two most promising CVD diamond deposition conditions were highlighted in yellow. It was possible to recognise that deposition conditions with chamber pressure of 15 Torr during the CVD deposition are the most suited deposition conditions in the case of the MPCVD equipment used, at the selected surface deposition temperatures. Higher deposition pressure of 20 Torr was found to be causing too high stresses in the deposited diamond films upon cooling, which was resulting in their delamination. Lower deposition pressure of 12 Torr was, on the other hand, too low to facilitate a good levels of adhesion of the deposited diamond films, which also led to diamond film's delamination upon cooling down from the deposition temperature. Both of the delamination problematics can be seen in the Figure 3.37.

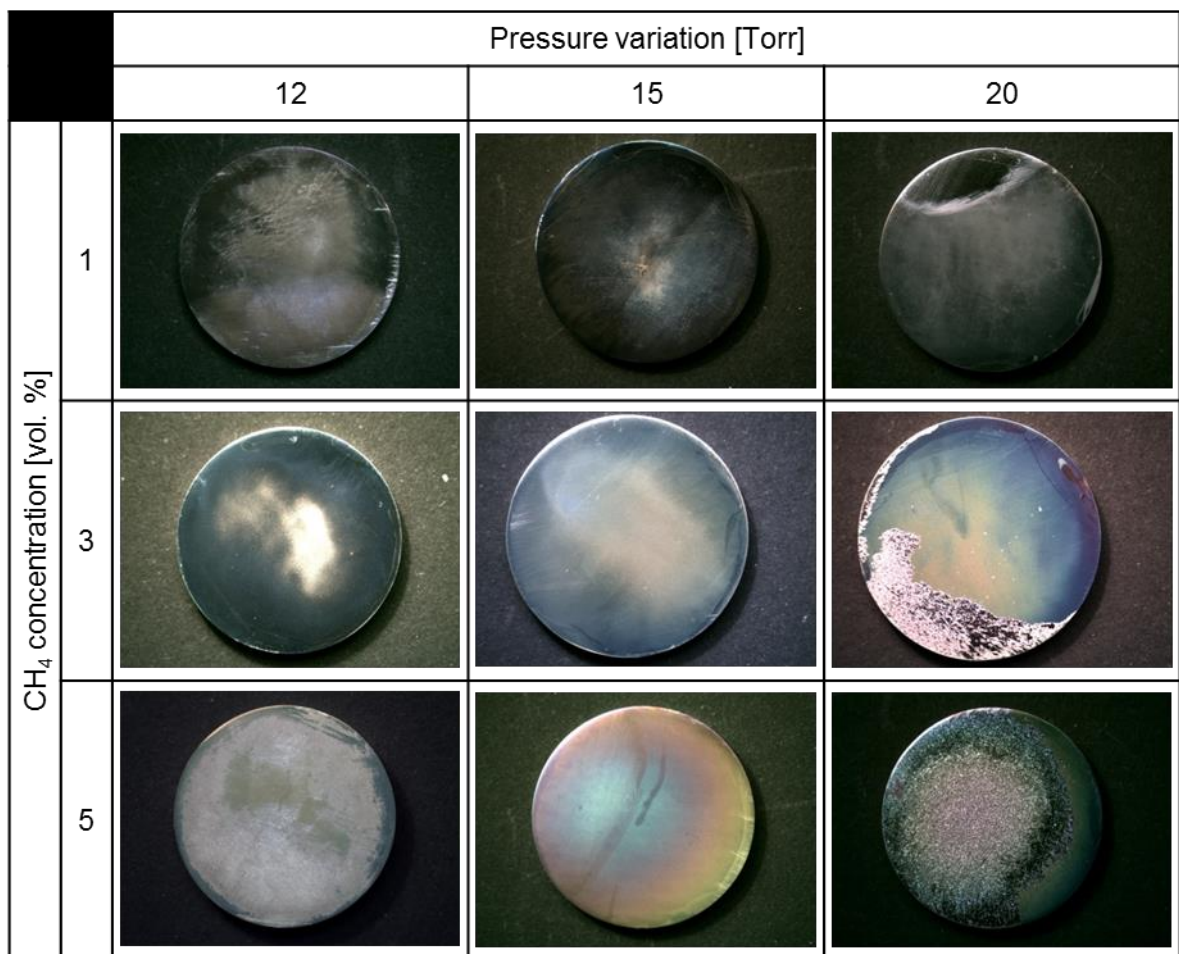


**Figure 3.37 Macroscopic images of various diamond deposition runs on M42 steel with MoW-2 interlayer at 650 °C; samples are 25 mm in diameter.**

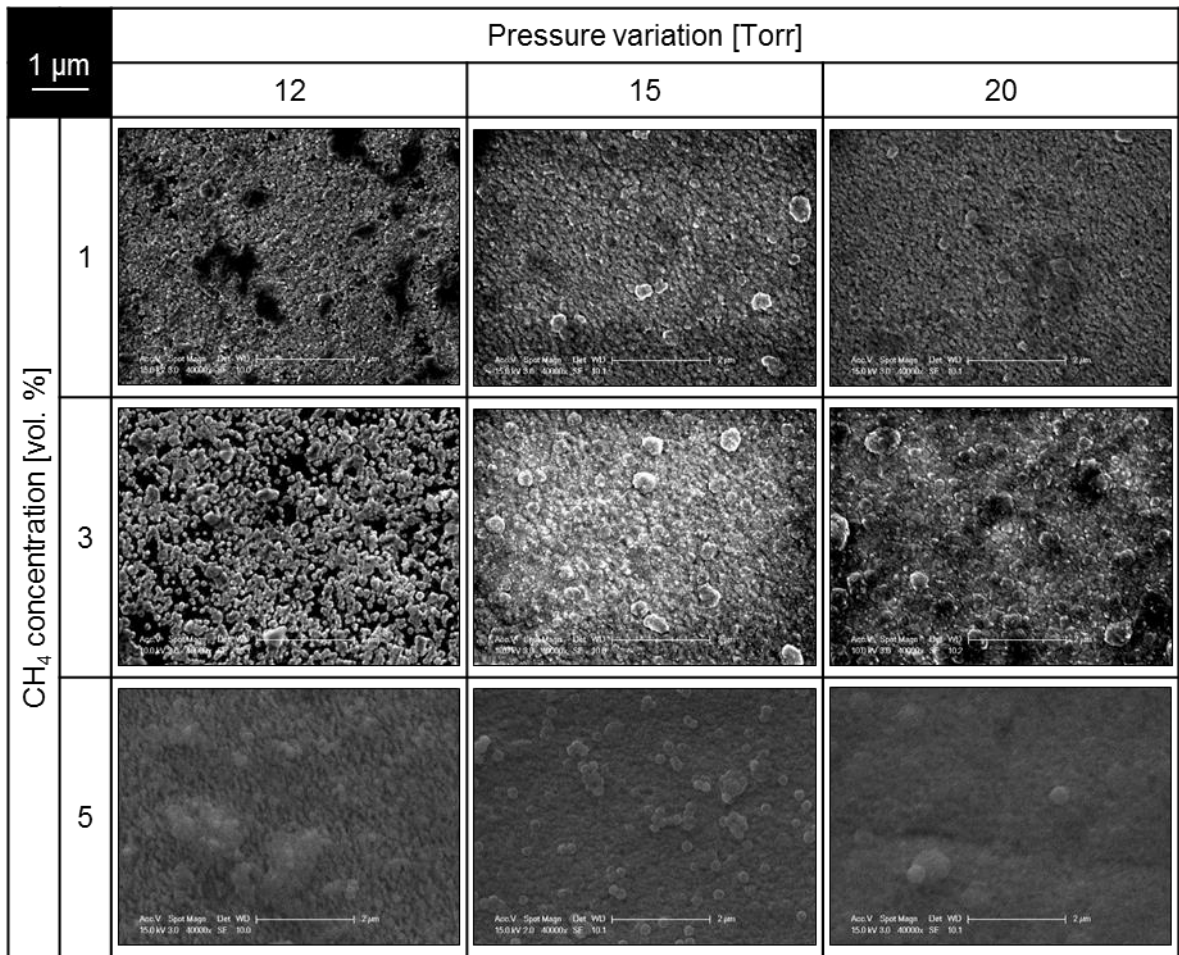


**Figure 3.38 SEM images of surface features of various diamond deposition runs on M42 steel with MoW-2 interlayer at 650 °C.**

**Table 3.18 Brief summary of structure and properties of diamond films grown at 650 °C on MoW-2 coated M42 steel substrates.**

		Pressure variation [Torr]		
		12	15	20
CH <sub>4</sub> concentration [vol. %]	1	Not coalescent Partial adhesion	Not coalescent Partial adhesion	Not coalescent No adhesion
	3	Not coalescent Adherent	Coalescent Adherent	Coalescent Partial delamination
	5	Coalescent Delamination	Coalescent Adherent	Coalescent Delamination

The results of Rockwell C hardness are displayed in Table 3.19. A minimum of three Rockwell C indents were used to determine the average Rockwell C hardness for every measured sample. It can be seen that the Rockwell hardness after the various diamond deposition conditions did not divert from the initial hardness of MoW-2 coated steel samples (65 HRC). The overall HRC average was within the overlapping inaccuracy of the Rockwell C hardness method. No trends were detected within the obtained hardness matrix.

**Table 3.19 Summary of averages of Rockwell C hardness of samples after the investigated low temperature CVD deposition conditions.**

CH <sub>4</sub> [vol. %]	HRC at pressures of:			Average HRC
	12 Torr	15 Torr	20 Torr	
1	63.5	64.8	64.0	64.1
3	64.0	65.0	63.3	64.0
5	63.3	63.7	64.2	63.7

\*Overall HRC average 63.9

The two mentioned samples deposited under CVD condition of 15 Torr at methane ratios of 3 and 5 vol. % were selected for further investigation. The enlarged SEM images of these can be seen in Figure 3.39. The sample deposited under 3 vol. % of methane is composed of fully crystalline nanodiamond, while the sample deposited under 5 vol. % of methane exhibits nanodiamond grains which are semi-crystalline and semi-ball-like shaped.

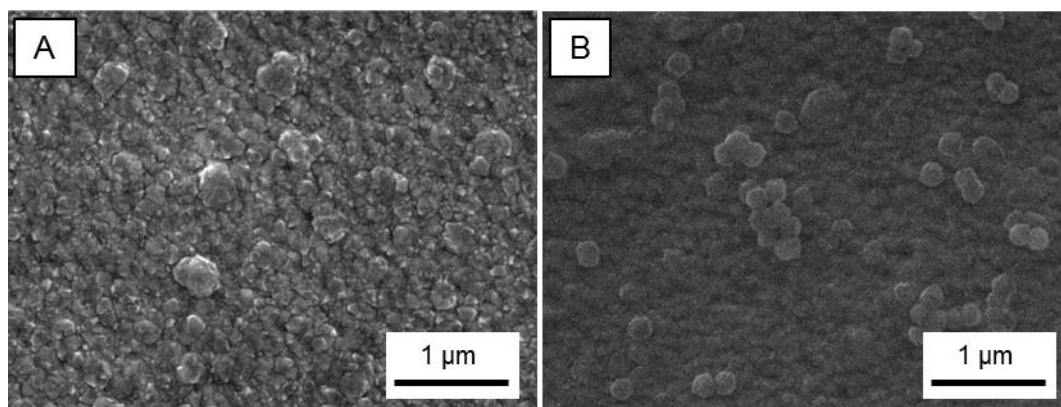


**Figure 3.39 SEM images of diamond surface of samples deposited at 15 Torr with 3 vol. % of methane (A) and 5 vol. % of methane (B).**

Figure 3.40 shows Raman spectra of the deposited diamond films. The diamond peak positions are situated at 1336.2 cm<sup>-1</sup> and 1335.7 cm<sup>-1</sup> for sample deposited under 3 and 5 vol. % of methane, respectively. Diamond films were therefore under compressive stress and in case of lower methane deposition conditions the stress present in the film was only marginally higher. One can observe that the spectra look similar, with high intensities of sp<sup>2</sup> bonded carbon species almost overshadowing the diamond peak. Although it is noticeable

that the spectrum of sample deposited under higher methane concentration has higher intensities of D, G and transpolyacetylene peaks when compared to the spectrum of diamond deposited under 3 vol. % of methane.

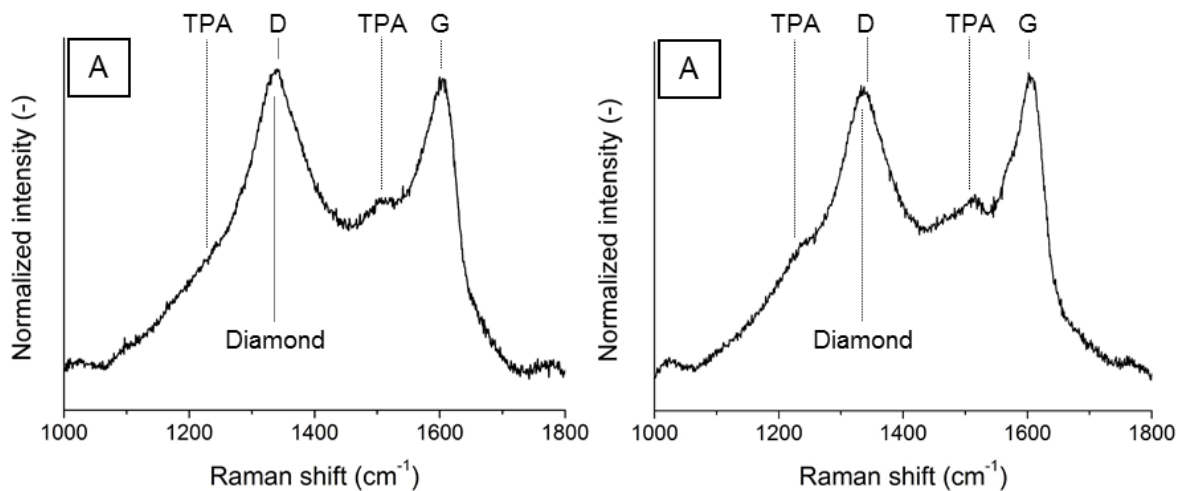


**Figure 3.40 Raman spectra of diamond films deposited at 15 Torr with 3 vol. % of methane (A) and 5 vol. % of methane (B); identified peaks in the spectra belong to diamond, D and G  $sp^2$  peaks and two transpolyacetylene (TPA) peaks.**

Two different scratch tests were performed on the two MoW-2 samples deposited at 15 Torr with methane concentrations of 3 and 5 vol. %. Initially, a 5-30 N scratch test with conditions identical to the scratch conditions used for diamond coated MoW-2 samples was used (5 mm WC ball indenter, 100 N/min loading rate and velocity of 10 mm/min). Four such scratches were performed for each set of specific diamond CVD deposition conditions. Examples of resulting racetracks of the 5-30 N scratch tests can be seen in Figure 3.41. It is seen that the delamination of the diamond coating consists of individual diamond chips and progresses along the racetrack into total delamination of deposited diamond film within the racetrack itself. In the case of sample deposited at 3 vol. % of methane, the diamond delamination also exceeds the area of scratch track. The darker zone showing in the middle region of the racetrack is a result of chipped parts of diamond film being lodged into the WC ball which then go on to pulverise the top of the MoW interlayer. The large amount of spallation suggests that interfacial bonding between MoW and diamond has been significantly weakened by the decrease in diamond CVD deposition temperature. The adhesion failure of diamond films occurred at the start of the scratch tracks and therefore no determination of critical load values was possible.

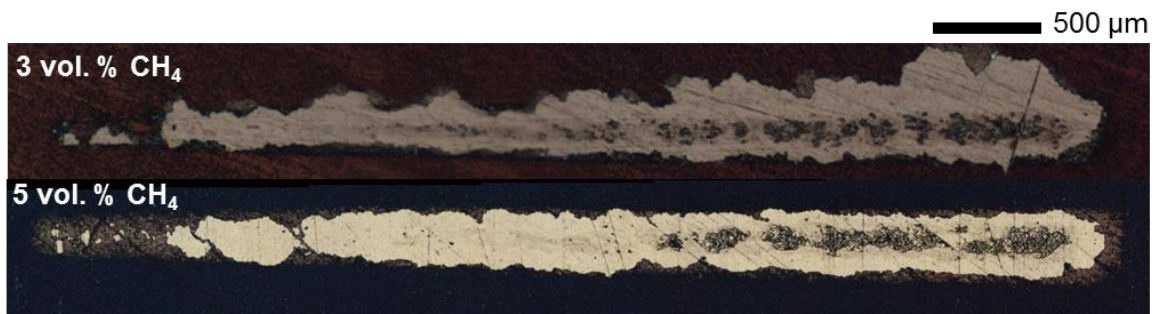


**Figure 3.41 5-30 N scratch tracks of diamond film on MoW-2 coated M42 steel.**

A new set of scratch tests of 1-15 N load was performed in order to investigate if lower initial loads will provide an estimate of the critical loads of diamond films deposited. The scratch testing conditions were kept identical with the previous 5-30 N scratch, the only exception being the difference in the range of used loads. Again, four scratches were performed for each set of specific diamond CVD deposition conditions. Figure 3.42 shows the stitched panoramic images of examples of the 1-15 N scratch tests. Comparing the images of obtained scratch tracks with previous scratch tracks at 5-30 N it is seen that the delamination of samples deposited at 3 vol. % of methane improved in terms of its scale, since any diamond delamination is localised within the scratch area. The sample deposited at 5 vol. % of methane, on the other hand, showed a large amount of diamond delamination far outreaching the area of contact between the sample and WC ball. Derived arithmetic mean value of critical load for samples deposited at 3 vol. % of methane was 3.3 N. The minimal and maximal values of adhesion failure being 1.8 N and 4.7 N. In the case of the sample deposited at 5 vol. % of methane, only one non-zero value of critical loads was possible to obtain from the total of four scratches, which was 1.9 N.

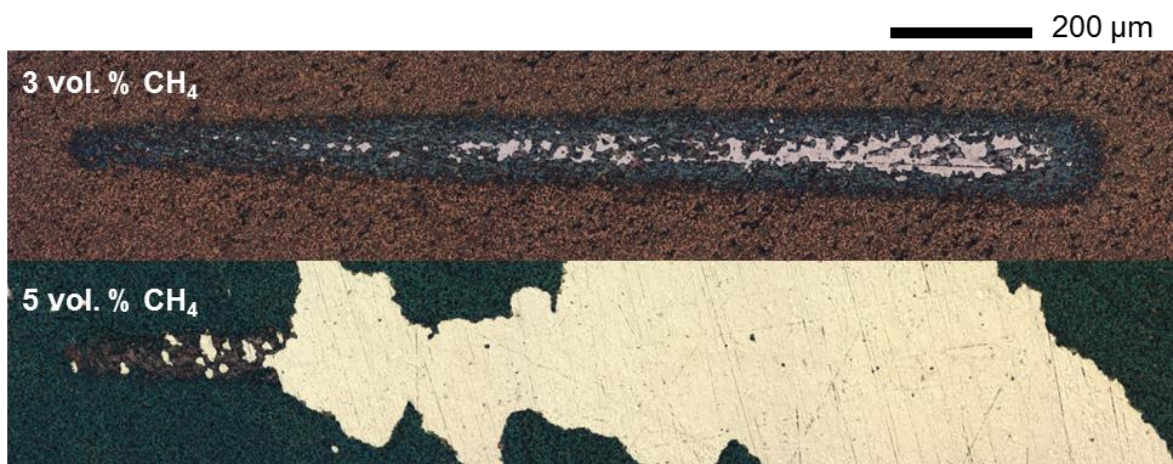


**Figure 3.42 1-15 N scratch tracks of diamond film on MoW-2 coated M42 steel.**

The mode of failure for all preformed scratches was buckling spallation. The mode of failure is not recognisable from the used images of scratch tracks since the delaminated diamond film was taken off the sample's surface in order to be able to identify the points corresponding to the values critical loads. The smearing of the WC ball over the scratch track was observed upon examination of indenter's surface.

The average thickness of the grown diamond film deposited under 15 Torr and 3 vol. % of methane was 246 nm with accuracy of  $\pm 23$  nm. The estimated growth rate being  $\approx 60$  nm/h. The diamond film deposited under 15 Torr and 5 vol. % of methane for longer CVD deposition time was of average thickness of 504 nm with accuracy of  $\pm 39$  nm. The estimated growth rate being  $\approx 80$  nm/h. The RMS surface roughness of deposited diamond films was 66 nm and 74 nm for diamond films deposited at 3 and 5 vol. % of methane over  $30 \times 30 \mu\text{m}$  scanning areas, respectively.

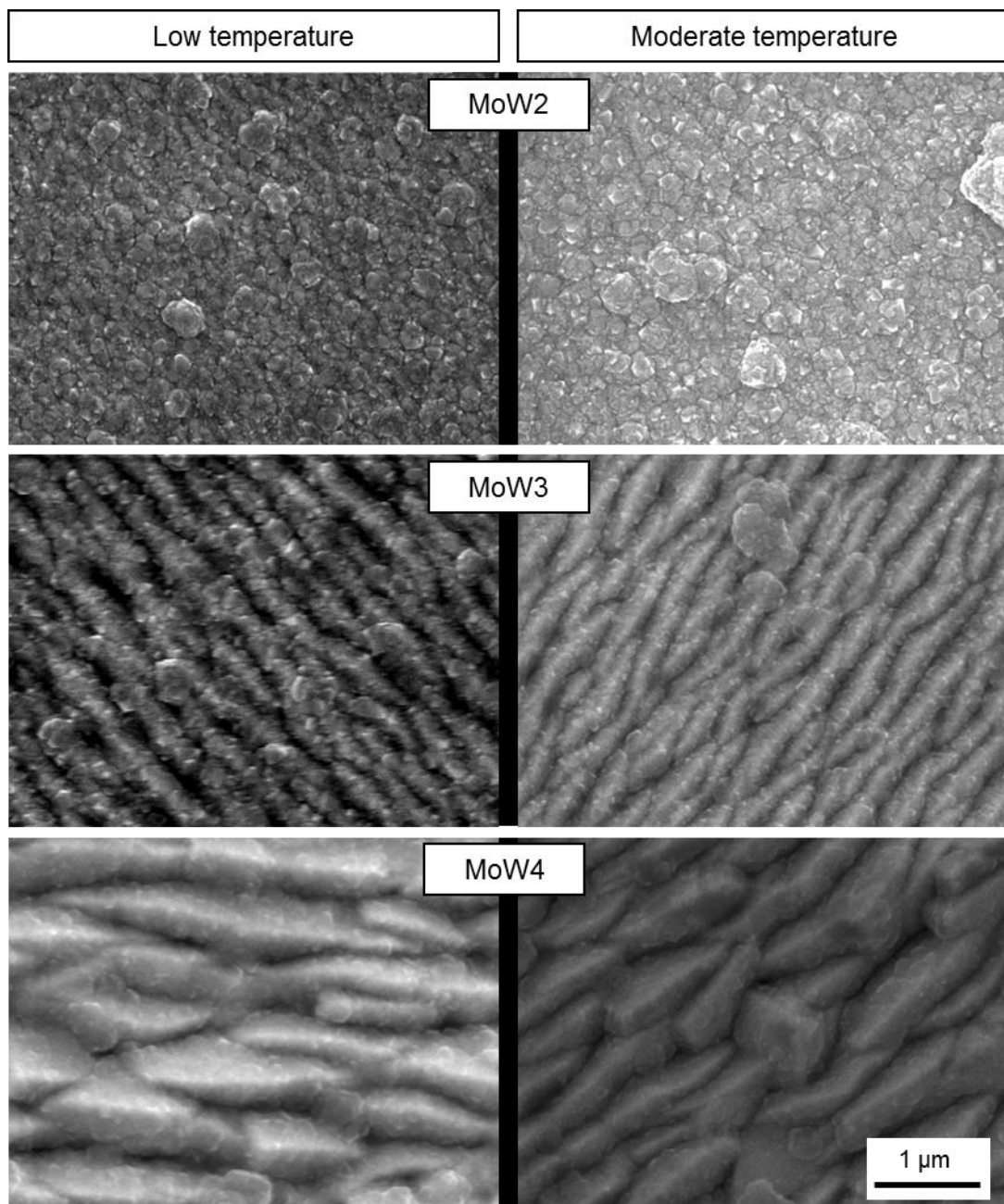
#### **3.4.4 Diamond deposition on MoW-2,3,4 interlayers**

Figure 3.43 shows a comparison of SEM images of diamond coated MoW-2,3,4 substrates. It can be seen that the structure of deposited diamond films at low and moderate diamond deposition temperatures was very similar, if one compared the MoW films with corresponding thickness. The thin layer of formed diamond coating was found to copy the substrate surface features of MoW interlayer which were very pronounced in case of both diamond films deposited on MoW-3 and MoW-4 coated steel substrates.

Comparison of the values of diamond film thickness, substrate roughness and sample hardness can be seen in Figure 3.37. The average of measured thickness of diamond films was in the region of  $\approx 250$  nm for all the investigated samples. In the case of MoW-4 coated at low temperature it was not possible to find a suitable area for the thickness measurements on the sample's surface, even after mechanical testing such as Rockwell C indentation. Surface roughness was found, as expected, to increase in respect to the MoW coated steel samples prior to diamond deposition (which can be found in Table 3.14, page 120). Comparing the values of surface roughness for low and moderate diamond CVD deposition the samples deposited at low CVD temperatures show slightly lower values of average RMS roughness. The values of Rockwell C sample hardness stayed within the previously found regions for both the low and the moderate CVD deposition conditions.

**Table 3.20 Comparison of surface thickness, surface roughness and Rockwell C hardness of diamond deposited at low and moderate temperatures on MoW-2,3,4 coated steel substrates.**

Sample	Thickness		RMS roughness		HRC hardness	
	Low T	Mod. T	Low T	Mod. T	Low T	Mod. T
	[nm]	[nm]	[nm]	[nm]	[-]	[-]
MoW-2	246	245	63	66	63.5	60
MoW-3	237	251	68	97	63	60
MoW-4	NA	243	81	106	64	59



**Figure 3.43 SEM comparison of diamond films deposited under low and moderate CVD deposition conditions on MoW-2,3,4 coated steel substrates.**

The indentation testing method was selected to assess the adhesion quality of deposited diamond films. The resulting indented areas are shown on SEM images in Figure 3.44 and Figure 3.45 for results of 10-200 N indentation using the Rockwell type of indenter and WC ball. The SEM images of indents were taken using a combination of secondary and back scattered electron imaging to provide the most informative images.

In case of indentation using Rockwell indenter, the diamond films deposited at moderate CVD deposition conditions were similar to each other in terms of size of the area of spallation of diamond film. The most notable difference in this case was the size of the actual diamond chips, which was smaller with an increase in MoW thickness. Rockwell indentation results on diamond coated samples under low temperature CVD conditions showed a different trend, where a decrease in spallation area with increasing thickness of MoW is clearly observable. Also, comparing the delamination area in respect of the change in temperature it is seen that the low temperature CVD deposited diamond films spalled significantly less than the ones deposited at moderate temperature.

Indentation results when the WC ball was used showed no diamond spallation outside of the indents. Indents in diamond films deposited at moderate CVD deposition conditions displayed an increase of diamond delamination within the indent area with an increase of the MoW interlayer thickness. The indents in diamond films deposited under low temperature CVD deposition conditions on MoW-2 and MoW-3 were looking similar to each other with the delaminated area of diamond film being the entire area within the indent, while the diamond film deposited on MoW-4 showed improved adhesion of the diamond film and only a small number of delamination signs was observable within the indent's region. Comparing the results in respect to the different CVD depositions it was seen that there is an improvement in diamond adhesion towards the substrate in case of MoW-2 and MoW-3 samples when CVD deposition temperature increased. Contradicting the trend are results for MoW-4 samples, where the diamond adhesion towards the steel surface improved with lowering the CVD deposition temperature.

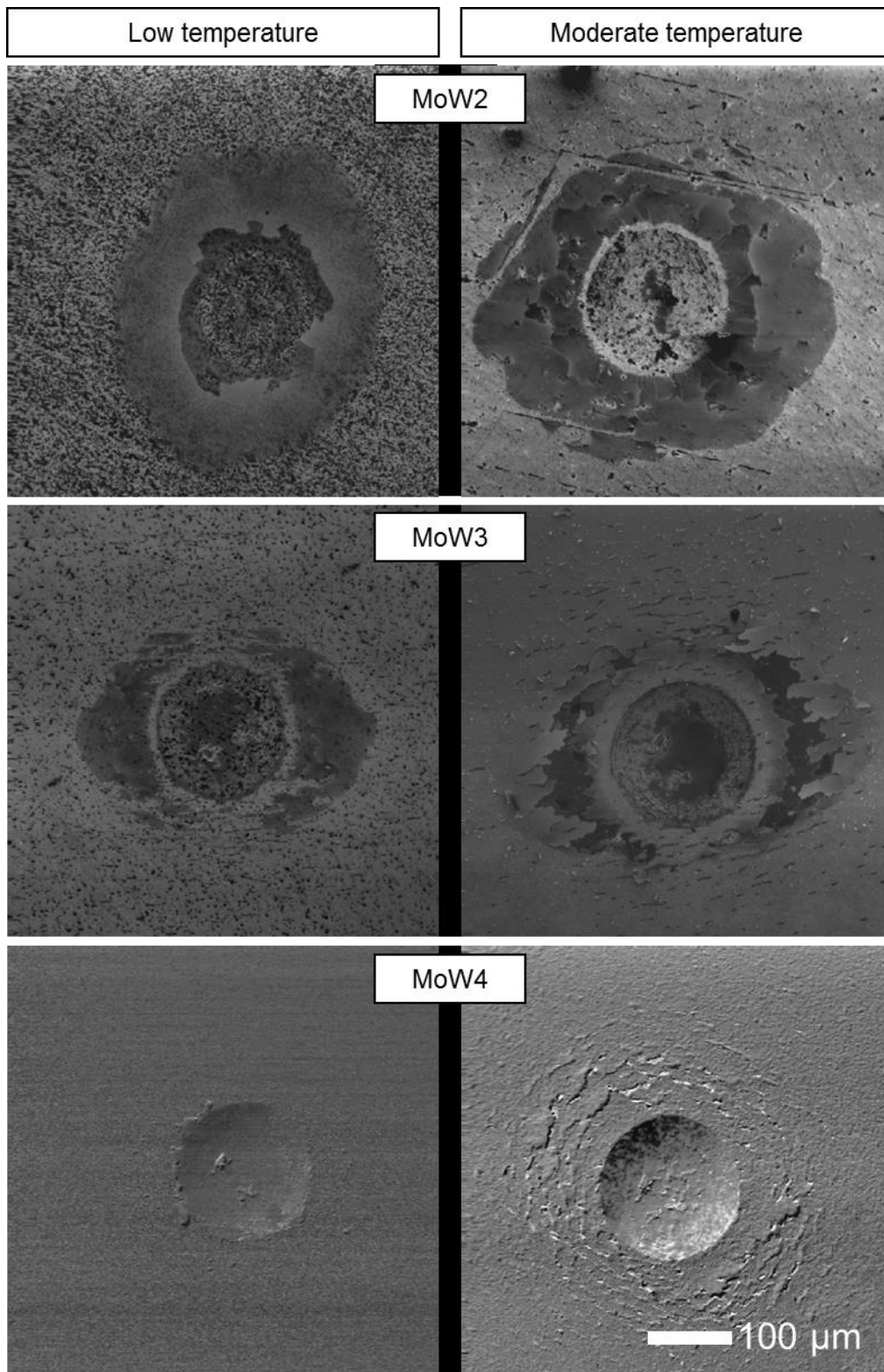


**Figure 3.44 SEM images of 10-200 N indentation test with Rockwell type indenter; diamond films were deposited under low and moderate CVD deposition conditions on MoW-2,3,4 coated steel substrates.**

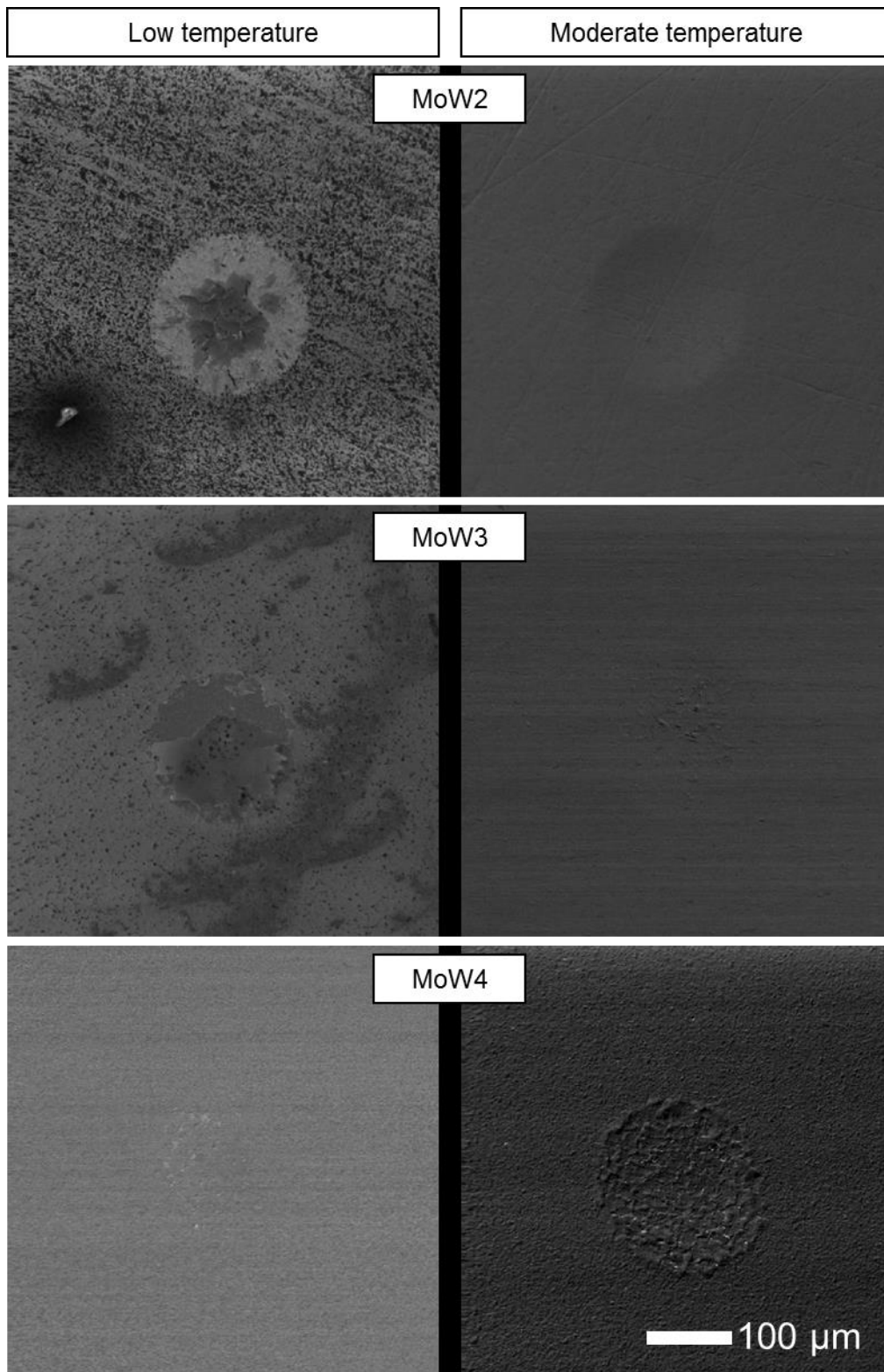


**Figure 3.45 SEM images of 10-200 N indentation test with WC ball 1/16'' ( $\approx 1.6$  mm); diamond films were deposited under low and moderate CVD deposition conditions on MoW-2,3,4 coated steel substrates.**

Raman spectra of diamond coated samples are displayed in Figure 3.46. There are two spectra for every diamond coated sample, adherent diamond (black colour) and delaminated diamond (red colour). The only exception being the MoW-4 diamond coated sample at low CVD deposition temperature, where no delaminated diamond Raman spectrum was possible to obtain for the lack of diamond's delamination. Presented spectra showed the peaks typical for nanocrystalline diamond films. All obtained Raman spectra had the diamond peak present, although they were not particularly pronounced due to the stronger intensity of  $sp^2$  D peak ( $\approx 1345\text{ cm}^{-1}$ ). The spectra also contains  $sp^2$  G peak ( $\approx 1600\text{ cm}^{-1}$ ) as well as the peaks assigned to transpolyacetylene ( $1100\text{-}1250\text{ cm}^{-1}$  and  $1450\text{-}1550\text{ cm}^{-1}$ ). On comparing Raman spectra of adherent and delaminated diamond films, it can be seen that the intensity of diamond peak increases in respect to the intensity of G peak for all compared samples.

Table 3.21 shows diamond peak positions for each obtained spectrum together with the calculated stress levels in adherent diamond films according to the equation (17) on page 53. The diamond peak positions, in the case of adherent diamond films, shifted to the higher wavelengths which is a result of stress development within the diamond film. After delamination the diamond peak positions shift to lower wavelengths. The observed shift into lower wavelengths was into a region below the wavelength of unstressed diamond peak ( $\approx 1332\text{ cm}^{-1}$ ) for all samples. The delaminated, or partially adhered, diamond films were therefore under tensile stresses.

A positive trend towards lowering the compressive stress levels can be seen when one compares the positions of diamond peaks on adherent diamond films. Both lower diamond CVD deposition temperature as well as a thicker MoW layer, contributed to the decrease in the calculated stress values.

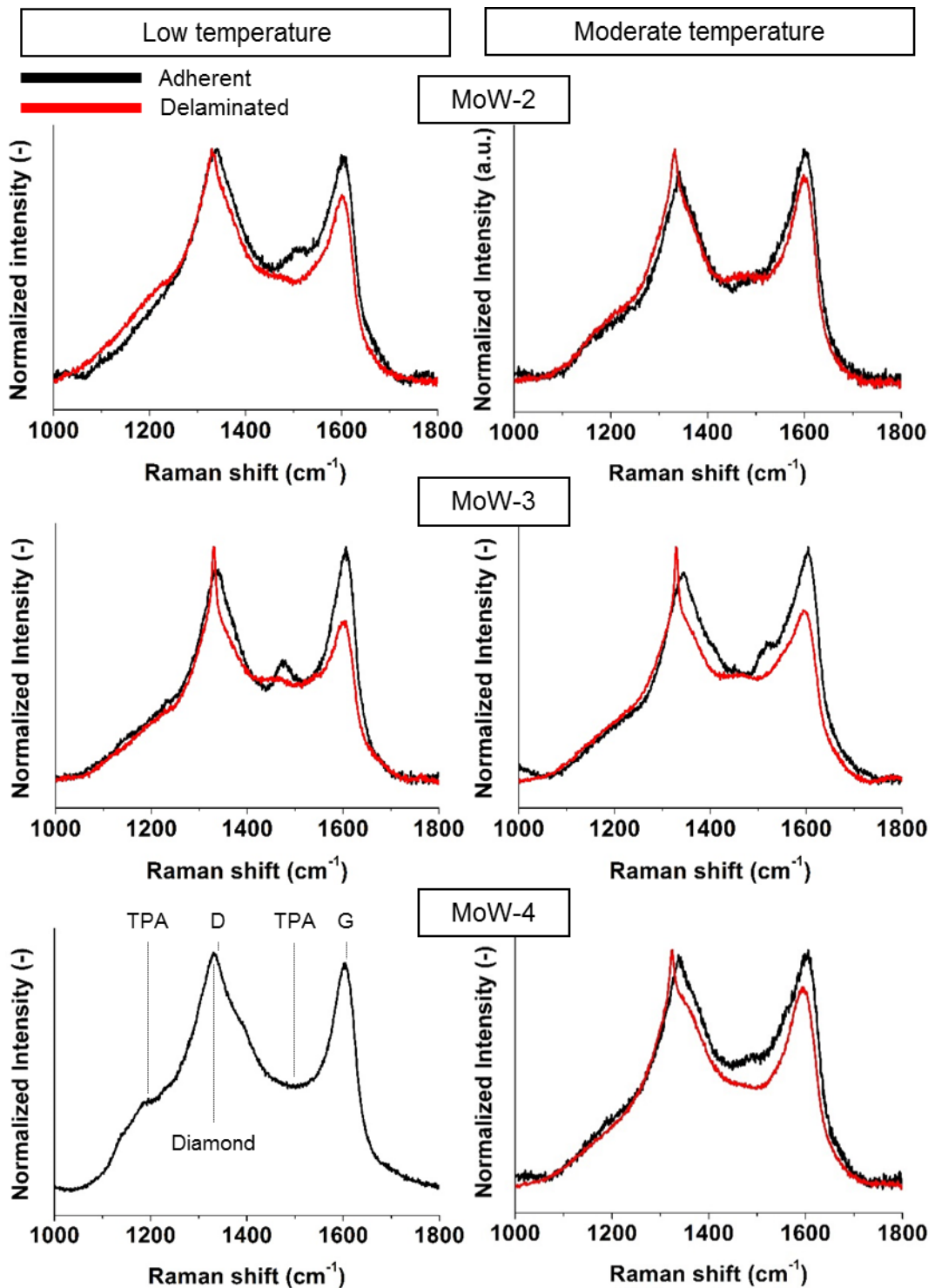


**Figure 3.46** Raman spectra of adherent and delaminated diamond films deposited under low and moderate diamond CVD deposition conditions on MoW-2,3,4 coated steel substrates; identified peaks in are highlighted in the image of Raman spectrum for diamond film deposited on MoW-4 at low temperature (bottom left image), where the Raman peaks which are present in every image are identified as diamond, D and G  $sp^2$  carbon and tow transpolyacetylene (TPA) peaks.

The results of 10-200 N indentation test using Rockwell indenter also corresponds well with the results from Rockwell C indentation, which can be seen in Figure 3.47. The Rockwell C indentation test on MoW-4 sample coated at low CVD temperature was of particular interest,

since it did not show any expected diamond spallation. Its Rockwell C indents were further studied by SEM and an example can be seen in Figure 3.48. One can see the edge of the area of Rockwell indentation with no visible diamond delamination.

**Table 3.21 Summary of diamond peak positions derived from Raman spectra of diamond films deposited under low and moderate CVD deposition conditions on MoW-2,3,4 coated steel substrates.**

Substrate	Deposition temperature	Adherent diamond	Delaminated diamond	Stress in diamond film
	[°C]	[cm <sup>-1</sup> ]	[cm <sup>-1</sup> ]	[GPa]
MoW-2	785	1341.1	1331.4	-5.2
MoW-3	785	1340.0	1328.6	-4.5
MoW-4	785	1337.5	1324.5	-3.1
MoW-2	650	1336.2	1329.4	-2.4
MoW-3	650	1335.5	1330.5	-2.0
MoW-4	650	1334.9	NA	-1.6

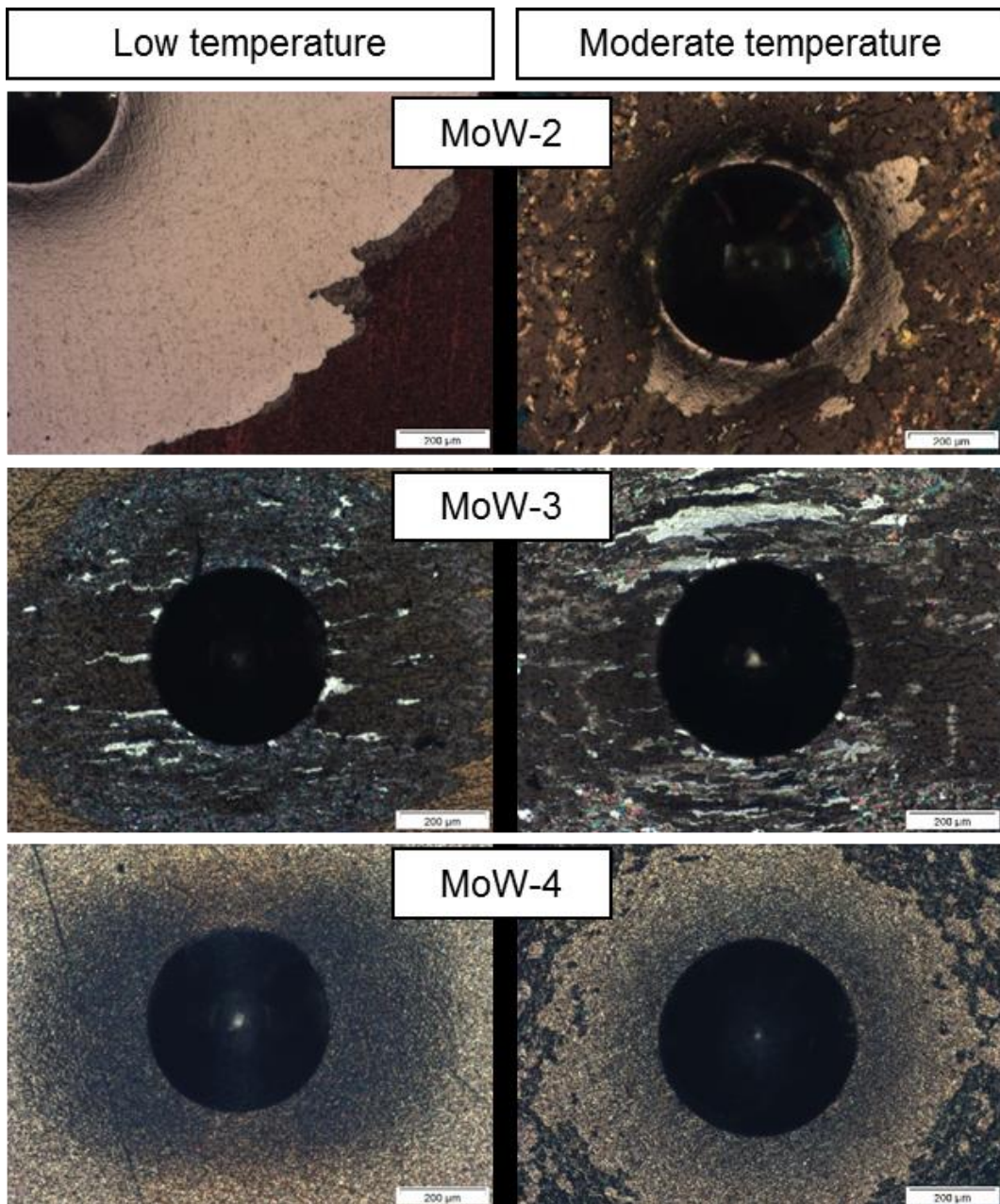


**Figure 3.47 Comparison of Rockwell C indents on samples after low and moderate temperature diamond CVD deposition on MoW-2,3,4 coated steel substrates.**

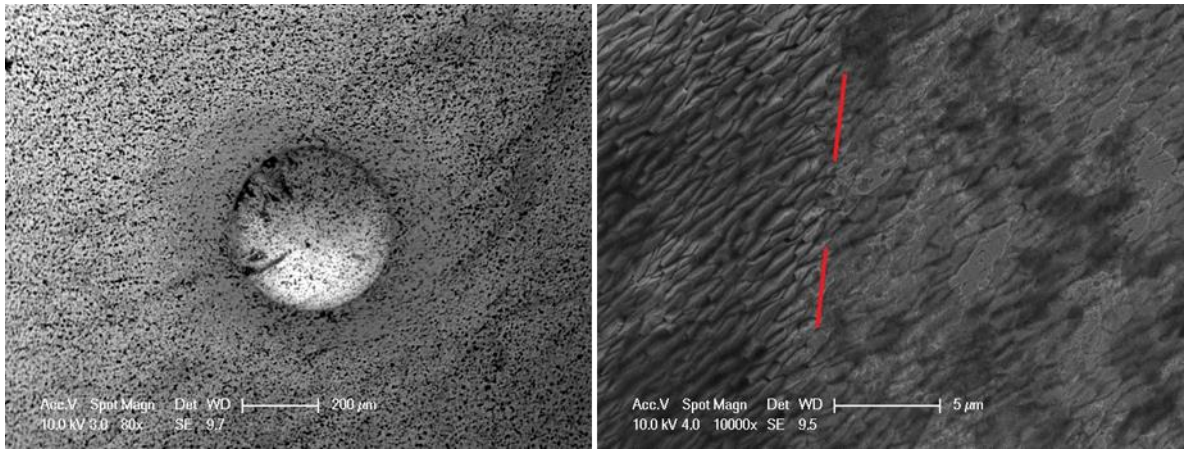


**Figure 3.48 SEM images of Rockwell C indent of low temperature CVD deposited diamond film on MoW-4 coated steel substrate.**

After establishing the good adhesion of the low CVD temperature of diamond coated MoW-4 steel sample, the sample was tested by 5-30 N scratch with the same testing conditions as were previously used (WC ball 5 mm in diameter; loading rate 100 N/min, linear velocity 10 mm/min). Part of the scratch track can be seen in Figure 3.49, where one can see a magnified view of one of the localised buckling spallation failures of the deposited diamond film. It can be seen from the picture, that the delaminated film shows an identically looking structures to the surface features seen on deposited MoW-4 film (Figure 3.30, page 120).

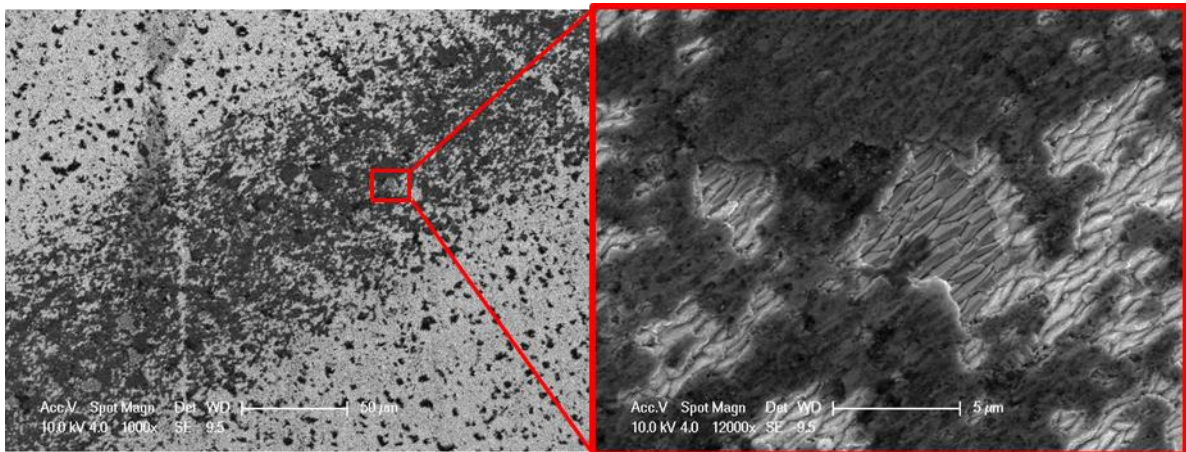


**Figure 3.49 SEM images of 5-30 N scratch test on low temperature CVD deposited diamond film on MoW-4 coated steel substrate; image on the right hand side is a magnified part of the scratch track.**

EDS analysis was performed on the delaminated and adherent part of the scratch track in order to verify the observation from SEM images. Figure 3.50 shows the SEM image of part of the scratch track with identified points of EDS analysis, whose results can be seen in Table 3.22. Points 1 and 2 are from the adherent part of diamond film where one can see a higher proportion of detected carbon, if compared with the points 3 and 4, which were

obtained from the diamond delaminated area. Co found in points 1 and 2 originates from the smeared WC ball, where it is used as a binder during the balls manufacturing process. Points 3 and 4 show large proportion of the investigated area being W and only  $\approx 4.5$  wt. % being carbon. The oxygen presence in points 1, 2 and 3 was most likely caused by an oxidation originating from the reactions with the air in the atmosphere. The larger amount of oxygen detected at the adherent diamond film is most likely due to the oxidation of the smeared WC ball. From those results it is possible to conclude that the delamination was caused by interfacial failure between the diamond film and tungsten, whose top surface has been partially carburised during the diamond's CVD deposition process. No values of critical adhesion strength was possible to obtain, since the localised adhesion failure was observed from the start of the scratch track. AFM diamond films thickness measurements have not been conclusive on the localised adhesion failures within the scratch tracks. The reason being uncertainty if the obtained data included part of smeared material from the WC ball.

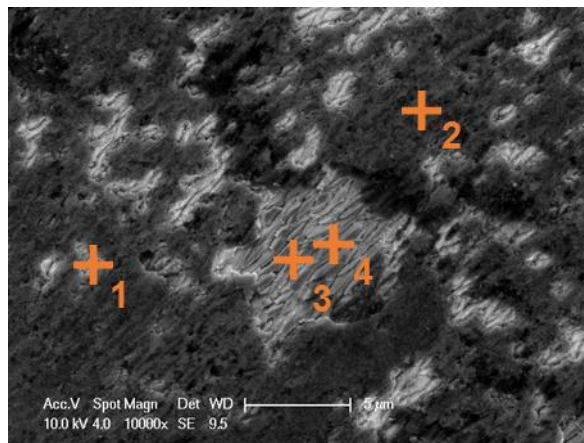


**Figure 3.50 SEM image of 5-30 N scratch on low temperature CVD deposited diamond film on MoW-4 coated steel substrate with identified points where EDS spectra was taken from.**

**Table 3.22 EDS analysis results of 5-30 N scratch on low temperature CVD deposited diamond film on MoW-4 coated steel substrate; points 1 and 2 are on adherent diamond film; points 3 and 4 are on delaminated part of the diamond coating.**

EDS points	Weight %			
	C	O	Co	W
Point 1	19.48	4.85	1.06	74.61
Point 2	24.76	3.08	0.59	71.57
Point 3	4.67	-	-	95.33
Point 4	4.26	0.71	-	95.03

## 4 Discussion

### 4.1 Diamond deposition using DLC buffer layer

Experimental results concerning the diamond film growth using DLC buffer layer are discussed all together in this part.

The technique of using a DLC buffer layer for diamond growth has a high appeal for possible large scale manufacturing, since it excludes any need for time consuming operations of mechanical seeding. The cleanliness of the coated parts would be ensured at the start of coating process due to the argon etching. The parts would then be coated with an adhesion promoting interlayer, DLC film and subsequently subjected to diamond growth possibly in one deposition system. A setup such as this would diminish the problems of immersing parts for diamond seeding, the subsequent drying and the overall number of needed operational steps where a contamination is possible to occur.

A thin layer of amorphous carbon film was observed to develop prior to diamond nuclei formation on substrates such as Cu, Mo and Si [37] and confirmed by TEM study of diamond nucleation mechanism by Singh et al [75]. Based on those observations it was logical to investigate whether diamond film growth can be enhanced by deposition on amorphous thin films. Several groups were investigating the amorphous carbon films for diamond film growth at the end of the twentieth century, when diamond film deposition on foreign substrates started to receive wide attention [61,70,71,73,189].

The results of the initial experiment of feasibility of diamond deposition using DLC as a buffer layer provided a sample with fully diamond covered substrate. The diamond film was of considerable thickness while the diamond deposition times were only five hours. Such results were highly encouraging if compared to reported results of [71,72], where the total diamond CVD deposition times used to obtain coalescent diamond film were in the region of one day.

The attempts to reproduce the results of 67391 run were unsuccessful. Two significant contributions played an important role in this outcome. Firstly it was found that the deposition conditions for the DLC layer were unstable. Arcing is a long standing problem of deposition techniques where magnetron sputtering is part of the process [190]. The recorded instability of chamber pressure on the other hand, is an unusual occurrence and reasons for it have not been exactly identified. Effects such as contamination of the pressure detecting sensor, malfunctioning pressure regulating valve, vacuum pump, and/or electronic fault may be the reason. Secondly, repetition of the experiment was problematic because of the presence of uncoated parts of the sample where the samples were clamped on the coating rig. The uncoated area of each sample used for initial diamond growth

experiment as well as the run number 69063 was bare steel. The naked steel surface has a detrimental effect on diamond formation [191], as it acts as a carbon sink, which promotes formation of non-diamond carbon structures and also can influence diamond growth in the surrounding areas. The focus of this study then shifted into understanding the effect of the DLC thickness and CVD deposition parameters on the resulting diamond film structure.

The diamond CVD deposition was divided into two stage deposition as promoted in the literature [72]. Feng et al [70] demonstrated the benefits of such a method, where diamond deposition is divided into two specifically oriented stages – nucleation promoting stage and growth promoting stage. In the first stage higher methane ratios and lower plasma intensity are used in order to promote formation of diamond nuclei together with various other non-diamond carbon species. The plasma intensity had to be low in order to suppress the effect of atomic hydrogen etching which would etch the non-diamond species, but could also destroy the diamond nuclei while they were not yet of a critical size. Yang et al [61] studied thicker DLC interlayers of up to 0.4  $\mu\text{m}$  and found out that with an increase of DLC thickness it is important to suppress the hydrogen etching efficiency. Their results and observations did match the examined Dymon-iC coated steel samples which were subject to diamond growth in this study, where presence of strong hydrogen etching has been identified. They observed similar formations of carbon islands with diamond crystals growing on top of those islands. Low temperature plasma pre-treatment was one of the options which significantly enhanced the diamond nucleation densities.

With the start of the new millennia, the focus somewhat shifted from DLC buffer layer as well as substrate biasing onto substrate ultrasonication in diamond suspensions [16]. The benefits of this form of pre-treatment will be addressed in the following section. Relatively recent report of Nibennanoune et al [74] brought the topic of using thin DLC layer in combination with diamond ultrasonic seeding on titanium alloy to lower the post-deposition stresses within the diamond film. Their argument for the stress reduction was in the thin DLC layer (50 nm) being able to soften the effect of thermal expansion mismatch. The reported stress reduction is in accordance with study of Endler et al [189], who demonstrated that diamond films grown on DLC buffer layer displayed poor adhesion characteristics. This observation is in accordance with the observed island formation during the diamond growth in this study. Diamond particles are formed on and within the amorphous carbon layer. The bonding process between substrate and diamond is possible only after the carbon layer which separates the two, diminishes. However, the strength of the bonding decreases because of the shortened time for the creation of well adherent interface.

Based on the observed results it was understood that more knowledge of separate diamond growth issues is needed before any future diamond growth using DLC interlayer is repeated. Separate investigations of optimised diamond deposition conditions with the possibility of controlled temperature, access to equipment capable of determination of  $sp^2/sp^3$  ration within DLC coatings and stress development within the diamond films influenced by steel substrate, were identified as the key points of successful diamond growth from DLC buffer layer.

## **4.2 Diamond deposition of CrW interlayer**

### **4.2.1 Magnetron sputtering of CrW interlayer**

Good adhesion of the magnetron sputtered film is critical to the subsequent diamond growth step. Direct sputtering of W on a steel surface resulted in very poor adhesion of the deposited film as was seen from the Rockwell C indents (Figure 3.14 on page 99), where a large amount of spallation was observed. It was concluded that such poor adhesion characteristics were due to the formation of Fe-W intermetallics at the steel-tungsten interface [192]. The formed intermetallics then facilitate the detachment of deposited W film when put under a mechanical stress. Therefore a new multi-structured film of CrW was designed and used as an alternative to the pure W film. The Rockwell C indentation test of CrW coated steel also resulted in a delaminated area around the indent, but at a significantly lower magnitude, since the delamination region extended only to the region where the material transfer creates the raised edges around the indent, which induces large stresses on the coating in that area.

From the obtained data it was not possible to conclude if the adhesion failure was due to the interfacial adhesion problem or a cohesion problem within the sputtered CrW film. Cr bonds with steel readily and is commonly used as a base layer in multistuctured coatings to ensure a good adhesion[193,194]. It was therefore unexpected to conclude that the adhesion failure was indeed at the steel/CrW interface. The XPS results were dominated by a large amount of oxygen and carbon which are commonly found on surfaces which are exposed to the atmosphere. More important were the results of detection of Fe on both substrate as well as the tape. Supporting results also showed that a significant amount of Cr was detected on the tape side, while none was found on the substrate side (even though that the chemical composition of M42 contains Cr, as can be seen in Table 2.2 on page 72. Similarly Mo has been found on the substrate and not on the tape side.

The reasons for the unusually premature delamination of CrW film from the steel surface were not fully understood, but the interfacial delamination suggest a contamination of the

interface which then lead to the failure of the adhesion of the coating. Nevertheless, the coating was deemed stable enough for further diamond CVD growth, since its delamination occurred only under relatively tough testing conditions.

#### **4.2.2 Nanocrystalline diamond seeding experiment**

The seeding approach using dip-in method was a variation on published works of Liu et al [52] and Makita et al [40]. Interestingly the author did not find any reports in the literature of the problems experienced with drying samples after the agitation seeding step. The diamond powder which forms maps on the surface was later found to be causing problems of uneven stress distribution through the diamond grown films on steel substrate causing delamination, where the build-up of diamond powder during the drying process occurred. Although, the nanocrystalline diamond used for nanodiamond seeding was of average size of 5 nm, it forms aggregates of circa 150 nm in diameter [45]. Ultrasonication of the diamond powders alone cannot disperse the aggregates and laborious methods such as wet milling [47] has to be used for one to get a monodispersed detonated nanodiamonds. The stability of dispersed nanodiamonds in water, when 0.2 wt. % of nanodiamond powder was used, was remarkably long. In one week the suspension holds the same colour, although there was a small sedimentation of nanodiamond powder at the bottom of the container.

The nanodiamond dip-in seeding method provided a good precursor to obtain a full diamond coverage over the substrates surface. As shown in section 3.2.2, starting on page 101, the diamond films grown using the dip-in seeding method were comparable with the nanodiamond agitation method in terms of the substrate's roughness (which is directly related to the number of diamond nuclei present on the substrate surface when thin diamond films are being grown) and the diamond's purity, which was typical for similarly grown diamond films [195].

#### **4.2.3 Diamond deposition on CrW interlayer**

Data obtained by Raman spectroscopy revealed a presence of diamond on all investigated samples with the exception of CrW11, which were not conclusive due to the high intensity of  $sp^2$  related D peak. CrW11 sample was still considered to have a strong diamond presence on the substrate surface after examination by SEM. It can be seen in Figure 3.18 on page 106, that the surface of CrW11 is covered in diamond particles which are in the form of semi ball-like shaped and facet shaped diamond particles which are in the process of coalescing to form a diamond film. Two hours of deposition revealed the possibility of full coalescent diamond films being obtained in the selected investigation range of diamond

deposition conditions. The most pronounced diamond peak was detected on sample CrW13 which showed, as the only sample, a total post-deposition delamination of diamond film. It was therefore not possible to take the Raman spectra of any adherent part of the film which resulted in not observing any large shift of diamond peak wavelength as compared with the other measured diamond peak position for the rest of the diamond coated samples. This can be explained by the state of the film and the penetration depth of Raman laser beam. Diamond has the widest optical transparency region from known solids [196] and therefore enables Raman laser beam to penetrate the diamond film to a relatively high depths [197]. In case of thin diamond films it means that Raman spectra should be rich on information of the base substrate as well as giving information about the diamond thin film. Since in this case the substrate was W and as a metal is not Raman active [161] there was no triggered response from it. At the same time the Raman signal was strong at the diamond/substrate interface where a larger amount of non-diamond carbon is expected to reside when compared to the diamond film itself (in the case of crystalline diamond films grown without significant re-nucleation) due to the nature of crystalline diamond growth [198]. Delaminated diamond film will then provide less signal from the species in the diamond/substrate region and therefore the intensity of diamond peak will increase with respect to the intensity of non-diamond carbon.

Results obtained from investigations of selected responses from factorial design (Table 3.7 and Figure 3.20) show that all the investigated factors are dependent on each other in the selected region of investigation. This result makes the improvement of the diamond deposition conditions to be based simply on changing one of the factors unattainable. The observations of the plasma ball behaviour (change of size, position) during CVD deposition made during this work, as well as reported by others [6,38,77,78] support the results of factor dependency. Namely that each chosen factor (microwave power, chamber pressure, gas ratio) effects the deposition process through interaction with the other selected parameters. The plasma ball changes its size, colour and position within the chamber depending on the combination of deposition parameters. Most importantly, all of the three studied factors are linked to the deposition temperature on the substrate surface as well as in the plasma itself. CVD deposition is a temperature driven process and therefore a small change to the reported responses will change the diamond deposition chemistry. Despite the respective factors being dependant the effect of pressure has the most pronounced effect of the quality and characteristics of obtained diamond films. Its increase led to higher crystallinity and more delamination of the diamond films in three cases out of four. Buchkremer-Hermanns et al [78] also identified the pressure to be the main influencing parameter through the use of orthogonal experimental design. Diamond CVD deposition

conditions providing the coalescent diamond film in two hours of CVD deposition were found during the follow up investigation after the factorial design of experiments.

The problems of different types of failure of CrW coating cause delays in the experimental work. Reasons of the CrW failure were already discussed in the previous section. The weak point of the reported results in this work as well as in the literature [77,78] is the fact that surface deposition temperature has been omitted from the requirements. One will therefore identify good deposition parameters for diamond deposition with limitations to the combination of chosen values and will not take into account any possible detrimental effects caused by temperature on the whole sample structure, as was seen in the case of diamond delamination from the sample surface due to the large thermal expansion coefficient mismatch of the two materials (steel and diamond). The problems of thermal expansion are addressed in later parts of the discussion in this work. Applicability of selected diamond deposition conditions on temperature sensitive materials is not certain due to the fact that the substrate deposition temperature is unknown. Therefore, an accurate temperature measurement was the next focus in this work.

### **4.3 Diamond CVD deposition temperature calibration**

The decision of mounting the thermocouple at the back of the holder was based on the need of protecting the naked thermocouple wires from the active plasma atmosphere. Otherwise, the thermocouple wire would get affected by the deposition and diffusion of carbon which would affect the subsequent temperature readings. Based on this decision a series of temperature diffusion experiments had to be performed in order to gain accurate temperature readings.

The heat transfer between the sample surface and the thermocouple at the back of the substrates' consists of two modes of heat transfer – conduction (transport of heat through the solid materials) and convection (transport of heat through the gas in the atmosphere). Both types of heat transfer greatly influenced the obtained temperature data of temperature diffusion displayed in Figure 3.26 and Figure 3.27 on a page 116. As can be seen from those figures the role of pressure and gas composition is profound and greatly influences the temperature reading at the back of the substrate holder. The proportion of heat transferred by conduction to the thermocouple is unaffected by the gas presence and therefore will be the same in case of all the investigated gasses. The amount of heat which is transferred through convection is influenced by the chamber pressure, the gas type present in the chamber, as well as the amount of heat generated. Hydrogen has the highest thermal conductivity of the three gases [199] and therefore it has the most pronounced rate of rise in detected temperature at the back of the substrate holder. The fitted logarithmic

curves for the three gases describe clearly how the increase of pressure (populating the chamber with gas atoms) makes the temperature reading very much dependant on the convection type of heat transfer. The most pronounced effect takes place in the region up to  $\approx 30$  Torr; in the case of this work, where a small increase of pressure makes pronounced effects on the rate of rise of detected temperature at the back of the substrate holder.

Changing the temperature of the sample surface while maintaining the same levels of pressure, produces linear dependency of detected temperature values at the back of the substrates holder. This can be seen in the example of data for the shallow holder with hydrogen atmosphere (Figure 3.28, page 117) and in coefficients of determination for both types of substrate holders and all three gases (Table 3.12, page 118). There is a linear dependency between the temperature detected by the thermocouple with the temperature at the substrate holder for given pressure and corresponds with linear increase of thermal conductivity of gases and metals [199].

The overall accuracy of the thermocouple measurements were reported to have an inaccuracy of up to  $\pm 50$  °C as reported by Argon Labs [83]. The  $\pm 50$  °C is a reasonable margin of error for the thermocouple measurements and was adopted. The placement of a thin quartz glass sheet between the thermocouple and the sample, together with the temperature calculations being based on average readings from the experimental data, certainly caused some degree of inaccuracy in the temperature readings. Even though the thermocouples were shielded from direct contact with the plasma ball through being hidden at the back of the substrate holder, over time the carbon sooth was still being deposited on the thermocouple itself. The accuracy of the thermocouples was therefore periodically checked and a lifetime of 10-15 hours under CVD deposition conditions with carbon carrying gas present was established. Despite the issues with the use of thermocouples it is still a straightforward, practical and reasonably accurate solution for temperature readings under such challenging conditions.

## **4.4 Diamond Deposition on MoW interlayer**

### **4.4.1 Magnetron sputtering of MoW interlayers**

Rockwell C indents into the MoW coated substrates showed good adhesion properties for all three different MoW thicknesses and was therefore deemed suitable for further diamond deposition. Measured values of sample hardness were identical to the hardness values of bare M42 steel confirming that the substrate properties have not been affected by the magnetron sputtering process. Increased roughness with increasing film thickness is typical

for columnar growth due to the competition of different growing speeds in different crystallographic directions [26,200].

EDS and XRD results found no contamination of the top surface and near surface region, confirming the appropriately selected deposition conditions, where no co-sputtering and cross-contaminants within the chamber lead to deterioration of intended purity of MoW films. The use of Bragg-Brentano geometry in X-ray diffraction had the benefit of observing only the crystallographic planes parallel to the surface. It was therefore possible to identify the preferred growth direction of the tungsten sputtered layer being  $\langle 110 \rangle$ . This result corresponds well with the SEM observations. The increase of size of tungsten's crystallites as obtained from XRD data correlated with the thickness of MoW layer, which is in accordance with tungsten crystals becoming increasingly well-defined with less faults as they grow larger [201]. As investigated MoW coated steel samples were deemed to be capable of not influencing the CVD diamond deposition results.

#### **4.4.2 Diamond deposition on MoW-2 interlayer**

The identical look of diamond coating deposited on MoW-2 and CrW interlayer confirmed a good reproducibility of diamond CVD deposition conditions. The obtained diamond spectra of deposited diamond film with diamond peak centred at  $1332 \text{ cm}^{-1}$  shows that the diamond film was completely unstressed, which was untrue. The relatively high CVD deposition conditions together with the pronounced differences of CTEs of diamond and steel would inevitably result in compressive stress being present in the diamond film. Therefore the area where the Raman spectrum was taken from had to be a delaminated, or otherwise mechanically unstressed region. Further discussion about stress within diamond films is part of this work and can be found in section 4.4.4 on page 154. The actual average diamond peak position for MoW-2 coated diamond under such conditions is  $1341.1 \text{ cm}^{-1}$ , showing a great amount of compressive stress being accumulated during the post-deposition CVD cooling process.

The diameter of the WC ball used to perform the scratch tests was large enough not to be inducing mostly compressive stresses, rather than bending stresses, on the diamond film and so was suitable for adhesion evaluation [148]. The adhesion failure of diamond film was therefore confined to only the inside of the scratch trace with well adhering diamond film surrounding it. Lu et al [202] reported that critical load of diamond films on WC increases from 11.2 N for diamond films thickness of  $1.5 \mu\text{m}$  to 14.5 N for samples with thickness of  $4.5 \mu\text{m}$ . Endler et al [189] reported the critical load for diamond coatings on steel substrates was within the region of 6-22 N for diamond films with thickness of 3-5  $\mu\text{m}$ . Whilst the deposited diamond samples in this study ( $\approx 240 \text{ nm}$  thickness) using Mo-W interlayers are

much thinner than others reported, they show a similar level of critical loads of 11.4 N on average. It is difficult to make a quantitative comparison among samples measured at different evaluation conditions from different research groups [203]. This is because the surface and interface of samples is of as high importance as a precise description of testing conditions [204]. Qualitative comparison of our films with reported values can confirm similar level of adhesion properties and reflects the positive contribution of the Mo-W interlayer.

The SEM and EDS analysis of scratch tracks identified the region of adhesion failure to be at the MoW-2/diamond interface. Elements present in the delaminated regions were W and C, presumably forming a  $W_xC$  during the diamond CVD deposition. Elements detected on adherent diamond coating were W, C, Co and O. The presence of Co confirmed that the smearing of the WC ball during the scratch tests resulted in a well adhering connection between the indenter and the diamond coated sample. Detected oxygen was ascribed to the oxidation of the WC ball indenter which was transferred onto the diamond film.

The EDS cross-sectional analysis showed that no steel elements and CVD deposited carbon cross-diffusion was detected, which confirmed the expected properties of the developed coating. It is worth mentioning that the EDS spectra obtained doesn't possess as high a spatial resolution as would be desirable [205]. It is therefore reasonable to assume that the distribution contour plots between the elements are even sharper than the obtained EDS line scan profile. The effectiveness of Mo-W interlayer as a diffusion barrier can also be indirectly assessed through changes in a sample's hardness. Overlong exposure to elevated temperature during CVD diamond growth will lead to the hardening of the steel substrates due to atomic hydrogen diffusion and carbide formation [63]. However, the Mo-W coated steel sample before and after diamond deposition shows a slight decrease in their respective hardness from 64 HRC to 61 HRC. Calculated penetration depth for Rockwell C [145] indent for value 61 HRC is 78  $\mu\text{m}$ , which is far beyond the thickness of the deposited diamond films (250 nm) and Mo-W interlayer (1.1  $\mu\text{m}$ ). In such case the hardness measurement reflects mostly the intrinsic properties of the steel substrates. Furthermore any involvement of hard, thin Mo-W and diamond film can only increase the measured HRC value due to the hardness of both coatings. It is likely that the softening of measured samples implies the effectiveness of Mo-W interlayers being a fully functional diffusion barrier preventing diffusion of plasma species such as atomic hydrogen and carbon into the steel.

The observed sample softening implies that the diamond CVD deposition conditions are not very well suited for steel samples since it is affecting the properties of the steel. A development of CVD deposition conditions at lower temperatures, which would not affect the steel substrate, should be considered for the next deposition of diamond on steel. Also

it was discussed that actually the deposited diamond films are under a considerable amount of compressive stress, which should be possible to lower or ideally diminish with a decrease in DVD deposition temperature.

#### **4.4.3 Investigation of low temperature diamond CVD deposition**

The deposited diamond films under the selected CVD conditions showed a variety of resulting diamond structures being formed. Low methane concentration results in small number of carbon radicals being available to form diamond crystals [45]. This led to the observed non-coalescent diamond films in the experimental conditions, where 1 vol. % of methane was used, which improved with an increased concentration of methane in the deposition chamber. Methane concentration was identified to be the principal influence on the diamond growth rate which agrees with [78]. A higher number of methane radicals also lead to lower crystalline quality which was observed for samples deposited with the highest methane concentration. Increase of chamber pressure increased the diamond growth rates due to the plasma species being active at closer distance to the substrate as was observed by [206]. Higher activity of atomic hydrogen near the substrate due to increase in chamber pressure is also connected with increased crystallinity of as grown diamond [206]. Such tendency was not observed during this investigation. The most likely cause is the relatively low and narrow region of selected pressure values, which in combination with a decrease of microwave power, led to similar etching activity of the atomic hydrogen.

The author's mistake in the diamond CVD deposition time difference did not have a high impact on the results of the investigation due to the observation of adherent diamond film at pressure of 15 Torr and 5 vol. % methane concentration. As seen from the results, increase in methane concentration to 5 vol. % led to observed delamination of the coatings deposited at both 12 and 20 Torr. Therefore, it was reasonable to assume that coating deposited at 15 Torr and 3 vol. % of methane also should not delaminate. The unusual results of better adherent diamond films deposited at 15 Torr is deemed to be connected with the specific combination of microwave power and chamber pressure, although no definitive reason was made and no suggestions were found in the literature.

The resulting sample hardness tests using Rockwell C indentation confirmed the intended low impact of CVD deposition on the substrate properties. Half of the sample hardness values after the diamond CVD deposition were within the inaccuracy region of Rockwell C indentation technique, while the hardness values of the other half of samples were just below the inaccuracy region. The thermocouple technique was therefore considered a reliable means of temperature measurement.

The two selected condition of low temperature diamond CVD deposited were further investigated. SEM topography images showed that diamond structure using 5 vol. % of methane during the CVD deposition results in semi-crystalline diamond films. The cause being low atomic hydrogen activity leading to less hydrogen etching and less defined diamond structure of the deposited film. Raman spectra showed that the amount of compressive stress decreased when compared to the results previously discussed in the case of diamond deposition at moderate CVD temperatures. Nevertheless, the contribution of thermal expansion mismatch between the diamond and the substrate resulted in the development of compressive stresses within the diamond films.

Both of the tested samples for adhesion showed very poor characteristics. The adhesion results of 5-30 N scratch test for samples grown at 3 vol. % of methane were directly comparable to the results of MoW-2 coated sample at moderate temperatures. Both of the films were of similar thickness and both have been deposited under 3 vol. % of methane, had very similar values of surface roughness and also their respective surface SEM images showed high similarity of the deposited diamond grains in terms of their size and overall orientation. It was clearly observed that the adhesion strength of diamond films towards the substrates dropped drastically when a lower CVD deposition temperature was used. The interfacial adhesion strength of diamond films is dependent on several factors: carbide interlayer formation, mechanical embedding of diamond particles into the substrate's surface and contamination of interface with non-diamond species and the type and amount of stress the system is under. Reports of poor adhesion when carbon amorphous layer is formed at the interface are well known [191]. Buijnster et al [49] observed a decrease in critical adhesion strength with the increase of methane concentration. Expanding on this observation, one can conclude that when more non-diamond species are present at the diamond/substrate interface the less adhesive strength will the diamond film possess. Therefore, with an increase of methane concentration, a decrease in deposition temperature and the decrease in atomic hydrogen activity will all lead to decrease of the adhesion strength of the obtained diamond film. The possibly suitable diamond seeding method which would mechanically embed the diamond particles into the substrate surface, as is mechanical scratching with diamond pastes, or substrate agitation by micron sized diamond particles [41], but one has to be aware of possible surface damage. Biasing the substrate to enhance the interfacial adhesion strength is also an option, although there is a problem with reproducibility [58,59] Ultrasonic agitation of samples in solvents with micron sized diamond particles showed a certain degree of diamond embedding [16] and might be a promising seeding treatment, or possibly a combination of nanodiamond and micron sized diamond can improve the adhesion strength even further. Also, the ASTeX AX5010 CVD setup used at Aston University has its limitations through being relatively old technology

and due to its design the diamond CVD deposition conditions are already at the edge of its capabilities. Changing the deposition setup into one more suited to low temperature deposition with the ability of maintaining higher atomic hydrogen activity at even lower deposition temperatures with a good diamond growth rates, such as [46,109], would be a possible solution to the adhesion problem.

It is worth mentioning the reasons for the scratch tests not starting from zero loads. The ST-3001 scratch test device used had certain limitations in respect to initial loads. The inaccuracy of the applied initial load was in the region of  $\pm 0.5$  N. Such fluctuation were of little significance for initial loads from 5 N onwards, but in the case of zero, or very low initial loads it could cause an unintended variation to the testing procedure which could possibly have an effect on interpretation of the data. In this study the calculation of critical values of adhesion was adjusted for individual inaccuracy of initial load from the data log for each test.

#### **4.4.4 Diamond deposition on MoW-2,3,4 interlayers**

The no available means of clear measurements of the thickness of diamond film deposited under low CVD temperatures on MoW-4 prevented competition of the thickness investigation. Nevertheless, it is reasonable to assume that the thickness of diamond films deposited on MoW-4 coated steel substrates at low temperatures falls in the same region of values as the rest of the five diamond coated films. The values of Rockwell C hardness further confirmed previous results of little or no influence of CVD deposition conditions on the properties of the steel substrates.

Comparing the SEM topography images of deposited diamond films showed a high level of similarity between the morphology of diamond films growth at lower and moderate CVD temperatures which was observed also on the values of roughness, where diamond films deposited at higher temperature showed only a small increase of average roughness values. The measured increase in surface roughness with increasing roughness of thicker MoW was expected, since the diamond thin films were copying the MoW surface features, as was observed in the SEM images.

The similar thickness of deposited diamond films enabled a direct comparison between the samples deposited at lower and higher deposition temperature in terms of the levels of stress and adhesion properties of the deposited diamond films. In general, the indentation results showed a difference in diamond film spallation around Rockwell indents while no spallation was detected outside the indents made by WC ball for the same indentation loads. Such difference was possible to observe due to the indenters' different geometries. The

displacement of material by Rockwell indenter (diamond cone with 120° angle and 200 µm rounded tip) was far greater than in case of WC ball and forced more substrate material outside of the indent creating atoll-like profile around the indent. This in turn put higher stresses onto the diamond film and led to greater diamond film spallation around the indent. The WC-Co ball indenter's larger spherical shape causes lower displacement of material outside of the indent, which leads to lower bending stresses around the indent [148].

The delamination area of diamond films grown at moderate CVD deposition temperature was the same for each of the Rockwell indents, while the actual size of delaminated chips of diamond got smaller with the increase in MoW roughness. Similarly, the delamination within the WC-Co indent region was more pronounced with increase in the roughness of MoW. In case of rougher surface the force applied by indenter is distributed onto smaller amount of asperities, which then experience larger amount of force leading to higher amount of delamination within the indent [203]. The same analogy explains the smaller size of delaminated diamond chips around the Rockwell indents, where the bending stresses on diamond films at the tops and valleys of profile of MoW interlayers were higher for rougher MoW interlayers which led to smaller sizes of chipped diamond.

Rockwell indents on diamond coated samples deposited under low temperature CVD conditions display progressive decrease in the area affected by spallation resulting is no spalled area in case of MoW-4 interlayer. The tendency of diamond chips to become smaller with increasing substrate roughness was also observed. In case of WC ball indents the diamond delamination within the indent region was comparatively similar for MoW-2 and MoW-3, while the indent in sample MoW-4 displayed significantly less of delaminated diamond. The accepted explanation of such behaviour was the observed lower amount of stress as calculated from the Raman spectra. The deposited diamond film on MoW-4 under low temperature CVD conditions was under only 1.6 GPa of compressive stress and therefore the thin film was able to deform elastically and only localised adhesion failures were observed. Careful consideration of direct comparison of indents on diamond films deposited at low and moderate temperatures should be taken. The reason being the sample softening process in case of diamond deposition under moderate CVD temperature. As one can see, the indents on moderate temperature grown diamond are slightly large due to the indenter penetrating the substrate into large depth. This in turn induced more plastic deformation and material flow, which can have an effect of the area of diamond's delamination.

In order to verify the stress levels calculated from Raman spectra a thermal stress was calculated using equation (12) on page 50. Thermal stress originating from the CTE mismatch between diamond and steel substrate was identified as the main contributor to

stress developed within diamond films [123–126]. Therefore a relative match of the calculated thermal stress values with the values of stress obtained from Raman spectra would support the validity of presented data. Three order polynomial functions were used for CTE of diamond and tungsten based on experimental data taken from [182]. For steel substrate the best fitting was provided by natural logarithm function based of available data from [183]. The problematic part of the thermal stress equation is the biaxial modulus consisting from Young's modulus and Poisson's ration. Values of Young's modulus and Poisson's ratio for nanocrystalline diamond differ from the values of natural bulk diamond and CVD bulk diamond and their exact values vary in literature [165,207–209] between 400-1120 GPa and 0.012-0.034, respectively. It has been demonstrated that the value of Young's modulus depends of on the CVD diamond deposition pre-treatment [208] as well as on diamond CVD deposition parameters [165], where increase in methane concentration and decrease in plasma density leads to a lower values of Young's modulus. Poisson's ratio also depends on the diamond film structure as well and increases with the film's grain size reduction[210]. Based on the available literature and the experimental data it is reasonable to assume that diamond films grown at moderate deposition temperature should have a different values of Young's modulus and possibly even Poisson's ratio [210] in comparison with the diamond films grown at lower temperatures. Consulting the available literature, a values of Young's modulus and Poisson's ratio of similar nanocrystalline diamond films were selected. Those were Young's modulus of 517 GPa for diamond grown at low temperatures and 720 GPa for diamond grown at moderate temperatures, while Poisson's ration was kept at 0.12 in both cases [208]. Calculation of diamond thermal stress values originating from tungsten/diamond interface provided stress levels of  $\approx -0.7$  GPa for low temperature CVD deposition and  $\approx -1.0$  GPa for moderate temperature CVD deposition. The values of thermal stress obtained using steel substrate and diamond were  $\approx -3.2$  GPa and  $\approx -5.4$  GPa for low and moderate temperature CVD deposition, respectively.

The stress values, calculated stress from Raman spectra, present in the diamond film are in between the values of thermal stress when calculated for tungsten/diamond and steel/diamond interface, which agrees with MoW interlayer being present, while being significantly thinner than the steel substrate. Therefore the thinner the MoW interlayer, the less significant contribution it will have on the resulting stress in the diamond film. Micron thin interlayers were already previously reported [48] to follow the contraction of steel substrate and to offer little protection in terms of stress reduction of stress levels. It was also reported [211] that the development of carbide layer formed at the interlayer-diamond interface has a negligible effect on the values of residual stress within the diamond films.

Comparing the values of compressive stresses obtained from Raman microscopy showed that an increase in the thickness of MoW interlayer form 1.1  $\mu\text{m}$  to 8.3  $\mu\text{m}$  let to a decrease

of stress within diamond films grown at fixed CVD deposition temperatures by  $\approx 33$  and  $\approx 40$  % for CVD deposition temperatures of 650 °C and 785 °C, respectively. Even if, as mentioned previously, thin interlayers were providing little protection against thermally induced stresses induced by the steel substrate, the interlayer contribution to lowering the impact of thermal stresses becomes pronounced when several micrometres are used. In contrast, lowering the CVD deposition temperature led to a decrease of stress in the diamond film by 48-56 %.

Lowering the thermally induced stresses by lowering the CVD deposition conditions was found to have a slightly more pronounced effect on the reduction of stress levels within diamond films, than an increase of interlayer thickness (within the selected regions of CVD deposition temperatures and interlayer thicknesses).

In the selected region of CVD deposition temperatures and interlayer thicknesses it was found that a reduction in diamond CVD deposition temperature from 785 °C to 650 °C had a slightly more pronounced effect on lowering of the post deposition stress in diamond films, than an increase of interlayer thickness from 1.1  $\mu\text{m}$  to 8.3  $\mu\text{m}$ . Only through using both of the stress relieving approaches it was possible to produce adherent diamond coatings with low residual compression stresses of 1.6 GPa, which were able to withstand indentation tests with no diamond coating failures being detected outside of the indent region. The MoW interlayer starts to be effective CVD deposition stress barrier only with a substantial increase to its thickness as was demonstrated in this study.

The observed contradictory results of diamond film on MoW-4 coated steel under low temperature CVD deposition conditions, where it was able to withstand Rockwell C indentation, while delaminating at the start of 5-30 N scratch tests were concluded to be due to the difference in testing conditions. Indentation using diamond indenter provided non-sticking form of contact. Scratch and indentation tests using a WC indenter, on the other hand, formed a bonding between the WC indenter and the diamond film which resulted in embedding part of the diamond film in the WC material. Upon release of the contact the pulling force exerted onto the diamond film are higher which leads to a detachment of either the part of the WC ball (observed as smearing), or the diamond film (observed as localised delamination) [203]. Similar behaviour would be also expected for steel indenters, which were found [212] to produce a relatively high friction when used as indenters on diamond films.

## 5 Conclusions

Main topic of this work was the diamond film growth on steel substrates, which was divided into three stages according to what type of interlayer has been used to enhance and overall improve the properties of diamond films grown on steel. The used interlayers were DLC, CrW and MoW coatings. The outline of the conclusions is structured as a chronological outline of performed work which informs about the outcomes as well as describes the progress made throughout this work.

Diamond deposition on steel using DLC films as a buffer layer for subsequent diamond growth was found capable of providing a several micron thick diamond coating within five hours of diamond deposition, which encouraged further research. Further research in this direction proved hard to repeat the initial results due to the complexity of events leading to the deposited diamond film. High diamond growth rates capable of formation of  $>10\ \mu\text{m}$  diamond crystals were observed during the investigation, but very low diamond nucleation densities were rendering the deposition process unsuitable for coalescent diamond films. It was understood that a more insight into the diamond CVD growth conditions was needed in order to improve the results.

Second stage of diamond deposition on CrW coated steel substrates involved a development of magnetron sputtered CrW coating, nanodiamond seeding investigation and optimization of CVD deposition parameters. Tungsten was selected as interlayer material for its diffusion barrier properties, suitable CTE, being carbide forming material and having no susceptibility to hydrogen embrittlement. Cr was used as a bonding facilitator between the steel and tungsten. The adhesion of CrW onto the steel substrates was found problematic, but deemed to be still suitable for subsequent CVD deposition. Nanodiamond seeding experiment confirmed the possibility of obtaining a high diamond nucleation densities which facilitate the subsequent growth of dense diamond coating. The drawback of the nanodiamond seeding technique is being an additional step where samples would have to be taken from one deposition chamber and placed into another. The optimisation of diamond CVD deposition parameters provided a stable conditions for reputable deposition of adherent diamond films. The optimised CVD deposition conditions being: chamber pressure of 25 Torr; microwave power of 550 Watt; 3 vol. % of  $\text{CH}_4$  in  $\text{H}_2$ ; total gas flow of 100 sccm and deposition time of 2 hours. The CrW interlayer was found to be a cause of occasional spontaneous delamination and cracking of the CrW interlayer together with the deposited diamond films. The adhesion failure was identified to be at the interface of steel/CrW. The concluded explanation was in contamination of steel surface before the magnetron sputtering process took place. The need for substrate temperature detection during the CVD deposition was understood. It led to a development of temperature

measuring setup using K-type thermocouple mounted at the back of the substrate holder, followed by the setup's testing in various simulated deposition conditions, in order to establish a calculations accounting for the distance between the substrate surface and the thermocouple. The capability of precise temperature detection gave a further insight to the CVD deposition. It was found that the substrate surface temperature was 785 °C for the previously optimised CVD deposition conditions.

Third stage was marked by development of MoW interlayer which provided an enhanced adhesion between Mo and W layers and was adopted as an interlayer for investigation of benefits of W on diamond growth on steel substrates. Initially the diamond was deposited on steel coated with MoW-2 1.1 µm thick interlayer using the optimised diamond CVD deposition conditions with substrate temperature of 785 °C. The resulting diamond film was of nanocrystalline nature and had a good adhesion towards the MoW-2 coated steel substrate as was investigated by scratch tests. The functionality of MoW-2 coating, as a diffusion barrier between the steel and diamond film, was proven through the use of EDS chemical analysis. No steel elements were detected to diffuse into the diamond film and vice versa. Rockwell C hardness tests revealed a softening of the steel substrate caused by diamond CVD deposition at 785 °C. The unintended change to the steel properties led to an investigation of suitable diamond CVD deposition parameters with no or low effect on the functionality of the steel substrate. The suitable deposition conditions for diamond film deposition at 650 °C were found to be: chamber pressure of 15 Torr; microwave power of 440 W, 3 vol. % of CH<sub>4</sub> in H<sub>2</sub> and 100 sccm gas flow. In 4 hours the selected diamond CVD deposition conditions produced diamond films of thickness of ≈ 250 nm, which was similar to the thickness of diamond films deposited at 785 °C in 2 hours. The measured sample hardness was within the accuracy range of the Rockwell C method. Softening of steel was prevented and the thermocouple temperature detection method was proven reliable. Samples were found to have a poor mechanical characteristics which stemmed from lower interfacial adhesion strength at the substrate/diamond interface. A change of diamond seeding procedure and/or change of the CVD deposition equipment is needed for the adhesion improvement.

An investigation of the influence of interlayer thickness and the temperature of CVD deposition process was carried out to determine their effect on stress found within the diamond films. Three MoW films of different thickness (1.1 µm, 4.5 µm and 8.3 µm) were coated with diamond films deposited at low (650 °C) and moderate (785 °C) diamond CVD deposition conditions. The indentation tests showed a decrease of stress within the diamond film corresponding to both, the decrease in CVD deposition temperature as well as the increase of the thickness of MoW interlayer. The lowest measured amount of compressive stress in diamond film was 1.6 GPa, which was measured on sample

deposited at low temperature CVD conditions and the thickest MoW interlayer. The coating was able to withstand Rockwell C indentation without signs of delamination, although its adhesion during scratch test (5-30 N, 5 mm WC ball) was found still unsatisfactory.

## 6 Future work

Three main directions of future work were identified. First being an investigation into an enhancement of diamond adhesion through a variation in seeding process. Particularly focused on different intensities of sample agitation and the use of different suspensions containing different sizes and mixtures of diamond particles.

Second being an investigation of variation in the interlayer used for diamond deposition. The aim of the study being a deposition of relatively thin (several micron thick) interlayer combining function of diffusion barrier, carbide forming, as well as being able to accommodate the compressive stresses in diamond film resulting from the CTE mismatch between the diamond and steel. Sandwich coatings containing W, or Mo as the materials providing diffusion barrier and good adhesion combined with soft material such as Cu, Al, or Ag to be able to compensate the CTE mismatch.

Third direction being the use of different CVD deposition equipment. The aim being to determine the most suitable CVD deposition technique providing enhanced adhesion of diamond film at low deposition temperatures, to prevent affecting the mechanical properties of steel substrates, and with acceptable diamond growth rate ( $\geq 100$  nm/hour).

## 7 List of References

- [1] R.B. Heimann, S.E. Esvukov, Y. Koga, Carbon allotropes: a suggested classification scheme based on valence orbital hybridization, *Carbon N. Y.* 35 (1997) 1654–1658. doi:10.1016/S0008-6223(97)82794-7.
- [2] E. a. Belenkov, V. a. Greshnyakov, Classification schemes for carbon phases and nanostructures, *Xinxing Tan Cailiao/New Carbon Mater.* 28 (2013) 273–283. doi:10.1016/S1872-5805(13)60081-5.
- [3] Z. Ren, Y. Lan, Y. Wang, Aligned Carbon Nanotubes: Physics, concepts, fabrication and devices, *Nanosci. Technol.* 5 (2013) 1–6. doi:10.1007/978-3-642-30490-3.
- [4] O.A. Shenderova, V. V. Zhirnov, D.W. Brenner, Carbon Nanostructures, *Crit. Rev. Solid State Mater. Sci.* 27 (2002) 227–356. doi:10.1080/10408430208500497.
- [5] P.W. May, Diamond thin films: a 21st-century material, *Philos. Trans. R. Soc. LONDON Ser. A-MATHEMATICAL Phys. Eng. Sci.* 358 (2000) 473–495. doi:10.1098/rsta.2000.0542.
- [6] S.-T. Lee, Z. Lin, X. Jiang, CVD diamond films: nucleation and growth, *Mater. Sci. Eng. R Reports.* 25 (1999) 123–154. doi:10.1016/S0927-796X(99)00003-0.
- [7] N. Ali, Q.H. Fan, J. Gracio, E. Pereira, W. Ahmed, A comparison study of diamond adhesion on ductile metals, *Thin Solid Films.* (2000) 193–197. <http://www.sciencedirect.com/science/article/pii/S0040609000012967> (accessed November 2, 2012).
- [8] J. Gracio, Q. Fan, J.C. Madaleno, Diamond growth by chemical vapour deposition, *J. Phys. D. Appl. Phys.* 43 (2010) 374017. <http://stacks.iop.org/0022-3727/43/i=37/a=374017> (accessed July 4, 2012).
- [9] J. Hu, Y.K. Chou, R.G. Thompson, Nanocrystalline diamond coating tools for machining high-strength Al alloys, *Int. J. Refract. Met. Hard Mater.* 26 (2008) 135–144. doi:10.1016/j.ijrmhm.2007.05.012.
- [10] F. Qin, Y.K. Chou, D. Nolen, R.G. Thompson, Coating thickness effects on diamond coated cutting tools, *Surf. Coatings Technol.* 204 (2009) 1056–1060. doi:10.1016/j.surfcoat.2009.06.011.
- [11] K. Miyoshi, R.L.C. Wu, A. Garscadden, P.N. Barnes, H.E. Jackson, Friction and wear of plasma- deposited diamond films, *J. Appl. Phys.* 74 (1993).
- [12] P. Hollman, O. Wänstrand, S. Hogmark, Friction properties of smooth nanocrystalline diamond coatings, *Diam. Relat. Mater.* 7 (1998) 1471–1477. doi:10.1016/S0925-9635(98)00215-5.
- [13] S. Mitura, A. Mitura, P. Niedzielski, P. Couvrat, Nanocrystalline Diamond Coatings, *Chaos, Solitons & Fractals.* 10 (1999) 2165–2176. doi:10.1016/S0960-0779(98)00251-3.
- [14] M. Amaral, P.S. Gomes, M.A. Lopes, J.D. Santos, R.F. Silva, M.H. Fernandes, Nanocrystalline Diamond as a Coating for Joint Implants: Cytotoxicity and Biocompatibility Assessment, *J. Nanomater.* 2008 (2008) 1–9. doi:10.1155/2008/894352.
- [15] R.J. Narayan, *Diamond-Based Materials for Biomedical Applications*, Elsevier Ltd., 2013. <http://www.scopus.com/inward/record.url?eid=2-s2.0-84902339424&partnerID=tZOtx3y1>.
- [16] O.A. Williams, Nanocrystalline Diamond, *Diam. Relat. Mater.* 20 (2011) 621–640. doi:10.1016/j.diamond.2011.02.015.

- [17] P. Hofmann, *Solid State Physics: An Introduction*, Wiley-VCH, 2008.
- [18] D.M. Mattox, *Handbook of Physical Vapor Deposition (PVD) Processing*, William Andrew Publishing/Noyes, 1998. [http://app.knovel.com/web/toc.v/cid:kpHPVDPVD3/viewerType:toc/root\\_slug:handbook-physical-vapor/url\\_slug:kt0060PZP1](http://app.knovel.com/web/toc.v/cid:kpHPVDPVD3/viewerType:toc/root_slug:handbook-physical-vapor/url_slug:kt0060PZP1) (accessed May 8, 2015).
- [19] J.H. Yao, K.R. Elder, H. Guo, M. Grant, Theory and simulation of Ostwald ripening, *Phys. Rev. B.* 47 (1993) 14110–14125. doi:10.1103/PhysRevB.47.14110.
- [20] C. V. Thompson, GRAIN-GROWTH IN THIN-FILMS, *Annu. Rev. Mater. Sci.* 20 (1990) 245–268.
- [21] C. V. Thompson, STRUCTURE EVOLUTION DURING PROCESSING OF POLYCRYSTALLINE FILMS, *Annu. Rev. Mater. Sci.* 30 (2000) 159–190. doi:10.1146/annurev.matsci.30.1.159.
- [22] C. Ratsch, J.A. Venables, Nucleation theory and the early stages of thin film growth, *J. Vac. Sci. Technol. A.* 21 (2003).
- [23] T. Vetter, M. Iggländ, D.R. Ochsenein, F.S. Hänseler, M. Mazzotti, Modeling Nucleation, Growth, and Ostwald Ripening in Crystallization Processes: A Comparison between Population Balance and Kinetic Rate Equation, *Cryst. Growth Des.* 13 (2013) 4890–4905. doi:10.1021/cg4010714.
- [24] J.A. Venables, G.D.T. Spiller, M. Hanbucken, Nucleation and growth of thin films, *Reports Prog. Phys.* 47 (1984) 399. <http://stacks.iop.org/0034-4885/47/i=4/a=002>.
- [25] M. Ohring, *The Materials Science of Thin Films*, First edit, Academic Press, London, 1992.
- [26] P. Smereka, X. Li, G. Russo, D.J. Srolovitz, Simulation of faceted film growth in three dimensions: Microstructure, morphology and texture, *Acta Mater.* 53 (2005) 1191–1204. doi:10.1016/j.actamat.2004.11.013.
- [27] J.A. Thornton, High Rate Thick Film Growth, *Annu. Rev. Mater. Sci.* 7 (1977) 239–260. doi:10.1146/annurev.ms.07.080177.001323.
- [28] B.A. Movchan, A.V. Demchish, Study of Structure and Properties of Thick Vacuum Condensates of Nickel, Titanium, Tungsten, Aluminium Oxide and Zirconium, *Phys. Met. Metallogr. - USSR.* 28 (1969).
- [29] J.A. Thornton, The microstructure of sputter deposited coatings, *J. Vac. Sci. Technol. A.* 4 (1986).
- [30] I. Petrov, P.B. Barna, L. Hultman, J.E. Greene, Microstructural evolution during film growth, *J. Vac. Sci. Technol. A Vacuum, Surfaces, Film.* 21 (2003) S117. doi:10.1116/1.1601610.
- [31] A. Anders, A structure zone diagram including plasma-based deposition and ion etching, *Thin Solid Films.* 518 (2010) 4087–4090. doi:10.1016/j.tsf.2009.10.145.
- [32] D. Choudhary, J. Bellare, Manufacture of gem quality diamonds: a review, *Ceram. Int.* 26 (2000) 73–85. doi:10.1016/S0272-8842(99)00022-X.
- [33] J.C. Angus, Diamond synthesis by chemical vapor deposition: The early years, *Diam. Relat. Mater.* 49 (2014) 77–86. doi:10.1016/j.diamond.2014.08.004.
- [34] R.F. Davis, *Diamond Films and Coatings*, Noyes Publications, New Jersey, 1993. [http://www.knovel.com/web/portal/browse/display?\\_EXT\\_KNOVEL\\_DISPLAY\\_bookid=81](http://www.knovel.com/web/portal/browse/display?_EXT_KNOVEL_DISPLAY_bookid=81).
- [35] K.O. and H.F. and K.S. and A. Sawabe, Fabrication of Epitaxial Diamond Thin Film on Iridium, *Jpn. J. Appl. Phys.* 36 (1997) L1214. <http://stacks.iop.org/1347-4065/36/i=9A/a=L1214>.

- [36] H. Liu, D.S. Dandy, *Diamond Chemical Vapor Deposition*, William Andrew Publishing/Noyes, 1995. [http://www.knovel.com/web/portal/browse/display?\\_EXT\\_KNOVEL\\_DISPLAY\\_bookid=80](http://www.knovel.com/web/portal/browse/display?_EXT_KNOVEL_DISPLAY_bookid=80).
- [37] H. Liu, D.S. Dandy, Studies on nucleation process in diamond CVD: an overview of recent developments, *Diam. Relat. Mater.* 4 (1995) 1173–1188. doi:10.1016/0925-9635(96)00297-2.
- [38] S.B. Abu Suilik, D. Shimamoto, H. Kitagawa, K. Hasezaki, Y. Noda, Experimental study of nucleation and quality of CVD diamond adopting two-step deposition approach using MPECVD, *Diam. Relat. Mater.* 15 (2006) 1765–1772. doi:10.1016/j.diamond.2006.03.009.
- [39] H. Ye, C.Q. Sun, P. Hing, H. Xie, S. Zhang, Nucleation and growth dynamics of diamond films by microwave plasma-enhanced chemical vapor deposition (MPECVD), *Surf. Coatings.* 123 (2000) 129–133. doi:10.1016/S0257-8972(99)00527-7.
- [40] H. Makita, K. Nishimura, N. Jiang, A. Hatta, T. Ito, A. Hiraki, Ultrahigh particle density seeding with nanocrystal diamond particles, *Thin Solid Films.* 281-282 (1996) 279–281. doi:10.1016/0040-6090(96)08652-X.
- [41] J.C. Arnault, L. Demuyneck, C. Speisser, F. Le Normand, Mechanisms of CVD diamond nucleation and growth on mechanically scratched Si(100) surfaces, *Eur. Phys. J. B - Condens. Matter Complex Syst.* 11 (1999) 327–343. doi:10.1007/s100510050943.
- [42] A. Krüger, F. Kataoka, M. Ozawa, T. Fujino, Y. Suzuki, A.E. Aleksenskii, et al., Unusually tight aggregation in detonation nanodiamond: Identification and disintegration, *Carbon* N. Y. 43 (2005) 1722–1730. doi:10.1016/j.carbon.2005.02.020.
- [43] M. Varga, T. Ižák, A. Kromka, M. Veselý, K. Hruška, M. Michalka, Study of diamond film nucleation by ultrasonic seeding in different solutions, *Cent. Eur. J. Phys.* 10 (2012) 218–224. doi:10.2478/s11534-011-0078-4.
- [44] M. Varga, M. Vojs, M. Marton, L. Michalíková, M. Veselý, R. Redhammer, et al., Diamond thin film nucleation on silicon by ultrasonication in various mixtures, *Vacuum.* 86 (2012) 681–683. doi:10.1016/j.vacuum.2011.07.035.
- [45] M. Daenen, O.A. Williams, J. D’Haen, K. Haenen, M. Nesládek, Seeding, growth and characterization of nanocrystalline diamond films on various substrates, *Phys. Status Solidi.* 203 (2006) 3005–3010. doi:10.1002/pssa.200671122.
- [46] K. Tsugawa, S. Kawaki, M. Ishihara, J. Kim, Y. Koga, H. Sakakita, et al., Nanocrystalline diamond growth in a surface-wave plasma, *Diam. Relat. Mater.* 20 (2011) 833–838. doi:10.1016/j.diamond.2011.03.031.
- [47] O.A. Williams, O. Douhéret, M. Daenen, K. Haenen, E. Ōsawa, M. Takahashi, Enhanced diamond nucleation on monodispersed nanocrystalline diamond, *Chem. Phys. Lett.* 445 (2007) 255–258. doi:10.1016/j.cplett.2007.07.091.
- [48] J.G. Buijnsters, P. Shankar, W. Fleischer, W.J.P. van Enckevort, J.J. Schermer, J.J. ter Meulen, CVD diamond deposition on steel using arc-plated chromium nitride interlayers, *Diam. Relat. Mater.* 11 (2002) 536–544. doi:10.1016/S0925-9635(01)00628-8.
- [49] J.G. Buijnsters, P. Shankar, W.J.P. van Enckevort, J.J. Schermer, J.J. ter Meulen, Adhesion analysis of polycrystalline diamond films on molybdenum by means of scratch, indentation and sand abrasion testing, *Thin Solid Films.* 474 (2005) 186–196. doi:10.1016/j.tsf.2004.09.021.

- [50] J.G. Buijnsters, P. Shankar, W.J.P. van Enkevort, J.J. Schermer, J.J. ter Meulen, The applicability of ultra thin silicon films as interlayers for CVD diamond deposition on steels, *Phys. Status Solidi*. 195 (2003) 383–395. doi:10.1002/pssa.200305947.
- [51] X. Xiao, B.W. Sheldon, E. Konca, L.C. Lev, M.J. Lukitsch, The failure mechanism of chromium as the interlayer to enhance the adhesion of nanocrystalline diamond coatings on cemented carbide, *Diam. Relat. Mater.* 18 (2009) 1114–1117. doi:http://dx.doi.org/10.1016/j.diamond.2009.02.012.
- [52] H.W. Liu, C.X. Gao, X. Li, C.X. Wang, Y.H. Han, G.T. Zou, Selective deposition of diamond films on insulators by selective seeding with a double-layer mask, *Diam. Relat. Mater.* 10 (2001) 1573–1577. doi:10.1016/S0925-9635(01)00411-3.
- [53] A. V. Sumant, P.U.P. a. Gilbert, D.S. Grierson, A.R. Konicek, M. Abrecht, J.E. Butler, et al., Surface composition, bonding, and morphology in the nucleation and growth of ultra-thin, high quality nanocrystalline diamond films, *Diam. Relat. Mater.* 16 (2007) 718–724. doi:10.1016/j.diamond.2006.12.011.
- [54] K. Tsugawa, M. Ishihara, J. Kim, Y. Koga, M. Hasegawa, Nucleation enhancement of nanocrystalline diamond growth at low substrate temperatures by adamantane seeding, *J. Phys. Chem. C*. 114 (2010) 3822–3824. doi:10.1021/jp910555x.
- [55] S.Z. Rotter, J.C. Madaleno, Diamond CVD by a Combined Plasma Pretreatment and Seeding Procedure, *Chem. Vap. Depos.* 15 (2009) 209–216. doi:10.1002/cvde.200806745.
- [56] M.M. García, I. Jiménez, O. Sánchez, C. Gómez-Aleixandre, L. Vázquez, Model of the bias-enhanced nucleation of diamond on silicon based on atomic force microscopy and x-ray-absorption studies, *Phys. Rev. B*. 61 (2000) 10383–10387. doi:10.1103/PhysRevB.61.10383.
- [57] B.R. Stoner, G.-H.M. Ma, S.D. Wolter, J.T. Glass, Characterization of bias-enhanced nucleation of diamond on silicon by invacuo surface analysis and transmission electron microscopy, *Phys. Rev. B*. 45 (1992) 11067–11084. http://link.aps.org/doi/10.1103/PhysRevB.45.11067.
- [58] W. Kulisch, L. Ackermann, B. Sobisch, On the Mechanisms of Bias Enhanced Nucleation of Diamond, *Phys. Status Solidi*. 154 (1996) 155–174. doi:10.1002/pssa.2211540113.
- [59] Y. Tang, Y.S.S. Li, C. Zhang, L. Zhang, L. Yang, Q. Yang, et al., Study of nanocrystalline diamond synthesis in MPCVD by bias enhanced nucleation and growth, *Diam. Relat. Mater.* 25 (2012) 87–91. doi:10.1016/j.diamond.2012.02.003.
- [60] Z. Feng, M.A. Brewer, K. Komvopoulos, I.G. Brown, D.B. Bogy, Diamond nucleation on unscratched silicon substrates coated with various non-diamond carbon films by microwave plasma-enhanced chemical vapor deposition, *J. Mater. Res.* 10 (1995) 165–174.
- [61] W.S. Yang, T.S. Kim, J.H. Je, Effects of hydrogenated amorphous carbon interlayer on diamond nucleation, *J. Mater. Res.* 13 (1998) 596–603. doi:10.1557/JMR.1998.0076.
- [62] P.S. Weiser, S. Praver, Chemical vapour deposition of diamond onto iron based substrates—The use of barrier layers, *Diam. Relat. Mater.* 4 (1995) 710–713. doi:10.1016/0925-9635(94)05269-7.
- [63] F.J.G. Silva, A.J.S. Fernandes, F.M. Costa, A.P.M. Baptista, E. Pereira, A new interlayer approach for CVD diamond coating of steel substrates, *Diam. Relat. Mater.* 13 (2004) 828–833. doi:10.1016/j.diamond.2003.10.081.

- [64] F.J.G. Silva, A.P.M. Baptista, E. Pereira, Microwave plasma chemical vapour deposition diamond nucleation on ferrous substrates with Ti and Cr interlayers, *Diam. Relat. Mater.* 11 (2002) 1617–1622. doi:10.1016/S0925-9635(02)00029-8.
- [65] Q. Fan, A. Fernandes, J. Gracio, Diamond coating on steel with a titanium interlayer, *Diam. Relat. Mater.* 7 (1998) 5–8. <http://www.sciencedirect.com/science/article/pii/S0925963597002872> (accessed July 1, 2013).
- [66] J. Spinnewyn, M. Nesládek, C. Asinari, Diamond nucleation on steel substrates, *Diam. Relat. Mater.* 2 (1993) 361–364. <http://www.scopus.com/inward/record.url?eid=2-s2.0-0027569326&partnerID=40&md5=42df4d68d51192649dd3c67da8b6c213>.
- [67] a. Laikhtman, L. Rapoport, V. Perfilyev, A. Moshkovich, R. Akhvlediani, A. Hoffman, et al., Tribological and Adhesion Properties of CVD Diamond Films Grown on Steel with a Cr-N Interlayer, *AIP Conf. Proc.* 157 (2009) 157–161. doi:10.1063/1.3203226.
- [68] R. Haubner, B. Lux, Diamond deposition on steel substrates using intermediate layers, *Int. J. Refract. Met. Hard Mater.* 24 (2006) 380–386. doi:10.1016/j.jirmhm.2005.11.008.
- [69] S. Schwarz, S.M. Rosiwal, Y. Musayev, R.F. Singer, High temperature diffusion chromizing as a successful method for CVD-diamond coating of steel—Part II, *Diam. Relat. Mater.* 12 (2003) 701–706. doi:10.1016/S0925-9635(03)00061-X.
- [70] Z. Feng, K. Komvopoulos, D.B. Bogy, J.W. Ager, S. Anders, A. Anders, et al., Effect of pretreatment process parameters on diamond nucleation on unscratched silicon substrates coated with amorphous carbon films, *J. Appl. Phys.* 79 (1996) 485. doi:10.1063/1.360855.
- [71] Z. Feng, S. Anders, A. Anders, J.W. Ager, I.G. Brown, K. Komvopoulos, et al., Diamond growth on hard carbon films, *Diam. Relat. Mater.* 5 (1996) 1080–1086. <http://www.sciencedirect.com/science/article/pii/S0925963596005183>.
- [72] Z. Feng, K. Komvopoulos, I.G. Brown, D.B. Bogy, A pretreatment process for enhanced diamond nucleation on smooth silicon substrates coated with hard carbon films, *J. Mater. Res.* 9 (1994) 2148–2153. doi:10.1557/JMR.1994.2148.
- [73] K. Komvopoulos, T. Xu, Transmission electron microscopy study of diamond nucleation and growth on smooth silicon surfaces coated with a thin amorphous carbon film, *Diam. Relat. Mater.* 9 (2000) 274–282. doi:10.1016/S0925-9635(99)00296-4.
- [74] Z. Nibennanoune, D. George, F. Antoni, S. Ahzi, D. Ruch, J. Gracio, et al., Improving diamond coating on Ti6Al4V substrate using a diamond like carbon interlayer: Raman residual stress evaluation and AFM analyses, *Diam. Relat. Mater.* 22 (2012) 105–112. doi:10.1016/j.diamond.2011.12.023.
- [75] J. Singh, Nucleation and growth mechanism of diamond during hot-filament chemical vapour deposition, *J. Mater. Sci.* 29 (1994) 2761–2766. <http://www.springerlink.com/index/w427362742k48618.pdf> (accessed July 2, 2012).
- [76] M.H. Nazare, A.J. Neves, Properties, Growth and Applications of Diamond, Institution of Engineering and Technology, 2001. [http://www.knovel.com/web/portal/browse/display?\\_EXT\\_KNOVEL\\_DISPLAY\\_book\\_id=1142](http://www.knovel.com/web/portal/browse/display?_EXT_KNOVEL_DISPLAY_book_id=1142).
- [77] H. Buchkremer-Hermanns, H. Ren, J. Utsch, H. Weiss, T.E.R. Als, Optimization of MW-PACVD diamond deposition parameters for high nucleation density and growth rate on Si<sub>3</sub>N<sub>4</sub> substrate, *Diam. Relat. Mater.* 6 (1997) 411–416. <http://www.sciencedirect.com/science/article/pii/S092596359600711X>.

- [78] H. Buchkremer-Hermanns, H. Ren, H. Weiß, Optimization of diamond nucleation and growth using MW-PACVD method, *Diam. Relat. Mater.* 5 (1996) 312–316. doi:10.1016/0925-9635(95)00353-3.
- [79] K. Kobashi, *Diamond Films Chemical Vapor Deposition for Oriented and Heteroepitaxial Growth*, 1st Editio, Elsevier Ltd., Oxford, 2005. [http://store.elsevier.com/product.jsp?locale=en\\_UK&isbn=9780080447230](http://store.elsevier.com/product.jsp?locale=en_UK&isbn=9780080447230).
- [80] S.M. Leeds, P.W. May, E. Bartlett, M.N.R. Ashfold, K.N. Rosser, Molecular beam mass spectrometry studies of the gas-phase chemistry occurring during microwave plasma assisted chemical vapour deposition of diamond, *Diam. Relat. Mater.* 8 (1999) 1377–1382. doi:10.1016/S0925-9635(99)00014-X.
- [81] Y.F. Zhang, F. Zhang, Q.J. Gao, X.F. Peng, Z.D. Lin, The roles of argon addition in the hot filament chemical vapor deposition system, *Diam. Relat. Mater.* 10 (2001) 1523–1527. doi:10.1016/S0925-9635(01)00383-1.
- [82] Y. Chu, G. Jiang, C. Chang, Room-temperature diamond seeding and microwave plasma enhanced CVD growth of nanodiamond with a tungsten interfacial layer, ... (IEEE-NANO), 2011 .... (2011) 1367–1370. [http://ieeexplore.ieee.org/xpls/abs\\_all.jsp?arnumber=6144477](http://ieeexplore.ieee.org/xpls/abs_all.jsp?arnumber=6144477) (accessed August 20, 2014).
- [83] Y.-C. Chu, C.-H. Tu, G. Jiang, C. Chang, C. Liu, J.-M. Ting, et al., Systematic studies of the nucleation and growth of ultrananocrystalline diamond films on silicon substrates coated with a tungsten layer, *J. Appl. Phys.* 111 (2012) 124328. doi:10.1063/1.4729798.
- [84] D.M. Gruen, S. Liu, A.R. Krauss, J. Luo, X. Pan, Fullerenes as precursors for diamond film growth without hydrogen or oxygen additions, *Appl. Phys. Lett.* 64 (1994).
- [85] J.R. Rabeau, P. John, J.I.B. Wilson, Y. Fan, The role of C<sub>2</sub> in nanocrystalline diamond growth, *J. Appl. Phys.* 96 (2004).
- [86] J.E. Butler, A. V. Sumant, The CVD of Nanodiamond Materials, *Chem. Vap. Depos.* 14 (2008) 145–160. doi:10.1002/cvde.200700037.
- [87] K. Tsugawa, M. Ishihara, J. Kim, Y. Koga, M. Hasegawa, Nanocrystalline diamond film growth on plastic substrates at temperatures below 100 °C from low-temperature plasma, *Phys. Rev. B.* 82 (2010) 1–8. doi:10.1103/PhysRevB.82.125460.
- [88] P.K. Bachmann, H.J. Hagemann, H. Lade, D. Leers, D.U. Wiechert, H. Wilson, et al., Thermal properties of C/H-, C/H/O-, C/H/N- and C/H/X-grown polycrystalline CVD diamond, *Diam. Relat. Mater.* 4 (1995) 820–826. doi:10.1016/0925-9635(94)05229-8.
- [89] Š. Potocký, O. Babchenko, K. Hruška, A. Kromka, Linear antenna microwave plasma CVD diamond deposition at the edge of no-growth region of C-H-O ternary diagram, *Phys. Status Solidi Basic Res.* 249 (2012) 2612–2615. doi:10.1002/pssb.201200124.
- [90] K. Tsugawa, M. Ishihara, J. Kim, M. Hasegawa, Y. Koga, Large-Area and Low-Temperature Nanodiamond Coating by Microwave Plasma Chemical Vapor Deposition, *New Diam. Front. Carbon Technol.* 16 (2007).
- [91] M. Asmann, J. Heberlein, E. Pfender, A review of diamond CVD utilizing halogenated precursors, *Diam. Relat. Mater.* 8 (1999) 1–16. <http://www.sciencedirect.com/science/article/pii/S0925963598003653>.
- [92] V. Baranauskas, S.F. Durrant, M.C. Tosin, A.C. Peterlevitz, B. Bin Li, S.G. Castro, Nitrogenated diamond produced by introducing ammonia into the gas feed in hot-filament CVD, *Thin Solid Films.* 355-356 (1999) 157–161. doi:10.1016/S0040-6090(99)00501-5.

- [93] R. Schirhagl, K. Chang, M. Loretz, C.L. Degen, Nitrogen-vacancy centers in diamond: nanoscale sensors for physics and biology, *Annu. Rev. Phys. Chem.* 65 (2014) 83–105. doi:10.1146/annurev-physchem-040513-103659.
- [94] T.D. Corrigan, D.M. Gruen, a. R. Krauss, P. Zapol, R.P.H. Chang, The effect of nitrogen addition to Ar/CH<sub>4</sub> plasmas on the growth, morphology and field emission of ultrananocrystalline diamond, *Diam. Relat. Mater.* 11 (2002) 43–48. doi:10.1016/S0925-9635(01)00517-9.
- [95] J.A. Smith, J.B. Wills, H.S. Moores, A.J. Orr-Ewing, M.N.R. Ashfold, Y. a. Mankelevich, et al., Effects of NH<sub>3</sub> and N<sub>2</sub> additions to hot filament activated CH<sub>4</sub>/H<sub>2</sub> gas mixtures, *J. Appl. Phys.* 92 (2002) 672–681. doi:10.1063/1.1481961.
- [96] Y. a. Mankelevich, N. V. Suetin, J.A. Smith, M.N.R. Ashfold, Investigations of the gas phase chemistry in a hot filament CVD reactor operating with CH<sub>4</sub>/N<sub>2</sub>/H<sub>2</sub> and CH<sub>4</sub>/NH<sub>3</sub>/H<sub>2</sub> gas mixtures, *Diam. Relat. Mater.* 11 (2002) 567–572. doi:10.1016/S0925-9635(01)00557-X.
- [97] W. Kwaśny, Predicting properties of PVD and CVD coatings based on fractal quantities describing their surface, *Manuf. Eng.* 37 (2009) 125–192.
- [98] J. Robertson, Diamond-like amorphous carbon, *Mater. Sci. Eng. R Reports.* 37 (2002) 129–281. doi:10.1016/S0927-796X(02)00005-0.
- [99] M. Jarratt, J. Stallard, N.M. Renevier, D.G. Teer, An improved diamond-like carbon coating with exceptional wear properties, *Diam. Relat. Mater.* 12 (2003) 1003–1007. doi:10.1016/S0925-9635(02)00296-0.
- [100] M. Ritala, J. Niinisto, S. Krumdieck, P. Chalker, H. Aspinall, M.E. Pemble, et al., *Chemical Vapour Deposition*, The Royal Society of Chemistry, 2009. doi:10.1039/9781847558794.
- [101] H.O. Pierson, *Handbook of Chemical Vapor Deposition (CVD) - Principles, Technology and Applications (2nd Edition)*, William Andrew Publishing/Noyes, 1999. [http://www.knovel.com/web/portal/browse/display?\\_EXT\\_KNOVEL\\_DISPLAY\\_bookid=60](http://www.knovel.com/web/portal/browse/display?_EXT_KNOVEL_DISPLAY_bookid=60).
- [102] P.J. Kelly, Magnetron sputtering: a review of recent developments and applications, *Vacuum.* 56 (2000) 159–172. doi:10.1016/S0042-207X(99)00189-X.
- [103] W.D. Westwood, *Sputter Deposition*, AVS, 2003.
- [104] K.E. Cooke, J. Hamsphire, W. Southall, D.G. Teer, The industrial application of pulsed DC bias power supplies in closed field unbalanced magnetron sputter ion plating, *Surf. Coatings Technol.* 177-178 (2004) 789–794. doi:10.1016/j.surfcoat.2003.06.009.
- [105] Y. Xiang, W. Chengbiao, L. Yang, Recent developments in magnetron sputtering, *Plasma Sci.* 337 (2006). <http://iopscience.iop.org/1009-0630/8/3/20> (accessed July 4, 2012).
- [106] G. Bräuer, B. Szyszka, M. Vergöhl, R. Bandorf, Magnetron sputtering – Milestones of 30 years, *Vacuum.* 84 (2010) 1354–1359. doi:10.1016/j.vacuum.2009.12.014.
- [107] J.R. Creighton, P. Ho, Introduction to Chemical Vapour Deposition, in: *Chem. Vap. Depos. SE - 1*, Springer London, 2010: pp. 1–28. doi:10.1007/978-1-84882-894-0\_1.
- [108] J.-H. Park, T.S. Sudarshan, eds., *Chemical Vapor Deposition*, ASM International, 2001.
- [109] F. Fendrych, A. Taylor, L. Peksa, I. Kratochvilova, J. Vlcek, V. Rezacova, et al., Growth and characterization of nanodiamond layers prepared using the plasma-enhanced linear antennas microwave CVD system, *J. Phys. D. Appl. Phys.* 43 (2010) 374018. doi:10.1088/0022-3727/43/37/374018.

- [110] M. Liehr, M. Dieguez-Campo, Microwave PECVD for large area coating, *Surf. Coatings Technol.* 200 (2005) 21–25. doi:10.1016/j.surfcoat.2005.02.061.
- [111] H. Brune, Epitaxial Growth of Thin Films, in: *Surf. Interface Sci.*, Wiley-VCH Verlag GmbH & Co. KGaA, 2013: pp. 421–492. doi:10.1002/9783527680566.ch20.
- [112] J.G. Kim, J. Yu, Behavior of residual stress on CVD diamond films, *Mater. Sci. Eng. B.* 57 (1998) 24–27. doi:10.1016/S0921-5107(98)00215-3.
- [113] M.D. Drory, J.W. Hutchinson, Measurement of the Adhesion of a Brittle Film on a Ductile Substrate by Indentation, *Proc. R. Soc. A Math. Phys. Eng. Sci.* 452 (1996) 2319–2341. doi:10.1098/rspa.1996.0124.
- [114] E. Chason, B.W. Sheldon, L.B. Freund, J.A. Floro, S.J. Hearne, Origin of Compressive Residual Stress in Polycrystalline Thin Films, *Phys. Rev. Lett.* 88 (2002) 156103. <http://link.aps.org/doi/10.1103/PhysRevLett.88.156103>.
- [115] F. Spaepen, Interfaces and stresses in thin films, *Acta Mater.* 48 (2000) 31–42. doi:10.1016/S1359-6454(99)00286-4.
- [116] R.W. Hoffman, Stress distributions and thin film mechanical properties, *Surf. Interface Anal.* 3 (1981) 62–66. doi:10.1002/sia.740030113.
- [117] F.A. Doljack, R.W. Hoffman, The origins of stress in thin nickel films, *Thin Solid Films.* 12 (1972) 71–74. doi:10.1016/0040-6090(72)90396-3.
- [118] W.D. Nix, B.M. Clemens, Crystallite coalescence: A mechanism for intrinsic tensile stresses in thin films, *J. Mater. Res.* 14 (1999) 3467–3473.
- [119] L.B. Freund, E. Chason, Model for stress generated upon contact of neighboring islands on the surface of a substrate, *J. Appl. Phys.* 89 (2001).
- [120] G. Thurner, R. Abermann, Internal stress and structure of ultrahigh vacuum evaporated chromium and iron films and their dependence on substrate temperature and oxygen partial pressure during deposition, *Thin Solid Films.* 192 (1990) 277–285. doi:10.1016/0040-6090(90)90072-L.
- [121] A.C. Ferrari, S.E. Rodil, J. Robertson, W.I. Milne, Is stress necessary to stabilise sp<sup>3</sup> bonding in diamond-like carbon?, *Diam. Relat. Mater.* 11 (2002) 994–999. doi:10.1016/S0925-9635(01)00705-1.
- [122] M.F. Doerner, W.D. Nix, Stresses and deformation processes in thin films on substrates, *Crit. Rev. Solid State Mater. Sci.* 14 (1988) 225–268. doi:10.1080/10408438808243734.
- [123] V.G. Ralchenko, A.A. Smolin, V.G. Pereverzev, E.D. Obraztsova, K.G. Korotoushenko, V.I. Konov, et al., Diamond deposition on steel with CVD tungsten intermediate layer, *Diam. Relat. Mater.* 4 (1995) 754–758. doi:10.1016/0925-9635(94)05299-9.
- [124] M.M. Nagl, W.T. Evans, The mechanical failure of oxide scales under tensile or compressive load, *J. Mater. Sci.* 28 (1993) 6247–6260. doi:10.1007/BF01352181.
- [125] S. Praver, R.J. Nemanich, Raman spectroscopy of diamond and doped diamond., *Philos. Trans. A. Math. Phys. Eng. Sci.* 362 (2004) 2537–65. doi:10.1098/rsta.2004.1451.
- [126] H. Gomez, D. Durham, X. Xiao, M. Lukitsch, P. Lu, K. Chou, et al., Adhesion analysis and dry machining performance of CVD diamond coatings deposited on surface modified WC–Co turning inserts, *J. Mater. Process. Technol.* 212 (2012) 523–533. doi:10.1016/j.jmatprotec.2011.10.020.
- [127] G.C.A.M. Janssen, Stress and strain in polycrystalline thin films, *Thin Solid Films.* 515 (2007) 6654–6664. doi:10.1016/j.tsf.2007.03.007.

- [128] F. a Kandil, J.D. Lord, a T. Fry, P. V Grant, A review of residual stress measurement methods - A guide to technical selection, 2001.
- [129] S. Suresh, A.E. Giannakopoulos, A new method for estimating residual stresses by instrumented sharp indentation, *Acta Mater.* 46 (1998) 5755–5767. doi:10.1016/S1359-6454(98)00226-2.
- [130] U. Welzel, J. Ligot, P. Lamparter, a. C. Vermeulen, E.J. Mittemeijer, Stress analysis of polycrystalline thin films and surface regions by X-ray diffraction, *J. Appl. Crystallogr.* 38 (2005) 1–29. doi:10.1107/S0021889804029516.
- [131] E. Anastassakis, A. Pinczuk, E. Burstein, F.H. Pollak, M. Cardona, Effect of static uniaxial stress on the Raman spectrum of silicon, *Solid State Commun.* 8 (1970) 133–138. doi:10.1016/0038-1098(70)90588-0.
- [132] I. DeWolf, Raman Spectroscopy: About Chips and Stress, *Spectrosc. Eur.* 15 (2003) 6–13.
- [133] J.W. Ager, M.D. Drory, Quantitative measurement of residual biaxial stress by Raman spectroscopy in diamond grown on a Ti alloy by chemical vapor deposition, *Phys. Rev. B.* 48 (1993) 2601–2607. [http://prb.aps.org/abstract/PRB/v48/i4/p2601\\_1](http://prb.aps.org/abstract/PRB/v48/i4/p2601_1) (accessed July 22, 2013).
- [134] D. Liu, P.E.J. Flewitt, Chapter 5 Raman measurements of stress in films and coatings, in: *Spectrosc. Prop. Inorg. Organomet. Compd. Vol. 45*, The Royal Society of Chemistry, 2014: pp. 141–177. doi:10.1039/9781782621485-00141.
- [135] T. Gries, L. Vandenbulcke, P. Simon, A. Canizares, Polarized micro-Raman spectroscopy for studying stresses in as-grown and tensile-tested diamond films, *Surf. Coatings Technol.* 202 (2008) 2263–2267. doi:10.1016/j.surfcoat.2007.08.050.
- [136] M. Rudigier, R. Haubner, Characterisation of diamond coatings with different morphologies by Raman spectroscopy using various laser wavelengths., *Anal. Bioanal. Chem.* 403 (2012) 675–81. doi:10.1007/s00216-012-5808-y.
- [137] A.C. Ferrari, J. Robertson, Origin of the 1150-cm<sup>-1</sup> Raman mode in nanocrystalline diamond, *Phys. Rev. B.* 63 (2001) 121405. doi:10.1103/PhysRevB.63.121405.
- [138] H. Windischmann, K.J. Gray, Stress measurement of CVD diamond films, *Diam. Relat. Mater.* 4 (1995) 837–842. doi:10.1016/0925-9635(94)05327-8.
- [139] A.A. Volinsky, N.R. Moody, W.W. Gerberich, Interfacial toughness measurements for thin films on substrates, *Acta Mater.* 50 (2002) 441–466. doi:10.1016/S1359-6454(01)00354-8.
- [140] A.A. Volinsky, D.F. Bahr, M.D. Kriese, N.R. Moody, W. Gerberich, *Comprehensive Structural Integrity*, Elsevier, 2003. doi:10.1016/B0-08-043749-4/08142-8.
- [141] K.L. Mittal, Adhesion Measurement of Thin Films, *Electrocompon. Sci. Technol.* 3 (1976) 21–42. doi:10.1155/APEC.3.21.
- [142] S. Zhang, D. Sun, Y. Fu, H. Du, Toughness measurement of thin films: a critical review, *Surf. Coatings Technol.* 198 (2005) 74–84. doi:10.1016/j.surfcoat.2004.10.021.
- [143] J. Malzbender, J.M.J. den Toonder, A.R. Balkenende, G. de With, Measuring mechanical properties of coatings: a methodology applied to nano-particle-filled sol-gel coatings on glass, *Mater. Sci. Eng. R Reports.* 36 (2002) 47–103. doi:10.1016/S0927-796X(01)00040-7.
- [144] W.C. Oliver, G.M. Pharr, Measurement of hardness and elastic modulus by instrumented indentation: Advances in understanding and refinements to methodology, *J. Mater. Res.* 19 (2004) 3–20. doi:10.1557/jmr.2004.19.1.3.

- [145] K. Herrmann, *Hardness Testing - Principles and Applications*, ASM International, 2011.  
[http://app.knovel.com/web/toc.v/cid:kpHTPA0004/viewerType:toc/root\\_slug:hardness-testing-principles/url\\_slug:hardness-testing-principles/](http://app.knovel.com/web/toc.v/cid:kpHTPA0004/viewerType:toc/root_slug:hardness-testing-principles/url_slug:hardness-testing-principles/) (accessed February 14, 2015).
- [146] W. Heinke, A. Leyland, A. Matthews, G. Berg, C. Friedrich, E. Broszeit, Evaluation of PVD nitride coatings, using impact, scratch and Rockwell-C adhesion tests, *Thin Solid Films*. 270 (1995) 431–438. doi:10.1016/0040-6090(95)06934-8.
- [147] N. Vidakis, A. Antoniadis, N. Bilalis, The VDI 3198 indentation test evaluation of a reliable qualitative control for layered compounds, *J. Mater. Process. Technol.* 143-144 (2003) 481–485. doi:10.1016/S0924-0136(03)00300-5.
- [148] Y. Xie, H. Hawthorne, Effect of contact geometry on the failure modes of thin coatings in the scratch adhesion test, *Surf. Coatings Technol.* 155 (2002) 121–129. doi:10.1016/S0257-8972(02)00064-6.
- [149] S.J. Bull, Failure mode maps in the thin film scratch adhesion test, *Tribol. Int.* 30 (1997) 491–498. doi:10.1016/S0301-679X(97)00012-1.
- [150] S.J. Bull, E.G. Berasetegui, An overview of the potential of quantitative coating adhesion measurement by scratch testing, *Tribol. Int.* 39 (2006) 99–114. doi:10.1016/j.triboint.2005.04.013.
- [151] Y. Hamaguchi, *Optical microscopy*, Tanpakushitsu Kakusan Koso. 42 (1997) 1026–1032. doi:10.1002/0471143030.cb1206s17.
- [152] D.B. Murphy, *Fundamentals of light microscopy and Electronic*, Wiley-Liss, Inc., 2001.
- [153] Z. Wang, W. Guo, L. Li, B. Luk'yanchuk, A. Khan, Z. Liu, et al., Optical virtual imaging at 50 nm lateral resolution with a white-light nanoscope, *Nat Commun.* 2 (2011) 218. <http://dx.doi.org/10.1038/ncomms1211>.
- [154] P.J. Goodhew, J. Humphreys, R. Beanland, The scanning electron microscope, in: *Electron Microsc. Anal.*, Third, Taylor & Francis, 2000: p. 65.
- [155] J. Zach, M. Haider, Aberration correction in a low voltage SEM by a multipole corrector, *Nucl. Instruments Methods Phys. Res. Sect. A Accel. Spectrometers, Detect. Assoc. Equip.* 363 (1995) 316–325. doi:10.1016/0168-9002(95)00056-9.
- [156] F.J. Giessibl, AFM's path to atomic resolution, *Mater. Today*. 8 (2005) 32–41. doi:10.1016/S1369-7021(05)00844-8.
- [157] S.N. Magonov, D.H. Reneker, CHARACTERIZATION OF POLYMER SURFACES WITH ATOMIC FORCE MICROSCOPY, *Annu. Rev. Mater. Sci.* 27 (1997) 175–222. doi:10.1146/annurev.matsci.27.1.175.
- [158] R.L. McCreery, *Collection and Detection of Raman Scattering*, in: *Raman Spectrosc. Chem. Anal.*, John Wiley & Sons, Inc., 2005: pp. 35–47. doi:10.1002/0471721646.ch3.
- [159] E. Smith, G. Dent, *Modern Raman Spectroscopy — A Practical Approach*, 2005. doi:10.1002/jrs.1320.
- [160] P.L. Stiles, J.A. Dieringer, N.C. Shah, R.P. Van Duyne, *Surface-Enhanced Raman Spectroscopy*, (2008). doi:10.1146/annurev.anchem.1.031207.112814.
- [161] I.R. Lewis, H.G.M. Edwards, eds., *Handbook of Raman Spectroscopy: From the Research Laboratory to the Process Line*, First, CRC Press, 2001.
- [162] J. Lauer, *Raman Spectra of Quasi-Elemental Carbon*, in: *Handb. Raman Spectrosc.*, CRC Press, 2001. doi:doi:10.1201/9781420029253.ch22.

- [163] S. Kaciulis, Spectroscopy of carbon: from diamond to nitride films, *Surf. Interface Anal.* (2012). doi:10.1002/sia.4892.
- [164] A. Whitley, The Use of Raman Spectroscopy to Monitor the Quality of Carbon Overcoats in the Disk Drive Industry, in: *Handb. Raman Spectrosc.*, CRC Press, 2001. doi:10.1201/9781420029253.ch24.
- [165] O.A. Williams, A. Kriele, J. Hees, M. Wolfer, W. Müller-Sebert, C.E. Nebel, High Young's modulus in ultra thin nanocrystalline diamond, *Chem. Phys. Lett.* 495 (2010) 84–89. doi:10.1016/j.cplett.2010.06.054.
- [166] A.C. Ferrari, J. Robertson, Resonant Raman spectroscopy of disordered, amorphous, and diamondlike carbon, *Phys. Rev. B.* 64 (2001) 1–13. doi:10.1103/PhysRevB.64.075414.
- [167] S.M. Huang, Z. Sun, Y.F. Lu, M.H. Hong, Ultraviolet and visible Raman spectroscopy characterization of chemical vapor deposition diamond films, *Surf. Coatings Technol.* 151-152 (2002) 263–267. doi:10.1016/S0257-8972(01)01566-3.
- [168] J. Filik, Raman spectroscopy : a the lightest touch, *Spectrosc. Eur.* 17 (2005) 10–16. <http://www.chm.bris.ac.uk/pt/diamond/pdf/se17.pdf> (accessed October 3, 2013).
- [169] P.W. May, J.A. Smith, K.N. Rosser, 785 nm Raman Spectroscopy of CVD Diamond Films, in: *Symp. P – Diam. Electron. to Appl. II*, 2007. doi:10.1557/PROC-1039-P15-02.
- [170] M. Birkholz, Principles of X-ray Diffraction, in: *Thin Film Anal. by X-Ray Scatt.*, Wiley-VCH Verlag GmbH & Co. KGaA, 2005: pp. 1–40. doi:10.1002/3527607595.ch1.
- [171] C.C. Chusuei, D.W. Goodman, X-Ray Photoelectron Spectroscopy, *Encycl. Phys. Sci. Technol.* (Third Ed. (2003) 921–938. doi:10.1016/B0-12-227410-5/00830-9.
- [172] G.M. Wilson, An investigation of thin amorphous carbon-based sputtered coatings for MEMS and micro-engineering applications, Aston University, 2008.
- [173] J.G. Huang, P. Liatsis, K. Cooke, Improving Measurement Repeatability of Ball Crater Method by Using Image Processing Techniques, *Proc. Int. MultiConference Eng. Comput. Sci. I* (2011) 16–19.
- [174] Teer Coatings Ltd, ST-3001 Scratch Test Device, (2015).
- [175] C. Hojerslev, Tool Steels, Riso Natioanl Laboratory, Roskilde, 2001. [http://orbit.dtu.dk/fedora/objects/orbit:88113/datastreams/file\\_7728903/content](http://orbit.dtu.dk/fedora/objects/orbit:88113/datastreams/file_7728903/content).
- [176] ASTM A600-90a(2004), Standard Specification for Tool Steel High Speed, ASTM International, West Conshohocken, PA, 2004. doi:10.1520/A0600-92AR04.
- [177] R. Pfeiffer, H. Kuzmany, P. Knoll, S. Bokova, N. Salk, B. Günther, Evidence for trans-polyacetylene in nano-crystalline diamond films, *Diam. Relat. Mater.* 12 (2003) 268–271. doi:10.1016/S0925-9635(02)00336-9.
- [178] E.D. Obraztsova, K.G. Korotushenko, S.M. Pimenov, V.G. Ralchenko, A.A. Smolin, V.I. Konov, et al., Raman and photoluminescence investigations of nanograined diamond films, *Nanostructured Mater.* 6 (1995) 827–830. doi:10.1016/0965-9773(95)00187-5.
- [179] A.K. Arora, M. Rajalakshmi, T.R. Ravindran, V. Sivasubramanian, Raman spectroscopy of optical phonon confinement in nanostructured materials, *J. Raman Spectrosc.* 38 (2007) 604–617. doi:10.1002/jrs.1684.
- [180] N.N. Naguib, J.W. Elam, J. Birrell, J. Wang, D.S. Grierson, B. Kabius, et al., Enhanced nucleation, smoothness and conformality of ultrananocrystalline diamond (UNCD) ultrathin films via tungsten interlayers, *Chem. Phys. Lett.* 430 (2006) 345–350. doi:10.1016/j.cplett.2006.08.137.

- [181] C.Z. Zhang, H. Niakan, L. Yang, Y.S. Li, Y.F. Hu, Q. Yang, Study of diamond nucleation and growth on Ti6Al4V with tungsten interlayer, *Surf. Coatings Technol.* 237 (2013) 248–254. doi:10.1016/j.surfcoat.2013.05.049.
- [182] G.A. Slack, S.F.F. Bartram, Thermal expansion of some diamondlike crystals, *J. Appl. Phys.* 46 (1975) 89–98. doi:10.1063/1.321373.
- [183] Böhler, Böhler S500 Material Data Steet, (2008) 12. <http://www.boehler-edelstahl.com/english/files/S500DE.pdf>.
- [184] G. Box, J. Hunter, W. Hunter, *Statistics for experimenters: design, innovation, and discovery*, 2nd ed., John Wiley & Sons, Inc., New Jersey, 2005. <http://onlinelibrary.wiley.com/higheredbcs/WileyCDA/WileyTitle/productCd-0471718130.html?0471718130=> (accessed September 24, 2013).
- [185] J. Gerth, U. Wiklund, The influence of metallic interlayers on the adhesion of PVD TiN coatings on high-speed steel, *Wear.* 264 (2008) 885–892. doi:10.1016/j.wear.2006.11.053.
- [186] P. Franke, D. Neuschütz, eds., *Binary Systems from Mn-Mo to Y-Zr*, Springer Berlin Heidelberg, 2006. doi:10.1007/b76778.
- [187] a. S. Kurlov, a. I. Gusev, Tungsten carbides and W-C phase diagram, *Inorg. Mater.* 42 (2006) 121–127. doi:10.1134/S0020168506020051.
- [188] V. Kunderát, X. Zhang, K. Cooke, H. Sun, J. Sullivan, H. Ye, A novel Mo-W interlayer approach for CVD diamond deposition on steel, *AIP Adv.* 5 (2015). doi:10.1063/1.4918969.
- [189] I. Endler, A. Leonhardt, H.-J. Scheibe, R. Born, Interlayers for diamond deposition on tool materials, *Diam. Relat. Mater.* 5 (1996) 299–303. doi:10.1016/0925-9635(95)00352-5.
- [190] D.C. Carter, Arc Prevention in Magnetron Sputtering Processes, *Soc. Vac. Coaters.* (2008) 380–385.
- [191] J.G. Buijnsters, P. Shankar, J.J. ter Meulen, Direct deposition of polycrystalline diamond onto steel substrates, *Surf. Coatings Technol.* 201 (2007) 8955–8960. doi:10.1016/j.surfcoat.2007.04.012.
- [192] E. Lassner, W.W.-D. Schubert, *Tungsten: Properties, Chemistry, Technology of the Elements, Alloys, and Chemical Compounds*, Springer Science & Business Media, New York, 1999. <http://books.google.com/books?hl=en&lr=&id=foLRISkt9gcC&oi=fnd&pg=PA1&dq=Tungsten:+Properties,+Chemistry,+Technology+of+the+Element,+Alloys,+and+Chemical+Compounds&ots=-tsMF5nZBX&sig=WUgMFJApEOTZX1vp9Qhtle9OnEo> (accessed August 21, 2014).
- [193] C.-C. Chen, F.C.-N. Hong, Interfacial studies for improving the adhesion of diamond-like carbon films on steel, *Appl. Surf. Sci.* 243 (2005) 296–303. doi:10.1016/j.apsusc.2004.09.085.
- [194] S.K. Field, M. Jarratt, D.G. Teer, Tribological properties of graphite-like and diamond-like carbon coatings, *Tribol. Int.* 37 (2004) 949–956. doi:10.1016/j.triboint.2004.07.012.
- [195] I.B. Yanchuk, M.Y. Valakh, A.Y. Vul', V.G. Golubev, S.A. Grudinkin, N.A. Feoktistov, et al., Raman scattering, AFM and nanoindentation characterisation of diamond films obtained by hot filament CVD, *Diam. Relat. Mater.* 13 (2004) 266–269. doi:10.1016/j.diamond.2003.11.001.

- [196] T.P. Mollart, K.L. Lewis, C.S.J. Pickles, C.J.H. Wort, Factors affecting the optical performance of CVD diamond infrared optics, *Semicond. Sci. Technol.* 18 (2003) S117–S124. doi:10.1088/0268-1242/18/3/317.
- [197] R.L. McCreery, Raman Spectroscopy of Surfaces, in: *Raman Spectrosc. Chem. Anal.*, John Wiley & Sons, Inc., 2005: pp. 373–413. doi:10.1002/0471721646.ch13.
- [198] D. Das, R.N. Singh, A review of nucleation, growth and low temperature synthesis of diamond thin films, *Int. Mater. Rev.* 52 (n.d.) 29–64. <http://www.ingentaconnect.com/content/maney/imr/2007/00000052/00000001/art00003>.
- [199] E.W. Lemmon, M.O. McLinden, D.G. Friend, NIST Standard Reference Database Number 69, NIST Chem. Webb. (n.d.) 20899. <http://webbook.nist.gov> (accessed July 20, 2015).
- [200] C. Wild, N. Herres, P. Koidl, Texture formation in polycrystalline diamond films, *J. Appl. Phys.* 68 (1990) 973. doi:10.1063/1.346663.
- [201] H.-L. Chen, Y.-M. Lu, W.-S. Hwang, Effect of Film Thickness on Structural and Electrical Properties of Sputter-Deposited Nickel Oxide Films, *Mater. Trans.* 46 (2005) 872–879. doi:10.2320/matertrans.46.872.
- [202] P. Lu, H. Gomez, X. Xiao, M. Lukitsch, D. Durham, A. Sachdev, et al., Coating thickness and interlayer effects on CVD-diamond film adhesion to cobalt-cemented tungsten carbides, *Surf. Coatings Technol.* 215 (2013) 272–279. doi:10.1016/j.surfcoat.2012.08.093.
- [203] I.M. Hutchings, *Tribology: Friction and Wear of Engineering Materials*, Elsevier Ltd., 1992.
- [204] J.G. Buijnsters, P. Shankar, W.J.P. van Enckevort, J.J. Schermer, J.J. ter Meulen, The adhesion of hot-filament CVD diamond films on AISI type 316 austenitic stainless steel, *Diam. Relat. Mater.* 13 (2004) 848–857. doi:10.1016/j.diamond.2003.11.012.
- [205] J.J. Friel, C.E. Lyman, X-ray mapping in electron-beam instruments, *Microsc. Microanal.* 12 (2006) 2–25. doi:10.1017/S1431927606060211.
- [206] S. Schwarz, S.M. Rosiwal, M. Frank, D. Breidt, R.F. Singer, Dependence of the growth rate, quality, and morphology of diamond coatings on the pressure during the CVD-process in an industrial hot-filament plant, *Diam. Relat. Mater.* 11 (2002) 589–595. doi:10.1016/S0925-9635(01)00702-6.
- [207] M. Mohr, A. Caron, P. Herbeck-Engel, R. Bennewitz, P. Gluche, K. Brühne, et al., Young's modulus, fracture strength, and Poisson's ratio of nanocrystalline diamond films, *J. Appl. Phys.* 116 (2014) -. doi:<http://dx.doi.org/10.1063/1.4896729>.
- [208] J. Philip, P. Hess, T. Feygelson, J.E. Butler, S. Chattopadhyay, K.H. Chen, et al., Elastic, mechanical, and thermal properties of nanocrystalline diamond films, *J. Appl. Phys.* 93 (2003) 2164. doi:10.1063/1.1537465.
- [209] J. Sermeus, B. Verstraeten, R. Salenbien, P. Pobedinskas, K. Haenen, C. Glorieux, Determination of elastic and thermal properties of a thin nanocrystalline diamond coating using all-optical methods, *Thin Solid Films.* (2015). doi:10.1016/j.tsf.2015.08.007.
- [210] H. Tanei, K. Tanigaki, K. Kusakabe, H. Ogi, N. Nakamura, M. Hirao, Stacking-fault structure explains unusual elasticity of nanocrystalline diamonds, *Appl. Phys. Lett.* 94 (2009) -. doi:<http://dx.doi.org/10.1063/1.3077124>.

- [211] C. Bareiß, M. Perle, S.M. Rosiwal, R.F. Singer, Diamond coating of steel at high temperatures in hot filament chemical vapour deposition (HFCVD) employing chromium interlayers, *Diam. Relat. Mater.* 15 (2006) 754–760. doi:10.1016/j.diamond.2005.10.053.
- [212] S.Y. Luo, J.-K. Kuo, B. Yeh, J.C. Sung, C.-W. Dai, T.J. Tsai, The tribology of nano-crystalline diamond, *Mater. Chem. Phys.* 72 (2001) 133–135. doi:10.1016/S0254-0584(01)00422-9.

## 8 Appendix

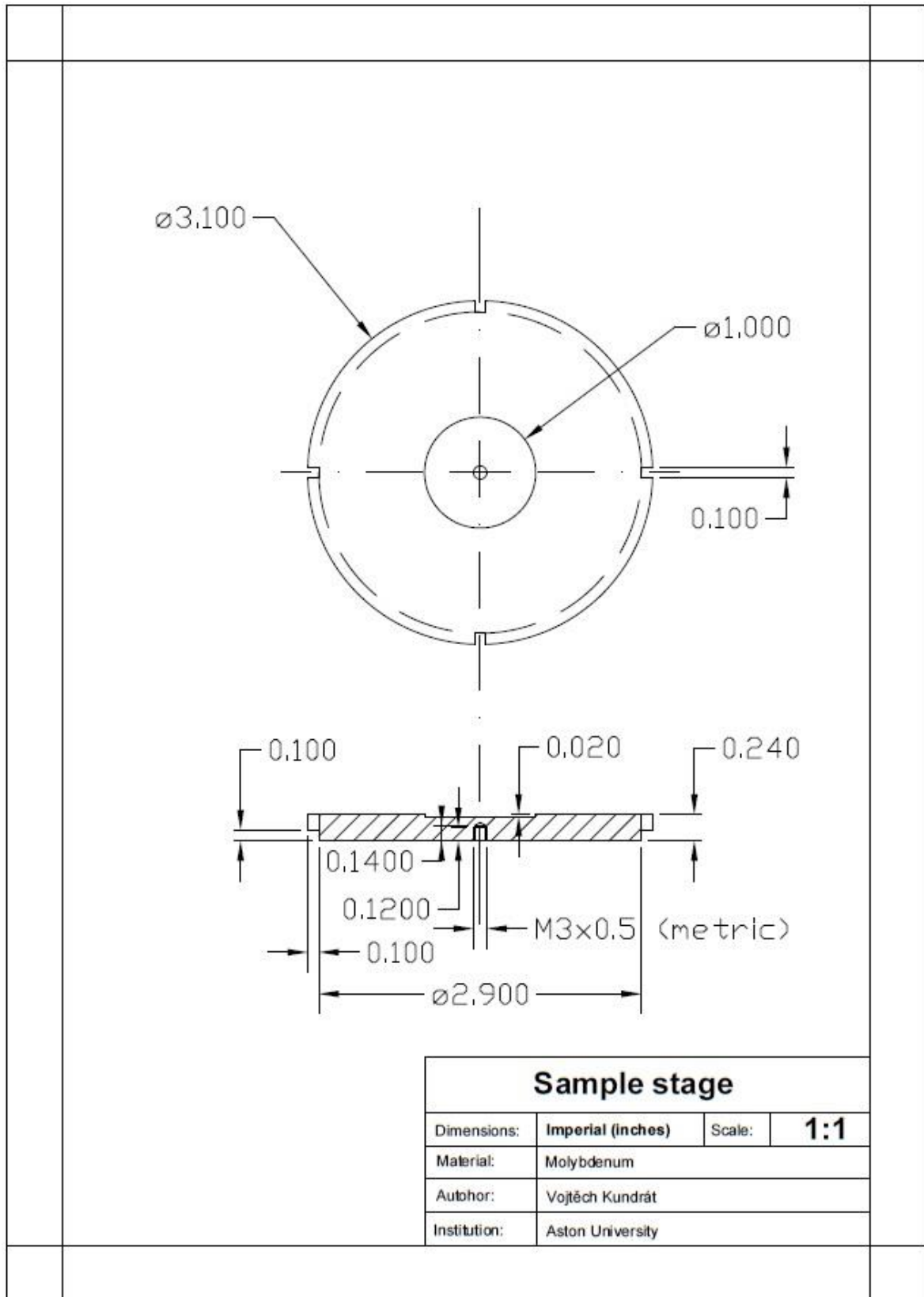


Figure 8.1 Copy of drawing of shallow sample holder.

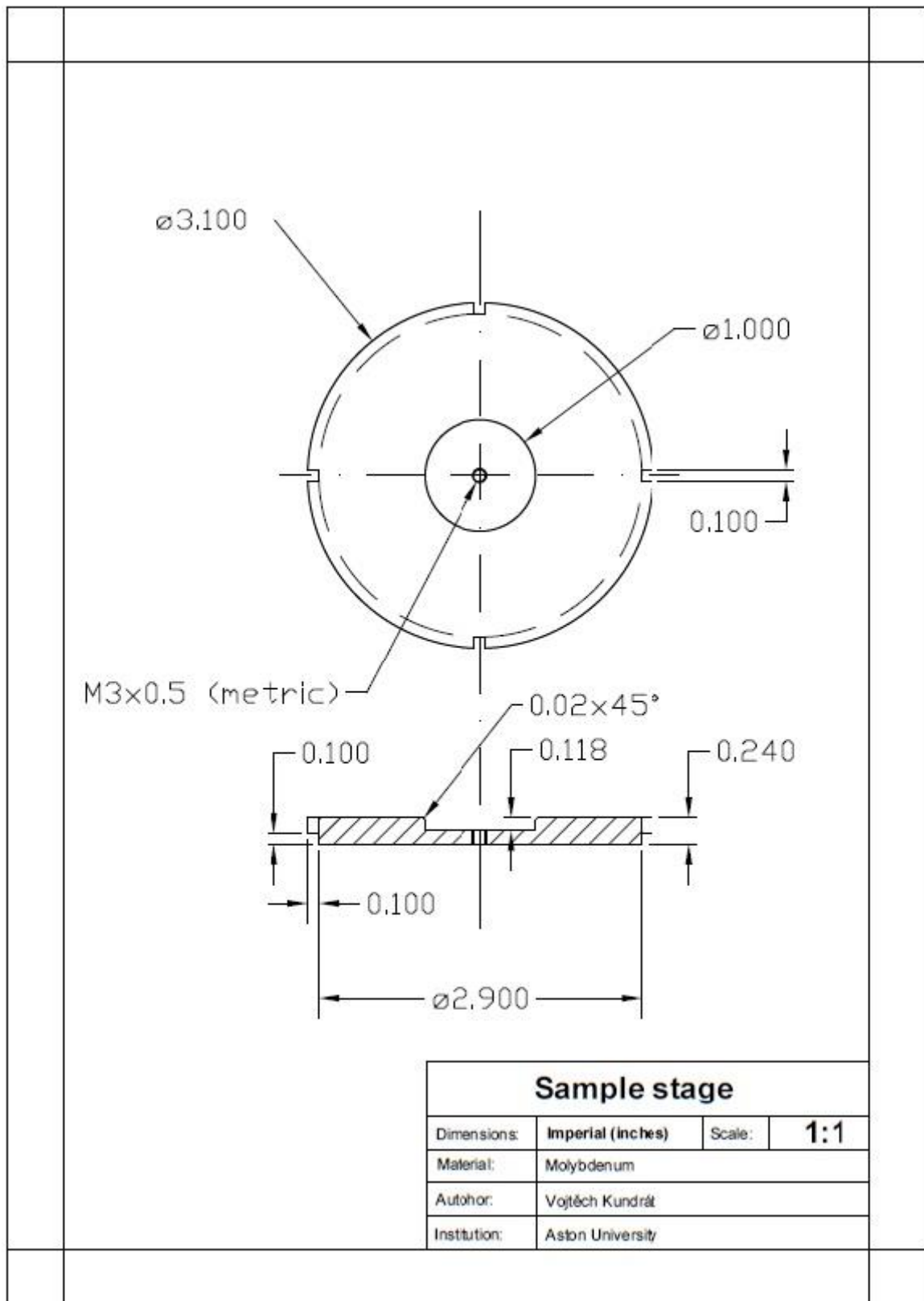


Figure 8.2 Copy of drawing of deep sample holder.